Discovery and Characterization of a Higgs boson using four-lepton events from the CMS experiment

by

Christopher B. Martin

A dissertation submitted to The Johns Hopkins University in conformity with the requirements for the degree of Doctor of Philosophy.

Baltimore, Maryland

July, 2015

© Christopher B. Martin 2015

All Rights Reserved

Abstract

A new particle decaying to a pair of vector bosons was discovered in 2012 by the ATLAS and CMS experiments at the Large Hadron Collider. In the wake of this discovery a rush of measurements was made to characterize this particle. The four-lepton final state has been instrumental in both the discovery and characterization of this new particle. With only about 20 events seen in the resonance peak at 125 GeV the CMS experiment has been able to make considerable progress in characterizing the Higgs-like boson using the wealth of information in this final state in concert with other decay modes. In addition to the search for this new boson we present three recent results in the study of the Higgs-like boson properties: studies of the production mode, total width, and spin-parity quantum numbers.

First we present the search for this new resonance using the $H \to ZZ \to 4\ell$ decay channel. Then we discuss the production mode measurement using this final state. Next, we present two results that provided breakthroughs in the study of the Higgs-like resonance. One is the measurement of the width from an interplay between the off-shell and on-shell production, setting a limit three orders of magnitude tighter

than previous limits. The other is the tensor structure measurement of the bosons interactions with pairs of vector bosons, leading to constraints on its spin-parity properties, where only limited measurements had been done before. All of these results provide further confirmation that CMS has discovered a Higgs boson near 125 GeV.

Primary Reader: Andrei Gritsan

Secondary Reader: Morris Swartz

Acknowledgements

I would be remiss to begin this section by thanking anyone other than my advisor Andrei. I consider myself lucky to have worked with you these past years. You are a brilliant scientist with great vision, insight, and determination. I will always appreciate the leadership you showed and the guidance, motivation, and confidence you instilled in me. I am thankful that I had the ability to learn invaluable skills such as organization and productivity from you.

Next I would like to thank my colleagues at JHU. Meng and Sara you are amazing scientists. You have taught me so much and I want to thank you for your patience throughout this process. Ian, you have kept me sane and together we have produced an amazing set of results, I wouldnÕt have made it without you. To all the current and former graduate students, I would like to thank you for all of your help in making these studies a reality. I can only hope that I have helped you with your work half as much as you have helped me.

To my colleagues in the CJLST working group, I have tried to say it many times but once more cannot hurt: I have benefited greatly from the impeccable wheel that

you have set in motion. It has been an uphill battle but at every turn we have met the call. I hope you understand the gratitude I have for your efforts.

To the CMS Higgs, HZZ, and Tracker Alignment working groups, I would like to thank you for the discussions (and arguments) we have had as well as the support, guidance, and patience you have shown. The CMS collaboration may be a large unwieldy group, but together we have produced amazing science and people.

I would also like to take an opportunity to thank the two professors who started me down this path: Prof. Alice Bean from the University of Kansas and Prof. Tim Bolton from Kansas State University. Each of you helped me begin this journey and I hope that you know how happy I am that you did.

While this document presents the peak of my scientific and academic achievements to date, I would also like to take some time to thank all of the people who turned me into a person capable of a work of this magnitude. I have had the great fortune of living with, working with, playing with, etc... some of the greatest people in the world.

To all of my friends in Genevé who made my two years there great, I want to say thanks and I hope to see you all again soon somewhere in this world. To all of my friends in Baltimore who helped me get through the difficult times with classes, exams, and medical emergencies, I want to say thank you for supporting and working with me. To my friends from Zürich who opened my eyes to the world beyond my home, I would like to say thank you. To my friends from Lawrence, I would like to

thank you for all the laughs and stories. Finally to all of my friends in Manhattan, you helped shape me into who I am and I cannot come close to repaying you for that. To all of you whom I have leaned on and learned from, I would like to thank you!

Lastly, I would like to take time to thank my family. I am so blessed to have such a large and loving family. As I began thinking about how many of you I owe thanks, I realized that there were too many of you to list explicitly. Instead, I will have to address most of you in groups.

To my Martin family, I would like to thank you for all of the support and love. Specifically, Grandma and Grandpa have been such an important presence in my life that no words can repay. You are the glue that holds together one of the most loving and caring families that has ever existed. To my aunts, uncles, and cousins: you have provided me with a wonderful family. Whether we are related by blood or experience, I want you all to know that I wouldnÕt trade our time together for anything.

To my Dysart family, I want to thank you for your encouragement and sacrifice. While I never got to know my Grandmother, I assume that she was one of the most loving and caring people based on how you live your lives . You have shown me so much support and love that I cannot imagine her any other way. I also would like to thank you and my Grandfather for teaching me the value of sacrifice and community. I see in all of you, and saw in him, individuals who choose to do things for those around them ahead of themselves. Whether for your immediate loved ones or for wider groups of people, at every turn, I see you looking to better everyones lives, not

just your own.

To my Rice/McGinnity family, I would like to thank you for making me a part of your lives. I am so happy to have been adopted by such a wonderful group of people. I would like to thank you for giving me your support and guidance. I am so happy to see our family growing!

To my parents Susan Dysart-Martin and Randy Martin, thank you. I could try to put together a list of ways that you have helped me get to this point, but it would be woefully incomplete. Everything I am, I owe to you. For the support, encouragement, advice, drive, passion - for everything - thank you. None of this work could have happened without you. This is a testament to you as people and parents, thank you.

Finally I would like to thank my sister Layne Elizabeth Martin. You may not know or believe it, but you are my brightest inspiration. I constantly feel like an older brother who needs to prove to his younger sister that he can keep up. You are passionate, driven, caring, and selfless. I am so lucky that you are in my corner and I will always be there for you.

Contents

Abstract **ii**

Acknowledgements **iv**

List of Tables **xiv**

List of Figures **xvii**

1 Introduction **1**

1.1 Symmetries in Physics 2

1.1.1 Noether's Theorem 2

1.1.2 Angular Momentum and the Rotation Group 3

1.1.3 Inherent Spin and SU(2) 5

1.2 Scattering Amplitudes 7

1.2.1 Scattering Matrix 7

1.2.2 Amplitudes and Feynman Diagrams 8

1.3 The Standard Model 12

1.3.1 Matter 14

1.3.1.1 Quarks 14

1.3.1.2 Leptons 16

1.3.2 Forces 17

1.3.3 Electroweak Symmetry Breaking 21

1.3.3.1 Implications of the Higgs field: Fermion Masses . . . 29

1.4 Limitations of the SM: Higgs boson as a tool 30

1.4.1 CP-violation: The Matter-Antimatter Asymmetry 31

1.4.2 The Graviton: An Unexplained Force 33

1.4.3 Beyond the SM: The Dark Matter, Hierarchy & Fermion Problems 34

2 The Experiment: LHC and CMS 36

2.1 The Large Hadron Collider (LHC) 37

2.2 The Compact Muon Solenoid (CMS) 42

2.2.1 The Magnet 46

2.2.2 The Inner Tracker System 49

2.2.2.1 Pixel Tracker 49

2.2.2.2 Strip Tracker 52

2.2.3 Electromagnetic Calorimeter 54

2.2.4 Hadronic Calorimeter 57

2.2.5 Muon System 60

2.3 Triggering and Particle Reconstruction 65

2.3.1 CMS Trigger 65

2.3.2 Particle Flow 67

2.3.3 Electrons 68

2.3.4 Muons 72

2.3.5 Jets 74

2.4 CMS Tracker Alignment 75

2.4.1 Silicon Pixel Alignment in Prompt Calibration Loop 79

3 Higgs boson at the LHC: Phenomenology 87

3.1 Higgs boson production at LHC 88

3.2 Higgs boson decay to $ZZ \to 4\ell$ 92

3.3 Higgs boson width: off resonance production and decay 96

3.4 Spin and Parity of a Single-Produced Resonance 103

3.4.1 Decay of a spin-zero resonance 104

3.4.2 Decay of a spin-one resonance 107

3.4.3 Decay of a spin-two resonance 108

4 $H \to ZZ \to 4\ell$ search & Production Mechanism 111

4.1 General overview of $H \to ZZ \to 4l$ 112

4.2 Object Selection 113

4.3 Event Selection, Simulation, & Categorization 116

4.3.1 Simulated Data Samples 116

4.3.2 Selection & Categorization 117

4.3.3 Background estimation 119

4.4 Kinematic Distributions 123

4.4.1 Four-lepton mass spectrum 124

4.4.2 Matrix Element Likelihood Approach (MELA) kinematic discriminant 126

4.4.3 Transverse momentum and Jet Kinematic Discriminant 132

4.5 Search Results 137

4.5.1 Quantifying the observation 142

4.5.2 Search for additional Higgs bosons 149

4.6 Production Mechanism Results 151

5 Total Width of the Higgs Boson 154

5.1 General Overview of Width Measurement 154

5.2 Event Selection, Simulation, & Categorization 156

5.2.1 Simulated Data Samples 158

5.3 Kinematic Distributions 160

5.3.1 Four-lepton mass spectrum 160

5.3.2 Four-lepton MELA discriminant 163

5.3.3 $2\ell 2\nu$ m_T discriminant 166

5.4 Off Resonance Width Results 167

5.4.1 Fitting for Width 170

6 Spin & Parity of a Higgs Boson **176**

6.1 Summary of Spin/Parity Measurements 177

6.2 Simulated Data and 4ℓ Selection 179

6.2.1 Simulated Data 182

6.3 MELA Spin/Parity Analysis 183

6.3.1 Observables in the $H \to VV \to 4\ell$ analysis 183

6.3.2 MELA Observables 186

6.4 Spin/Parity Results 192

6.4.1 Likelihood fits 192

6.4.2 Exotic-spin study with the $H \to ZZ \to 4\ell$ channel 195

6.4.3 Study of spin-zero HVV couplings 200

6.4.3.1 Study of HZZ couplings with the $H \to ZZ \to 4\ell$ channel 200

6.4.3.2 Study of $HZ\gamma$ and $H\gamma\gamma$ couplings with the $H \to VV \to 4\ell$ channel 206

7 Conclusions & Extensions **211**

7.1 $H \to ZZ \to 4\ell$ Search & Production Mechanism 212

7.1.1 Extensions 213

7.2 $H \to ZZ$ Constraints on Total Width 215

7.2.1 Extensions 216

7.3 $H \to VV \to 4\ell$ Spin/Parity Measurements 218

7.3.1 Extensions 219

7.4 Implications: What did we find? 221

Bibliography **224**

Vita **245**

List of Tables

1.1 First generation fermions and their different charges, grouped in left(right)-handed doublets(singlets). 17

1.2 List of Fundamental Forces their relative strengths and ranges. 20

2.1 Parameters of the CMS superconducting solenoid. 47

2.2 Detector types in the silicon strip tracker. 53

3.1 List of spin-two models with the decay couplings of an exotic X particle. The subscripts m (minimal couplings), h (couplings with higher-dimension operators), and b (bulk) distinguish different scenarios. . . 110

4.1 The number of observed candidate events compared to the mean expected background and signal rates for each final state. Uncertainties include statistical and systematic sources. The results are given integrated over the full mass measurement range $m_{4\ell} > 100$ GeV and for 7 and 8 TeV data combined. 123

4.2 The number of observed candidate events compared to the mean expected background and signal rates for each final state. Uncertainties include statistical and systematic sources. The results are integrated over the mass range from 121.5 to 130.5 GeV and for 7 and 8 TeV data combined. 137

4.3 The number of observed candidate events compared to the mean expected background and signal rates for the sum of the three final states for each of the two analysis categories. Uncertainties include statistical and systematic sources. The results are integrated over the mass range from 121.5 to 130.5 GeV and for 7 and 8 TeV data combined. The expected signal yield for a SM Higgs boson with $m_H = 126$ GeV is reported, broken down by the production mechanism. 139

4.4 Effect of systematic uncertainties on the yields of signal ($m_H = 126$ GeV) and background processes for the 8 TeV data set and 0/1-jet category. Uncertainties appearing on the same line are 100% correlated, with two exceptions: those related to the missing higher orders are not correlated, and those from the α_S + PDF (gg) in $t\bar{t}H$ are 100% anti-correlated. Uncertainties for the 7 TeV data set are similar. 141

5.1 Expected and observed number of events for $m_{ZZ} \geq 220$ GeV per channel and for the sum of the $4e$, 4μ and $2e2\mu$ channels. The numbers for the gg signal and the total gg contribution are given for $\mu = 1$ (SM). The numbers correspond to the sum of 7 and 8 TeV data. VBF errors are negligible with respect to the corresponding gg sources, so they are not reported. 167

5.2 Expected and observed numbers of events in the 4ℓ and $2\ell2\nu$ channels in gg-enriched regions, defined by $m_{4\ell} \geq 330$ GeV and $\mathcal{D}_{gg} > 0.65$ (4ℓ), and by $m_T > 350$ GeV and $E_T^{\text{miss}} > 100$ GeV ($2\ell2\nu$). The numbers of expected events are given separately for the gg and VBF processes, and for a SM Higgs boson ($\Gamma_H = \Gamma_H^{\text{SM}}$) and a Higgs boson width and squared product of the couplings scaled by a factor 10 with respect to their SM values. The unphysical expected contributions for the signal and background components are also reported separately, for the gg and VBF processes. For both processes, the sum of the signal and background components differs from the total due to the negative interferences. The quoted uncertainties include only the systematic sources. 168

5.3 Detailed fit results on the signal strength in several combinations from the 4ℓ final state on and off resonance peak. The μ column represents alternative fits where we make the hypothesis $\mu_{\text{VBF}} = \mu_{\text{ggH}} = \mu$ (only two parameters floated). 172

5.4 Expected and observed 95% C.L. limits for the 4ℓ and $2\ell2\nu$ analyses and for the combination. For the observed results, the central fitted values and the 68% C.L. total uncertainties are also quoted. The Higgs mass is set to the measured value in the 4ℓ decay channel of 125.6 GeV. 175

6.1 List of anomalous HVV couplings considered in the measurements assuming a spin-zero Higgs boson. The definition of the effective fractions is discussed in the text and the translation constant is given in each case. The effective cross sections correspond to the processes $H \to VV \to 2e2\mu$ and the Higgs boson mass $m_H = 125.6$ GeV using the JHUGen calculation. The cross-section ratios for the $HZ\gamma$ and $H\gamma\gamma$ couplings include the requirement $\sqrt{q_V^2} \geq 4$ GeV. 178

6.2 Number of background (Bkg.) and signal events expected in the SM, and number of observed candidates, for the $H \to VV \to 4\ell$ analysis after the final selection in the mass region $105.6 < m_{4\ell} < 140.6$ GeV. The signal and ZZ background are estimated from MC simulation, while the $Z+$jets background is estimated from data. Only systematic uncertainties are quoted. 181
6.3 List of observables $\vec{x}$ used in the analysis of the HVV couplings. The J^P notation for spin-two refers to the ten scenarios defined in table 3.1. 190
6.4 List of spin-one models tested in the $X \to ZZ$ analysis. The expected separation is quoted for two scenarios, for the signal production cross section obtained from the fit to data for each hypothesis and using the SM expectation ($\mu = 1$). The observed separation shows the consistency of the observation with the SM Higgs boson model or the alternative J^P model, from which the CL_s value is derived. 197
6.5 List of spin-two models tested in the $X \to ZZ$ analysis. The expected separation is quoted for two scenarios, for the signal production cross section obtained from the fit to data for each hypothesis, and using the SM expectation ($\mu = 1$). The observed separation shows the consistency of the observation with the SM Higgs boson or an alternative J^P model, from which the CL_s value is derived. 199
6.6 Summary of allowed 68% C.L. (central values with uncertainties) and 95% C.L. (ranges in square brackets) intervals on anomalous coupling parameters in HVV interactions under the assumption that all the coupling ratios are real ($\phi_{ai}^{VV} = 0$ or π). The ranges are truncated at the physical boundaries of $f_{ai}^{VV} = 1$. The last column indicates the observed (expected) confidence level of a pure anomalous coupling corresponding to $f_{ai}^{VV} = 1$ when compared to the SM expectation. . . 201
6.7 Summary of the allowed 95% C.L. intervals on the anomalous couplings in HZZ interactions using results in table 6.6. The coupling ratios are assumed to be real (including $\cos(\phi_{\Lambda_1}) = 0$ or π). 203
6.8 Summary of the allowed 68% C.L. (central values with uncertainties) and 95% C.L. (ranges in square brackets) intervals on anomalous coupling parameters in the HZZ interactions under the condition of a given phase of the coupling (0 or π) or when the phase or other parameters are unconstrained (any value allowed). Expectations are quoted in parentheses following the observed values. 207
6.9 Summary of the allowed 95% C.L. intervals on the anomalous couplings in $HZ\gamma$ and $H\gamma\gamma$ interactions using results in table 6.6. The coupling ratios are assumed to be real ($\cos\left(\phi_{ai}^{VV}\right) = 0$ or π). 209

List of Figures

1.1 Euler angles for three dimensional Cartesian coordinates. 4
1.2 Feynman diagram depicting electron-electron scattering via the electromagnetic interaction. 10
1.3 A comedic example of a complicated Feynman diagram designed to appear similar to a Jayhawk. 11
1.4 A Summary Infographic of The Standard Model. 13
1.5 A 2D illustration of the scalar potential, $V(\Phi)$, when $\mu^2 > 0$. The horizontal axes form the complex plane ϕ_1 vs ϕ_2, while the vertical axis is $V(\Phi)$. 23
1.6 A 1D illustration of the scalar potential, $V(\Phi)$, when $\mu^2 > 0$. 23
1.7 A 2D illustration of the scalar potential, $V(\Phi)$, when $\mu^2 < 0$. The horizontal axes form the complex plane ϕ_1 vs ϕ_2, while the vertical axis is $V(\Phi)$. 24
1.8 A 1D illustration of the scalar potential, $V(\Phi)$, when $\mu^2 > 0$. 25
1.9 A 2D illustration of oscillations in the the scalar potential, $V(\Phi)$, parameterized by χ and ψ. 28

2.1 A cross section schematic of the LHC Dipole magnet showing the two center beam pipes, superconducting coils (red), and other supporting structures. 38
2.2 The peak luminosity delivered to the four main LHC experiments during the 2011 7 TeV (left) and 2012 8 TeV (right) runs. 40
2.3 This CERN accelerator complex. Showing the full chain of accelerators used for the LHC protons: LINAC2, Booster, PS, SPS, and LHC. Additionally, the four large experiments on the LHC are shown: ALICE, ATLAS, CMS, LHCb. 41
2.4 The integrated luminosity delivered and collected by the CMS experiment during the 2011 7 TeV (left) and 2012 8 TeV (right) runs. . . . 43

2.5 Sectional view of the CMS detector. The LHC beams travel in opposite directions along the central axis of the CMS cylinder colliding in the middle of the CMS detector. 44
2.6 Value of magnetic field $|B|$ (left) and field lines (right) predicted on a longitudinal section of the CMS detector, for the underground model at a central magnetic flux density of 3.8 T. Each field line represents a magnetic flux increment of 6 Wb. 48
2.7 Schematic view of one quarter of the silicon tracker in the r–z plane. The positions of the pixel modules are indicated within the hatched area. At larger radii within the lightly shaded areas, solid rectangles represent single strip modules, while hollow rectangles indicate pairs of strip modules mounted back-to-back with a relative stereo angle. . 50
2.8 Layout of the pixel detectors in the CMS tracker. 50
2.9 Layout of the pixel sensor in the CMS tracker. 51
2.10 Predicted resolution of several track parameters for single muons with 1, 10, and 100 GeV: transverse momentum (left), transverse impact parameter (center), and longitudinal impact parameter (right). 54
2.11 Layout of the CMS electromagnetic calorimeter showing the arrangement of crystal modules, supermodules and end caps, with the preshower in front. 55
2.12 Effective momentum resolution σ_{eff}/p for electrons in the EB as a function of the momentum for the ECAL-only, the tracker-only, and the combined estimates. 57
2.13 A quarter slice of the CMS HCAL detectors. The right end of the beam line is the interaction point, HF (not pictured) would be located far to the left. In the diagram, the numbers on the top and left refer to segments in η, and the numbers on the right and the bottom refer to depth. Colors/shades indicate the combinations of layers that form the different depth segments, which are numbered sequentially starting at 1, moving outward from the interaction point. The outer calorimeter is assigned depth 4. Segmentation along ϕ is not shown. 58
2.14 The jet transverse energy resolution as a function of the simulated jet transverse energy for barrel jets ($|\eta| < 1.4$), endcap jets ($1.4 < |\eta| < 3.0$) and very forward jets ($3.0 < |\eta| < 5.0$) 60
2.15 The muon momentum resolution verses p using the muon system only, the inner tracker only, or both ("full system"). (left) Barrel $|\eta| < 0.2$ and (right) endcap $1.8 < |\eta| < 2.0$. 61
2.16 Layout of one quarter of the CMS muon system for initial low luminosity running. The RPC system is limited to $|\eta| < 1.6$ in the endcap, and for the CSC system only the inner ring of the ME4 chambers have been deployed 63

2.17 Distribution of electron BDT output for training sample W+jets, test sample Z+jets on 2012 data (fakes) and prompt electrons ($Z \to ee$ simulation) in the barrel (left) and endcap(right) 69

2.18 (left) Relative difference between the dilepton mass peak positions in data and simulation as obtained from Z, J/ψ and $\Upsilon\,(nS)$ resonances as a function of the transverse momentum of one of the electrons regardless of the second for dielectron events before p_T dependent correction. (right) Relative difference between the dilepton mass peak positions in data and simulation as obtained from Z, J/ψ and $\Upsilon\,(nS)$ resonances as a function of the transverse momentum of one of the electrons regardless of the second for dielectron events. 71

2.19 (left) Relative difference between the dilepton mass peak positions in data and simulation as obtained from Z, J/ψ and $\Upsilon\,(nS)$ resonances as a function of the average muon p_T^{μ} for dimuon events. (right) Relative difference between the dimuon mass resolutions in data and simulation as measured fromZ, J/ψ and $\Upsilon\,(nS)$ decays as functions of the average muon 73

2.20 An example event of jets formed with the anti-k_T clustering algorithm. 75

2.21 Hierarchy of the CMS silicon pixel detector structures. 78

2.22 Hierarchy of the CMS silicon strip detector structures. 78

2.23 Shifts in Pixel Tracker large scale structures as detected by the alignment algorithm in Prompt Calibration Loop using very first runs of CMS data at $\sqrt{s} = 13$ TeV with the full magnetic field (3.8 T). Green histograms show shifts, with black error bars as uncertainties. Red entries and error bars represent thresholds in movement and uncertainty that are considered significant, respectively. Please note the axis range for the z and θ_z shifts are twice (200 µm) that of their x and y counterparts. 81

2.24 Shifts in Pixel Tracker large scale structures after correction for shifts detected by the alignment algorithm in Prompt Calibration Loop using very first runs of CMS data at $\sqrt{s} = 13$ TeV with the full magnetic field (3.8 T). Green histograms show shifts, with black error bars as uncertainties. Red entries and error bars represent thresholds in movement and uncertainty that are considered significant, respectively. Please note the axis range for the z and θ_z shifts are identical to that of their x and y counterparts. 82

2.25 The distribution of median residuals is plotted for the local x- and y-directions in the barrel (top) and forward (bottom) pixel detector, using 20 million collision tracks collected with the magnetic field at 3.8 T. The blue line shows the Run I geometry, which is no longer valid for Run II data, primarily because of temperature changes and pixel re-centering and repair. The black line shows the starting geometry for data taking, which was valid for data taken with the magnetic field turned off, as it was produced with the MILLEPEDE II and HIP algorithms using cosmic ray and 0 T collision data. The alignment shown in violet was adjusted from this geometry by an automated alignment process of the pixel detector that will be run as part of the Prompt Calibration Loop as data is collected and processed, and shows improvements over the initial geometry. The changes resulted primarily from the change in the magnetic field. The RMS of the distribution reduces, the double-peak structure in y present when assuming the initial geometry in the track refit is corrected by the PCL-style alignment of the pixel detector. 84

2.26 The distribution of median residuals is plotted for the tracker inner barrel, using 20 million collision tracks collected with the magnetic field at 3.8 T. The blue line shows the Run I geometry, which is no longer valid for Run II data, primarily because of temperature changes and pixel re-centering and repair (since tracks are fitted using hits in both the pixel and the strip detectors, the large movements of the pixel detectors also affect the DMR performance in the strip detectors). The black line shows the starting geometry for data taking, which was valid for data taken with the magnetic field turned off, as it was produced with the MILLEPEDE II and HIP algorithms using cosmic ray and 0 T collision data. The alignment shown in violet was adjusted from this geometry by an automated alignment process of the pixel detector that will be run as part of the Prompt Calibration Loop as data is collected and processed, and shows improvements over the initial geometry. The changes resulted primarily from the change in the magnetic field. The RMS of the distribution reduces for the Run I, initial, and aligned geometry, respectively. 85

2.27 Day-by-day value of the relative longitudinal shift between the two half-shells of the BPIX as measured with the primary vertex residuals, for the last month of pp data taking in 2012. Red crosses show the shift observed using the data coming from the prompt reconstruction. The same events, re-reconstructed after the 2012 alignment campaign, which accounts for the major changes in the positions of the half-shells, are represented by black lozenges. A major displacement of the half-shells O(100) µm, occurred during the technical stop in the week of 20th of November, is recovered by the prompt alignment of the BPIX large structures that became active on the 30th November. 86

3.1 Standard Model Higgs boson production cross sections and relative uncertainties at $\sqrt{s} = 7$ TeV and $\sqrt{s} = 8$ TeV. From top to bottom these are $pp \to H$, blue, $pp \to H + 2$jets, red, $pp \to H + W$, green, $pp \to H + Z$, grey, $pp \to H + t\bar{t}$, purple. 89

3.2 Feynman diagram depicting Higgs boson production through gluon-gluon fusion $gg \to H$. The fermion loop is dominated by top quarks, however all quarks contribute according to their masses. 89

3.3 Feynman diagram depicting Higgs boson production through vector boson fusion $qq \to H + 2$jets. 90

3.4 Feynman diagram depicting Higgs boson production associated with a vector boson $qq \to H + W/Z$. 91

3.5 Feynman diagram depicting Higgs boson production in association with two top quarks $gg \to H + t\bar{t}$. 91

3.6 (left) Standard Model Higgs boson decay branching ratios for selected decay modes, of specific interest for this thesis is the ZZ branching ratio. (right) Branching ratio times cross section for selected final states, of specific interest for this thesis is the $ZZ \to 4\ell\,(\ell^+\ell^-\ell^+\ell^-)$. . 93

3.7 Feynman diagram depicting Higgs boson decay into two Z bosons and subsequently into four leptons $H \to ZZ \to 4\ell$. 94

3.8 Feynman diagram depicting the quark production of two Z bosons $qq \to ZZ$. 95

3.9 Feynman diagram depicting the gluon production of two Z bosons $gg \to ZZ$. 95

3.10 Total width of the SM Higgs boson as a function of its mass. 97

3.11 (top) Feynman diagram depicting Higgs boson production through gluon-gluon fusion and subsequent decay to two Z bosons $gg \to H \to ZZ$. (bottom) Feynman diagram depicting ZZ production through gluon-gluon fusion $gg \to ZZ$. These two diagrams will interfere with eachother having an affect on the final number of events observed in the 4ℓ final state. 98

3.12 The NNLO ZZ (black) and WW (red) invariant mass distributions for $m_H = 125$ GeV. 99

3.13 The LO ZZ invariant mass distribution $gg \to ZZ$ for $m_H = 125$ GeV. Black is the total $gg \to \ldots \to ZZ$ contribution once all interfrence effects are taken into account. Red is the $gg \to H^* \to ZZ$ signal only, and cyan is the $gg \to \ldots \to ZZ$ contribution ignoring the interference between the two contributions. For scale, the $q\bar{q} \to ZZ$ contribution is shown in blue. 102

3.14 Distribution of the expected four-lepton reconstructed mass in full analysis mass range for the sum of the $4e$, 4μ, and $2e2\mu$ channels and for $gg + VV \to ZZ$ processes for a Higgs boson mass of 125.6 GeV. The expected distribution for a scenario corresponding to a scaling of the width by 25 is also shown. This illustrates the expected change in $gg + VV \to ZZ$ production when changing the Higgs boson width and at the same time constraining the peak cross section to the SM expectation. 103

4.1 Efficiency, as a function of the lepton p_T^ℓ, for reconstructing and selecting (left) electrons and (right) muons, measured with a $Z \to \ell\ell$ data sample by using a tag-and-probe method. 115

4.2 Geometrical acceptance times selection efficiency for the SM Higgs boson signal as a function of m_H in the three final states for gluon fusion production. Points represent efficiency estimated from full CMS simulation; lines represent a smooth polynomial curve interpolating the points, used in the analysis. The vertical dashed line represents $m_H = 126$ GeV. 119

4.3 (left) Validation of the method using the SS control sample. The observed $m_{4\ell}$ distribution (black dots), prediction of the reducible background (dark green area), and expected contributions from ZZ (light blue area) are shown. (right) Prediction for the reducible background in all three decay channels together (black dots) fitted using an empirical shape (blue curve) with indicated total uncertainty (yellow band). The contributions from the 2P2F-like (solid green) and 3P1F-like (dashed red) processes are fitted separately. 122

4.4 Distribution of the four-lepton reconstructed mass in the full mass range $70 < m_{4\ell} < 1000$ GeV for the sum of the $4e$, $2e2\mu$, and 4μ channels. Points with error bars represent the data, shaded histograms represent the backgrounds, and the unshaded histogram represents the signal expectation for a mass hypothesis of $m_H = 126$ GeV. Signal and the ZZ background are normalized to the SM expectation; the $Z+$jets background to the estimation from data. The expected distributions are presented as stacked histograms. No events are observed with $m_{4\ell} > 800$ GeV. 125

4.5 The $H \to ZZ \to 4\ell$ invariant mass distribution for $m_H = 126$ GeV in the (left) $4e$, (center) $2e2\mu$, and (right) 4μ channels. The distributions are fitted with a double-sided CB function and the fitted values of the CB width σ_{dCB} are indicated. The values of effective resolution, defined as half the smallest width that contains 68.3% of the distribution, are also indicated. The distributions are arbitrarily normalized. 126

4.6 Illustration of the production and decay of a particle H, $gg(q\bar{q}) \to H \to ZZ \to 4\ell$, with the two production angles θ^* and Φ_1 shown in the H rest frame and three decay angles θ_1, θ_2, and Φ shown in the Z_1, Z_2, and H rest frames, respectively. 127

4.7 Distributions of the seven kinematic observables used in the $H \to ZZ \to 4\ell$ analysis: m_{Z_1}, m_{Z_2}, $\cos\theta^*$, $\cos\theta_1$, $\cos\theta_2$, Φ, and Φ_1. The observed data (points with error bars), the expectations for the SM background (shaded areas), the SM Higgs boson signal (open areas under the solid histogram), and the alternative spin-zero resonances (open areas under the dashed histograms) are shown, as indicated in the legend. The mass of the resonance is taken to be 125.6 GeV and the SM cross section is used. All distributions, with the exception of $m_{4\ell}$, are presented with the requirement $121.5 < m_{4\ell} < 130.5$ GeV. . . 129

4.8 Distribution of the kinematic discriminant $\mathcal{D}_{\mathrm{bkg}}^{\mathrm{kin}}$ versus the four-lepton reconstructed mass $m_{4\ell}$ in the (left) low-mass and (right) high-mass regions. The color scale represents the expected relative density in linear scale (in arbitrary units) of background events. The points show the data and the measured per-event invariant mass uncertainties as horizontal bars. One $2e2\mu$ event with $m_{4\ell} \approx 220$ GeV and small $\mathcal{D}_{\mathrm{bkg}}^{\mathrm{kin}}$ has a huge mass uncertainty, and it is displayed as the horizontal line. No events are observed for $m_{4\ell} > 800$ GeV. 130

4.9 (left) Distribution of $\mathcal{D}_{\rm bkg}^{\rm kin}$ versus $m_{4\ell}$ in the low-mass range with colors shown for the expected relative density in linear scale (in arbitrary units) of background plus the Higgs boson signal for $m_H = 126$ GeV. The points show the data, and horizontal bars represent the measured mass uncertainties. (right) Distribution of the kinematic discriminant $\mathcal{D}_{\rm bkg}^{\rm kin}$ for events in the mass region $121.5 < m_{4\ell} < 130.5$ GeV. Points with error bars represent the data, shaded histograms represent the backgrounds, and the unshaded histogram the signal expectation. Signal and background histograms are stacked. 131

4.10 Main observables discriminating production mechanisms in 0/1 jet and Dijet categories in arbitrary units. $q\bar{q}H$ denotes VBF production. (top left) $\mathcal{D}_{\rm jet}$ discriminant combining VBF discrimination variables. (top right) p_T of the four-lepton system. (bottom left) $\Delta\eta$ of the two leading jets. (bottom right) Invariant mass of the two jets. 134

4.11 (left) Distribution of $p_T^{4\ell}$ versus $m_{4\ell}$ in the low-mass-range 0/1-jet category with colors shown for the expected relative density in linear scale (in arbitrary units) of background plus the Higgs boson signal for $m_H = 126$ GeV. No events are observed for $p_T^{4\ell} > 150$GeV. The points show the data, and horizontal bars represent the measured mass uncertainties. (right) Distribution of $p_T^{4\ell}$ in the 0/1-jet category for events in the mass region $121.5 < m_{4\ell} < 130.5$ GeV. Points with error bars represent the data, shaded histograms represent the backgrounds, and the red histograms represent the signal expectation, broken down by production mechanism. Signal and background histograms are stacked. 135

4.12 (left) Distribution of $\mathcal{D}_{\rm jet}$ versus $m_{4\ell}$ in the low-mass-range dijet category with colors shown for the expected relative density in linear scale (in arbitrary units) of background plus the Higgs boson signal for $m_H = 126$ GeV. The points show the data and horizontal bars represent the measured mass uncertainties. (right) Distribution of $\mathcal{D}_{\rm jet}$ in the dijet category for events in the mass region $121.5 < m_{4\ell} < 130.5$ GeV. Points with error bars represent the data, shaded histograms represent the backgrounds, and the red histograms represent the signal expectation, broken down by production mechanism. Signal and background histograms are stacked. 136

4.13 Distribution of the four-lepton reconstructed mass for the sum of the $4e$, $2e2\mu$, and 4μ channels for the mass region $70 < m_{4\ell} < 180$ GeV. Points with error bars represent the data, shaded histograms represent the backgrounds, and the unshaded histogram represents the signal expectation for a mass hypothesis of $m_H = 126$ GeV. Signal and the ZZ background are normalized to the SM expectation, the $Z+$jets background to the estimation from data. 138

4.14 Observed and expected 95% C.L. upper limit on the ratio of the production cross section to the SM expectation. The expected $\pm 1\sigma$ and $\pm 2\sigma$ C.L. ranges of expectation for the background-only model are also shown with green and yellow bands, respectively. 146

4.15 (left) Significance of the local excess with respect to the SM background expectation as a function of the Higgs boson mass in the full mass range 110–1000 GeV. Results obtained using the 1D fit, 2D fit, and the nominal 3D fit. (right) Significance of the local excess with respect to the SM background expectation as a function of the Higgs boson mass for the 1D fit, 2D fit, and the nominal 3D fit. Results are shown for the full data sample in the low-mass region only. 147

4.16 Signal to background ratio's for expected and observed events, computed from the 1D (left), 2D (middle), and 3D (right) likelihoods. These plots are made from the $m_{4\ell} \in 121.5$–130.5 GeV region to study the observed peak. The signal used as the Higgs boson hypothesis corresponds to $m_H = 126$ GeV.These plots are preliminary and unpublished. 148

4.17 (left) Observed and expected 95% C.L. upper limit on the ratio of the production cross section to the SM expectation where a 126 GeV Higgs boson with SM cross section is added as background. The expected $\pm 1\sigma$ and $\pm 2\sigma$ C.L. ranges of expectation for the background-only model are also shown with green and yellow bands, respectively. (right) Significance of the local excess with respect to the SM background + 126 GeV Higgs boson expectation as a function of the BSM Higgs boson mass and compared to the expected and observed significance of the SM Higgs boson. These results were obtained from a preliminary version of the 4ℓ analysis and are unpublished. 150

4.18 (left) Values of μ for the two categories. The vertical line shows the combined μ together with its associated $\pm 1\sigma$ uncertainties, shown as a green band. The horizontal bars indicate the $\pm 1\sigma$ uncertainties in μ for the different categories. The uncertainties include both statistical and systematic sources of uncertainty. (right) Likelihood contours on the signal-strength modifiers associated with fermions ($\mu_{ggH,t\bar{t}H}$) and vector bosons ($\mu_{\mathrm{VBF},VH}$) shown at a 68% and 95% C.L.. 152

5.1 Distribution of the four-lepton invariant mass in the range $100 < m_{4\ell} < 800$ GeV. Points represent the data, filled histograms the expected contributions from the reducible (Z+jets) and $q\bar{q}$ backgrounds, and from the sum of the gluon fusion (gg) and vector boson fusion (VV) processes, including the Higgs boson mediated contributions. The inset shows the distribution in the low mass region after a selection requirement on the MELA likelihood discriminant $\mathcal{D}_{\rm bkg}^{\rm kin} > 0.5$. In this region, the contribution of the $t\bar{t}H$ and VH production processes is added to the dominant gluon fusion and VBF contributions. 161

5.2 Distributions of (left) the four-lepton invariant mass as used in that analysis (right) the four-lepton invariant mass after an artificial selection requirement on the MELA likelihood discriminant $\mathcal{D}_{gg} > 0.65$. Points represent the data, filled histograms the expected contributions from the reducible (Z+X) and $q\bar{q}$ backgrounds, and from the gluon fusion (gg) and vector boson fusion (VV) SM processes (including the Higgs boson mediated contributions). The dashed line corresponds to the total expected yield for a Higgs boson width and a squared product of the couplings scaled by a factor 10 with respect to their SM values. In the top plot, the bin size varies from 20 to 85 GeV and the last bin includes all entries with masses above 800 GeV. 162

5.3 Distributions of the kinematic observables used in the $\mathcal{D}_{gg}$ discriminant: m_{Z_i}, $\cos\theta^*$, $\cos\theta_i$, Φ, and Φ_1. The distributions for m_{Z_1} and m_{Z_2}, and $\cos\theta_1$ and $\cos\theta_2$, are summed together. The observed data (points with error bars), the expectations for the SM background and the SM Higgs boson signal (shaded area), and the Higgs boson with a width $\Gamma_H = 10 \times \Gamma_H^{\rm SM}$ (unfilled area) are shown. The mass of the resonance is taken to be 125.6 GeV and the gg enriched off resonance region is shown ($m_{4\ell} > 330$ GeV). 164

5.4 (left) Distribution of the MELA discriminant $\mathcal{D}_{gg}$ in full analysis mass range for the sum of the $4e$, 4μ, and $2e2\mu$ channels. Points represent the data, shaded histograms represent the background and dotted-shaded histogram the $gg + VV \to ZZ$ expectations for a Higgs mass of 125.6 GeV. The expected distributions are presented as stacked histograms. The measurements are presented for of the data collected at $\sqrt{s} = 7$ and 8 TeV in the 220–1600 GeV range. (right) The $\mathcal{D}_{gg}$ likelihood discriminant for $m_{4\ell} > 330$ GeV in the 4ℓ channel. Points represent the data, filled histograms the expected contributions from the reducible (Z+jets) and $q\bar{q}$ backgrounds, and from the gluon fusion (gg) and vector boson fusion (VV) SM processes (including the Higgs boson mediated contributions). The dashed line corresponds to the total expected yield for a Higgs boson width and a squared product of the couplings scaled by a factor 10 with respect to their SM values. . 165

5.5 Distribution of the transverse mass in the $2\ell 2\nu$ channel. Points represent the data, filled histograms the expected contributions from the backgrounds, and from the gluon fusion (gg) and vector boson fusion (VV) SM processes (including the Higgs-mediated contributions). The dashed line corresponds to the total expected yield for a Higgs boson width and a squared product of the couplings scaled by a factor 10 with respect to their SM values. The bin size varies from 80 to 210 GeV and the last bin includes all entries with transverse masses above 1 TeV. . 166

5.6 Fit results for (left) the 1D analysis using $m_{4\ell}$, and (right) 1D analysis using $\mathcal{D}_{gg}$, observed limits from data (solid) and expected (dashed) results are both shown. 173

5.7 Scan of the negative log-likelihood, $-2\Delta \ln \mathcal{L}$, as a function of Γ_H for the combined fit of the 4ℓ and $2\ell 2\nu$ channels (blue thick lines), for the 4ℓ channel alone in the off-shell and on-shell regions (dark red lines), and for the $2\ell 2\nu$ channel in the off-shell region and 4ℓ channel in the on-shell region (light red lines). The solid lines represent the observed values, the dotted lines the expected values 174

6.1 Distributions of the eight kinematic observables used in the $H \to VV \to 4\ell$ analysis: $m_{4\ell}$, m_1, m_2, $\cos\theta^*$, $\cos\theta_1$, $\cos\theta_2$, Φ, and Φ_1. The observed data (points with error bars), the expectations for the SM background (shaded areas), the SM Higgs boson signal (open areas under the solid histogram), and the alternative spin-zero resonances (open areas under the dashed histograms) are shown, as indicated in the legend. The mass of the resonance is taken to be 125.6 GeV and the SM cross section is used. All distributions, with the exception of $m_{4\ell}$, are presented with the requirement $121.5 < m_{4\ell} < 130.5$ GeV. . . 185

6.2 Distributions of the kinematic discriminants for the observed data (points with error bars), the expectations for the SM background (shaded areas), the SM Higgs boson signal (open areas under the solid histogram), and the alternative spin-zero resonances (open areas under the dashed histograms) are shown, as indicated in the legend. The mass of the resonance is taken to be 125.6 GeV and the SM cross section is used. Top row from left to right: $\mathcal{D}_{\rm bkg}$, $\mathcal{D}_{0-}$, $\mathcal{D}_{CP}$; bottom row from left to right: $\mathcal{D}_{0h+}$, $\mathcal{D}_{\rm int}$, $\mathcal{D}_{\Lambda 1}$. All distributions, with the exception of $\mathcal{D}_{\rm bkg}$, are shown with the requirement $\mathcal{D}_{\rm bkg} > 0.5$ to enhance signal purity. 191

6.3 Distributions of the test statistic $q = -2\ln(\mathcal{L}_{J^P}/\mathcal{L}_{0^+})$ as a function of f_{b2} for the spin-one J^P models tested against the SM Higgs boson hypothesis in the $q\bar{q} \to X \to ZZ$ (left) and decay-only $X \to ZZ$ (right) analyses. The median expectation for the SM Higgs boson is represented by the red squares with the green (68% C.L.) and yellow (95% C.L.) solid color regions and for the alternative J^P hypotheses by the blue triangles with the red (68% C.L.) and blue (95% C.L.) hatched regions. The observed values are indicated by the black dot. 197

6.4 Distributions of the test statistic $q = -2\ln(\mathcal{L}_{J^P}/\mathcal{L}_{0^+})$ for the spin-two J^P models tested against the SM Higgs boson hypothesis in the $X \to ZZ$ analyses. The expected median and the 68.3%, 95.4%, and 99.7% C.L. regions for the SM Higgs boson (orange, the left for each model) and for the alternative J^P hypotheses (blue, right) are shown. The observed q values are indicated by the black dots. 198

6.5 Summary of allowed confidence level intervals on anomalous coupling parameters in HVV interactions under the assumption that all the coupling ratios are real ($\phi_{ai}^{VV} = 0$ or π). The expected 68% and 95% C.L. regions are shown as the green and yellow bands. The observed constraints at 68% and 95% C.L. are shown as the points with errors and the excluded hatched regions. In the case of the $f_{\Lambda 1}^{Z\gamma}$ measurement, there are two minima and two 68% C.L. intervals, while only one global minimum is indicated with a point. The combination of the HZZ and HWW measurements is presented, assuming the symmetry $a_i = a_i^{WW}$. 201

6.6 Expected (dashed) and observed (solid) likelihood scans for the effective fractions $f_{\Lambda 1}$, f_{a2}, f_{a3} (from top to bottom) describing HZZ interactions. Plots on the left show the results when the couplings studied are constrained to be real and all other couplings are fixed to the SM predictions. The $\cos\phi_{ai}$ term allows a signed quantity where $\cos\phi_{ai} = -1$ or $+1$. Plots on the right show the results where the phases of the anomalous couplings and additional HZZ couplings are left unconstrained, as indicated in the legend. 204

6.7 Observed likelihood scans for pairs of effective fractions $f_{\Lambda 1}$ vs. f_{a2}, $f_{\Lambda 1}$ vs. f_{a3}, and f_{a2} vs. f_{a3} (from top to bottom) describing HZZ interactions. Plots on the left show the results when the couplings studied are constrained to be real and all other couplings are fixed to the SM predictions. Plots on the right show the results when the phases of the anomalous couplings are left unconstrained. The SM expectations correspond to points (0,0) and the best fit values are shown with the crosses. The confidence level intervals are indicated by the corresponding $-2\,\Delta\ln\mathcal{L}$ contours. 205

6.8 Expected (dashed) and observed (solid) likelihood scans for the effective fractions $f_{\Lambda 1}^{Z\gamma}$ (top), $f_{a2}^{Z\gamma}$ (middle left), $f_{a3}^{Z\gamma}$ (middle right), $f_{a2}^{\gamma\gamma}$ (bottom left), and $f_{a3}^{\gamma\gamma}$ (bottom right). The couplings studied are constrained to be real and all other couplings are fixed to the SM predictions. The $\cos\phi_{ai}^{VV}$ term allows a signed quantity where $\cos\phi_{ai}^{VV} = -1$ or $+1$. 208

7.1 Combined results of $H \to ZZ$ and $H \to WW$ in the search of a heavy, SM-like Higgs boson with SM couplings, line shape and decays. Upper limits at 95% C.L. set for each of the contributing final states and their combination. 214

7.2 (left) Values of the best-fit σ/σ_{SM} for the combination (solid vertical line) and for subcombinations by predominant decay mode and additional tags targeting a particular production mechanism. (right) The 68% C.L. regions (bounded by the solid curves) for signal strength of the ggH and $t\bar{t}H$, and of the VBF and VH production mechanisms: $\mu_{ggH,t\bar{t}H}$ and $\mu_{\mathrm{VBF},VH}$, respectively 215

7.3 The $m_{4\ell}$ distributions in the off-shell region in the simulation of the $gg \to 4\ell$ process with the anomalous Λ_Q, a_3, a_2, and Λ_1 terms (open histograms) as well as the a_1 (SM filled histogram) term in decreasing order of enhancement at high $m_{4\ell}$. In all cases, the background and its interference with the different signal hypotheses are included except in the case of the pure background (dashed black). The on-shell signal yield and the width Γ_H are constrained to the SM expectations. . . . 217

7.4 Distributions of the test statistic $q = -2\ln(\mathcal{L}_{J^P}/\mathcal{L}_{0^+})$ for the spin-one and spin-two J^P models tested against the SM Higgs boson hypothesis in the combined $X \to ZZ$ and WW analyses. The expected median and the 68.3%, 95.4%, and 99.7% C.L. regions for the SM Higgs boson (orange, the left for each model) and for the alternative J^P hypotheses (blue, right) are shown. The observed q values are indicated by the black dots. 220

7.5 Expected (dashed) and observed (solid) likelihood scans for effective fractions $f_{\Lambda 1}$ (left), f_{a2} (middle), f_{a3} (right). The couplings studied are constrained to be real and all other anomalous couplings are fixed to the SM predictions. The $\cos\phi_{ai}$ term allows a signed quantity where $\cos\phi_{ai} = -1$ or $+1$. Plots show the combined $H \to WW$ and $H \to ZZ$ results in terms of the HZZ couplings for well motivated choices of the WW and ZZ coupling relationships. 220

7.6 Summary of precision in f_{CP}(generalization of f_{a3}) for HVV couplings ($V = W, Z$) at the moment of 3σ measurement. Points indicate central values and error bars indicate 1σ deviations in the generated experiments modeling different luminosity scenarios at proton (solid red) or e^+e^- (open blue) colliders. Measurements in three topologies VH (triangles), VBF (squares), and decay $H \to VV$ (circles) are shown. . . 221

Chapter 1

Introduction

In this document we outline the search for and characterization of the last undiscovered particle predicted by the Standard Model of Particle Physics. This model presents explanations for matter and energy in the universe. It has been tested and verified at the smallest distance scales and highest energies in the universe. To present the ideas outlined in this thesis, it is necessary to start with a collection of definitions. Some will be given here, while others are left to references or outside sources.

The natural starting point of this discussion is to present a useful example of symmetries that are observed in the world and how these are classified in physics. Next, a basic discussion of quantum field theory and scattering amplitudes will be presented. From these examples, the discussion will expand to a categorization of the particles, fields, and symmetries that make up the Standard Model of Particle Physics, including an introduction of Electroweak Symmetry Breaking. Equipped

with these ideas an outline of Limitations of the Standard Model are presented using the Higgs boson as a tool for understanding them.

1.1 Symmetries in Physics

Symmetry is one of, if not the, most important features in the physics of the natural world. As we pull together the various pieces needed to present the state of the art in particle physics, we will define multiple symmetries that exist in nature and how we use them to test our current and hypothetical models.

1.1.1 Noether's Theorem

To begin, let us define the *symmetry group* of the system, G, as the local group that transforms solutions into other solutions. If x is a solution and g is a group element, then $g \cdot x$ will also be a solution. In Physics, the solutions that we consider either that maximize or minimize the action:

$$\mathcal{S} = \int d^4x \mathscr{L}, \tag{1.1}$$

where the integrand, $\mathscr{L}$, is the *Lagrangian* of the system, $\mathscr{L} = T - V$. The T and V are the kinetic and potential energy, respectively. So a symmetry group of a physical system would be the set of transformations that leave the Lagrangian invariant. This concept became one of most important in physics after Emmy Noether

proved that these symmetries of the action correspond to conserved quantities that do not change as the system evolves [1].

1.1.2 Angular Momentum and the Rotation Group

To demonstrate the importance of Noether's Theorem, let us consider the group of rotations in 3 dimensional space, the special orthogonal group in 3 dimensions, SO(3). Given any unit vector $\hat{\mathbf{n}}$ a rotation about this vector by an angle ψ is denoted by $R_{\hat{\mathbf{n}}}(\psi)$. Here we will use the Euler Angles to parameterize R, where the rotations about the (x, y, z) axis are given by (α, β, γ) respectively. It will also be useful to note that performing a rotation R_1 followed by another rotation R_2 is equivalent to a single rotation R_3, or that the set of rotations is closed.

A arbitrary rotation $R(\alpha, \beta, \gamma)$ can be decomposed into rotations about the fixed axes, $R(\alpha, \beta, \gamma) = R_x(\alpha)R_y(\beta)R_z(\gamma)$. Figure 1.1 shows these angles for the transformation of vector N from (x, y, z) to (X, Y, Z). At this point it is useful to express the rotations $R_{x,y,z}$ in terms of their matrix formulation, equations (1.2), (1.3), (1.4). Where the angle of rotation must satisfy $0 \leq \psi \leq 2\pi$.

$$R_z(\gamma) = \begin{pmatrix} \cos\gamma & -\sin\gamma & 0 \\ \sin\gamma & \cos\gamma & 0 \\ 0 & 0 & 1 \end{pmatrix} \tag{1.2}$$

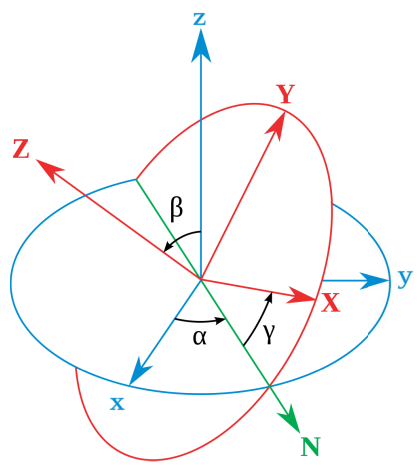

Figure 1.1: Euler angles for three dimensional Cartesian coordinates. [2]

$$R_y(\beta) = \begin{pmatrix} \cos\beta & 0 & \sin\beta \\ 0 & 1 & 0 \\ -\sin\beta & 0 & \cos\beta \end{pmatrix} \tag{1.3}$$

$$R_x(\alpha) = \begin{pmatrix} 1 & 0 & 0 \\ 0 & \cos\alpha & -\sin\alpha \\ 0 & \sin\alpha & \cos\alpha \end{pmatrix} \tag{1.4}$$

The reader should note that a vector along the z-axis direction will be left unchanged due to a R_z rotation. More generally, we can apply Noether's Theorem when the Lagrangian for a physical system does not depend on infinitesimal rotations about any axis, $\mathscr{L} - \mathscr{L}(\delta\alpha, \delta\beta, \delta\gamma) = 0$. This symmetry corresponds to the classical conservation of angular momentum, J, when the Lagrangian has spherical symmetry.

This symmetry will become important as we discuss the kinematics of the particles we use to study new discoveries.

1.1.3 Inherent Spin and SU(2)

If one fixes a direction in equations (1.2), (1.3), and (1.4) then the rotations about that direction will form a subgroup of SO(3). This becomes clear when you consider the closure, identity, and inverse group axioms for the subset of rotations R_z. Specifically, the subgroup is isomorphic to the special unitary group of rotations in two dimensions, SU(2). One way to write this new transformation is:

$$R(\phi) = \begin{pmatrix} \cos\phi & -\sin\phi \\ \sin\phi & \cos\phi \end{pmatrix} \tag{1.5}$$

The simplest way to represent a group is to find the elements that all other elements of the group can be made from. To find these elements for SU(2) start with equation (1.5) and consider an infinitesimal rotation $d\phi$. Since $R(\phi)$ is differentiable one can derive an equation to write all possible rotations in terms of the operator matrix J which we will call the *generator* of SU(2). Explicitly, $R(\phi)$ can be written as:

$$R(\phi) = e^{-i\frac{\phi}{2}\mathrm{J}}, \tag{1.6}$$

where $\mathrm{J}_i = \tau_i$ and τ_i is one of the Pauli matrices:

$$\tau_1 = \begin{pmatrix} 0 & 1 \\ 1 & 0 \end{pmatrix}, \tau_2 = \begin{pmatrix} 0 & -i \\ i & 0 \end{pmatrix}, \tau_3 = \begin{pmatrix} 1 & 0 \\ 0 & -1 \end{pmatrix} \tag{1.7}$$

In this formulation $R(\phi)$ operates on states that are linear combinations of *two-component spinors* given by equation (1.8). These spinor eigenstates have an inherent conserved spin of $\pm\hbar/2$.

$$\chi_+ = \begin{pmatrix} 1 \\ 0 \end{pmatrix}, \chi_- = \begin{pmatrix} 0 \\ 1 \end{pmatrix} \tag{1.8}$$

These states can be expressed as linear combinations of these two component spinors, but we will find it more useful to transform the basis so that they can be rewritten in terms of the two component spinors ψ_R (right-handed) and ψ_L (left-handed) that are eigenstates of the parity transformation[1].

$$\psi = \begin{pmatrix} \psi_R \\ \psi_L \end{pmatrix} \tag{1.9}$$

These states, called *fermions*, and the group SU(2) will be two of the major building blocks that are used when we discuss the Standard Model of particle physics. Before we describe this model we will take some time to discuss Scattering Amplitudes.

[1] As position transforms from $\vec{x} \to -\vec{x}$ the momentum transforms as $\vec{p} \to -\vec{p}$

1.2 Scattering Amplitudes

Particle physics research at its core is not very different from pre-school; we want to see what is inside of something but can't get our hands in the tiny spaces, so we smash it apart. The complexity that is swept under the rug in this statement is that we can map what is happening in these small spaces to what we observe using scattering amplitudes, which tell us the behavior of particles as they "break away" from the things we are trying to study. More generally, a scattering matrix tells us how a system of particles will evolve over time, either because of collisions between particles or other natural processes.

1.2.1 Scattering Matrix

To explain how particle physics explains the evolution of a system over time, we will follow a procedure outlined in [3]. Let us consider a set of particle fields with certain characteristics denoted $|\psi\rangle(t)$. The system at a time t is given in Dirac notation [4]. We will denote the initial state of the system as $|\psi_i\rangle = |\psi\rangle(t_i)$, and the final state as $|\psi_f\rangle = |\phi\rangle(t_f)$. These states can be single or multiple particle states and typically quantities like momentum, spin, or helicity[2] are used to specify them in this notation.

[2]Projection of spin onto momentum, $\vec{S} \cdot \hat{p}$

The evolution of a system from state $|\psi_i\rangle$ to $\langle\psi_f|$ is given by

$$\langle\psi_f| S |\psi_i\rangle , \tag{1.10}$$

where S is a quantum mechanical operator associated with the scattering matrix.

To give a concrete example you can consider a plane wave evolving over time. In this case, $S = e^{-iH(t-t_i)}$. For this explanation, we use a Hamiltonian H instead of a Lagrangian, but a Hamiltonian is simply the Legendre transformation of a Lagrangian, so they are equivalent for our purpose. In this case, equation (1.10) becomes

$$\langle\psi_f| e^{-iH\left(t_f-t_i\right)} |\psi_i\rangle . \tag{1.11}$$

In the limit that $t_f - t_i \to \infty$ the operator between the states is the *scattering matrix* and maps some initial state to a final state at some other time.

1.2.2 Amplitudes and Feynman Diagrams

Each of the states outlined in the previous section, $|\psi\rangle(t)$, will have specific properties. For example, the initial state may be in eigenstate a for some commuting operator, while the final state may be in eigenstate b of the same operator. Then the evolution of the system from $|a\rangle$ to $|b\rangle$ will be through a specific *matrix element*, $\mathcal{M}_{ab}$.

$$\mathcal{M}_{ab} = \langle b| S |a\rangle \tag{1.12}$$

These matrix elements can be used to describe the evolution of the system through very specific transitions. These matrix elements are also called *scattering amplitudes*, A, for a specific process.

$$\mathrm{A}_{ab} = \mathcal{M}_{ab} = \langle b| S |a\rangle \tag{1.13}$$

These amplitudes can also be expressed in a pictorial form, called *Feynman diagrams*, that we will use extensively in this document. These diagrams are used to do the calculations through rules mapping vertex points, internal, and external lines to terms in the matrix element pieces.

To use a concrete example, we will describe the interaction of electrons through the electromagnetic interaction. The Lagrangian for two fermions interacting elecgromagneticily is given by

$$\mathscr{L}_{EM} = \bar{\psi}\left(i\gamma^{\mu}\left(\partial_{\mu} + ieA_{\mu}\right) - m\right)\psi. \tag{1.14}$$

In this equation, the electromagnetic interaction terms are represented by the vector potential, A_{μ}, with e as the coupling constant of the particle to the electromagnetic field. The 4×4 Dirac matrices γ^{μ} are defined by the 2×2 Identity matrix (1) and the Pauli-matrices we have already seen

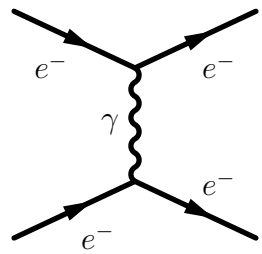

Figure 1.2: Feynman diagram depicting electron-electron scattering via the electromagnetic interaction.

$$\gamma^0 = \begin{pmatrix} 1 & 0 \\ 0 & -1 \end{pmatrix}, \gamma^i = \begin{pmatrix} 0 & \tau^i \\ -\tau^i & 0 \end{pmatrix}. \tag{1.15}$$

In the amplitude notation this can be written as

$$A = \langle \psi_1 \psi_2 | \, e^{\bar{\psi}(i\gamma^\mu(\partial_\mu + ieA_\mu) - m)\psi} \, | \psi_1 \psi_2 \rangle \tag{1.16}$$

The equivalent representation lowest order terms of equation (1.14) as Feynman diagrams will be figure 1.2. These diagrams can be used to quickly and simply represent complex interactions of particles and range from very simple, figure1.2, to extremely complex, as in the comedic example 1.3. Relevant and practical examples will be presented in section 3.

In this example we can see the properties of another group that will be important for the Standard Model. The electromagnetic interaction requires U(1) gauge symmetry. The conserved quantity for this group is the electric charge of the fermion, given by e in the equations above. Now that we have introduced many of the pieces

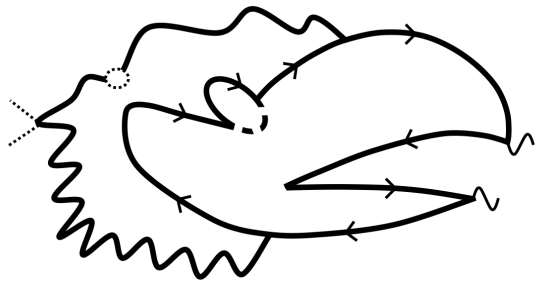

Figure 1.3: A comedic example of a complicated Feynman diagram designed to appear similar to a Jayhawk [5].

we need we will discuss the Standard Model of particle physics.

1.3 The Standard Model

So far we have considered very simple Lagrangians that describe very specific processes. These ideas are the basis for the construction of the *Standard Model* (SM) [6–9] of particle physics. This model attempts to describe and categorize the particles and interactions that make up the quantum world. The glaring omission is gravity, which is extremely weak compared to the other processes that are occurring at sub-atomic distance scales. Before we can discuss how the model describes the fundamental interactions we need to describe and categorize the material that the universe is made from.

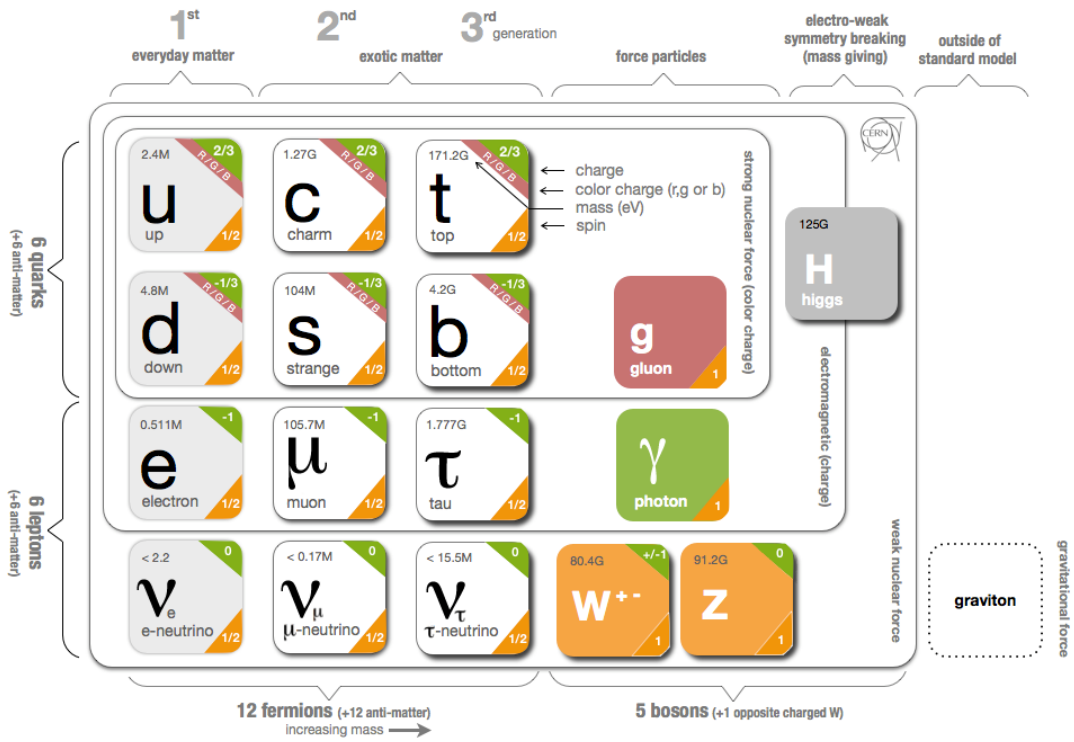

Figure 1.4: A Summary Infographic of the Standard Model. This is a modified version of original found at [10].

1.3.1 Matter

The SM provides a categorization of all the matter that makes up the universe. This categorization started with the first experiments attempting to describe atoms distinguishing the particles in the nucleus of an atom from the electrons that orbit around them. Today we know of matter in two categories, *quarks* and *leptons*, both of which are fermions with spins of $\hbar/2$, noted 1/2 from now on[3]. For each of these categories there are three generations of particles, each generation consisting of two quarks (q), two leptons (ℓ) and their antiparticles[4]($\bar{q}, \bar{\ell}$). The heavier second and third generation fermions typically decay quickly into the first generation particles that make up the world we live in[5].

1.3.1.1 Quarks

Quarks are the fundamental pieces that make up the nucleus of atoms. The protons and neutrons that are used to classify an atom are themselves built form combinations of quarks. The name “quark" was coined by Gell-Mann who credits the term to a passage from *Finnegans Wake* by James Joyce. Quarks come in six *flavors* arranged by mass into three generations of doublets, this flavor is preserved in electromagnetic and strong interactions. The first letter of the quark name is often used to designate them so up (u), down (d), charm (c), strange (s), top (t), and

[3]Here we have moved to the convention of natural units where $\hbar = c = 1$

[4]The antiparticle of a fermion is the C transform of the particle state. C transforms discussed more in section 1.4.1

[5]The neutrino's being the exception to this.

bottom (b). Each flavor has a different mass ranging from $\sim$ MeV (u and d) to ~ 170 GeV (t), the best knowledge of these masses is outlined in figure 1.4.

Everyday matter consists mainly of the first generation quarks, u and d, grouped into the protons and neutrons. Quarks are never observed alone due to a *color charge* that each posses[6]. This will be discussed more in section 1.3.2, but for now we will refer to it as a charge that can be "red" (r), "blue" (b), or "green"(g). To be stable, a particle must be seen as "white" ($\mathbb{w}$) to the outside world. Because matter must appear white, quarks group themselves into sets called *hadrons*. Hadrons come in classifications based on the number of valence quarks they have. Two quark states are quark-antiquark pairs called *mesons*, $\left(\mathrm{r}\bar{\mathrm{r}} + \mathrm{b}\bar{\mathrm{b}} + \mathrm{g}\bar{\mathrm{g}}\right)/\sqrt{3} = \mathbb{w}$. Common examples of mesons are pions ($\pi^0, \pi^\pm$) that come from cosmic rays. Three quark states are called *baryons*, $\mathrm{r} + \mathrm{b} + \mathrm{g} = \mathbb{w}$, everyday examples being protons and neutrons. Recent observations also suggest tetraquark states [11] consisting of four quarks.

Each quark generation doublet has one particle with electromagnetic charge[7] of $+2/3e$ and another with charge $-1/3e$. These will be combined so that all observable hadrons will have integer charges. The top-left section of figure 1.4 summarizes the properties and categorization of the quarks.

One additional item that will prove relevant is that quarks can be both right-handed and left-handed eigenstates of the parity transform. This will distinguish

[6]The property has nothing to do with optical color, but maps nicely to the mixing fundamental colors.

[7]"e" is used as the fundamental unit of electromagnetic charge. "$-e$" is defined as the charge of an electron.

their interactions when we discuss the weak force in section 1.3.2.

1.3.1.2 Leptons

Unlike the quarks, leptons cary no property that stops them from existing by themselves. All leptons are neutral to color charge preventing them from interacting via the strong nuclear force. The most common lepton again belongs to the first generation, the electron. Electrons orbiting the nucleus of an atom are the most common leptons. Similar to the heavier generations of the quarks, the electron also has corresponding heavier generation flavors, the muon (μ) and tau (τ) leptons. All three of these leptons cary an electromagnetic charge of "$-e$", range in mass from ~ 0.5 MeV(e) to ~ 1.7 GeV(τ), and can exist both as left or right-handed.

Each of these three leptons has a corresponding doublet parter as well, the neutrinos (ν_e, ν_μ, ν_τ). These particles are neutral in both color and electromagnetic charge, and are almost massless. Further complicating the story, they only exist as left-handed particles. They are extremely hard to interact with and detect since the electromagnetic and strong forces are invisible to them allowing them to only interact via the weak nuclear force. Additionally, unlike the quarks and the other leptons, they oscillate between different flavors without interacting with the environment because their mass eigenstates are not the same as their weak interaction eigenstates. In 1.4 the leptons occupy the bottom left portion of the table. A summary of the first generation fermion fields that are given in table 1.1 where the doublets are grouped

Fermion Field	EM charge (Q)	Weak Isospin (T_3)	Hyperchage (Y)	Color Charge
$L_L = \begin{pmatrix} \nu_L \\ e_L^- \end{pmatrix}$	$\begin{pmatrix} 0 \\ -1 \end{pmatrix}$	$\begin{pmatrix} +1/2 \\ -1/2 \end{pmatrix}$	-1	no
e_R^-	-1	0	-2	no
$Q_L = \begin{pmatrix} u_L \\ d_L \end{pmatrix}$	$\begin{pmatrix} +2/3 \\ -1/3 \end{pmatrix}$	$\begin{pmatrix} +1/2 \\ -1/2 \end{pmatrix}$	$+1/3$	yes
u_R	$+2/3$	0	$+4/3$	yes
d_R	$-1/3$	0	$-2/3$	yes

Table 1.1: First generation fermions and their different charges, grouped in left(right)-handed doublets(singlets).

together and the distinction between left and right-handed particles has been made.

While the only leptons in everyday matter are electrons, muons and neutrinos are also quite common. These particles exist as cosmic rays that are constantly bombarding us from the upper atmosphere and outer space. Muons offer a particularly interesting case because they are moving at relativistic speeds so that in our frame of reference they appear as long lived particles.

1.3.2 Forces

Now that we have introduced the building blocks of matter we can discuss how these particles interact. This description starts with a Lagrangian of terms describing particles and their interactions with each other, however this Lagrangian needs to preserve specific symmetries that we observe in nature. Specifically the SM Lagrangian should have U(1) $\times$ SU(2) $\times$ SU(3) local symmetry[8]. Each of these symmetries cor-

[8]The difference between a local and global symmetry has not been outlined in this document, but the author again refers you to [12–15] and many other places.

respond to physical interactions between the particles in the theory. Mathematically it is extremely similar to equation (1.14), however the $(\partial_\mu + ieA_\mu)$ is replaced by the more complicated covariant derivative $\mathcal{D}_\mu$.

$$\mathcal{D}_\mu = \partial_\mu - ig_1\frac{\mathrm{Y}}{2}B_\mu - ig_2\frac{\tau^i}{2}W^i_\mu - ig_3\frac{\lambda^a}{2}G^a_\mu \tag{1.17}$$

Each of these additional terms are present to preserve one of the local symmetries that we observe in the world. Each of the g_i variables are coupling constants that can be measured by experimental results. These new fields map to the fundamental forces and in turn *gauge bosons* that mediate each of the forces. They are called bosons because they have an integer unit of inherent spin, as apposed to the matter particles that all have half-integer spin. Particle physics models fermions interacting with each other as the exchange of these bosons between particles.

A rather glaring omission from both equation (1.14) and the extension using equation (1.17) is how these new fields (bosons) interact with themselves and each other. We will not take the time to introduce all of these terms but the relevant pieces will be used in section 1.3.3.

The term associated with g_1 is introduced to preserve local gauge invariance, U(1), introducing a spin-1 field B_μ. The generator, Y (*hypercharge*), will be a constant for every particle. This term, intertwined with the g_2 term, describes the *electromagnetic force*. The g_2 term, along with the g_1 term, describes the *weak nuclear force*. The details of their combination will be described in section 1.3.3.

The g_2 term preserves rotations in flavor space, SU(2), introducing three new vector fields W^i_μ where $i \in \{1, 2, 3\}$ and the generators τ^i (the Pauli matrices we have already seen). Similar to the case of angular momentum we have already seen, the $i = 3$ projection, T_3, is a conserved quantity called *weak isospin* that is useful in computations.

Additionally, the W^i_μ bosons are exclusively left-handed, meaning it can only interact with left-handed particles (right-handed antiparticles). For now, it is useful to note that both the B_μ and the W^3_μ terms represent interactions that preserve the original flavor of the fermions they act on. In the framework of equation (1.14) and figure 1.2 this means that the photon field, A_μ, is some linear combination of B_μ and W^3_μ and the electroweak charge, e, is a linear combination of $g_1 \frac{\mathrm{Y}}{2}$ and $g_2 \frac{\tau^3}{2}$.

The final term associated with g_3 represents the *strong nuclear force* and preserves rotations in the color charge space, SU(3). This term introduces eight new vector fields G^a_μ with $a \in \{1, 2, 3, 4, 5, 6, 7, 8\}$ and eight generators λ^a which are the analog of the Pauli matrices in 3 dimensions. Each of these fields corresponds to a *gluon* that mediates the strong force. These interactions are described by Quantum Chromodynamics (QCD), the quantum field theory for how particles with color charge (quarks & gluons) interact with each other. The conserved charge in this theory is the color; “redness", “blueness", and “greenness". Each of the eight gluons in this theory is a superposition of color charge states and “holds" quarks of specific colors together into colorless hadrons. An explicit listing of the gluon states is not

Force	Bosons	Relative Strength	Range (m)
Strong	gluons (g)	1	10^{-15}
Electromagnetic	photon (γ)	$\frac{1}{137}$	∞
Weak	$W^{\pm}, Z$ bosons	10^{-6}	10^{-18}
Gravity	graviton (G)	10^{-39}	∞

Table 1.2: List of Fundamental Forces their relative strengths and ranges.

provided here, but a basic introduction can be found in [16].

Before going through the details of the electromagnetic and weak forces, a quick note on the relative strength of these interactions. The electromagnetic force is common in every day life because it is a relatively strong interaction and operates over long distances, for example the light from a distant star can be seen at night. The strongest of the forces is the strong nuclear force which keeps the quarks grouped in hadrons and hadrons together in a nucleus is much stronger but only impacts particles that are very close together. At larger distances the weakest of the forces considered in particle physics is the creatively named weak nuclear force, which governs the decay of higher generation fermions into lower generation fermions. In table 1.2 you can find a summary of the different forces and their relative strengths and interaction ranges.

Included in this table is the gravitational force. There are theoretical models for describing quantum gravity in the same framework as these other forces, that will be discussed more in later sections but as yet these have not been confirmed with observations.

1.3.3 Electroweak Symmetry Breaking

As eluded to above, the weak and electromagnetic forces are deeply connected. In their combined form they are referred to as the *Electroweak force*. In the description we outlined, this means that the SM has SU(2) × U(1) symmetry, giving rise to four gauge bosons that would mediate these two forces; B_μ, W^1_μ, W^2_μ, and W^3_μ. In the mathematical construction that we have presented all of these W^i_μ bosons would be massless, but this would contradict the observed range of the weak force outlined in Table 1.2. To give these bosons mass, the symmetry of the system must be broken. The *Higgs Mechanism* [17–22] has been proposed as the source of the *Electroweak Symmetry Breaking* [23].

To see how this happens, focus on the kinetic energy terms of the W^i_μ and B_μ fields that we neglected previously. These are given by equation (1.18) following the Weinberg-Salam Model of electroweak interactions [6–9]. This equation is the first appearance of the Field Tensors, these take the form $B_{\mu\nu} = \partial_\nu B_\mu - \partial_\mu B_\nu$ and $W^i_{\mu\nu} = \partial_\nu W^i_\mu - \partial_\mu W^i_\nu + g\epsilon^{ijk} W^j_\mu W^k_\nu$.

$$\mathscr{L}_{KE} = -\frac{1}{4} W^i_{\mu\nu} W^{\mu\nu i} - \frac{1}{4} B_{\mu\nu} B^{\mu\nu} \tag{1.18}$$

When one adds an additional complex scalar SU(2) doublet, Φ, to this theory we find the key to giving some of these fields mass. We write this new scalar field in terms of its components shown in equation (1.19).

$$\Phi = \begin{pmatrix} \phi^+ \\ \phi^0 \end{pmatrix} = \begin{pmatrix} \phi^1 + i\phi^2 \\ \phi^3 + i\phi^4 \end{pmatrix} \tag{1.19}$$

What makes this new field the key is the special potential energy term that accompanies it. This potential, given in equation (1.20), and its parameters, λ and μ, define how the field interacts with itself and will be vital in our discussion.

$$V(\Phi) = \mu^2 \left|\Phi^\dagger \Phi\right| - \lambda \left(\left|\Phi^\dagger \Phi\right|\right)^2 \tag{1.20}$$

Putting all of the pieces together we can write a toy Lagrangian for the electroweak part of the SM[9] as

$$\mathscr{L}_{EW} = -\frac{1}{4} W^i_{\mu\nu} W^{\mu\nu i} - \frac{1}{4} B_{\mu\nu} B^{\mu\nu} + \left|\mathcal{D}_\mu \Phi\right|^2 - V(\Phi)\,. \tag{1.21}$$

When one investigates the behavior of this system as the total energy approaches zero[10] the fields will approach their ground state. Focusing on the scalar potential one can see the behavior depends on the sign of the parameters μ^2 and λ. We assume that $\lambda > 0$ so that a minimum state exists at all. If $\mu^2 > 0$ then the system will have a natural minimum where $\Phi = 0$ that preserves all of the symmetries that we have already outlined. This can be seen in the natural two-dimensional form and in the one-dimensional projection in figures 1.5 and 1.6 respectively.

[9] In what follows we omit QCD terms, while fermion terms are left for later discussion.
[10] A stable minimum energy state being analogous to the current state of the universe.

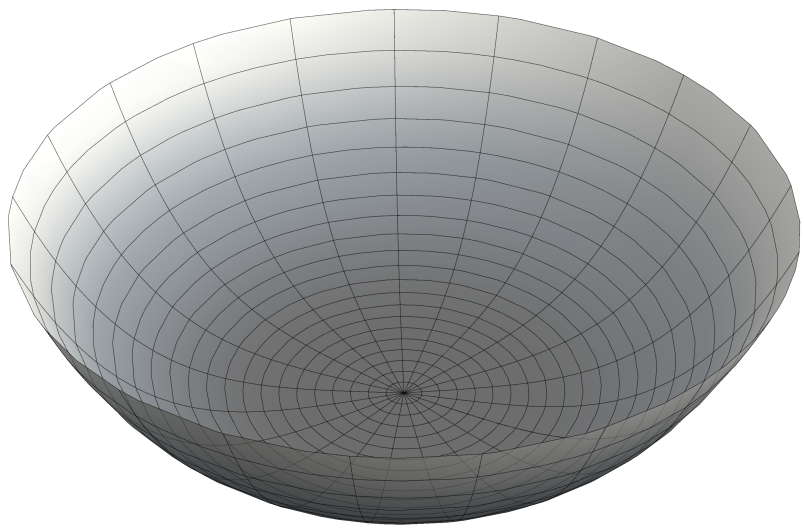

Figure 1.5: A 2D illustration of the scalar potential, $V(\Phi)$, when $\mu^2 > 0$. The horizontal axes form the complex plane ϕ_1 vs ϕ_2, while the vertical axis is $V(\Phi)$. Created with [24].

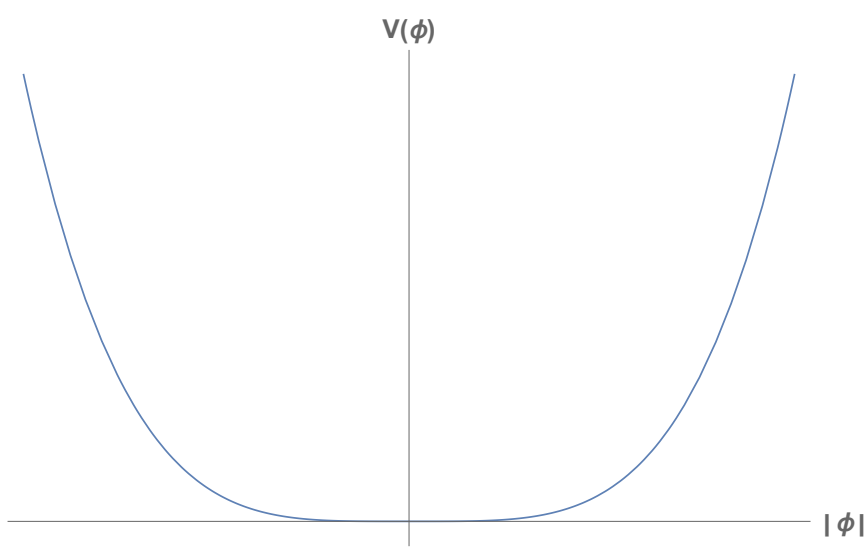

Figure 1.6: A 1D illustration of the scalar potential, $V(\Phi)$, when $\mu^2 > 0$. Created with [24].

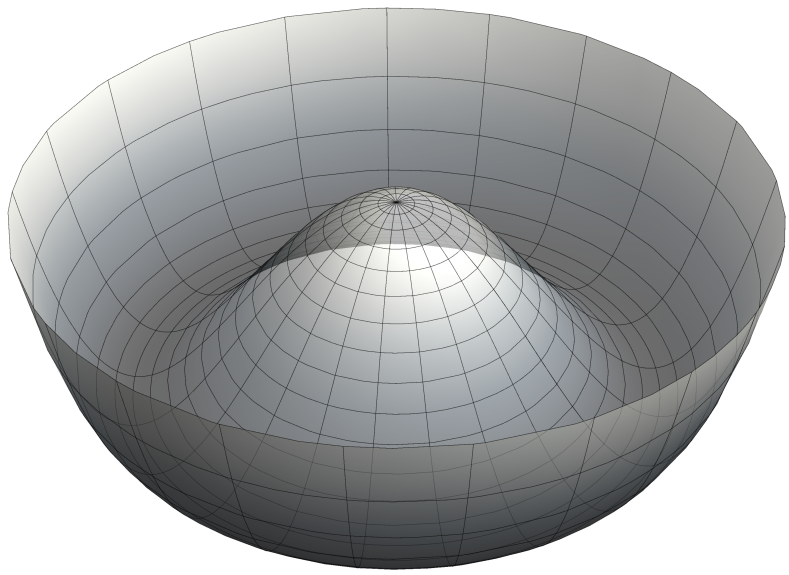

Figure 1.7: A 2D illustration of the scalar potential, $V(\Phi)$, when $\mu^2 < 0$. The horizontal axes form the complex plane ϕ_1 vs ϕ_2, while the vertical axis is $V(\Phi)$. Created with [24].

The more interesting case is when $\mu^2 < 0$. In this case the potential has a minimum that is not at $\Phi = 0$ but the minimum energy state will occur at what we call the *vacuum expectation value* (VEV) given in equation (1.22). This means that in the ground state, the scalar field will not go to zero but will have some amount of energy defined as $\frac{v}{\sqrt{2}}$ breaking the U(1) symmetry. Figures showing the natural two-dimensional potential and one-dimensional projection are seen in 1.7 and 1.8 respectively.

$$\langle \Phi \rangle = \sqrt{-\frac{\mu^2}{2\lambda}} \begin{pmatrix} 0 \\ 1 \end{pmatrix} \equiv \frac{1}{\sqrt{2}} \begin{pmatrix} 0 \\ v \end{pmatrix} \tag{1.22}$$

The choice of the VEV contribution to the ϕ^1, ϕ^2, ϕ^3 or ϕ^4 component in SU(2)

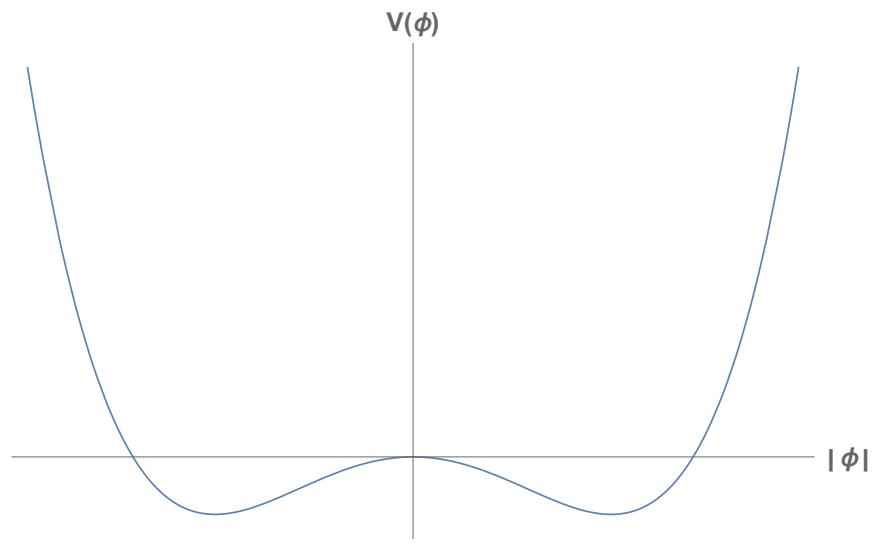

Figure 1.8: A 1D illustration of the scalar potential, $V(\Phi)$, when $\mu^2 > 0$. Created with [24].

space is arbitrary but we have chosen the conventional notation here, giving the new doublet a hypercharge of $Y_\Phi = 1$ and a electromagnetic charge $Q_{EM} = \frac{\tau^3+Y}{2}$. This gives an electromagnetically neutral ground state, even though the field retains its VEV. So, by giving the scalar field a non-zero expectation value in the ground state we have broken the SU(2) $\times$ U(1) symmetry to give a local $\mathrm{U}(1)_{EM}$ symmetry of the electromagnetic force[11].

We can see the difference between the masses of the original bosons by using the gauge invariance of the field to formulate our original scalar field Φ in terms of the VEV, v, and a remaining real scalar field, h, in equation (1.23).

[11] As required by the Lorentz invariance of the electromagnetic force

$$\Phi = \frac{1}{\sqrt{2}} \begin{pmatrix} 0 \\ v + h \end{pmatrix} \tag{1.23}$$

To see how these terms generate mass, it is convenient to perform a change of basis from τ^1, τ^2, τ^3 to the τ^+, τ^-, τ^3 representation given by equation (1.24). This change of basis also will change the $W^1_\mu, W^2_\mu, W^3_\mu$ to $W^+_\mu, W^-_\mu, W^3_\mu$ given by equation (1.25).

$$\tau^\pm = \frac{1}{\sqrt{2}} \left(\tau^1 \pm i\tau^2\right) \tag{1.24}$$

$$W^\pm_\mu = \frac{1}{\sqrt{2}} \left(W^1_\mu \mp iW^2_\mu\right) \tag{1.25}$$

Looking at the scalar kinetic term of equation (1.21), $|\mathcal{D}_\mu \Phi|^2$, more explicitly we can write the boson terms in the form equation (1.26), dropping terms that represent the dynamics and interactions of the h field.

$$\frac{v^2}{4} \left(g_2 W^3_\mu - g_1 B_\mu\right)^2 + \frac{g_2^2 v^2}{2} W^+_\mu W^{\mu -} \tag{1.26}$$

After another change of basis, we can recast the first term in equation (1.26) as the physical gauge fields we observe in nature. In equations (1.27) and (1.28), we see the Z and γ fields we are looking for and the masses of the bosons respectively.

$$\begin{aligned} Z_\mu &= \frac{g_2 W_\mu^3 - g_1 B_\mu}{\sqrt{g_1^2 + g_2^2}} \\ A_\mu &= \frac{g_2 W_\mu^3 + g_1 B_\mu}{\sqrt{g_1^2 + g_2^2}} \end{aligned} \tag{1.27}$$

$$\begin{aligned} m_W &= \frac{v}{\sqrt{2}} g_2 \\ m_Z &= \frac{v}{\sqrt{2}} \sqrt{g_2^2 + g_1^2} \\ m_\gamma &= 0 \end{aligned} \tag{1.28}$$

Thus we have broken the electroweak symmetry, giving the $W^\pm$ and Z bosons mass while keeping the γ massless. This provides a theory that predicts a new field, h, called the *Higgs field*, and allows us to describe the behavior of the weak and electromagnetic forces to fantastic accuracy.

To investigate the ramifications of this new field, we can formulate the h field as small permutations about the VEV. This gives a potential of the form $\phi(x) = v + \frac{1}{\sqrt{2}}(\chi(x) + i\psi(x))$. These permutations are illustrated in figure 1.9. From the figure it is clear that a small displacement in ψ does not cost energy, while oscilations in χ do cost energy. Thus χ corresponds to a new massive boson is called the *Higgs Boson* in common literature. Everything about this new boson can be predicted

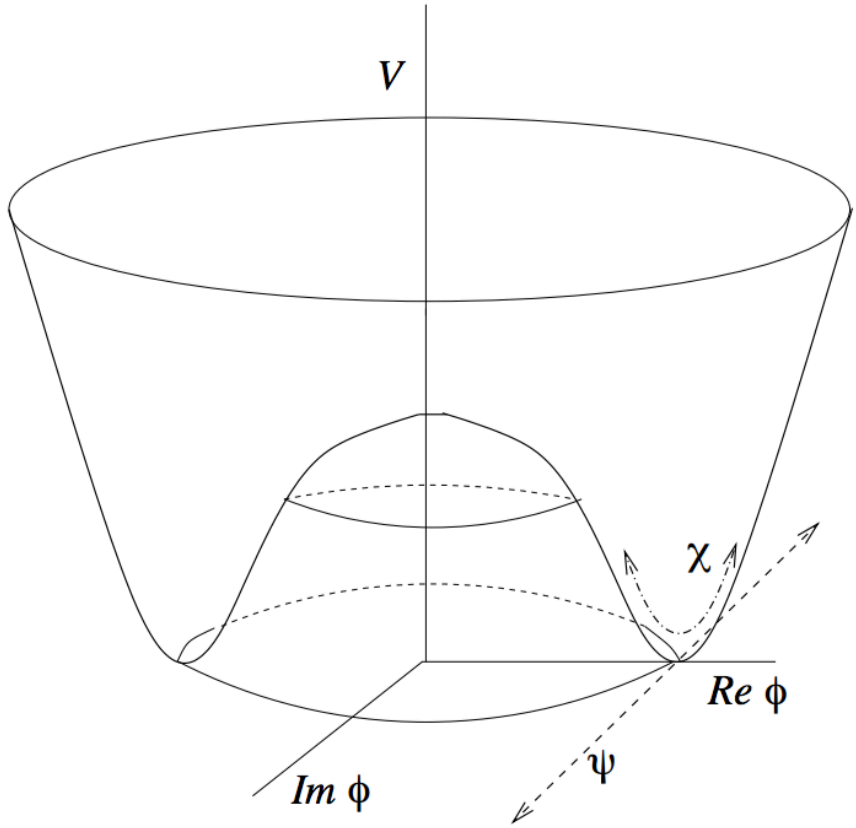

Figure 1.9: A 2D illustration of oscillations in the the scalar potential, $V(\Phi)$, parameterized by χ and ψ [25].

from the SM, except the two parameters, μ^2 and λ, or equivalently the VEV given in equation (1.29) and the mass of the Higgs Boson in equation (1.30).

$$v^2 = -\frac{\mu^2}{2\lambda} \tag{1.29}$$

$$m_h^2 = 2v^2\lambda \tag{1.30}$$

1.3.3.1 Implications of the Higgs field: Fermion Masses

When we first started our discussion of Fermions we simply wrote the mass of a fermion as $-m\bar{\psi}\psi$ in equation (1.14). However, this term would explicitly break the electroweak gauge invariance we have just spent so much time constructing. It turns out that the new scalar field h could also be responsible for the fermion masses in addition to the $W^{\pm}$ and Z masses. The term can be created by considering a Yukawa coupling between the scalar field and a fermion field. For the down quark this term follows equations (1.31)[12].

$$\begin{aligned}
\mathscr{L}_{\mathrm{d-mass}} &= -\lambda_d \bar{Q}_L \Phi d_R + h.c. \\
&= \frac{-\lambda_d}{\sqrt{2}} \begin{pmatrix} \bar{u_L} & \bar{d_L} \end{pmatrix} \begin{pmatrix} 0 \\ v+h \end{pmatrix} d_R + h.c. \\
&= \frac{-\lambda_d v}{\sqrt{2}} \bar{d_L} d_R + h.c.
\end{aligned} \tag{1.31}$$

Where the final equality comes from focusing on the terms that remain in the ground state of the scalar potential. From here its easy to see that the mass of the down quarks can be obtained from the vacuum expectation value of the scalar field and the down coupling to the Higgs field, λ_d.

[12]In these equations h.c. stands for the hermitian conjugate term.

$$m_d = \frac{\lambda_d v}{\sqrt{2}}$$

The masses of the other fermions follow from equations similar to (1.31) where the Higgs field, h, interacts with all the fermions. This will be the key to generating Higgs bosons at the LHC, particularly Higgs couplings to top quarks.

It seems that the Higgs Mechanism and the Higgs boson solve many of the issues that the SM has with describing the world we observe. However, there are many other unexplained phenomena in the universe and detailed study of the Higgs mechanism could lead unearth the origin of these discrepancies. The next subsection is an outline some of these discrepancies that will be discussed in this document.

1.4 Limitations of the SM: Higgs boson as a tool

The SM has been one of the most successful scientific theories ever proposed. The predictive power of the model is unparalleled, yet some questions remain. The first limitation we will discuss in this section will be the matter-antimatter asymmetry seen in the universe around us. Secondly, a discussion of the SM's inability to accurately describe gravity is presented. Finally, generalizations of the SM are discussed. These

models that could generate the dark matter seen in astronomical measurements, solve the hierarchy problem, or explain more about fermions. The Higgs field could offer keys to understanding all of these issues and the tests presented in this document are intended to address these questions.

1.4.1 CP-violation: The Matter-Antimatter Asymmetry

Outside of specific particle physics experiments, the universe we live in is dominated by matter. It seems that only a very small fraction of antimatter exists in the universe. However, within specific tests of SM no process is observed to generate this large of a discrepancy between matter and antimatter. Under the assumption that matter and antimatter started in equal amounts, after the Big Bang, matter and antimatter should still exits in relatively equal densities and amounts. The SM does not predict, nor has any experiment seen, a process that could generate enough CP-violation to create a universe that is so overwhelmingly dominated by matter.

So far we have only eluded to CP transformations when introducing the antiparticles that exist in the SM. In the most basic terms this is the combination of two discrete symmetries *charge conjugation* and *parity symmetry* (spatial inversion). The parity operation, P, is the spatial inversion through the origin. We saw the projections of a fermion onto the eigenstates of this operation at the end of section 1.1.3.

If $\psi(x)$ describes a fermion field at point x, then $P\psi(x) \rightarrow \psi(-x)$. This transformation will take $x \rightarrow -x$ and the momentum $p \rightarrow -p$ but leave the inherent spin and other quantum numbers unchanged. The charge conjugation operation, C, is the transformation of a particle to its antiparticle or vice versa. We used this transformation extensively in 1.3 but never wrote out the transformations explicitly. As an example, given an electron, e^-, then $Ce^- \rightarrow e^+$. This transformation will reverse the sign of all quantum numbers associated with the particle (inherent spin, weak isospin, charge, hypercharge, etc...). Particles that are their own antiparticle (π^0 meson, ν's, ...) remain unchanged under this operator (aside from a possible factor of -1).

Not all interactions allowed by the standard model will preserve these symmetries. The most explicit example is the weak interaction. Given that the weak force only interacts with left-handed particles, it is maximally parity violating[13]. However, in most cases CP together is a symmetry of the interactions. The notable exceptions to this are the decays of B mesons and Kaons [26]. These decays highlight the necessity for a CP-violating component in the SM described by the Cabibbo-Kobayashi-Moskawa Model [27]. The specifics of this model are beyond the scope of this document. However, the observed magnitudes of the terms in the CKM model cannot account for the large discrepancy that we observe in the universe.

One proposed solution to this asymmetry is the presence of more than one Higgs field, resulting in multiple Higgs bosons. The number of fields and bosons predicted

[13]Imagine a stationary pseudoscalar π^+ decaying into back-to-back μ^+ and ν_μ states via the weak interaction. Perform the parity operation on the initial and final states. The result requires a right-handed neutrino, which are unobserved.

varies depending to the model and any observed boson could have varied spin (J), charge (C), and parity (P) transformation properties. It could be charged, neutral, pure scalar, pure pseudoscalar, vector, pseudovector or a mixed vector-pseudovector state. In this document we outline tests proposed and performed to test the J^{CP} nature of a boson to see if a Higgs boson can offer any insights into the nature of the matter-antimatter asymmetry.

1.4.2 The Graviton: An Unexplained Force

Gravity would be the weakest of all the forces we know of but it is not yet included in the SM. There are many possible theories of gravity at small scales and its corresponding boson, the *graviton*. In Table 1.2 you can find a summary of the different forces and their relative strengths and interaction ranges, including gravity. Since gravity is so intimately connected with the mass of an object in relativistic mechanics it is expected to have similar couplings to the SM particles as the Higgs boson, but to match general relativity most theories claim that it must be a spin-2 particle. Generally, most theories predict that a graviton would be a massless particle to have an infinite interaction range. There is always the possibility of new physics spoiling our expectations so a detailed study of any new scalar particle found should be performed to determine if the spin is zero (as predicted by Higgs boson) or two (as predicted by a Beyond SM graviton).

In this analysis, we study a few possibilities for a graviton-like particle. This is

discussed in more detail in section 3.4.3, but generally we consider a Kaluza-Klein theories where a closed fifth dimension could give rise to a massive spin two graviton [28]. Exact definitions of the models tested, and references motivating them can be found in section 3.4.3.

1.4.3 Beyond the SM: The Dark Matter, Hierarchy & Fermion Problems

It has not been explicitly expressed in our discussion of SM phenomena but everything that we understand about the universe is really only valid at masses up to a certain sclae $\left(\sim m_{W/Z}\right)$. Using current models of the early universe, at early times we know that the energies are many orders of magnitude larger than what our SM theory can describe [29]. Many extensions of the SM to these high energies have been proposed and generally we will call them Beyond SM (BSM) theories in this document. These theories predict varied and wide ranging possibilities for new particles and physics and could be tested by examining a Higgs boson. Some BSM theories predict particles that could exist in relative obscurity on Earth but could be the *dark matter* observed in astronomical experiments [30].

Currently there is no explanation for why gravity is so much weaker, table 1.2, than the other forces. The SM requires a very specific values in order to explain this difference without theoretical motivation. This is called the *hierarchy problem* of the

SM. BSM theories offer natural solutions to this problem sometimes simultaneously with explanations for the dark matter abundance. Other issues that can be explained through BSM theories include the number of fermion generations and their masses. In principle, there is no preference for only three generations of fermions and not motivation for the specific masses of these particles.

Generally, BSM theories can come in almost any type imaginable. If these new particles interact with the scalar Φ field, then they could be seen as a deviation from the expected couplings (interactions) with SM particles. These deviations could take many forms, but those tested in this document include: Unusual production mechanisms, unexpected spin-parity behavior, and enhanced non-resonant production.

Chapter 2

The Experiment: LHC and CMS

In order to answer questions about the Standard Model (SM) we need to observe processes that are extremely rare in the universe. Many measurements to test the limits of the SM can be performed by observing nature. However, to test questions about the Higgs boson, waiting for events to happen naturally would take an extremely long time[1]. To study these processes, labs around the world create particle colliders to generate interesting phenomenon more frequently than nature would. The rate that any physics process will occur (at a collider or otherwise) is given by the effective area of the process, *cross section* (σ), and rate those reagents pass through the same area, *luminosity* ($\mathcal{L}$); equation (2.1).

$$\frac{dN}{dt} = \mathcal{L} \cdot \sigma \tag{2.1}$$

[1]In many cases much longer than the age of the universe.

The cross section for a process is the effective area of the reagents to interact in a specific way. A cross section can describe a particular number of final particles, or a specific boson used for the interaction, etc. Cross sections change depending on the energy of the interacting particles, and are usually given in units of *barns* (b = 10^{-24} cm^{-2}). They can be computed using the scattering amplitudes we have already introduced in section 1.2.

The luminosity is a measure characterizing the source of the reagents, with units that are typically cm^{-2}s^{-1}. We will discuss the particulars of this quantity for colliders, but generally luminosity is a measure of the flux of particles at a particular point in space and time.

When a particle physics experiment is designed, first numerous factors dictate what kind of particles you will accelerate and collide together. Once you have decided this, two properties define its ability to test the limits of the SM; the luminosity and the center of mass energy. With specific center of mass energies we can probe cross sections that are typically small at everyday energies. Using a higher luminosity we can increase the rate of rare events by generating interactions more often.

2.1 The Large Hadron Collider (LHC)

The Large Hadron Collider (LHC) is the largest and most powerful of these experiments in the world. It is located on the border between France and Switzerland

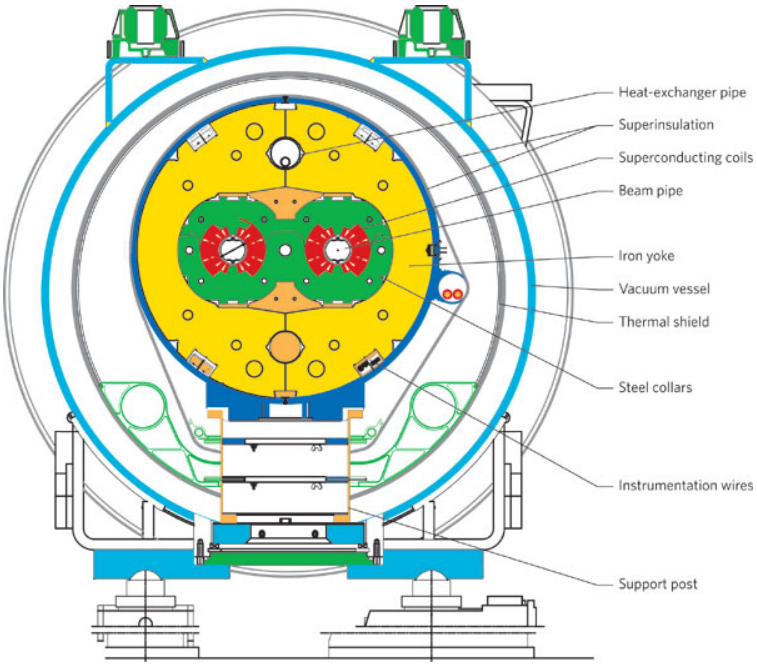

Figure 2.1: A cross section schematic of the LHC Dipole magnet showing the two center beam pipes, superconducting coils (red), and other supporting structures [31].

just outside the city of Genvève at CERN[2]. The LHC is a superconducting proton accelerator and collider measuring 27 km in circumference, approximately $\sim$ 100 m underground. It first accelerates, then collides two beams of protons circulating the ring in opposite directions[3]. These protons are circulated using 1232 dipole 'bending' superconducting magnets and a series of other quadrupoles, sextupoles, octupoles, decapoles, etc. used for controlling and focusing the beams. The layout of the dipole magnets is shown in figure 2.1 where the two beam pipes are shown along with the other magnetic, vacuum, and shielding structures.

[2]European Organization for Nuclear Research or Conseil Européen pour la Recherche Nucléaire
[3]The LHC also collides Lead ions with each other and protons, but those studies are beyond the scope of this document.

The LHC probes small cross sections by smashing two beams of high energy protons into each-other giving large center of mass energies. In the original design, each proton beam would have 7 TeV of energy giving 14 TeV in the center of mass frame. However, these studies will focus on the early years of LHC operation where the center of mass energies were 7 TeV (2011) and 8 TeV (2012).

The luminosity of the LHC depends on the geometrical and electrodynamic parameters of the beam. For a beam of particles that are Gaussian distributed, the luminosity is given by the product of the beam current ($f_{\text{rev}} n_b N_b$), brightness $\left(\frac{N_b}{\epsilon_N}\right)$, energy $\left(\frac{\gamma}{\beta^*}\right)$ and a geometric reduction factor (F):

$$\mathcal{L} = \frac{1}{4\pi} \cdot (f_{\text{rev}} n_b N_b) \cdot \frac{N_b}{\epsilon_N} \cdot \frac{\gamma}{\beta^*} \cdot F. \tag{2.2}$$

In this equation (2.2) the relevant factors that determine the beam current are the revolution frequency, (f_{rev}), the number of proton bunches in each beam, (n_b), and the number of protons in each bunch, (N_b). Generally, the LHC tries to maximize this beam current so that the number of protons in each beam is as large as possible. The brightness of the beam determines how likely two protons are to interact when one bunch crosses another. It is determined by the number of protons in a bunch and the normalized transverse beam emittance, (ϵ_n), which is a measures of the area of the beam in the position-momentum phase space. The energy of the beam is determined by the relativistic γ factor and the value of the beta function at the collision point, (β^*). The beta function describes transverse size of the beam and $*$ denotes that

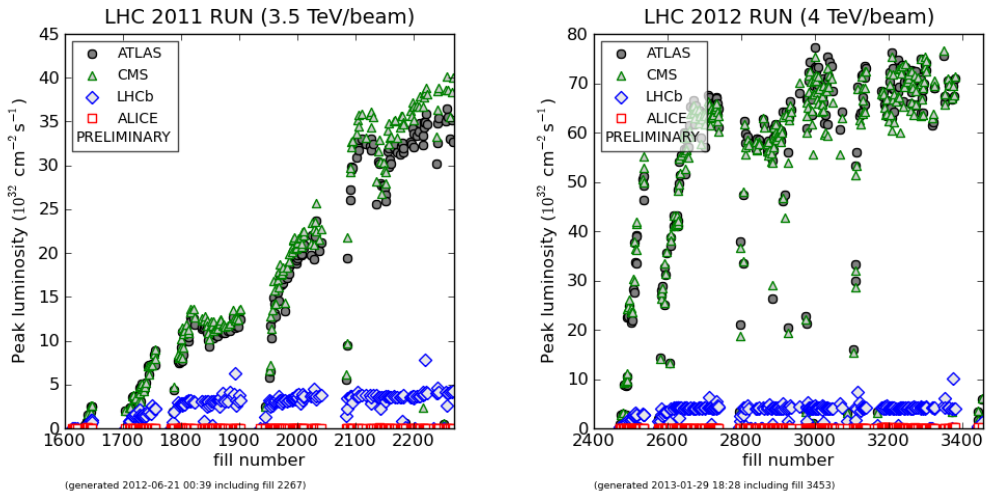

Figure 2.2: The peak luminosity delivered to the four main LHC experiments during the 2011 7 TeV (left) and 2012 8 TeV (right) runs [32].

this function should be evaluated at the collision point. The final term, (F), is the geometrical factor that describes the reduction in luminosity because the two beams cross each-other with some non-zero angle between them.

For the experiments that require the highest luminosities, the LHC was designed to provide 10^{34} cm^{-2}s^{-1}. The machine ran at lower luminosities for the first few years of operation as seen in the figures 2.2 [32].

To get the protons up to the necessary energies, protons are accelerated through a series of smaller accelerators which are pictured in figure 2.3. The process starts with the 50 MeV LINAC2 which shoots the protons into a multi-ring booster synchrotron that accelerates them up to 1.4 GeV. Next the protons are directed to the Proton Synchrotron (PS) machine which accelerates them up to 26 GeV and generates the bunching and spacing that the LHC uses. To accelerate the beam from 26 GeV up

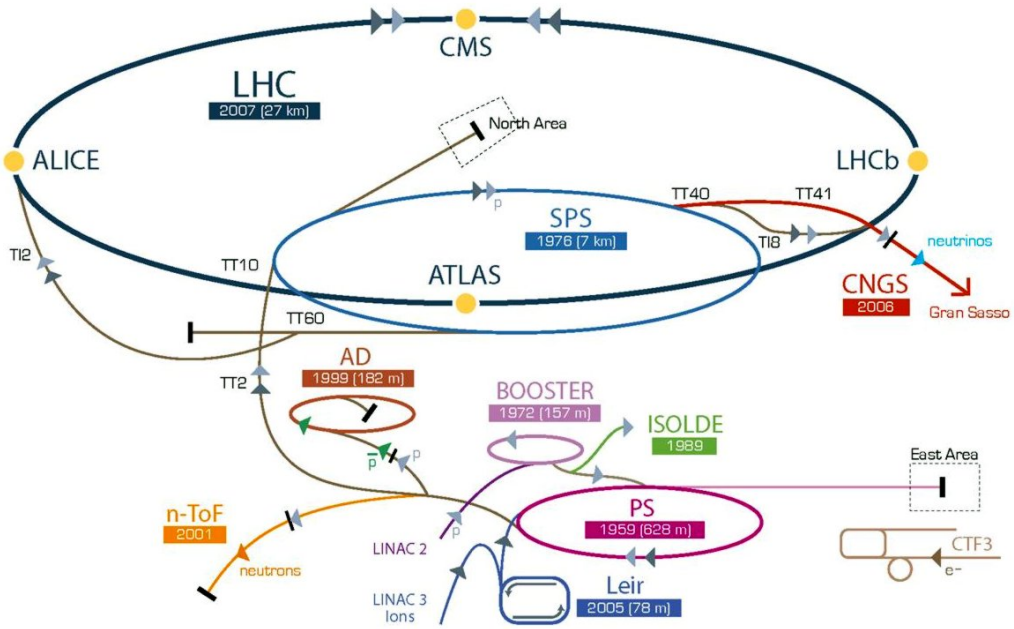

Figure 2.3: This CERN accelerator complex. Showing the full chain of accelerators used for the LHC protons: LINAC2, Booster, PS, SPS, and LHC. Additionally, the four large experiments on the LHC are shown: ALICE, ATLAS, CMS, LHCb [33].

to 450 GeV the beam is fed into the Super Proton Synchrotron (SPS). From the SPS the protons are fed into one of the LHC rings. Before the LHC accelerates these protons up to their final energies, this process is repeated 24 times, 12 to fill each of the two rings. Once the LHC has accelerated these proton bunches to their final energies, the beams are gradually brought together so that they will collide inside the four experiments.

The particle physics community built detectors to observe and categorize the particles that are produced when these protons (ions) are collided with each-other. Currently there are four experiments at the LHC: A Toroidal LHC ApparatuS (ATLAS), the Compact Muon Solenoid (CMS), A Large Ion Collider Experiment (ALICE), and

Large Hadron Collider beauty (LHCb). The ATLAS and CMS detectors are high luminosity, multi-purpose detectors designed to test many different aspects of the SM, including the Higgs boson. LHCb looks specifically at bottom (beauty) quark interactions, while ALICE is designed for ion collisions. This work took place at the CMS experiment, described in the next sections.

2.2 The Compact Muon Solenoid (CMS)

The Compact Muon Solenoid (CMS) experiment is one of the two largest experiments on the LHC. The general goal of the CMS experiment is to collect and study as many interesting events from LHC collisions as possible. To do this, CMS must identify interesting physics events and reconstruct these events as accurately as possible. At the designed energy and luminosity the LHC is expected to create ~ 1 billion collision events per second. It would not be possible to reconstruct all of these events, so CMS has an extensive online event selection process, called the 'Trigger', that reduces this to about 100 events per second. Some details of this process are presented in section 2.3, but we will first have a discussion of the different CMS subdetectors.

To quantify how much data CMS has collected we use *integrated luminosity*, which is the time integral of the luminosity, $\int \mathcal{L} dt$. This value tells experimenters how many events to expect for the specific processes they study, $N = \sigma \cdot \int \mathcal{L} dt$, and allows them to test smaller and smaller cross sections. Over the 2011 and 2012 runs[4] of the CMS

[4] A run is a period of time denoting specific conditions for the detector or LHC.

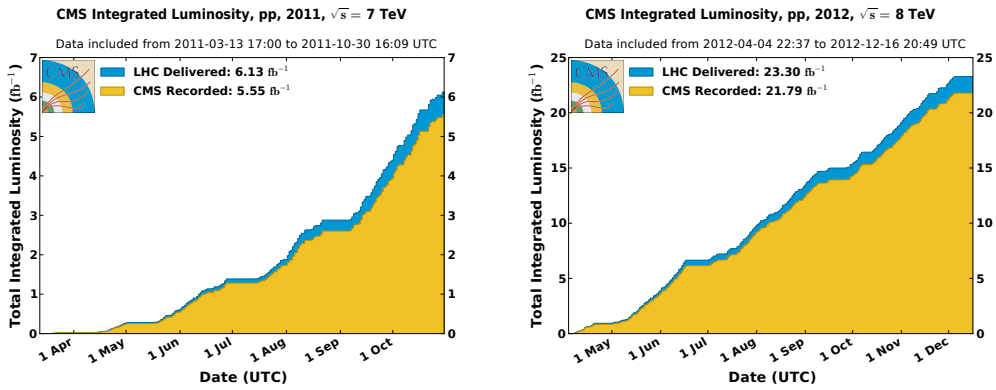

Figure 2.4: The integrated luminosity delivered and collected by the CMS experiment during the 2011 7 TeV (left) and 2012 8 TeV (right) runs, [34].

detector collected 5.1 fb^{-1} and 19.7 fb^{-1} of integrated luminosity respectively, shown in figure 2.4.

To maximize the physics results that can be pulled from this data, CMS was designed with key features that give credence to its name. While it may seem oxymoronic to call a 21.6 m long and 15 m in diameter experiment 'compact', the name is fitting because it is designed to put the sub-detectors within CMS close together. This compact design is a result of the 4 T magnetic field that is the heart of the CMS detector. The Magnet, discussed more in section 2.2.1, causes the charged particles generated in collisions to bend as the flow out from the interaction point so identifying particles and measuring their momentum requires detectors that are close together. Working in concert with this field, the CMS detectors are designed to fit together as a 'cylindrical onion'. The layers of detectors and sub-detectors radiate outward from the point where the protons collisions take place. Each layer is designed to maxi-

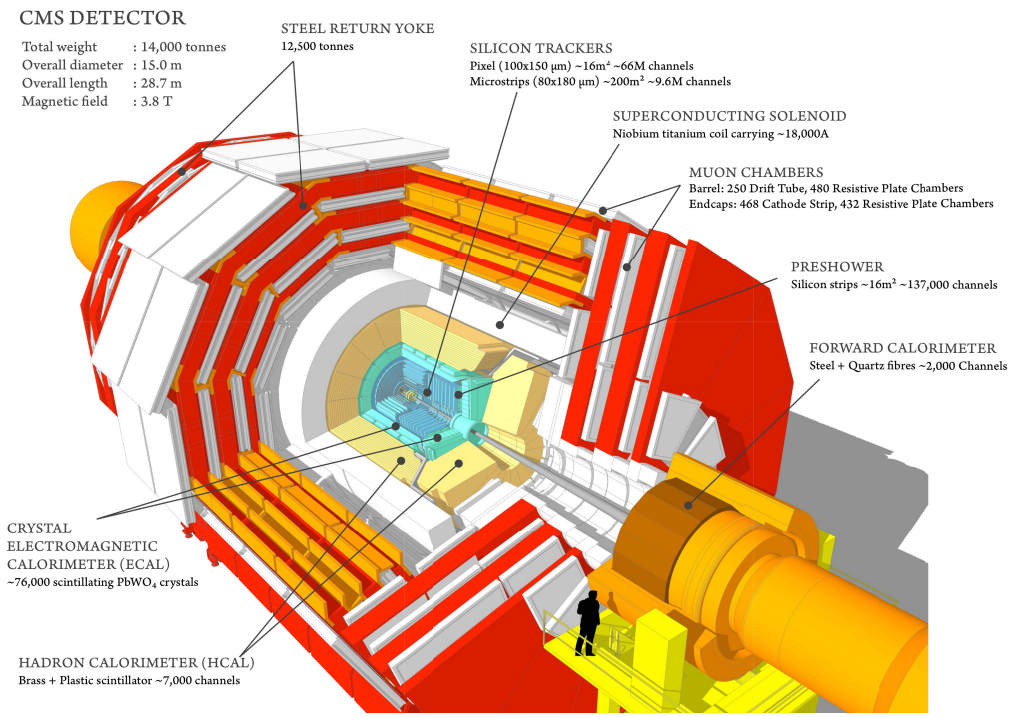

Figure 2.5: Sectional view of the CMS detector. The LHC beams travel in opposite directions along the central axis of the CMS cylinder colliding in the middle of the CMS detector [36].

mize the physics information that can be obtained at different distances from these collisions. The majority of the information in this section follows [35].

A sectional view of the CMS detectors can be seen in figure 2.5. From this image you can see a summary of the different subdetectors that we discuss from inside out. The innermost detector is the Silicon tracker, discussed in section 2.2.2, this detector is designed to give good momentum resolution for charged particles and high reconstruction efficiency requiring precise alignment of the tracking system. Additionally, this tracker needs to be able to efficiently tag τ's and b's, which will have a displaced

vertex due to their long lifetimes. This requires pixel detectors close to the interaction point.

Just outside of the tracking system is the Electromagnetic calorimeter (ECAL), discussed in section 2.2.3, which gives good energy and mass resolution for photons and electrons and wide geometric coverage. Further, the high segmentation of the system allows for great directional discrimination to determine the origin of the particles and to determine how isolated they are from other particles.

The final detector that still lies inside the bore of the solenoid is the Hadronic Calorimeter (HCAL), described in section 2.2.4. This detector allows for accurate measurements of quark-jet mass resolution and the lateral segmentation gives directional information that is key to determine any imbalance in the transverse energy of a collision, E_T^{miss}.

Outside of the solenoid magnet lies the Muon System, described in section 2.2.5, and the large Iron return yokes. This is the largest and heaviest part of the CMS detector[5]. This system gives good muon identification and good momentum resolution over a wide range of angles and energies for high momentum muons.

As we describe the CMS detector we will need to define a set of spacial coordinates so that we can locate ourselves within the detector. The coordinate system is defined to put the origin at the nominal collision point inside the experiment, the y-axis pointing vertically upward, the x-axis pointing along the radius of the LHC, and the

[5]When combined with the magnet and other subdetectors the full CMS detector weighs $\sim$ 14,000 tonnes.

z-axis pointing along the beam direction. The geometry of the detector is already cylindrical, so a modified form of cylindrical units are use for most studies. The azimuthal angle ϕ, is given by the angle from the x-axis in the x-y plane. The polar angle, θ (from the z-axis), normally used in cylindrical coordinates, is replaced by the pseudorapidity, $\eta = -\ln\tan(\theta/2)$. The z-axis is the same as the cartesian definition. Often, interesting physics events will show distinct features in the momentum or energy transverse to the beam direction, p_T and E_T respectively.

2.2.1 The Magnet

The defining feature of CMS is the superconducting solenoid magnet, the parameters are given in table 2.1. The large bending power that CMS is designed for is obtained form a reasonably-sized superconducting solenoid where the bending for charged particles starts at the primary vertex. The strong field is needed to give good momentum resolution. It bends muons tightly so that the charge is unambiguous and giving a momentum resolution of $\Delta p/p \sim 10\%$ at $p = 1$ TeV/c. This design also leads to a reasonable field in the forward region where many of the detected particles will be.

The magnet itself is constructed from high-purity aluminum-stabilized conductor and is indirectly cooled using a thermosiphon method. While this type of magnet has been used at other experiments, it was a large step up in many aspects from previous magnets. To create a solenoid with the field and dimensions, a four-layer

Field	4 T
Inner Bore	5.9 m
Length	12.9 m
Number of Turns	2168
Current	19.5 kA
Stored Energy	2.7 GJ
Hoop stress	64 atm

Table 2.1: Parameters of the CMS superconducting solenoid, [35].

conductive winding with a large diameter wire was used so it could withstand the large outward pressure (hoop stress). The conductor carries a 19.5 kA current and is co-extruded with pure and alloy aluminum to stabilize it thermally and mechanically. The conductor was manufactured in twenty continuous lengths, each of 2.65 km. Four of these lengths were used to make each of the five coil modules within the magnet.

Working in concert with the magnet is the iron return yoke of the muon system. As can be seen in figure 2.6, the superconducting magnet generates a large magnetic field inside the solenoid while the return flux of the field concentrates itself in the large iron structures that house the different muon detectors. These performance predictions were later confirmed by both monitors installed in the detector and with data collected from cosmic rays [37].

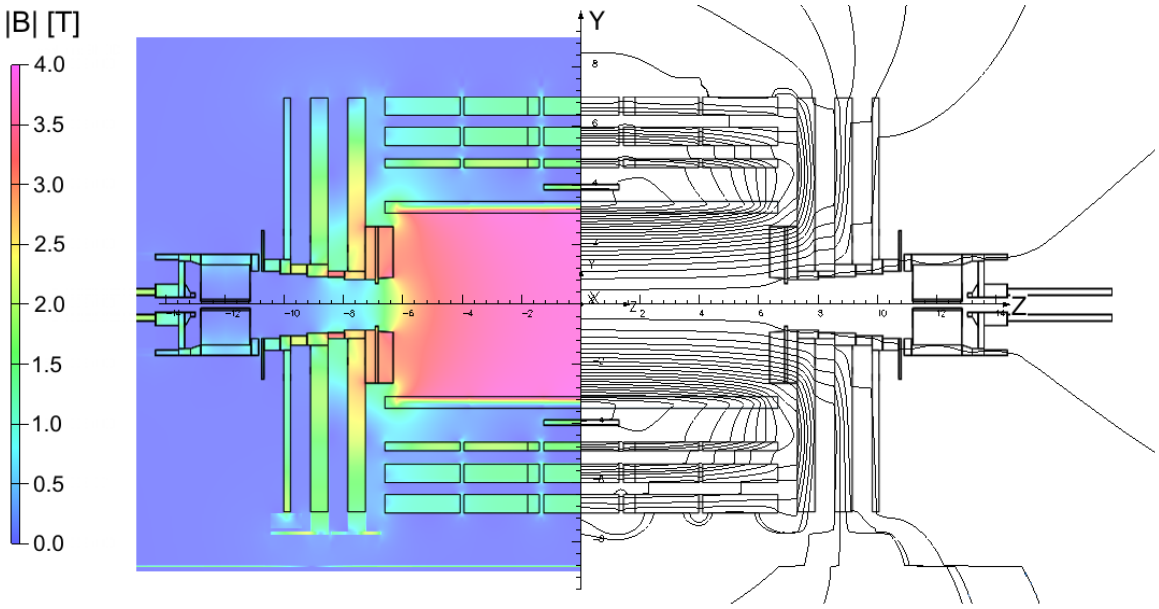

Figure 2.6: Value of magnetic field $|B|$ (left) and field lines (right) predicted on a longitudinal section of the CMS detector, for the underground model at a central magnetic flux density of 3.8 T. Each field line represents a magnetic flux increment of 6 Wb [37].

2.2.2 The Inner Tracker System

The inner tracker system is the first detector that a particle generated from an LHC collision will encounter. At the LHC, determining the origin of these particles is key and made more difficult due to the small gaps between proton bunches. The spatial resolution of the silicon tracker detector allows a particle to be mapped to the primary collision vertex (*primary vertex*), secondary vertices, or identify them as *pileup events*. At the designed luminosity, the LHC is expected to generate about 20 collisions[6] that will all be superimposed on an event of interest. This means that ~ 1000 charged particles will appear in the detector for every interesting event. The job of the inner tracker is to measure the charge and momentum of these particles, and determine which of these originate from what vertex. To do this, the tracker has two distinct types of detectors; the 66 million *silicon pixels* and 9.6 million *silicon strips*. It is also vital that the positions of these detectors is accurately known at all times so that the system can operate at its ideal level. The process of determining the positions of these detectors is called *Tracker Alignment* and an overview of work performed for this task is presented.

2.2.2.1 Pixel Tracker

Close to the interaction vertex the tracker consists of three layers of silicon pixel modules in the barrel region and two layers of silicon pixel modules in each forward

[6] We expect more moving forward.

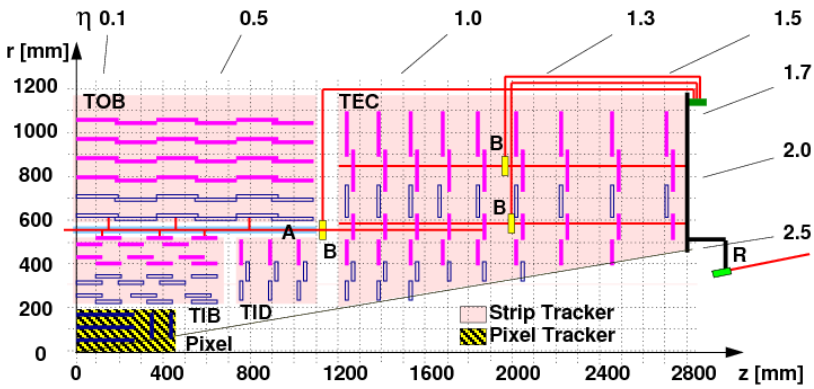

Figure 2.7: Schematic view of one quarter of the silicon tracker in the r–z plane. The positions of the pixel modules are indicated within the hatched area. At larger radii within the lightly shaded areas, solid rectangles represent single strip modules, while hollow rectangles indicate pairs of strip modules mounted back-to-back with a relative stereo angle [38].

region. The layout of the pixel detector is shown in figure 2.8. Each of the three barrel layers are located at radii 4.4 cm, 7.3 cm, and 10.2 cm from the nominal interaction point and each is 53 cm long. On either side of the three barrel layers are two end disks placed at $|z| = 34.5$ cm and 46.5 cm.

All of the pixel modules start from the same base array (52 column $\times$ 80 row) of

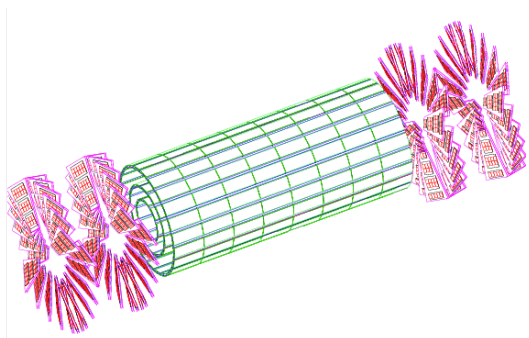

Figure 2.8: Layout of the pixel detectors in the CMS tracker [35].

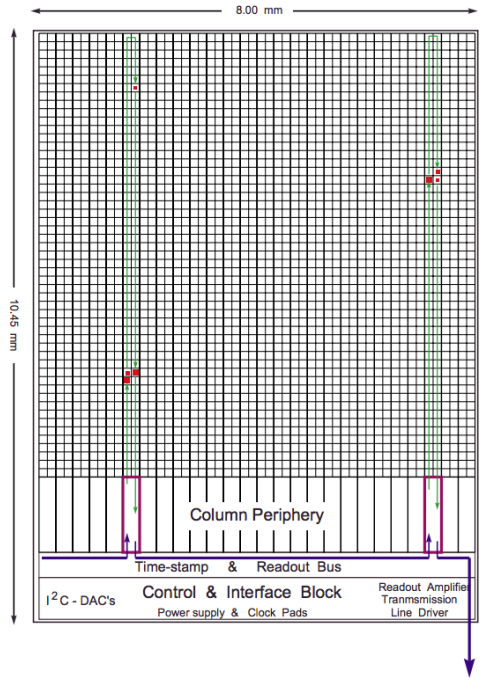

Figure 2.9: Layout of the pixel sensor in the CMS tracker [39].

pixels (size: 100 µm × 150 µm) bump-bonded to a readout chip (ROC). Each pixel is connected to its own amplifier, shaper, and comparator (including an individual 3-bit DAC threshold) which is connected to a 'double-column' group shown in figure 2.9. The periphery of each double-column contains a data buffer, timestamp, and corresponding control and readout electronics. ROC's are grouped into modules. Each module has a different number of ROCs depending on the geometry of the region where the detectors are placed.

The pixel barrel (BPIX) contains 768 modules grouped into three layers[7] and two *half-barrels*[8]. While the forward pixel detectors (FPIX) are made from 672 modules

[7]There are smaller substructures within each layer.
[8]All three layers together make one half-barrel.

grouped into two layers of turbine-like blades. The forward structures are also grouped into *half-cylinders* similar to the barrel region[9]. Both the barrel layers and the blades are oriented to benefit form the large Lorentz effect (charge drift in a magnetic field) that increases the resolution through charge sharing between the pixels.

In the end, the inner tracker comprises 66 million individual pixel channels readout using approximately 16000 ROCs, giving a spatial resolution of about ~ 10 µm in r-ϕ and 20 µm in z. This high resolution allows for precise momentum determination for particles as they curl in the high magnetic field. It is also key to determining the origin of the particles that CMS measures. The ~ 1 m^2 silicon pixel detector provides coverage up to $|\eta| < 2.4$.

2.2.2.2 Strip Tracker

Much larger than the pixel tracker is the ~ 200 m^2 silicon strip tracker. The strip tracker is divided into four parts: TIB (tracker inner barrel), TID (tracker inner disks), TOB (tracker outer barrel), and TEC (tracker end cap). The CMS tracker is the largest silicon detector ever built. Different regions of the strip tracking system have different module types summarized in table 2.2. All together, the Silicon Strip Tracker has complete coverage up to $|\eta| < 2.4$.

In the barrel region the coverage for the TIB and TOB is very different. The TIB has four layers and covers $|z| < 65$ cm with silicon sensor of a thickness of 320 µm.

[9]Again, the two layers together make the half-cylinders.

part	No. detectors	thickness (µm)	mean pitch (µm)
TIB	2724	320	81/118
TOB	5208	500	81/183
TID	816	320	97/128/143
TEC(inner)	2512	320	96/126/128/143
TEC(outer)	3888	500	143/158/183

Table 2.2: Detector types in the silicon strip tracker, [35].

The first two layers are made with “stereo" modules in order to provide both r-ϕ and r-z measurements. These stereo modules are made with a stereo angle of 100 mrad giving the TIB single-point resolution of 23-34 µm in r-ϕ and 23 µm in z. The TOB has six layers covering $|z| < 110$ cm with silicon sensor of a thickness of 500 µm. The first two layers of the TOB are also stereo modules with a stereo angle of 100 mrad. This gives the whole TOB a resolution of 35-52 µm in r-ϕ and 52 µm in z.

The each of the two TECs comprises nine disks that cover the 120 cm $< |z| <$ 280 cm forward region. While the TID covers the gap between the TIB and the TEC. Both the TID and TEC modules are arranged in rings centered at the beam line. The strips in these sensors radiate outward from the beam line so the pitch is different for each strip. The first two rings of the TID and the first, second, and fifth rings of the TEC are stereo modules as well allowing for more precise resolution. The TID and first three rings for the TEC have 320 µm sensors while the rest of the TEC has 500 µm sensors.

All of these structures (BPIX, FPIX, TIB, TOB, TID, TEC) are mounted in carbon-fiber structures and are cooled to ensure they operate correctly for a long

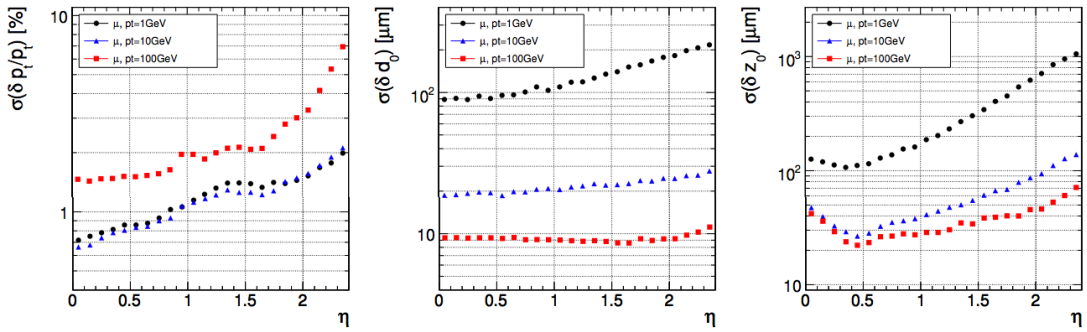

Figure 2.10: Predicted resolution of several track parameters for single muons with 1, 10, and 100 GeV: transverse momentum (left), transverse impact parameter (center), and longitudinal impact parameter (right). [40].

time[10]. Using the precise position information that the tracker provides CMS is able to determine with very high confidence the momentum and impact parameter (How close a particle's path is the the origin.) of particles, see figure 2.10. Careful consideration is taken when these detectors are moved and installed but precise determination of the exact location of all components is key to keep the optimal resolution of these detectors. This process is not only vital during the LHC startup but care needs to be taken as the detector takes data to ensure no loss in performance.

2.2.3 Electromagnetic Calorimeter

The CMS Electromagnetic Calorimeter (ECAL) is composed of 61200 lead tungstate ($PbWO_4$) crystals mounted in the barrel part of the detector and 7324 crystals in each of the two end caps. Together the barrel and end caps make a homogeneous and her-

[10]Because of technical problems during run 1 the detectors were not kept as cold as originally designed.

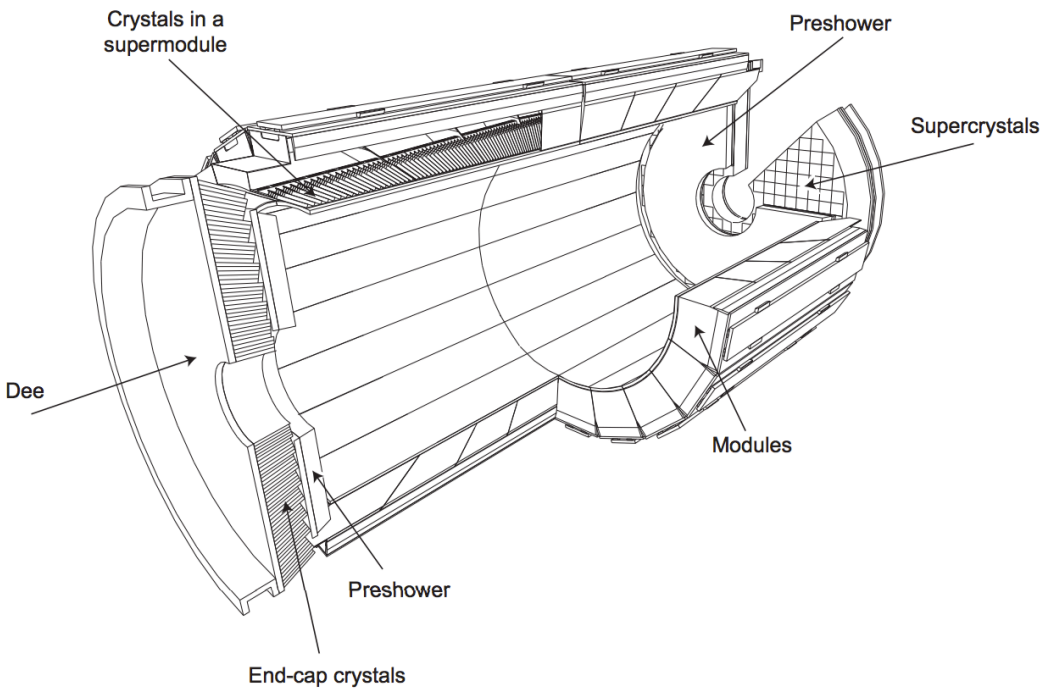

Figure 2.11: Layout of the CMS electromagnetic calorimeter showing the arrangement of crystal modules, supermodules and end caps, with the preshower in front. [40].

metic scintillating layer surrounding the Inner Tracker. The crystals were chosen to have short radiation and Moliere lengths while being fast radiation hard scintillators. Due to the low light yield of the crystal, silicon avalanche photo diodes (barrel) or vacuum phototriodes (end cap) are used because they can operate in the magnetic field. Additionally, to stabilize the response of the crystals and photo diodes a cooling system is used to maintain temperature stability. Thus, the ECAL is a compact calorimeter that is fast, has fine granularity, and is radiation resistant.

The ECAL barrel section (EB) has an inner radius of 129 cm and constructed as 36 identical “supermodules" each covering half the barrel length and covering a range

of $0 < |\eta| < 1.479$. The crystals are installed to be quasi-projective (axis tilted 3°) to the nominal vertex arranged in an η-ϕ grid. They have a front face cross-section of 22×22 m^2 and a length of 230 mm.

The ECAL end caps (EE) lie at a distance of 314 cm from the vertex and cover a range of $1.479 < |\eta| < 3.0$. The end cap crystals, like the barrel, are off-point from the nominal vertex but are arranged in an x-y grid. They have a larger face size than the barrel crystals, 28.6×28.6 m^2 and a length of 220 mm. Additionally, a preshower detector is placed in front of the EE consisting of two planes of silicon strip detectors each placed behind a layer of lead absorber disks.

While the specifics of particle reconstruction are discussed in section 2.3, figure 2.12 shows the electron resolution of the EB system compared to and then combined with the inner tracker system.

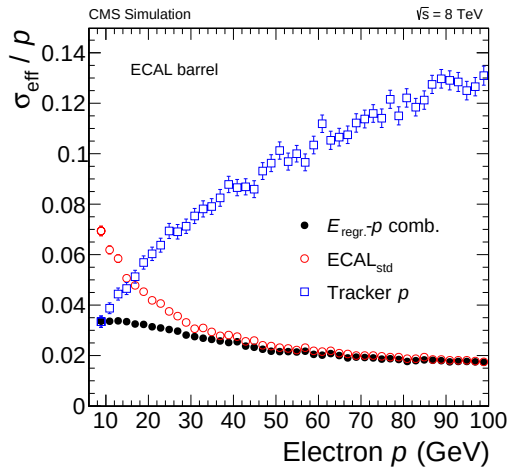

Figure 2.12: Effective momentum resolution σ_{eff}/p for electrons in the EB as a function of the momentum for the ECAL-only, the tracker-only, and the combined estimates. [41].

2.2.4 Hadronic Calorimeter

The design of the hadron calorimeter (HCAL) is strongly influenced by the choice of magnet parameters because most of the system is located inside the magnet coil and surrounds the ECAL system [35]. The HCAL system consists of a set of sampling calorimeters. The barrel (HB) and endcap (HE) calorimeters utilize alternating layers of brass as absorber and plastic scintillator as active material. The scintillation light is converted by wavelength-shifting fibers embedded in the scintillator and channeled to hybrid photodiode detectors via clear fibers. The outer calorimeter (HO) uses the CMS magnet and return yoke as the absorber while using the same active material and readout system as HB and HE. The HO system serves as a “tail-catcher" after the magnet oil, thus reducing the tails in the energy resolution function.

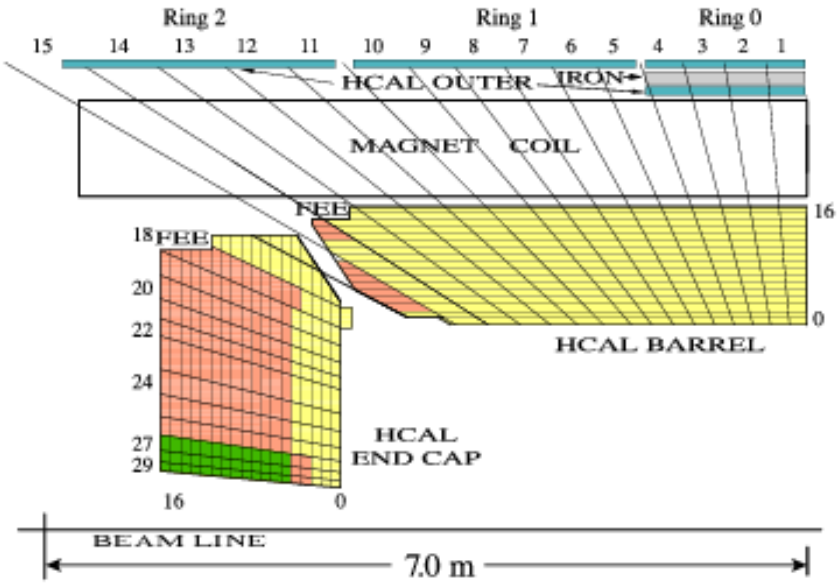

Figure 2.13: A quarter slice of the CMS HCAL detectors. The right end of the beam line is the interaction point, HF (not pictured) would be located far to the left. In the diagram, the numbers on the top and left refer to segments in η, and the numbers on the right and the bottom refer to depth. Colors/shades indicate the combinations of layers that form the different depth segments, which are numbered sequentially starting at 1, moving outward from the interaction point. The outer calorimeter is assigned depth 4. Segmentation along ϕ is not shown [42].

The HCAL is segmented into individual calorimeter cells along three coordinates, η, ϕ, and depth. The depth is an integer coordinate that enumerates the segmentation longitudinally, along the direction from the venter of the nominal interaction region. The layout of the system can be seen in figure 2.13. The HB system covers the region $-1.4 < \eta < 1.4$ constructed in 2 half barrels. The HE covers the region $1.3 < |\eta| < 3.0$, the segmentation is not uniform in order to maintain coverage and resolution.

Coverage between $3.0 < |\eta| < 5.0$ is provided by the steel/quartz fiber hadron

forward (HF) calorimeter. HF is unique in that it preferentially samples the neutral component of the hadron shower. This design leads to narrower showers and hence is ideally suited for the congested environment of the forward region. The HF detector is located outside of the muon system, 11.2 m from the interaction point. Unlike the scintillator that is used in the other HCAL systems, HF uses Cerenkov light emitted in the quartz fibers lay parallel to the beam and are placed in a square grid inside steel plates.

What is actually measured by the HCAL system are particle jets. This is a result of the QCD that was discussed in previous sections and is outlined a bit more in section 2.3. The granularity and sampling of the different components of the HCAL system have been chosen so that the jet energy resolution is similar in all three regions (HB, HE, HF). This is illustrated in figure 2.14 where the jet energy resolution is plotted as a function of the transverse energy. More details on this plot can be found in [35].

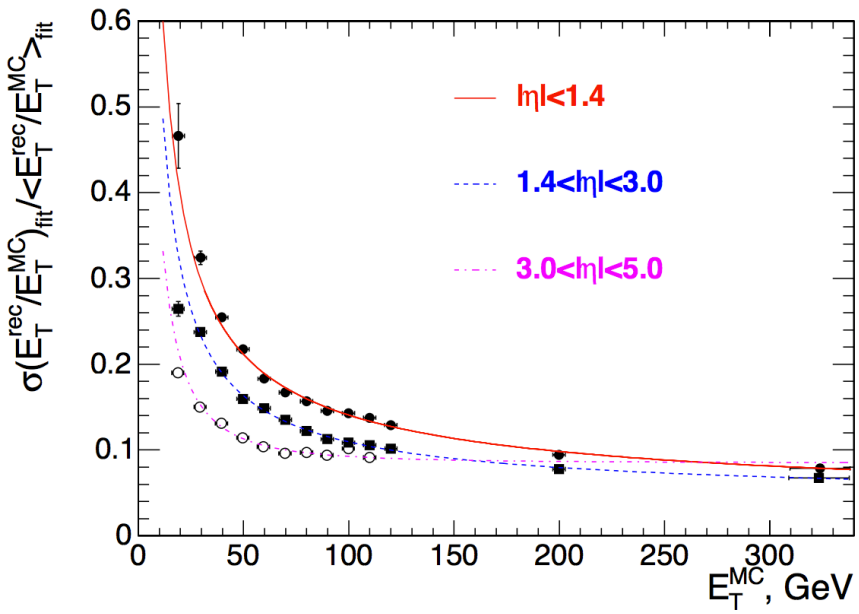

Figure 2.14: The jet transverse energy resolution as a function of the simulated jet transverse energy for barrel jets ($|\eta| < 1.4$), endcap jets ($1.4 < |\eta| < 3.0$) and very forward jets ($3.0 < |\eta| < 5.0$) [35].

2.2.5 Muon System

Muons at CMS are measured three times: in the inner tracker, after the magnet coil, and in the return flux. The muon system is designed to measure the path of the muons once they exit the magnet coil and as they traverse the return yoke. The momentum of the muons is measured by the bending angle of the muon's path as they exit the 4 T coil taking the interaction point as the origin of the muon. The resolution at the origin of this measurement (hereafter referred to as "muon system only") is dominated by multiple scatter in the material before the first muon station. This applies up to $p_T \sim 200$ GeV/c, at which point the spatial resolution of the chamber states to dominate. For low-momentum muons, the best momentum

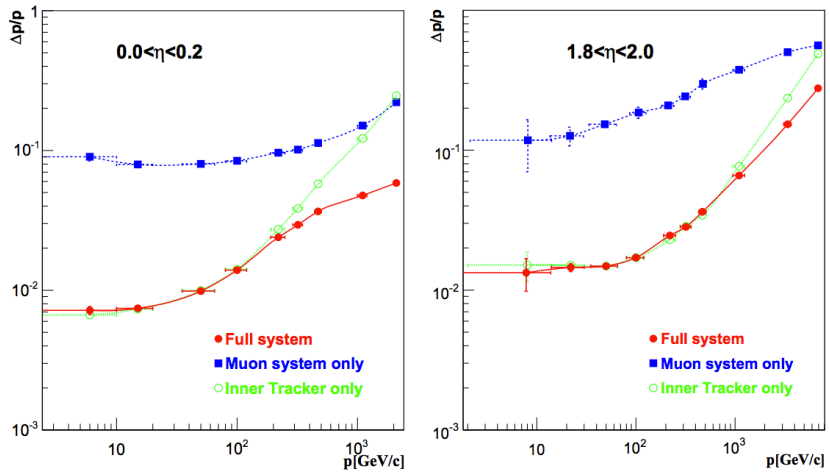

Figure 2.15: The muon momentum resolution verses p using the muon system only, the inner tracker only, or both ("full system"). (left) Barrel $|\eta| < 0.2$ and (right) endcap $1.8 < |\eta| < 2.0$ [35].

resolution is determined by the silicon tracker ("inner tracker only"). However both systems contain information about the momentum and origin of muons, so CMS uses both of them ("full system") in concert to determine the momentum of muons produced in collisions. The momentum resolution can be seen in figure 2.15.

The muon system contains three types of gaseous detectors designed to cover the very large surface and the different radiation environments. The barrel region ($|\eta| < 1.2$) is characterized by low neutron induced background, low muon rate, and low residual magnetic field in the chambers. For these reasons, drift tube (DT) chambers are used. In contrast the endcap region has high muon rates, neutron induced backgrounds, and residual magnetic field. So in the endcaps cathode strip chambers (CSC) are used to cover the region up to $|\eta| < 2.4$. Both the endcap and barrel regions also use resistive plate chambers (RPC) which provide a fast response

with good time resolution but lower position resolution than the DT and CSC systems. Taking the time information from the RPCs in concert with the position information from the CSCs and DTs provide necessary and complementary measurements. The whole system provides a precise and flexible detector that can be used for triggering and measurements.

The layout of one quarter of the CMS muon system is shown in figure 2.16. In the barrel region, four stations of detectors are arranged in cylinders interlayered with the iron return yoke. The segmentation follows the five wheels of the yoke. In each of the endcaps, the CSC and RPC detectors are arranged with four disks perpendicular to the beam in concentric rings. In total, the muon system contains ~ 25000 m^2 of active detection planes with ~ 1 million electronic channels.

The barrel detectors consist of 250 chambers organized in four layers inside the magnet return yoke, at radii of approximately 4.0, 4.9, 5.9, 7.0 m from the beam axis. Each DT chamber in the three innermost stations consists of 12 layers of drift tubes divided into three groups of four consecutive layers, hereafter called SuperLayers (SL). The tubes inside each SL are staggered by half a tube. Two SLs measure the $r - \phi$ coordinate in the bending plane (they have wires parallel to the beam line), and the third SL measures the z-coordinate running parallel to the beam. In the outermost station each DT chamber has only the two SLs that measure the $r - \phi$ coordinate. The two innermost stations consist of ÒsandwichesÓ made of a DT chamber placed between 2 RPCs. The two outermost stations consist of packages of a DT chamber

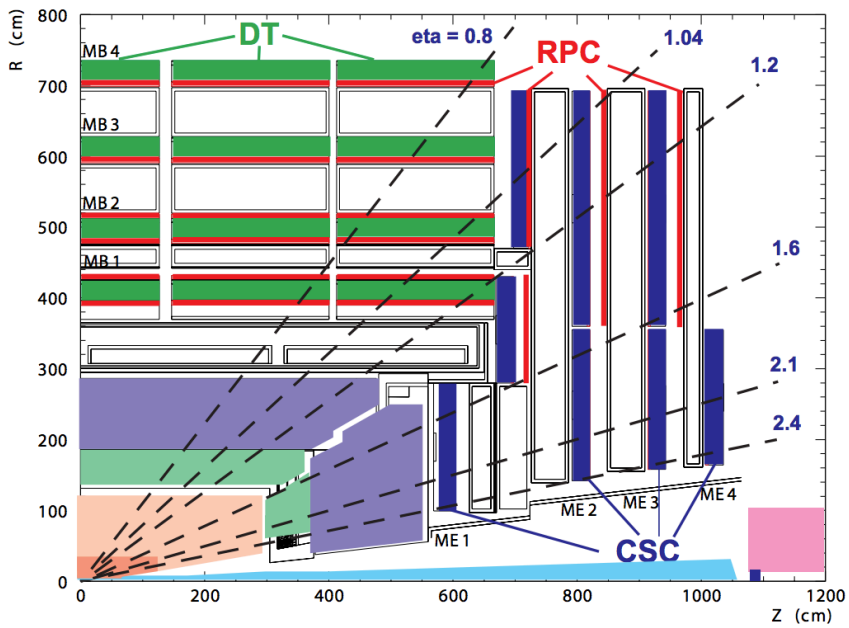

Figure 2.16: Layout of one quarter of the CMS muon system for initial low luminosity running. The RPC system is limited to $|\eta| < 1.6$ in the endcap, and for the CSC system only the inner ring of the ME4 chambers have been deployed [35].

coupled to a layer made of 1, 2, or 4 RPCs, depending on the sector and station, placed on the innermost side of the station. The maximum drift length in the barrel is 2.0 cm and the single-point resolution is $\sim$ 200 µm, giving a ϕ precision better than 100 µm in position and approximately 1 mrad in direction.

In the two endcaps, 468 CSCs arranged in four stations of chambers which are mounted in disks enclosing the CMS magnet, perpendicular to the beam direction. Each CSC is a trapezoidal in shape and consists of six gas gaps, each gap having a plane of radial cathode strips and plane of anode wires running almost perpendicularly to the strips. Most CSCs are overlapped in ϕ to avoid gaps in the muon acceptance[11]. Each ring station consists of 36 chambers, except for the innermost ring of the second, third, and fourth disks which have 18 chambers. A precise position measurement is made by determining the center-of-gravity of the charge distribution induced on the cathode strips with a spatial resolution $\sim$ 200 µm and angular resolution in $\phi \sim$ 10 mrad. Like in the Barrel, there are layers of double-gap RPCs in the endcaps, however, for the initial low-luminosity run there are RPCs only in the outer rings of each station, while they are staged in the internal rings. The RPC endcap system is thus limited to $\eta < 1.6$ for the first period of data taking.

[11]The exception being the third ring of the first endcap disk.

2.3 Triggering and Particle Reconstruction

At the designed specifications the LHC would lead to $\sim 10^9$ interactions/sec. Data from only about 10^2 crossings/sec can be written to archival media; hence, the trigger system has to achieve a rejection factor 10^6. This is performed by the CMS trigger and data acquisition system which consists of four parts: the detector electronics, the Level-1 trigger, the readout network, and an online event filter system (processor farm) that executes the software for the High-Level Triggers (HLT).

Once the data is archived, CMS must analyze this data and reconstruct the individual particles that make up the event. A particle flow event-reconstruction algorithm (PF) has been successfully deployed in the CMS experiment and is nowadays used by most of the analyses. It aims at identifying and reconstructing individually each particle arising from the LHC proton-proton collision, by combining the information from all the subdetectors. Using this algorithm individual particles can be identified as photons, electrons, muons, or charged/neutral hadrons.

2.3.1 CMS Trigger

The size of the LHC detectors and the underground caverns that they reside in imposes a minimum transit time for the signals from the front-end electronics to reach the services cavern which houses the Level-1 trigger logic. A signal must pass from the various subdetectors we have discussed to this Level-1 system and back again to

signal a readout of the full detector. The total time allocated for the transit and for reaching a decision to keep or discard data from a particular beam crossing is 3.2 µs. During this time, the detector data is held in buffers while trigger data is collected form the front-end electronics and decisions reached that discard a large fraction of events while regaining the small fraction of interactions of interest (approx. 1 in 1000). Of the total latency, the time allocated to the Level-1 trigger calculations is less than 1 µs.

Custom hardware processors form the Level-1 decision. The Level-1 triggers involve the calorimetry and muons systems, as well as some correlation of the information between these systems. These Level-1 decisions are based on the presence of "trigger primitive" objects such as photons, electrons, muons, and jets above a set of E_T and p_T thresholds that have reduced granularity and resolution. It also employs global sums of E_T and E_T^{miss}. The designed Level-1 pass rate is 100 kHz, but was limited to 50 kHz at startup.

Upon receipt of a Level-1 trigger, the data from the pipelines are transferred to front-end readout buffers. After further signal processing, zero-suppression and/or data-compression each event will have a size of about 1.5 MB for proton-proton interactions. Data from a given event are then transferred to a processor that runs the high-level trigger (HLT) software to reduce the Level-1 output rate of 100 kHz down to 100 Hz for mass storage. Rather than reconstruct all possible objects in an event for HLT, whenever possible only those objects and regions of the detector that are

actually needed for the decision are reconstructed. In that way events are discarded as soon as possible, events that still pass are then stored across the "LHC Computing Grid"[12] for later software analysis by individuals searching for specific physics phenomenon.

2.3.2 Particle Flow

The particle-flow event reconstruction aims at reconstructing and identifying all stable particles in the event, i.e., electrons, muons, photons, charged hadrons and neutral hadrons, with a thorough combination of all CMS sub-detectors towards an optimal determination of their direction, energy and type. This list of individual particles is then used to build jets (from which the quark and gluon energies and directions are inferred), to determine the missing transverse energy E_T^{miss} (which gives an estimate of the direction and energy of the neutrinos and other invisible particles), to reconstruct and identify taus, τ, from their decay products, to quantify charged lepton isolation with respect to other particles, to tag b jets, etc [43].

While this algorithm is extremely versatile we will focus our discussion on the pieces that are relevant for this analysis: electrons, muons, and jets. A small discussion will also be made of photons which are used in this analysis as well.

[12]Specifics of this vast and complex GRID computing network are not discussed here.

2.3.3 Electrons

The electron reconstruction combines ECAL and tracker information. Electron candidates are reconstructed from clusters of energy deposits in the ECAL, which are then matched to hits in the silicon tracker and silicon tracker seeds that are mapped to ECAL clusters. This dual approach improves the reconstruction efficiency for the very low p_T electrons. The CMS electron reconstruction algorithm is described in [41, 44].

For this physics analysis, the electron candidates are required to have transverse momentum $p_T^e > 7$ GeV/c and a reconstructed $|\eta| < 2.5$. The reconstruction efficiency for isolated electron is expected to be above 90% over the full ECAL acceptance, apart from some narrow “crack" regions.

The identification of electrons relies on a Boosted Decision Tree (BDT) multivariate technique that combines observables sensitive to the amount of bremsstrahlung along the electron trajectory, the geometrical and momentum matching between the electron trajectory and associated clusters, as well as shower-shape observables. The distribution of expected and observed electron BDT output is shown in figure 2.17. The selection is optimized in six regions of the electron p_T^e and $|\eta^e|$ to maximize the expected sensitivity for a low-mass Higgs boson. These regions correspond to two p_T^e ranges, 7–10 GeV and > 10 GeV, and three pseudorapidity regions, corresponding to two regions in the barrel with different material in front of the ECAL, the central barrel ($|\eta^e| < 0.8$) and the outer barrel ($0.800 < |\eta^e| < 1.479$), in addition to the endcap,

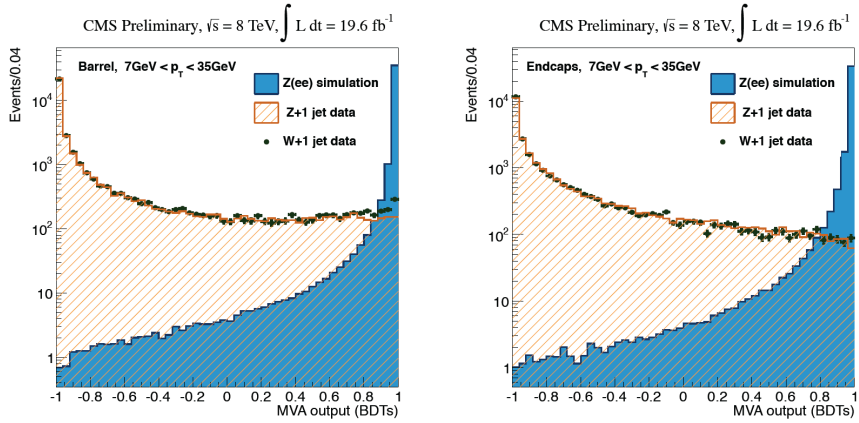

Figure 2.17: Distribution of electron BDT output for training sample W+jets, test sample Z+jets on 2012 data (fakes) and prompt electrons ($Z \to ee$ simulation) in the barrel (left) and endcap(right) [45].

$1.479 < |\eta^e| < 2.500$.

The quality of the momentum measurement for electrons can substantially vary depending on the electron characteristics. The resolution is mainly dominated by the fluctuations of the measured energy due to bremsstrahlung in the tracker material. This entails that the 4ℓ mass resolution varies broadly, by as much as a factor of 2-3. Therefore, mixing together events with well and poorly measured 4ℓ masses dilutes the Higgs boson search sensitivity, and mass measurement. The analysis uses the propagation of the lepton uncertainty to estimate the 4ℓ mass to proper accounting for the signal mass resolutions for individual events. In order to have a good determination of this uncertainty, but above all to have a description of the resolution of the signal model which corresponds to the data, we need to measure it on high statistics control samples, depending on the electron kinematics and quality,

which is done with $Z \to ee$ sample. The absolute scale has also to be calibrated on data, because the measurement of the Higgs boson mass depends crucially on the uncertainty that we can assign to the leptons in the full phase space of the analysis for a 125 GeV Higgs boson, so covering from 7–100 GeV, which can be covered with $Z \to ee$ and low mass resonances.

For electrons, the calibration procedure consists of three steps. First, a set of corrections for the momentum scale is obtained by comparing the displacement of the peak position in the distributions of the Z-boson mass in the data and in the simulation in different η regions and in two categories depending on the amount of bremsstrahlung. The corrections are derived as a function of time in order to account for the time-dependent crystal transparency loss. Second, a linearity correction to the momentum scale is applied to account for the p_T-dependent differences between data and simulation by comparing the dielectron mass distributions, binned in p_T^e of one of the two electrons, in data and in simulated $Z \to ee$ events. The $J/\psi \to ee$ and $\Upsilon\,(1S) \to ee$ events are used as validation for electron $p_T^e < 20$ GeV. All the corrections on the electron momentum scale from the first two steps are applied to data. The left of figure 2.18 shows the residual momentum scale difference before the linearity correction but after the time dependent corrections. Third, the energies of single electrons in the simulation are smeared by applying a random Gaussian multiplicative factor of mean 1 and width $\Delta\sigma$, in order to achieve the resolution observed in the data Z-boson sample. The result of this resolution correction is

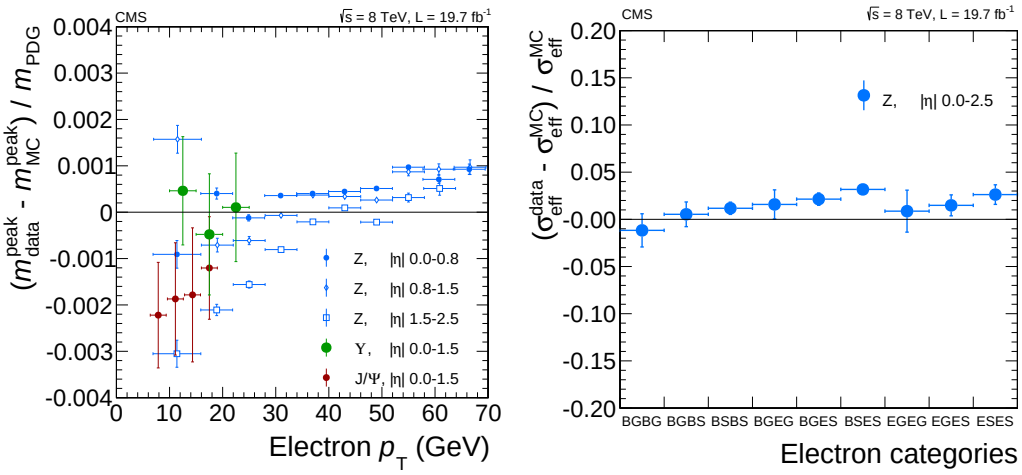

Figure 2.18: (left) Relative difference between the dilepton mass peak positions in data and simulation as obtained from Z, J/ψ and $\Upsilon\,(nS)$ resonances as a function of the transverse momentum of one of the electrons regardless of the second for dielectron events before p_T dependent correction. (right) Relative difference between the dilepton mass peak positions in data and simulation as obtained from Z, J/ψ and $\Upsilon\,(nS)$ resonances as a function of the transverse momentum of one of the electrons regardless of the second for dielectron events [41].

shown on the right of figure 2.18.

After the electron calibration, the relative momentum scale between data and simulation is consistent within 0.6% in the central barrel and up to $\sim$ 1.5% in the forward part of the ECAL endcaps. The residual dependence at low momentum is due to the use of wide bins in measured electron p_T^e in evaluating the Z-peak mass shift. The resulting shift of 0.3% (0.1%) for the $4e\,(2e2\mu)$ channel is assigned as a systematic uncertainty in the signal mass scale.

2.3.4 Muons

Muon candidates are required to have a transverse momentum $p_T^\mu > 5$ GeV and be within the geometrical acceptance, defined by $|\eta^\mu| < 2.4$. The reconstruction combines information from both the silicon tracker and the muon system. The matching between track segments is done either outside-in, starting from a track in the muon system, or inside-out, starting from a track in the silicon tracker. The muons are selected among the reconstructed muon track candidates by applying minimal requirements on the track segments in both the muon system and inner tracker system and taking into account compatibility with small energy deposits in the calorimeters [41].

For muons, an absolute measurement of momentum scale and resolution is performed by using a reference model of the Z line shape convolved with a Gaussian function. The bias in the reconstructed muon p_T is determined from the position of the Z mass peak as a function of muon kinematic variables, and a correction is derived for the data. A correction for the resolution is also derived for the simulation from a fit to the $Z \to \mu\mu$ mass spectrum. The large event sample based on low-mass dimuon resonances provides an additional calibration source for the momentum resolution in a similar manner. For muons, the agreement between the observed and simulated mass scales is within 0.1% in the entire pseudorapidity range of interest and assigned as a systematic.

A Z-boson decay into a lepton pair can be accompanied by final-state radiation,

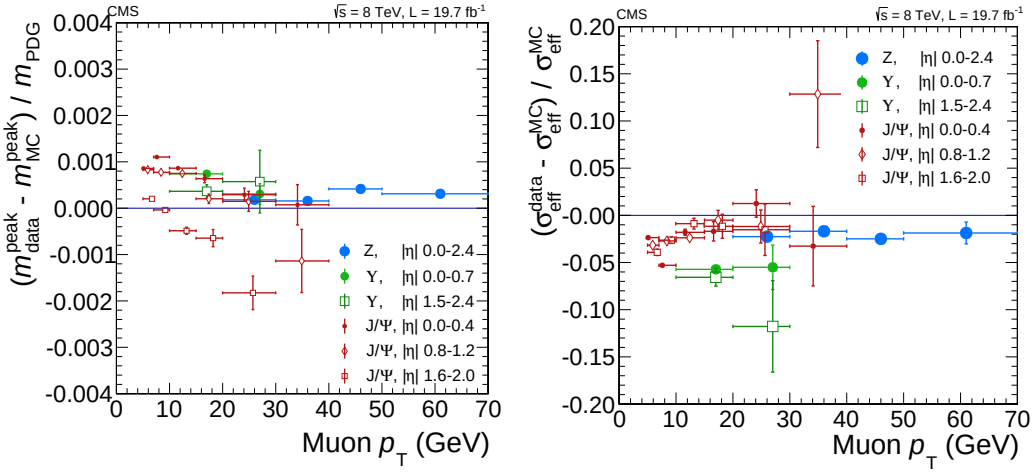

Figure 2.19: (left) Relative difference between the dilepton mass peak positions in data and simulation as obtained from Z, J/ψ and $\Upsilon\,(nS)$ resonances as a function of the average muon p_T^μ for dimuon events. (right) Relative difference between the dimuon mass resolutions in data and simulation as measured fromZ, J/ψ and $\Upsilon\,(nS)$ decays as functions of the average muon p_T^μ [41].

in which case it is desirable to identify and associate the radiated photon to the corresponding lepton to form the Z-boson candidate. Low-energy photons are identified and reconstructed with the PF reconstruction with a dedicated clustering algorithm designed to identify ECAL energy deposits near global muon tracks. Final-state radiated photons are mostly produced with a direction nearly collinear with the parent lepton and have a harder spectrum than background photons from initial-state radiation or pileup interactions. Therefore, to be identified as FSR, a reconstructed photon must be close to the muon they would be associated with and must make the lepton-pair mass closer to the nominal Z-boson mass. This FSR procedure is applied to muons but not to electrons because the measured electron energies, by

construction, already include a large fraction of these photons.

2.3.5 Jets

A jet is a narrow cone of hadrons and other particles produced by a quark or gluon as it emanates from a collision. When a quark or gluon is produced in a collision event the vacuum will generate particles and antiparticles because of the effects of QCD. This generates many particles that may leave tracks or energy deposits in the CMS detector. In the analysis the presence of jets is used as an indication of vector-boson fusion (VBF) or associated production with a weak boson, VH, with $V = W$ or Z, where the V decays hadronically.

In this analysis, jets are reconstructed using the anti-k_T clustering algorithm [46]. The inputs to this algorithm are charged hadrons identified by the PF algorithm by matching calorimeter energy clusters to tracks and PF neutral hadrons identified by calorimeter clusters without tracks[13].

The anti-k_T algorithm takes these particle tracks and evaluates the distances between particles and combines them into jets by merging together the objects with smallest separation distances. Once a merging has been applied the distances are recalculated and the procedure repeats. The unique part of the anti-k_T algorithm is that the distances are inversely weighted by the momentum (k_T) of the particles. This results in low momentum particles clustering with large momentum ones before

[13]The PF algorithm also has muon and electron pre-identification to omit them from hadron track construction.

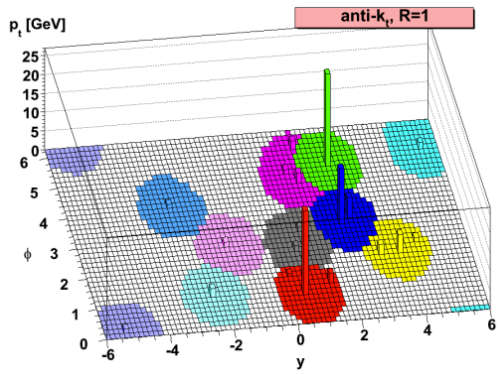

Figure 2.20: An example event of jets formed with the anti-k_T clustering algorithm [46].

many low momentum particles cluster with themselves. Figure 2.20 shows the jets that result from an example event.

In this analysis jets are only considered if they have $p_T^{\text{jet}} > 30$ GeV and $\left|\eta^{\text{jet}}\right| < 4.7$. Corrections and calibrations to the individual components of a jet according to its p_T^{jet} and η^{jet} following [47].

2.4 CMS Tracker Alignment

The precise alignment of the silicon sensors in the CMS Tracker is a necessary and challenging task. While external measurements of the positions of sub-detectors[14] can be a good start, they are woefully inadequate in determining the exact position, tilt angle, and deformation of an individual module. In order to maximize the performance in the complex hardware that is used in the tracker the position of each module

[14]Using survey measurements for example.

must be known to very high precision.

The goal of track-based alignment procedures is to determine the module positions from a large sample of reconstructed charge particle trajectories. Each trajectory is built form charge depositions on individual detectors. Using this method, the residual resolution is now below 10 µm [35]. This optimization problem can be formulated in the context of linear least squares. Module position corrections $\mathbf{p}$ are determined by minimizing an objective function

$$\chi^2 (\mathbf{p}, \mathbf{q}) = \sum_{j}^{\text{tracks}} \sum_{i}^{\text{hits}} \mathbf{r}_{ij}^T (\mathbf{p}, \mathbf{q}_j) \, \mathbf{V}_{ij}^{-1} \mathbf{r}_{ij} (\mathbf{p}, \mathbf{q}_j) \,, \tag{2.3}$$

which can be expressed as a sum over all hits i on all tracks j and track parameters $\mathbf{q}_j$, assuming negligible correlations between hits. Track residuals $\mathbf{r}_{ij} = \mathbf{m}_{ij} - \mathbf{f}_{ij} (\mathbf{p}, \mathbf{q}_j)$ are defined as the difference between the measured hit position and the estimated impact point from the trajectory without the hit in question. These residuals are given as either one- or two-dimensional vectors, and $\mathbf{V}_{ij}$ is either the squared error or the covariance matrix respectively [48].

In order to determine the 200000 different parameters, *alignment parameters*, that describe the locations of the 1440 silicon pixel and 15148 silicon microstrip modules two methods of minimizing track residuals are used, MILLEPEDE II and HIP. A *track* is a fit to the series of consecutive signals that a charged particle will leave in each layer of silicon as it passes through the CMS tracker. Each of the two algorithms minimizes the residual difference between the hits that make up a track and the

position of the track created without that hit.

The main difference between the two algorithms lies in how this minimization is done. MILLEPEDE II simultaneously determines the solutions of a complete matrix equation for global and local parameters using all tracks [49]. HIP, Hit and Impact Point, determines these parameters iteratively to solve for correlations between modules. The algorithm repeatedly fits a track and then changes a parameter, eventually minimizing the χ^2 for the fit [50].

Vital to the work done as part of this thesis is the connection between the global and local parameters. The tracks and hits are defined on the module level. However these modules are connected to each other and to other subdetectors through mechanical structures that can be used to constrain the system for minimization. In figures 2.21 and 2.22 we map the different structures that can are used to define the locations and constraints that should be used for a given track.

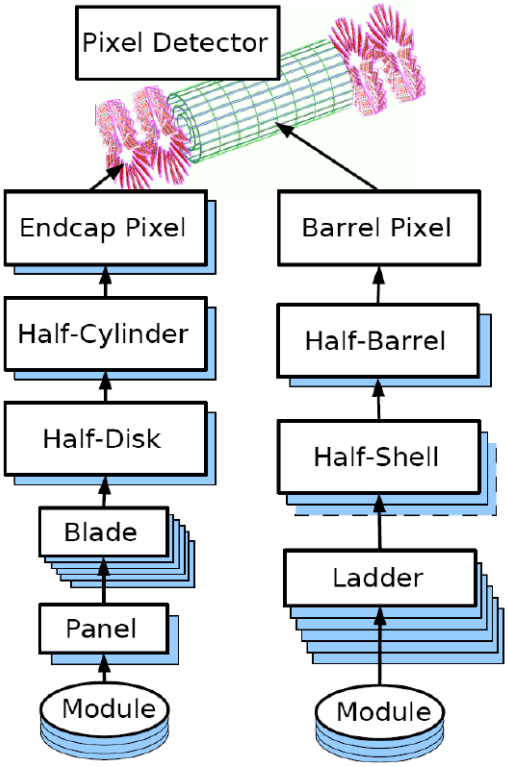

Figure 2.21: Hierarchy of the CMS silicon pixel detector structures [51].

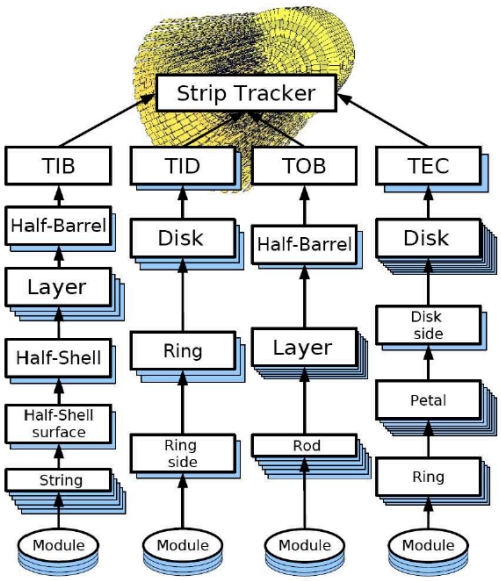

Figure 2.22: Hierarchy of the CMS silicon strip detector structures [52].

2.4.1 Silicon Pixel Alignment in Prompt Calibration Loop

Once a set of alignment parameters is determined, it is not valid forever. As the detector operates the different components may shift. A prime example of this is the pixel barrel, which is not in a fixed position. This is problematic because the CMS magnet may turn on and off, resulting in natural shifts in the positions of different detectors. Part of this thesis work was to develop and implement an active alignment algorithm that would detect and automatically update the detector positions as the CMS experiment takes data.

This active alignment algorithm was implemented in the CMS tracker Prompt Calibration Loop (PCL) for the start of the 2015 run of the LHC. The Prompt Calibration Loop is a collection of routines that are designed to monitor and automatically adjust parameters to optimize the performance of the the CMS tracking system. The alignment routine developed during this thesis work monitors and adjusts the 36 alignment parameters that describe the pixel detector global parameters. The monitored parameters are the positions (x, y, z) and rotations $(\theta_x, \theta_y, \theta_z)$ of the two BPIX half-barrels and the four half-cylinders of the FPIX system[15]. If a sufficient shift in one of these parameters is seen[16] then the database of tracker conditions is updated. These consistent updates allow CMS to continue operating at peak performance and

[15]Two half-cylinders each for FPIX+ and FPIX-.

[16]In this case, "sufficient" implies the parameter shifts between a pre-set minimum and maximum window and the significance of that shift is larger than a pre-set amount.

avoids rerunning computationally expensive data processing routines to correct the data.

This algorithm is also useful to determine the best position parameters immediately after the startup of the collider. This use case was demonstrated the week of July 6th, 2015. This week marked the beginning of data-taking for the CMS experiment at a new higher center of mass energy, $\sqrt{s} = 13$ TeV with the full magnetic field. The tracker geometry changed when the magnetic field was turned back on. Within 48 hours of the beginning of this data-taking this alignment workflow was run and produced results. These showed a movement of the Pixel detector compared to the positions that had been determined before the magnet was turned on. The magnitude of these initial shifts can be seen in figure 2.23. This plot shows the detected shifts in the BPIX and FPIX half-barrels and half-cylinders in positions (x, y, z) and rotations $(\theta_x, \theta_y, \theta_z)$. Note that the axis range for the z and θ_z shifts are twice (200 µm/µrad) that of their x and y counterparts. Further, this algorithm was able to correct this movement and produce a geometry that was more accurate and useful for the very next data. Figures 2.24 confirms that the next set of data would not trigger the creation of a new geometry because the residual differences are small.

Figure 2.25 shows the accuracy of the alignment object created by this workflow by comparing three iterations (1) before starting to take new data (blue), (2) before PCL alignment but after some alignment with a different magnetic field configuration (black), and (3) after PCL alignment (magenta). The top and bottom plots are distri-

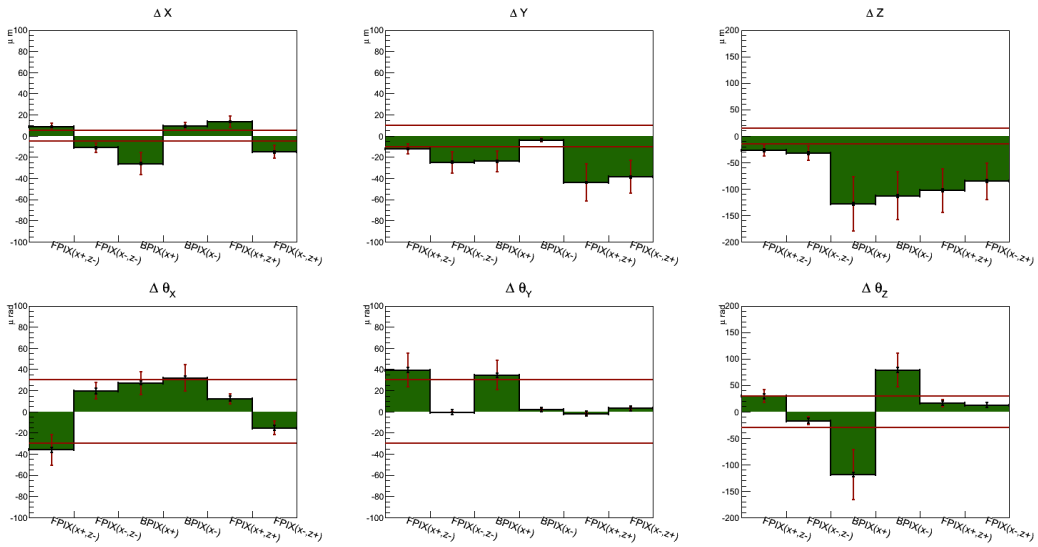

Figure 2.23: Shifts in Pixel Tracker large scale structures as detected by the alignment algorithm in Prompt Calibration Loop using very first runs of CMS data at $\sqrt{s} =$ 13 TeV with the full magnetic field (3.8 T). Green histograms show shifts, with black error bars as uncertainties. Red entries and error bars represent thresholds in movement and uncertainty that are considered significant. Please note the axis range for the z and θ_z shifts are twice (200 µm/µrad) that of their x and y counterparts.

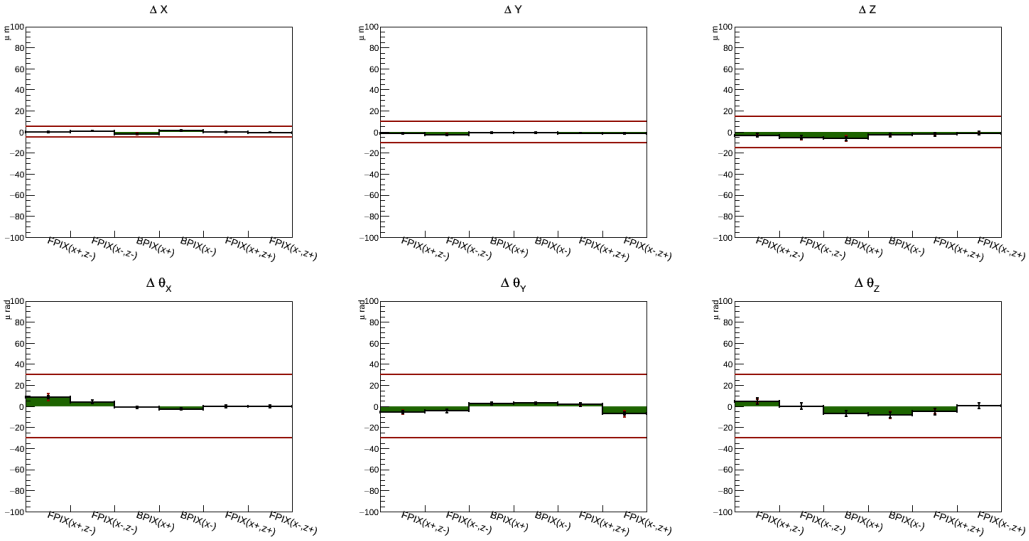

Figure 2.24: Shifts in Pixel Tracker large scale structures after correction for shifts detected by the alignment algorithm in Prompt Calibration Loop using very first runs of CMS data at $\sqrt{s} = 13$ TeV with the full magnetic field (3.8 T). Green histograms show shifts, with black error bars as uncertainties. Red entries and error bars represent thresholds in movement and uncertainty that are considered significant. Please note the axis range for the z and θ_z shifts are identical to that of their x and y counterparts.

butions of the medians of residuals (DMRs). These show that the median residual in the x(left) and y(right) direction for each module in BPIX (top) and FPIX(bottom) decreases after an alignment is performed. Similarly, one can see the impact that correct alignment of the BPIX and FPIX have on the other tracker subdetectors by observing the benefit of the PCL workflow in TIB DMR, figure 2.26 [53].

The effectiveness of this project (long term) is illustrated from similar algorithm that was used at the end of the 2012 run after a large shift in the pixel barrel position was seen. Figure 2.27 shows the longitudinal shift between the two half-shelf of the BPIX as measured with the primary vertex residuals. The previous monitoring procedure was implemented farther 'downstream' in the computing chain than the current implementation.

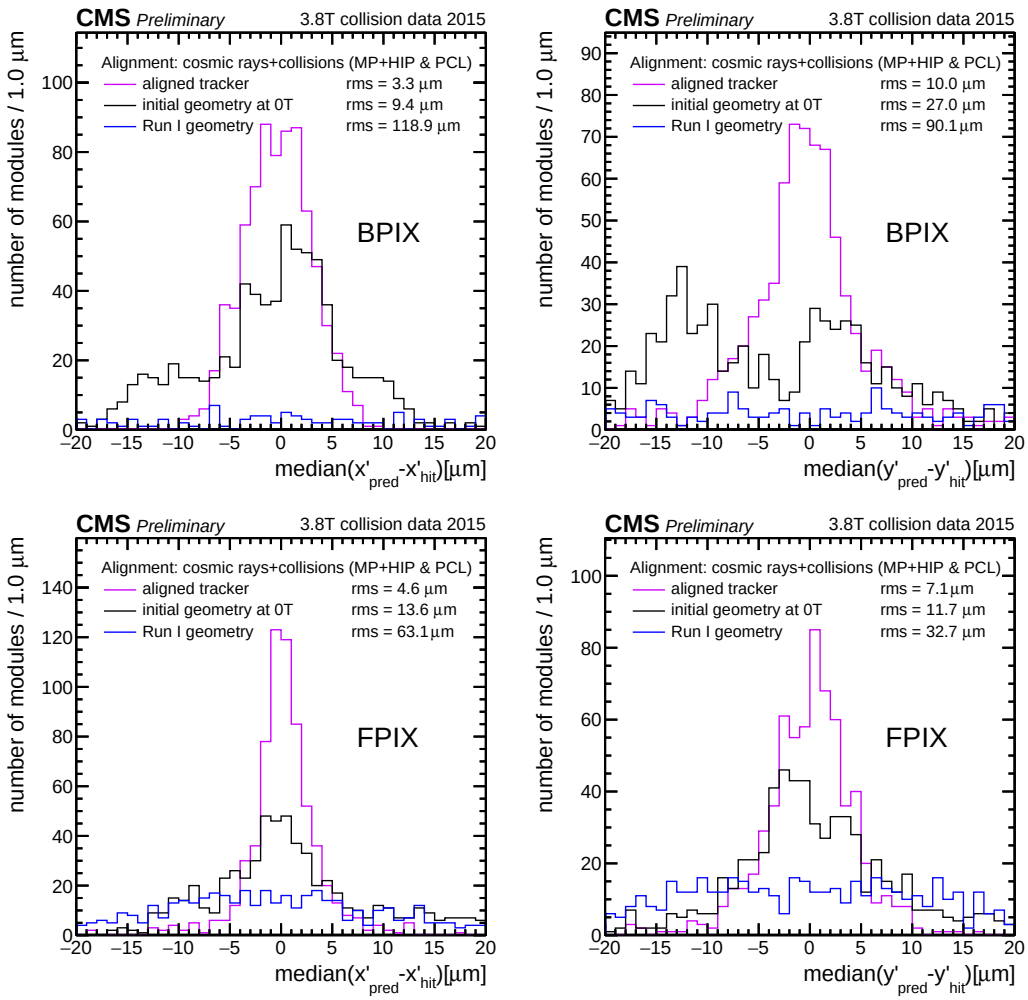

Figure 2.25: The distribution of median residuals is plotted for the local (left) x- and (right) y-directions in the barrel (top) and forward (bottom) pixel detector, using 20 million collision tracks collected with the magnetic field at 3.8 T. The blue line shows the Run I geometry, which is no longer valid for Run II data, primarily because of temperature changes and pixel re-centering and repair. The black line shows the starting geometry for data taking, which was valid for data taken with the magnetic field turned off, as it was produced with the MILLEPEDE II and HIP algorithms using cosmic ray and 0 T collision data. The alignment shown in violet was adjusted from this geometry by an automated alignment process of the pixel detector that will be run as part of the Prompt Calibration Loop as data is collected and processed, and shows improvements over the initial geometry. The changes resulted primarily from the change in the magnetic field. The RMS of the distribution reduces, the double-peak structure in y present when assuming the initial geometry in the track refit is corrected by the PCL-style alignment of the pixel detector [53].

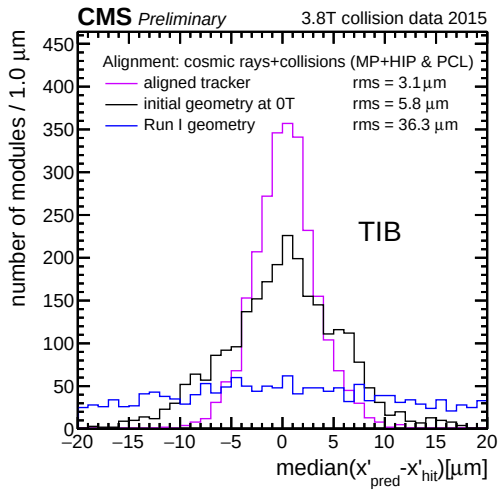

Figure 2.26: The distribution of median residuals is plotted for the tracker inner barrel, using 20 million collision tracks collected with the magnetic field at 3.8 T. The blue line shows the Run I geometry, which is no longer valid for Run II data, primarily because of temperature changes and pixel re-centering and repair (since tracks are fitted using hits in both the pixel and the strip detectors, the large movements of the pixel detectors also affect the DMR performance in the strip detectors). The black line shows the starting geometry for data taking, which was valid for data taken with the magnetic field turned off, as it was produced with the MILLEPEDE II and HIP algorithms using cosmic ray and 0 T collision data. The alignment shown in violet was adjusted from this geometry by an automated alignment process of the pixel detector that will be run as part of the Prompt Calibration Loop as data is collected and processed, and shows improvements over the initial geometry. The changes resulted primarily from the change in the magnetic field. The RMS of the distribution reduces for the Run I, initial, and aligned geometry, respectively [53].

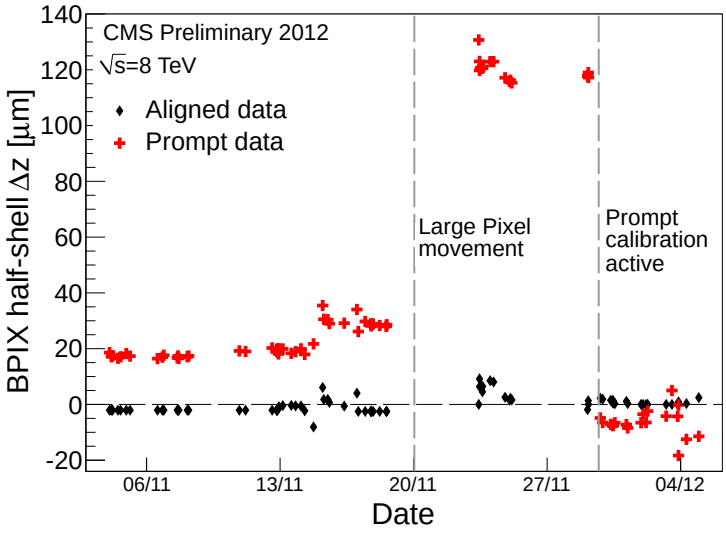

Figure 2.27: Day-by-day value of the relative longitudinal shift between the two half-shells of the BPIX as measured with the primary vertex residuals, for the last month of pp data taking in 2012. Red crosses show the shift observed using the data coming from the prompt reconstruction. The same events, re-reconstructed after the 2012 alignment campaign, which accounts for the major changes in the positions of the half-shells, are represented by black lozenges. A major displacement of the half-shells O(100) µm, occurred during the technical stop in the week of 20th of November, is recovered by the prompt alignment of the BPIX large structures that became active on the 30th November [54].

Chapter 3

Higgs boson at the LHC: Phenomenology

In this section we discuss specific phenomenological details that are studied for this thesis. First, we discuss the different modes of producing a Higgs boson at the LHC, and different features of these different production modes. Next, we will present the decay of a Higgs boson into two Z bosons and subsequently four leptons. Using this information we will present the implications of off resonance production and decay on the Higgs boson lifetime. Finally, we will discuss the spin and parity of a single-produced resonance and how we can use these relations to characterize a new particle found at the LHC.

3.1 Higgs boson production at LHC

In proton-proton collisions a SM Higgs boson can be produced through the coupling of a Higgs boson to either bosons or fermions. Each of these two categories of Higgs boson production will be dominated by specific production modes. Fermionic production of a Higgs boson can happen either through *gluon-gluon fusion* $gg \to H$ (ggH) and much less frequently through production in *association with two top quarks* $gg \to H + t\bar{t}$ ($t\bar{t}H$). Bosonic production of a Higgs boson can occur through *vector boson fusion* (VBF), where two quarks radiate vector bosons which produce the boson in association with two quark jets $qq \to H + 2$jets or through production *associated with a vector boson* $qq \to H + W/Z$ (VH).

The cross sections of these different production mechanisms as a function of the Higgs boson mass at the LHC are shown in figure 3.1 for the two center of mass energies used in this thesis; $\sqrt{s} = 7$ TeV and $\sqrt{s} = 8$ TeV [55, 56]. Notable features of these cross sections are the order of magnitude difference between gluon-gluon fusion and the bosonic production modes which are all much larger than the $H + t\bar{t}$ production. Additionally, one can see the boost in the gluon-gluon fusion production at $2m_t$, which corresponds to the top quark in the production loop going becoming on shell (explained in more detail below).

The main production mechanism at the LHC is gluon-gluon fusion. The Feynman diagram for this process is shown in figure 3.2. While the Higgs boson does not couple directly to gluons (because they are massless) this mode of production relies on the

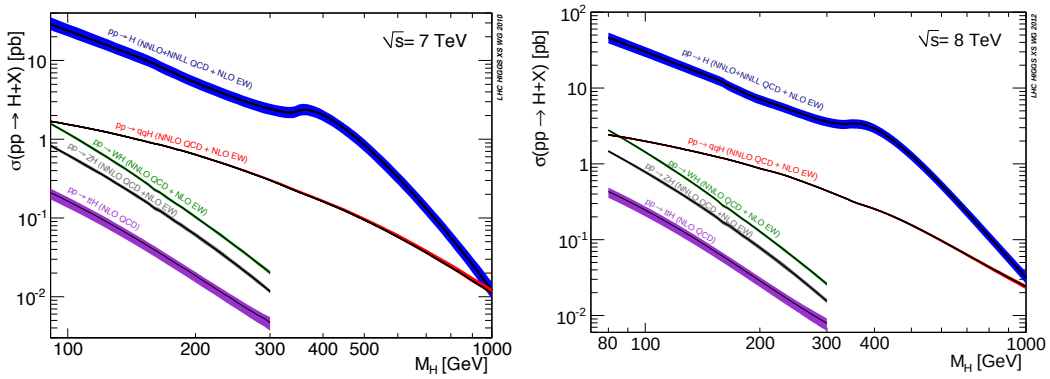

Figure 3.1: Standard Model Higgs boson production cross sections and relative uncertainties at $\sqrt{s} = 7$ TeV and $\sqrt{s} = 8$ TeV. From top to bottom these are $pp \to H$, blue, $pp \to H + 2$jets, red, $pp \to H + W$, green, $pp \to H + Z$, grey, $pp \to H + t\bar{t}$, purple [55, 56].

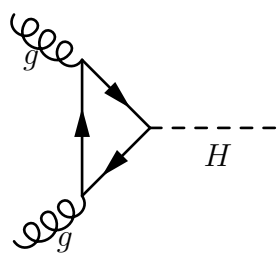

Figure 3.2: Feynman diagram depicting Higgs boson production through gluon-gluon fusion $gg \to H$. The fermion loop is dominated by top quarks, however all quarks contribute according to their masses.

Higgs boson coupling to fermions generated by the incoming gluons. Because the coupling of the Higgs boson is proportional to the mass of the fermion the dominant contribution is the Higgs boson – top coupling. This leads to a boost in the cross section when the mass of the Higgs boson is twice the top mass because the top in the loop shown is no longer virtual. For the entire mass range that is considered in this analysis this is the most common way to produce a Higgs boson at the LHC.

The second most likely way to produce a Higgs boson at the LHC is through

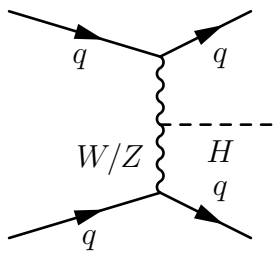

Figure 3.3: Feynman diagram depicting Higgs boson production through vector boson fusion $qq \to H + 2$jets.

vector boson fusion. To produce a Higgs boson this way two quarks each radiate a W or Z boson which fuse into the Higgs boson. This production mode relies on the Higgs boson coupling to the vector bosons, making it distinct compared to gluon-gluon fusion. the distinguishing feature of this production mode is the presence of two quark jets in the final state in addition to the Higgs boson. These jets contain information about the Higgs boson and can be exploited to refine searches and study the properties of a new particle. The Feynman diagram for this process is shown in figure 3.3.

Sub-dominant to these two production modes are processes that produce a Higgs boson in association with vector bosons or top quarks. This thesis does not tune the analysis to separate these modes from the dominant ones, instead they are grouped with the dominant modes by how the Higgs boson couples to the other standard model particles. VBF is grouped with VH because the Higgs boson is produced through a coupling to vector bosons while $t\bar{t}H$ is grouped with ggH because it relies on the Higgs boson coupling to fermions.

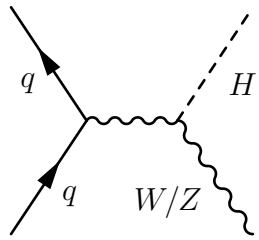

Figure 3.4: Feynman diagram depicting Higgs boson production associated with a vector boson $qq \to H + W/Z$.

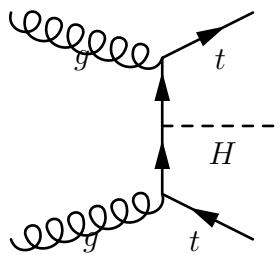

Figure 3.5: Feynman diagram depicting Higgs boson production in association with two top quarks $gg \to H + t\bar{t}$.

Producing the Higgs boson in association with a W or Z boson is conceptually similar to VBF production. Two quarks interact, producing a vector boson which radiates away a Higgs boson, shown in figure 3.4. Unique to this final state is that in addition to the Higgs boson you will also have the particles associated with the subsequent decay of a W or Z boson. The $t\bar{t}H$ production mode is the smallest of those considered here and is similar to ggH in that it relies on the Higgs boson coupling to top quarks. While the rates of $t\bar{t}H$ are very low, Higgs bosons produced in this way can be distinguished by the presence of two top quarks in addition to the decay product of the Higgs boson, as shown in figure 3.5.

More details are presented in section 4.6, this thesis uses the different properties of

ggH and VBF production modes to measure how often a Higgs boson is produced in each mode at the LHC. This work resulted in the first measurement of the production mechanism of Higgs bosons in the 4ℓ final state.

3.2 Higgs boson decay to $ZZ \to 4\ell$

The SM Higgs boson is an unstable particle that will decay before it can be detected with the CMS detector. However, we can search for this particle by looking at its decay products. To determine which decay products will be the most fruitful to use for a search, we look at the *branching ratio* $BR_X = \frac{N_X}{N_{tot}}$ of the Higgs boson decay for a specific final state in relation to the total number of Higgs bosons we expect. Thus, a high branching ratio will result in a larger number of signal events. In figure 3.6 we plot some of the interesting branching ratios as a function of the Higgs boson mass. To decide if a search is valuable we compare the number of events we expect from a specific decay mode (given by the luminosity times branching ratio times the cross section $\mathcal{L} \cdot BR_X \cdot \sigma_{tot}$) to the number of background events we expect in the search range.

Of specific interest for this thesis is the Higgs boson decay to the $ZZ \to 4\ell$ final state, shown in figure 3.7. Where we consider $\ell = e, \mu$ because these leptons will be long lived enough to be detected directly by CMS, making them distinct from τ leptons which often decay because of their high mass. The ZZ branching ratio

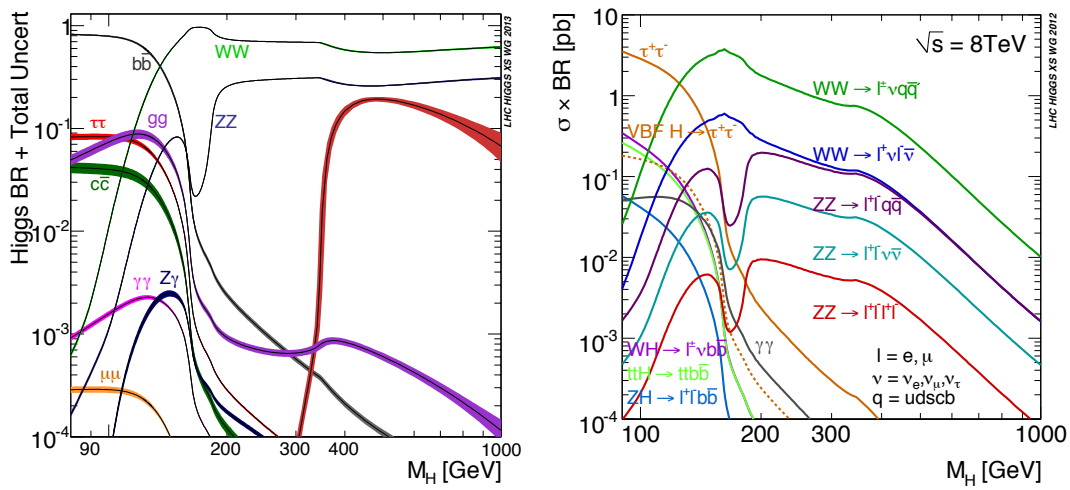

Figure 3.6: (left) Standard Model Higgs boson decay branching ratios for selected decay modes, of specific interest for this thesis is the ZZ branching ratio. (right) Branching ratio times cross section for selected final states, of specific interest for this thesis is the $ZZ \to 4\ell\,(\ell^+\ell^-\ell^+\ell^-)$ [56, 57].

is one of the highest across a wide rage of possible Higgs boson masses, making it advantageous for search and characterization studies. The 4ℓ final state is used not because it has a particularly high cross section times branching ratio (seen in figure 3.6 right), but because there are low SM background contributions and because all of the final particles are directly detected by the CMS detector.

This thesis considers all of the data collected by CMS during run 1 of the LHC proton-proton collisions. This corresponds to an integrated luminosity of 5.1 fb^{-1} collected at a center of mass energy of $\sqrt{s} = 7$ TeV and 19.7 fb^{-1} collected at $\sqrt{s} =$ 8 TeV. The search for and later characterization of a Higgs boson requires that there be two pairs of same-flavor, opposite-charge, well-identified isolated leptons ($e^+e^-e^+e^-, \mu^+\mu^-\mu^+\mu^-,$ or $e^+e^-\mu^+\mu^-$) compatible with an intermediate state of ZZ.

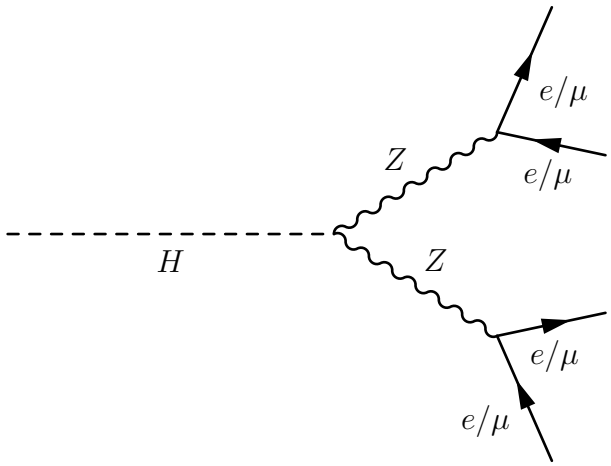

Figure 3.7: Feynman diagram depicting Higgs boson decay into two Z bosons and subsequently into four leptons $H \to ZZ \to 4\ell$.

Computability with ZZ is defined such that one or both of the Z's can be off the mass resonance of the Z-boson.

In this case, a Higgs boson signal will appear as a narrow mass peak on top of a smooth background when observing the four lepton mass distribution. The search is conducted in a mass range of $m_{4\ell} \in 110 - 1000$ GeV. For low-mass Higgs bosons ($m_H < 400$ GeV), the width of the resonance in $m_{4\ell}$ is very well peaked and described with a Breit-Wigner distribution. For higher mass Higgs bosons ($m_H > 400$ GeV), the width of the $m_{4\ell}$ mass peak is much broader and described in the complex pole scheme [55–57]. Detailed analysis of the width of the Higgs boson will be discussed in section 3.3.

The background in the 4ℓ final state is dominated by the SM $q\bar{q} \to ZZ \to 4\ell$ production, shown in figure 3.8. This background is not particularly large but it cannot be reduced with quality cuts on the leptons or tuning of phase space without

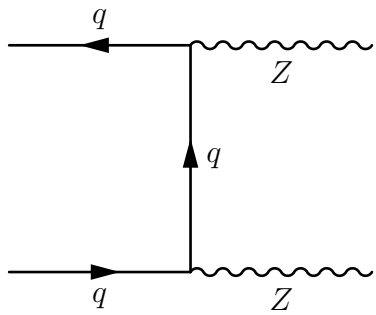

Figure 3.8: Feynman diagram depicting the quark production of two Z bosons $qq \to ZZ$.

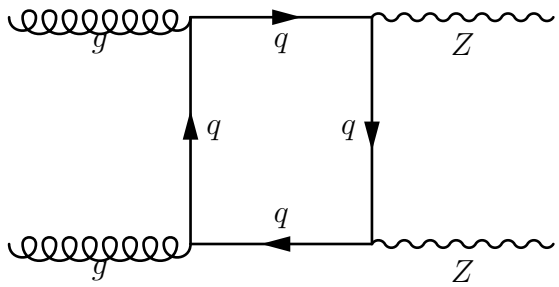

Figure 3.9: Feynman diagram depicting the gluon production of two Z bosons $gg \to ZZ$.

significant losses to the expected signal. Additionally, there will be SM $gg \to ZZ \to 4\ell$, shown in figure 3.9. Z boson production from gluons is also irreducible, but this contribution is about 10% of the dominant $qq \to ZZ \to 4\ell$ production. As discussed in the next section, this $gg \to ZZ$ contribution can actually be exploited to study the properties of any new resonance. There will also be background contributions from collisions that produce a Z boson in addition to other jets or particles that are mis-identified as leptons. This background is reducible by tuning the analysis to remove as much of this noise as possible. This tuning is done by adjusting the quality requirements on the leptons and requirements about where the events fall in phase space. This process is described more in section 4.3.3.

3.3 Higgs boson width: off resonance production and decay

When a new particle is observed, one of the fundamental properties that we would like to understand is the width of the mass resonance. From Einstein's mass–energy equivalence we know that the mass of a particle is equal to the amount of energy it has (in natural units). So by measuring the width of a resonance's mass spectrum (Γ) we have a measure of the natural spread in energies that the particle can take. For this discussion we will operate under the assumption that the Higgs boson mass $m_H \sim 125 - 126$ GeV. In later sections, will we present the results of the Higgs boson search upon which these were made.

Armed with this measurement of the natural energy spread of a particle, one can deduce the mean lifetime (τ) of the particle. The lifetime and a particles energy are related by the time–energy formulation of the Heisenberg uncertainty principle. Simply, this states that $\Delta E \Delta t \geq 1/2$. So measuring the spread in energies for an unstable particle one can deduce the lifetime by the simple relation $\Gamma/2 = 1/2 \cdot 1/\tau$.

This width can also illuminate possible new physics. The lifetime of a particle is determined by the rate that it decays into other particles. This rate is determined by the number of possible states it can decay into. So a particle that can only decay into a small number of particles will have a longer lifetime. The lifetime of the Higgs boson will be determined by its rate of decay into SM particles and particles not yet

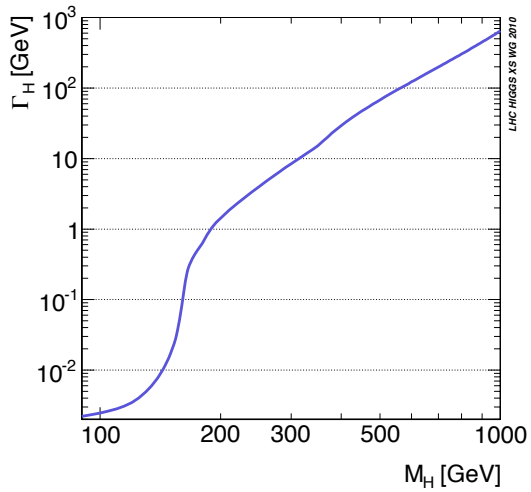

Figure 3.10: Total width of the SM Higgs boson as a function of its mass [55].

described by the SM. So gaining an accurate measurement of the Higgs boson lifetime can be a key into new possible particles that it couples to. The predicted width for a Higgs boson decaying only to SM particles is given in figure 3.10, if you compare this width to the plot of the branching rations in figure 3.6 (left) you will see that when new decay modes become available the width increases.

As described in section 2.3, CMS has a very fine momentum resolution for both electrons and muons. This allows CMS to accurately measure the mass and width of any new observed resonance very well, on the order of $\sim$ few GeV. However, as shown in figure 3.10 for low mass Higgs bosons the width can be quite small, on the order of $\sim$ MeV. Thus, direct measurement of the natural width of a low-mass Higgs boson will be dominated by the experimental resolution.

To overcome this, recent theoretical work has illuminated a way to measure the

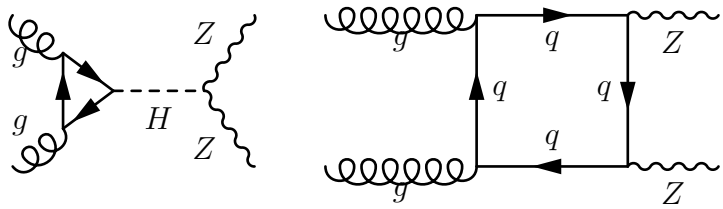

Figure 3.11: (top) Feynman diagram depicting Higgs boson production through gluon-gluon fusion and subsequent decay to two Z bosons $gg \to H \to ZZ$. (bottom) Feynman diagram depicting ZZ production through gluon-gluon fusion $gg \to ZZ$. These two diagrams will interfere with each other having an affect on the final number of events observed in the 4ℓ final state.

total width of a low-mass Higgs boson without looking at the width of the mass resonance directly. This technique relies on the ratio of the on resonance and off resonance production of the new boson. When the new boson is observed on resonance, the mass will be $m_H \sim 125 - 126$ GeV, because this mass $m_H < 2m_Z = 2\,(91.2\text{ GeV})$ the Higgs boson will be real and will decay into one or more virtual Z bosons. Virtual particles are particles who's mass is not at the natural resonance, usually denoted Z^*, while real particles which have a mass at the natural resonance. For the dominant production mechanism, we have $gg \to H \to Z^{(*)}Z^* \to 4\ell$.

However, the LHC will produce Higgs bosons far from this mass resonance as well. In this case, the Higgs boson will be virtual while the two Z bosons will both be real, $gg \to H^* \to ZZ \to 4\ell$. In reference [58] the authors point out that $\sim 10\%$ of the total Higgs boson cross section will produce Higgs bosons with a mass $m_{4\ell} > 2m_Z$. A plot of the Higgs boson mass shape is from this reference is shown in figure 3.12 for the ZZ and the WW final states. From this plot one can see the large fraction of the cross section that appears in this high mass window.

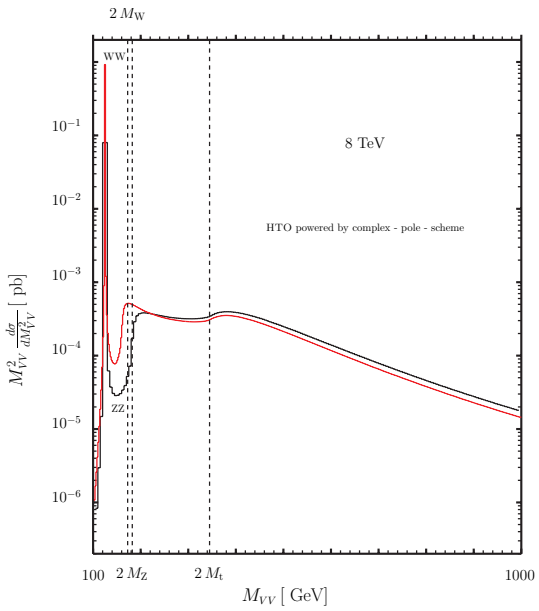

Figure 3.12: The NNLO ZZ (black) and WW (red) invariant mass distributions for $m_H = 125$ GeV [58].

Following [59], we can investigate the total width of the Higgs boson by comparing the on resonance and off resonance cross sections. Generally, the differential cross section of a Higgs boson produced through gluon-gluon fusion decaying into two Z bosons is given by equation (3.1). Where g_{ggH} is the effective coupling of the Higgs boson to gluons, g_{HZZ} is the coupling of the Higgs boson to Z bosons, and Γ_H is the total width of the Higgs boson. Also notice the demarcation of the observed mass of the 4ℓ system, $m_{4\ell}$, is not necessarily the same as the Higgs boson mass m_H.

$$\frac{d\sigma_{gg\to H\to ZZ}}{dm_{4\ell}} \sim \frac{g_{ggH}^2 g_{HZZ}^2}{\left(m_{4\ell}^2 - m_H^2\right)^2 + m_H^2\Gamma_H^2} \tag{3.1}$$

When a Higgs boson is produced on the resonance peak $m_{4\ell} \sim m_H$ then the mass integral can be evaluated assuming the second term in the denominator will be larger than the first. Giving the on peak cross section in equation (3.2) note that the cross section is proportional to the couplings and inversely the total width of the Higgs boson. However, if a Higgs boson is produced off of the resonance peak, specifically when $m_{4\ell} - m_H \gg \Gamma_H$, then the cross section becomes independent of the width. Shown in equation (3.3) the off peak cross section becomes proportional to the couplings but the width does not contribute.

$$\sigma_{gg\to H\to ZZ}^{\text{on peak}} \sim \frac{g_{ggH}^2 g_{HZZ}^2}{\Gamma_H} \tag{3.2}$$

$$\sigma^{\text{off peak}}_{gg\to H\to ZZ} \sim g^2_{ggH} g^2_{HZZ} \sim \sigma^{\text{on peak}}_{gg\to H\to ZZ} \times \Gamma_H \tag{3.3}$$

From these results we can see that the number of events that are produced on the mass resonance peak is dependent upon the total width of the new boson, while the number of events produced off peak are only dependent upon the couplings to the other SM particles. Thus, as pointed by [59] measuring the ratio of the on peak and off peak Higgs boson production is equivalent to measuring the total width of the new boson.

Complicating this story, is the quantum mechanical interference between the different $gg \to \ldots \to 4\ell$ processes. While this interference is present for the entire $m_{4\ell}$ range considered in this thesis, at low masses it is a very small and negligible. Above the $2m_Z$ mass, the interference between $gg \to ZZ \to 4\ell$ and $gg \to H^* \to ZZ \to 4\ell$, figure 3.11, processes needs to be considered. While the off peak signal contribution will scale by $\sigma^{\text{on peak}}_{gg\to H\to ZZ} \times \Gamma_H$ the interference between the signal and background term will scale by $\sqrt{\sigma^{\text{on peak}}_{gg\to H\to ZZ} \times \Gamma_H}$.

The impact of these three terms is seen in figure 3.13. Here, one can clearly see the large difference between ignoring (cyan) and correctly accounting (black) for the interference in this region. Neglecting interference one would anticipate a large increase in the yield of the high mass $gg \to \ldots \to ZZ$ contribution, but since the interference between off resonance Higgs boson production and the $gg \to ZZ$ continuum background is destructive, the SM actually predicts that the high mass

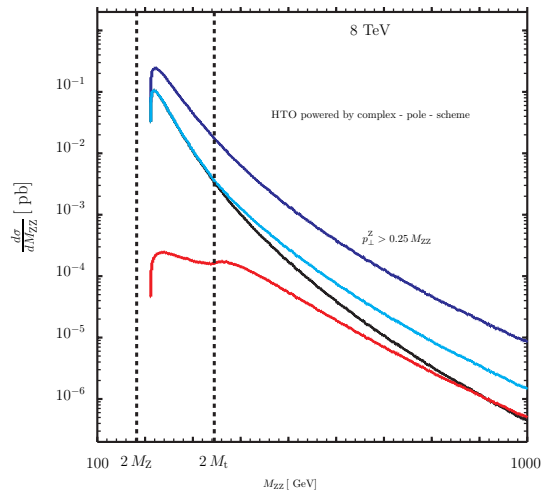

Figure 3.13: The LO ZZ invariant mass distribution $gg \to ZZ$ for $m_H = 125$ GeV. Black is the total $gg \to \ldots \to ZZ$ contribution once all interfrence effects are taken into account. Red is the $gg \to H^* \to ZZ$ signal only, and cyan is the $gg \to \ldots \to ZZ$ contribution ignoring the interference between the two contributions. For scale, the $q\bar{q} \to ZZ$ contribution is shown in blue [58].

contribution will be lower than otherwise anticipated.

The resulting $m_{4\ell}$ distributions for two hypothetical bosons are shown in figure 3.14, they both have the same on peak cross section but different total widths. The result is a change in the total number of events expected in the analysis. Additionally, the shape of the $m_{4\ell}$ distribution and the kinematics of the 4ℓ will be different. A detailed description of how all of these factors are used to determine the width is given in section 5. Also included in this image and analysis is the analogous effect for the VBF production mode.

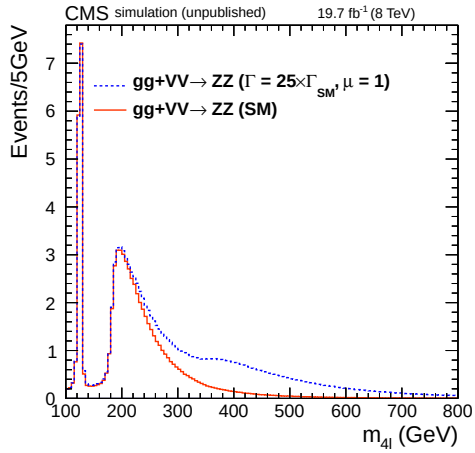

Figure 3.14: Distribution of the expected four-lepton reconstructed mass in full analysis mass range for the sum of the $4e$, 4μ, and $2e2\mu$ channels and for $gg + VV \to ZZ$ processes for a Higgs boson mass of 125.6 GeV. The expected distribution for a scenario corresponding to a scaling of the width by 25 is also shown. This illustrates the expected change in $gg+VV \to ZZ$ production when changing the Higgs boson width and at the same time constraining the peak cross section to the SM expectation [60].

3.4 Spin and Parity of a Single-Produced Resonance

Using the decay rates and kinematics of a newly observed resonance one can piece together the quantum mechanical properties of the original boson. Once a new particle is observed, its spin and parity quantum numbers need to be determined. This will confirm if the new particle is the Higgs boson that was predicted or something entirely, or partially, different. Using the $H \to ZZ \to 4\ell$ decay channel is the best way to study these properties because of the small, well understood background contributions, and because all of the final state particles can be detected by CMS and

have excellent precision.

In basic terms, when a new particle is produced in a collision its spin and parity quantum numbers restrict the allowed types of interactions it can have with SM particles. This feature can be observed by investigating the kinematic distributions of the decay products or the particles produced in association with the new resonance. Of particular interest for this thesis work are the $X \to VV$ couplings (HVV). Where V is any vector boson (Z, W, γ, g), and X is the new resonance. When this new resonance is spin-0, we will use H because the Higgs boson is predicted to be spin-0. While this vertex can be studied by using the production or decay of a new particle we will focus on the properties that can be determined from the decay products.

When a new boson is produced it can be either spin-zero, one, or two[1]. In this work each is considered as a possibility for a new resonance, and the differences between their kinematics are used to study and classify the newly observed boson. The relevant phenomenology for these interactions is presented below.

3.4.1 Decay of a spin-zero resonance

The scattering amplitude describing the interaction between a spin-zero H boson and two spin-one gauge bosons VV ($ZZ, Z\gamma, \gamma\gamma, WW$ or gg) can be defined as in equation (3.4). Where the coupling parameters a_i^{VV} can have both real and imaginary parts and in general are form factors which can depend on the suared Lorentz

[1]Unless, the resonance is actually two particles with a mass difference less than the experimental resolution.

invariant four-momenta of V_1 and V_2, q_{V1}^2 and q_{V2}^2. In this expression, terms of higher order than q_V^2 have been dropped in the expansion under the assumption that anomalous couplings will only have a small contribution. In this expression, we use a different notation than previous sections and label the field strength tensor of a gauge boson with momentum q_{Vi} and polaraization ϵ_{Vi} with $f^{(i)\mu\nu} = \epsilon_{Vi}^{\mu} q_{Vi}^{\nu} - \epsilon_{Vi}^{\nu} q_{Vi}^{\mu}$. $\tilde{f}_{\mu\nu}^{(i)} = \frac{1}{2}\epsilon_{\mu\nu\rho\sigma} f^{(i)\rho\sigma}$ is the dual field strength tensor, and the superscript $*$ designates a complex conjugate. The masses of the Z or W boson is labeled as m_{V1}, while in the case of massless bosons there is no contribution from this term. To understand the impact form factor will have on the a_1 term, an energy scale Λ_1 for beyond-SM physics that could impact the SM scattering amplitude is also studied [61].

$$A(H \to VV) \sim \left[a_1^{VV} + \frac{\kappa_1^{VV} q_{V1}^2 + \kappa_2^{VV} q_{V2}^2}{\left(\Lambda_1^{VV}\right)^2} \right] m_{V1}^2 \epsilon_{V1}^* \epsilon_{V2}^* + a_2^{VV} f_{\mu\nu}^{*(1)} f^{*(2)\mu\nu} + a_3^{VV} f_{\mu\nu}^{*(1)} \tilde{f}^{*(2)\mu\nu} \tag{3.4}$$

In the SM, the tree-level contribution from $ZZ\,(WW)$ correspond to $a_1^{ZZ(WW)} \neq 0$, while the loop-induced SM contribution for $Z\gamma, \gamma\gamma,$ and gg is $a_2^{VV} \neq 0$. Small SM contributions to the higher order a_i terms can come from loop level contributions but, in general, these should be small. Additional restrictions on the allowed values for the κ_i terms arise from symmetry and gauge invariance. For ZZ, they require $\kappa_1^{ZZ} = \kappa_2^{ZZ} = -\exp\left(-i\phi_{\Lambda 1}^{ZZ}\right)$ where $\phi_{\Lambda 1}^{ZZ}$ is the relative phase between the a_1^{ZZ} and Λ_1 terms.

The parity conserving contribution from a pseudoscalar particle ($0^{+-}, CP$-odd) would be generated by the a_3 term, while a higher order scalar ($0^{++}, CP$-even) would be generated by a_2 or Λ_1 contributions. Anomalous contributions for the $\Lambda_1, a_2,$ or a_3 terms could be a sign of BSM physics and can in general have be complex, allowing for a relative phase between them and the SM a_1 term. To determine if these anomalous terms contribute to an observed resonance, we parameterize the contribution of one of these terms in an effective cross section fraction. These fractions are given in equation (3.6), where σ_i is the cross section for an $a_i = 1, a_{j\neq i} = 0$ particle decaying to the $2e2\mu$ final state[2]. The phases ϕ_{ai} are used to generalize equation (3.4) so that the anomalous contributions to be complex.

$$\begin{aligned} f_{\Lambda 1} &= \frac{\tilde{\sigma}_{\Lambda 1}/(\Lambda_1)^4}{|a_1|^2\sigma_1+|a_2|^2\sigma_2+|a_3|^2\sigma_3+\tilde{\sigma}_{\Lambda 1}/(\Lambda_1)^4+\ldots}, \quad \phi_{\Lambda 1}, \\ f_{a2} &= \frac{|a_2|^2\sigma_2}{|a_1|^2\sigma_1+|a_2|^2\sigma_2+|a_3|^2\sigma_3+\tilde{\sigma}_{\Lambda 1}/(\Lambda_1)^4+\ldots}, \quad \phi_{a2} = \arg\left(\frac{a_2}{a_1}\right), \\ f_{a3} &= \frac{|a_3|^2\sigma_3}{|a_1|^2\sigma_1+|a_2|^2\sigma_2+|a_3|^2\sigma_3+\tilde{\sigma}_{\Lambda 1}/(\Lambda_1)^4+\ldots}, \quad \phi_{a3} = \arg\left(\frac{a_3}{a_1}\right), \end{aligned} \tag{3.5}$$

These fractions are especially useful because they allow for great flexibility in the measurements. They are independent of the collider energy so they can be used to compare measurements made at different facilities, they are independent of coupling notation so can be used to translate between many different formulations for the spin-

[2] $\tilde{\sigma}_{\Lambda 1}$ is the effective cross section of the process corresponding to $\Lambda_1 = 1$ TeV, given in units of fb $\cdot$ TeV^4.

0 interactions, and they are bounded between 0 and 1 which allows investigation of the full phase space.

In CMS studies of these results, analogous fractions are created for the $WW, Z\gamma, \gamma\gamma$ final states. These fractions can be combined for ZZ and WW under different assumptions about the relationships between the a_i^{VV} terms. These results were a direct consequence of these studies and are left as a reference for the reader [62].

3.4.2 Decay of a spin-one resonance

In the case of a spin-one resonance, the amplitude of its interaction with a pair of massive gauge bosons, ZZ or WW, consists of two independent terms, seen in equation (3.6).

$$A(X_{J=1} \to VV) \sim b_1^{VV}\left[(\epsilon_{V1}^* q)\,(\epsilon_{V2}^* \epsilon_X) + (\epsilon_{V2}^* q)\,(\epsilon_{V1}^* \epsilon_X)\right] + b_2^{VV}\epsilon_{\alpha\mu\nu\beta}\epsilon_X^{\alpha}\epsilon_{V1}^{*\mu}\epsilon_{V2}^{*\nu}\tilde{q}^{\beta} \quad (3.6)$$

Where ϵ_X is the polarization vector of the boson X with spin one, $q = q_{V1} + q_{V2}$ and $\tilde{q} = q_{V1} - q_{V2}$ [63,64]. Here the $b_1^{VV} \neq 0$ coupling corresponds to a vector particle, while the $b_2^{VV} \neq 0$ coupling corresponds to a pseudovector. The $Z\gamma$ interactions of the spin-one particle are not considered, while the $\gamma\gamma$ and gg interactions are forbidden by the Landau-Yang theorem [65,66], where the gg case is justified by the assumption that the state X is color-neutral.

The evidence for a new boson in the ZZ final state will be presented in section 4.5, similar resonances have been seen in the $H \to \gamma\gamma$ decay channel, preventing the observation from being spin-one [67–69]. In the case that the ZZ resonance is different than the one seen in these references, we test if an observed boson is more consistent with spin-one or the SM predicted Higgs boson.

Pure vector (1^+), pseudovector (1^-), and mixed vector-pseudovector states are tested using the fraction f_{b2}^{VV} given in equation (3.7). This f_{b2}^{VV} parameter is a continuous unique way to define any state that is a mixture of 1^+ and 1^-. Where σ_{bi} is the cross section of the process corresponding to $b_i = 1, b_{j\neq i} = 0$ in the $X \to ZZ \to 2e2\mu$ final state.

$$f_{b2}^{VV} = \frac{\left|b_2^{VV}\right|^2 \sigma_{b2}}{|b_1^{VV}|^2 \sigma_{b1} + |b_2^{VV}|^2 \sigma_{b2}}, \tag{3.7}$$

3.4.3 Decay of a spin-two resonance

In the case of a general spin-two resonance, we test if a new observation is more consistent with the SM Higgs boson or a spin-two boson. The amplitude to describe the $X \to ZZ$ production is given in equation (3.8) (This same amplitude describes the $gg \to X$ production with $m_V = 0$.) where $t^{\mu\nu}$ is the wavefunction of a spin-two particle X given by a symmetric traceless tensor, m_V is the mass of the considered gauge boson, and Λ is the scale of BSM physics [63, 64]. The couplings c_1^{VV} and c_5^{VV} correspond to the parity-conserving interaction of a spin-two tensor with minimal

gravity-like couplings. As in the spin-zero case, the couplings c_i^{VV} are in general momentum-dependent form factors. In this analysis it is assumed that the form factors are momentum-independent constants and, thus, only the lowest q_i^2 order terms in the scattering amplitude are considered [62].

$$
\begin{aligned}
A(X_{J=2} \to VV) \sim \Lambda^{-1} \Big[& 2c_1^{VV} t_{\mu\nu} f^{*1,\mu\alpha} f^{*2,\nu}_{\alpha} + 2c_2^{VV} t_{\mu\nu} \frac{q_\alpha q_\beta}{\Lambda^2} f^{*1,\mu\alpha} f^{*2,\nu\beta} \\
& + c_3^{VV} t_{\beta\nu} \frac{\tilde{q}^\beta \tilde{q}^\alpha}{\Lambda^2} (f^{*1,\mu\nu} f^{*2}_{\mu\alpha} + f^{*2,\mu\nu} f^{*1}_{\mu\alpha}) + c_4^{VV} t_{\mu\nu} \frac{\tilde{q}^\nu \tilde{q}^\mu}{\Lambda^2} f^{*1,\alpha\beta} f^{*2}_{\alpha\beta} \\
& + m_V^2 \left(2c_5^{VV} t_{\mu\nu} \epsilon^{*\mu}_{V1} \epsilon^{*\nu}_{V2} + 2c_6^{VV} t_{\mu\nu} \frac{\tilde{q}^\mu q_\alpha}{\Lambda^2} \left(\epsilon^{*\nu}_{V1} \epsilon^{*\alpha}_{V2} - \epsilon^{*\alpha}_{V1} \epsilon^{*\nu}_{V2} \right) + c_7^{VV} t_{\mu\nu} \frac{\tilde{q}^\mu \tilde{q}^\nu}{\Lambda^2} \epsilon^*_{V1} \epsilon^*_{V2} \right) \\
& + c_8^{VV} t_{\mu\nu} \frac{\tilde{q}^\mu \tilde{q}^\nu}{\Lambda^2} f^{*1,\alpha\beta} \tilde{f}^{*2}_{\alpha\beta} \\
& + m_V^2 \left(c_9^{VV} t^{\mu\alpha} \frac{\tilde{q}_\alpha \epsilon_{\mu\nu\rho\sigma} \epsilon^{*\nu}_{V1} \epsilon^{*\rho}_{V2} q^\sigma}{\Lambda^2} + c_{10}^{VV} t^{\mu\alpha} \frac{\tilde{q}_\alpha \epsilon_{\mu\nu\rho\sigma} q^\rho \tilde{q}^\sigma \left(\epsilon^{*\nu}_{V1} (q \epsilon^*_{V2}) + \epsilon^{*\nu}_{V2} (q \epsilon^*_{V1}) \right)}{\Lambda^4} \right) \Big]
\end{aligned}
\tag{3.8}
$$

In this work, we study the ten spin-two scenarios listed in table 3.1, under the assumption that the production is via gluon-gluon fusion, $q\bar{q}$ production, or without any assumption about the production mechanism. The $q\bar{q} \to X$ couplings are parameterized in terms of ρ_i to correctly set the polarization and defined in [62]. The 2^+_m represents a massive graviton-like boson as suggested in models with warped extra dimensions [70, 71]. A modified minimal coupling model 2^+_b is also considered, where the SM fields are allowed to propagate in the bulk of the extra dimensions [72], corresponding to $c_1^{VV} \ll c_5^{VV}$. Additionally eight spin-two models with higher dimension

Table 3.1: List of spin-two models with the decay couplings of an exotic X particle. The subscripts m (minimal couplings), h (couplings with higher-dimension operators), and b (bulk) distinguish different scenarios [62].

J^P Model	$gg \to X$ Couplings	$q\bar{q} \to X$ Couplings	$X \to VV$ Couplings
2^+_m	$c_1^{gg} \neq 0$	$\rho_1 \neq 0$	$c_1^{VV} = c_5^{VV} \neq 0$
2^+_{h2}	$c_2^{gg} \neq 0$	$\rho_1 \neq 0$	$c_2^{VV} \neq 0$
2^+_{h3}	$c_3^{gg} \neq 0$	$\rho_1 \neq 0$	$c_3^{VV} \neq 0$
2^+_h	$c_4^{gg} \neq 0$	$\rho_1 \neq 0$	$c_4^{VV} \neq 0$
2^+_b	$c_1^{gg} \neq 0$	$\rho_1 \neq 0$	$c_1^{VV} \ll c_5^{VV} \neq 0$
2^+_{h6}	$c_1^{gg} \neq 0$	$\rho_1 \neq 0$	$c_6^{VV} \neq 0$
2^+_{h7}	$c_1^{gg} \neq 0$	$\rho_1 \neq 0$	$c_7^{VV} \neq 0$
2^-_h	$c_8^{gg} \neq 0$	$\rho_2 \neq 0$	$c_8^{VV} \neq 0$
2^-_{h9}	$c_8^{gg} \neq 0$	$\rho_2 \neq 0$	$c_9^{VV} \neq 0$
2^-_{h10}	$c_8^{gg} \neq 0$	$\rho_2 \neq 0$	$c_{10}^{VV} \neq 0$

operators are considered [62].

Chapter 4

$H \to ZZ \to 4\ell$ search & Production Mechanism

In this section we discuss the search for a Higgs boson decaying to the 4 lepton final state at CMS. First, we provide a general overview of the analysis. Next, we discuss additional requirements that are made on the physics objects we have already introduced. Using this information we present the event selection, simulation, and categorization for the search and a summary of the expected signal and background estimations. Next, we introduce the kinematic distributions that are used to enhance our signal against the background processes. Specifically, the $m_{4\ell}$ mass distribution, the *Matrix Element Likelihood Approach* (MELA) kinematic discriminant, the $p_T^{4\ell}$, and the jet kinematic discriminant. Finally we present the results of this search and first major characterization study: The production mechanism measurements. The

studies presented in this section have been published in reference [41].

4.1 General overview of $H \to ZZ \to 4l$

While some of this information was introduced earlier in order to discuss specific theoretical and phenomenological aspects of this work, here we summarize the $H \to ZZ \to 4\ell$ search. This analysis searches for a scalar Higgs boson which would be the smoking gun that the Higgs Mechanism is responsible for electroweak symmetry breaking. This search covers the range of $m_{4\ell} \in$ 110–1000 GeV because the mass of the Higgs boson (m_H) is a free parameter in the theoretical basis for the theory. General theoretical considerations suggest that m_H should be less than $\approx$ 1 TeV [73–76], while precision electroweak measurements imply that $m_H < 152$ GeV [77]. Previously, direct searches for the Higgs boson have been made at the LEP collider setting the limit that $m_H > 114.4$ GeV [78], and the Tevatron collider, excluding $m_H \notin$ 90–109 GeV $\cup$ 149–182 GeV [79, 80].

In this thesis, the analysis of the $H \to ZZ \to 4\ell$ channel is presented using the entire dataset collected by the CMS experiment during the 2011-2012 LHC running period. The data correspond to an integrated luminosity of 5.1 fb^{-1} of proton-proton collisions at a center of mass energy of $\sqrt{s} = 7$ TeV, and 19.7 fb^{-1} at $\sqrt{s} = 8$ TeV. The search attempts to find a signal consisting of two pairs of same-flavor, opposite-charge, well-identified and isolated leptons compatible with a ZZ-system, appearing

as a narrow resonance on top of a smooth background in the four-lepton invariant mass distribution.

4.2 Object Selection

Given the very low branching fraction of the $H \to ZZ \to 4\ell$ decay, it is important to maintain a very high lepton selection efficiency in a wide range of momenta, to maximize the sensitivity for a Higgs boson in the full range $m_{4\ell} \in$ 110–1000 GeV. Additionally, because the signal sensitivity depends on the 4ℓ mass resolution it is crucial to calibrate the individual lepton momentum to understand the scale and resolution to a level such that the systematic uncertainties are small. A summary of the lepton identification, scale, and resolution is presented in section 2.3. Additional object selections including lepton isolation and vertex compatibility are presented here.

Lepton isolation is used to discriminate leptons originating from high-p_T boson decay, as in the case of the signal, from those arising from hadronic processes, which are typically immersed in a jet of other hadrons. The isolation of individual leptons, measured relative to their transverse momentum p_T^ℓ, is defined by:

$$R_{\text{Iso}}^{\ell} \equiv \left(\sum p_T^{\text{charged}} + \max\left[0, \sum p_T^{\text{neutral}} + \sum p_T^{\gamma} - p_T^{\text{PU}}(\ell)\right] \right) / p_T^{\ell}, \tag{4.1}$$

where the sums are over the charged, neutral, and photon particle candidates in

a cone $\Delta R = \sqrt{(\Delta\eta)^2 + (\Delta\phi)^2} < 0.4$ around the lepton direction at the interaction vertex (where $\Delta\eta$ & $\Delta\phi$ quantify the angular distance between the candidate from the lepton). In equation (4.1), the sums are computed for particles that originate from the primary vertex of the event (defined as the vertex with the the highest $\sum p_T^2$ of associated tracks). In this expression, the contribution from pileup $\left(p_T^{PU}(\ell)\right)$ is explicitly subtracted. This pileup contribution is computed separately for electrons and muons and outlined in [41]. In this isolation calculation, photons that qualify for FSR reconstruction are omitted from the p_T^{γ} sum. FSR is outlined in the muon reconstruction section 2.3.4.

In order to suppress leptons originating from in-flight decays of hadrons and muons from cosmic rays, all leptons are required to come from the same primary vertex. This is achieved by requiring that the significance of the interaction parameter in three dimensions is $\mathrm{SIP}_{3\mathrm{D}} < 4$, where $\mathrm{SIP}_{3\mathrm{D}} \equiv \mathrm{IP}_{3\mathrm{D}}/\sigma_{\mathrm{IP}_{3\mathrm{D}}}$ is the ratio of the impact parameter of the lepton track in three dimensions, with respect to the chosen primary vertex position, and its uncertainty.

The combined efficiency for the reconstruction, identification, and isolation (and conversion rejection for electrons) of prompt electrons or muons is measured in data using a Òtag and probeÓ method based on an inclusive sample of Z-boson events, separately for 7 and 8 TeV data. The efficiency is measured by fitting the Z mass distribution plus a background model to the dilepton mass distributions where the probe lepton passes or fails the selection criteria. This efficiency is calculated in both

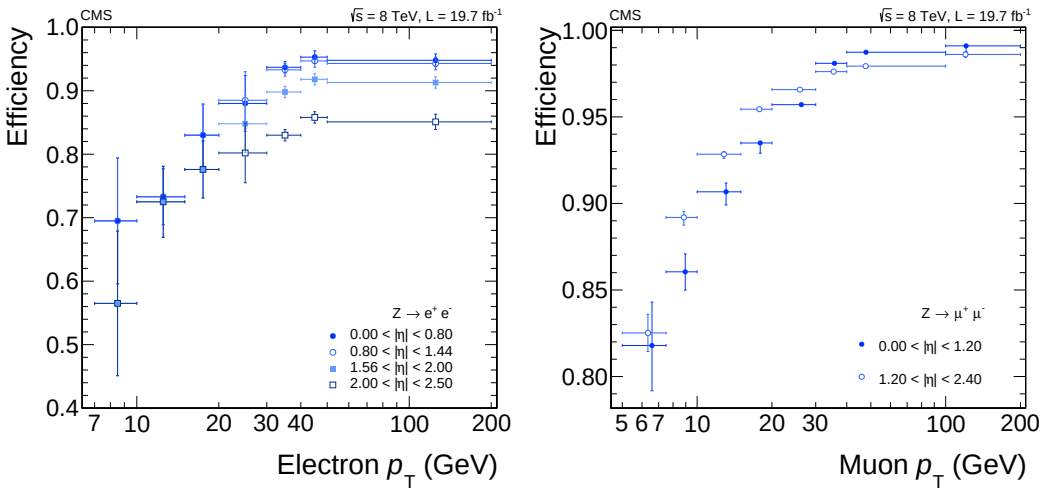

Figure 4.1: Efficiency, as a function of the lepton p_T^ℓ, for reconstructing and selecting (left) electrons and (right) muons, measured with a $Z \to \ell\ell$ data sample by using a tag-and-probe method [41].

simulation and data and used to correct the simulation accordingly. These efficiencies are shown in figure 4.1 for both electrons and muons.

In the analysis the presence of jets is used as an indication of vector-boson fusion (VBF) or associated production with a weak boson, VH, with $V = W$ or Z, where the V decays hadronically. Jets are reconstructed using the anti-k_T clustering algorithm with distance parameter $D = 0.5$, as discussed in section 2.3.5. Jets are only considered if they have $p_T^{\text{jet}} > 30$ GeV, $\left|\eta^{\text{jet}}\right| < 4.7$, originate from the primary vertex, and are required to be separated from the lepton candidates and from identified FSR photons by $\Delta R > 0.5$. Jet energy corrections are applied as a function of the jet p_T^{jet} and η^{jet} [47]. An offset correction is applied to subtract the energy contribution not associated with the high-p_T scattering, such as electronic noise and pileup, based on

the jet-area method [47, 81, 82].

4.3 Event Selection, Simulation, & Categorization

4.3.1 Simulated Data Samples

The Monte Carlo (MC) simulated data samples, generated with state-of-the-art theoretical calculations for both the SM Higgs boson signal and relevant background processes, are used to optimize the event selection and to evaluate the acceptance and systematic uncertainties. For the gluon-gluon fusion and vector-boson fusion Higgs boson signal, simulated events are generated with POWHEG [83–85] at Next-to-leading-order (NLO) QCD accuracy. The Higgs boson decay is modeled with JHUGen 3.1.8 [61, 63, 64] to include proper treatment of the interference effects associated with permutations of identical leptons in the four-electron and four-muon final states. Samples of WH, ZH, and $t\bar{t}H$ events are generated with PYTHIA 6.4.24 [86]. Higgs boson signal event cross section and p_T distribuiton for all production mechanisms are reweighted to include contributions from gluon fusion up to next-to-next-to-leading-order (NNLO) and next-to-next-to-leading logarithm (NNLL) [55,87–97], and from the vector-boson fusion contribution computed at NNLO [55, 98–102].

The two dominant irreducible background contributions for this analysis are the

SM $q\bar{q} \to ZZ$ and $gg \to ZZ$ events. The $q\bar{q} \to ZZ$ background is simulated at NLO using the POWHEG [103] program while the $gg \to ZZ$ contribution is simulated at LO using GG2ZZ [104]. The yields for these SM congribitons are calculated with MCFM [105–107]. The reducible backgrounds, including $Zb\bar{b}$, $Zc\bar{c}$, $Z\gamma + \text{jets}$, $WW + \text{jets}$, $WZ + \text{jets}$, etc. (referred to as $Z + \text{jets}$) are simulated with MADGRAPH [108] and used to cross check the data driven methods outlined in the next section (The $t\bar{t}$ contribution to this background is simulated at NLO with POWHEG).

To model the constituents (quarks & gluons) of the colliding protons correctly, parton distributions functions are used (CTEQ6L [109] for LO generators, CT10 [110] for NLO and higher-order generators). To model the underlying event, jet fragmentation, and showering all events are processed with PYTHIA 6.4.24 [86]. The CMS detector is simulated with great detail using a simulation based on GEANT4 [111, 112].

4.3.2 Selection & Categorization

The event selection is designed to give a set of signal candidates in the $H \to ZZ \to 4\ell$ final state in three mutually exclusive subchannels: $4e$, 4μ, and $2e2\mu$. Four well-identified and isolated leptons are required to originate from the primary vertex to suppress the $Z + \text{jets}$ and $t\bar{t}$ backgrounds.

Z candidates are formed with a pair of leptons of the same flavor and opposite charge ($\ell^+\ell^-$). When forming the Z-boson candidates, only FSR photons that make

the lepton-pair mass closer to the nominal Z-boson mass are incorporated. If the $m_{\ell\ell\gamma} > 100$ GeV, the photon is not considered, to minimize the fraction of misidentification.

Among all the possible opposite-charge lepton paris in the event, the one with an invariant mass closest to the nominal Z-boson mass is denoted Z_1 and retained if $40 < m_{Z_1} < 120$ GeV. Then, all remaining leptons are considered and a second same flavor opposite-charge pair $\ell^+\ell^-$ becomes Z_2 when the pair has the highest scalar sum of $p_T^{\ell\ell}$ in the event and $12 < m_{Z_2} < 120$ GeV. This selection procedure results in one or more of the Z-bosons to be off shell for $m_H < 180$ GeV.

Among the four selected leptons forming the Z_1 and the Z_2, at least one lepton is required to have $p_T^\ell > 20$ GeV, and another one is required to have $p_T^\ell > 10$ GeV. These p_T^ℓ thresholds ensure that the selected events have leptons on the efficiency plateau of the trigger. To further remove events with leptons originating from hadron decays produced by jet fragmentation or from the decay of low-mass hadron resonances, it is required that any opposite-charge pair of leptons chosen among the four selected leptons (irrespective of flavor) satisfy $m_{\ell^+\ell^-} > 4$ GeV. The phase space for the search of the SM Higgs boson is defined by restricting the measured mass range to $m_{4\ell} > 100$ GeV.

The efficiency versus m_H is shown in Fig. 4.2 for the gluon fusion Higgs boson production mode, and it is very similar for other production modes. The efficiency within the geometrical acceptance is ≈30% (58%), 43% (71%), and 62% (87%) for

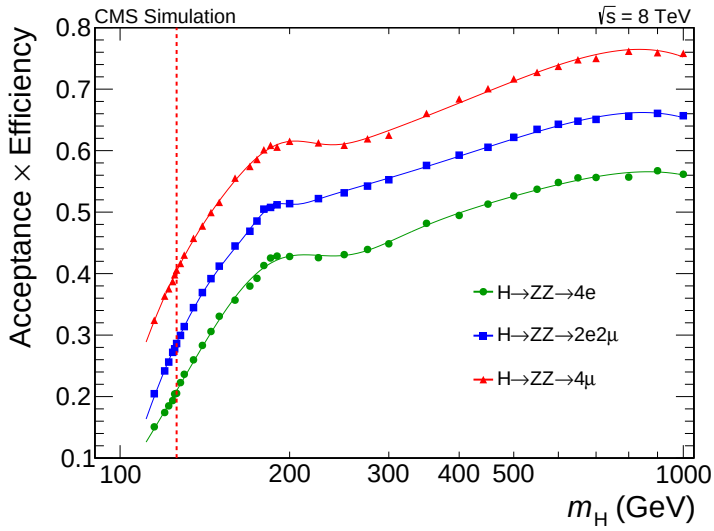

Figure 4.2: Geometrical acceptance times selection efficiency for the SM Higgs boson signal as a function of m_H in the three final states for gluon fusion production. Points represent efficiency estimated from full CMS simulation; lines represent a smooth polynomial curve interpolating the points, used in the analysis. The vertical dashed line represents $m_H = 126$ GeV [41].

the $4e, 2e2\mu,$ and 4μ channels, respectively, for $m_H = 126(200)$ GeV.

In order to improve the sensitivity to the Higgs boson production mechanisms, the event sample is split into two categories based on the jet multiplicity. These categories are defined as the 0/1-jet category, containing events with fewer than two jets, and the dijet category, containing events with at least two jets.

4.3.3 Background estimation

The dominant background contribution in the $H \to ZZ \to 4\ell$ search is irreducible and is due to direct ZZ production via $q\bar{q}$ annihilation and gluon fusion. The remaining subleading contributions arise from reducible multilepton sources, $Z +$ jets, $t\bar{t}$, and

$WZ +$ jets.

The expected yield and shape of the $q\bar{q} \to ZZ$ and $gg \to ZZ$ background is evaluated using the simulated events discussed above. The $gg \to ZZ$ contribution with respect to the $q\bar{q} \to ZZ$ varies from about 2% at $m_{4\ell} = 126$ GeV to 6% at $m_{4\ell} = 1$ TeV. These two background processes make up a dominant fraction of the total background in this analysis. In the region $100 < m_{4\ell} < 1000$ GeV these backgrounds contribute approximately $91\%, 94\%,$ and 97% in the $4e, 2e2\mu,$ and 4μ decay channels, respectively. Within the smaller range around the observed peak ($121.5 < m_{4\ell} < 130.5$ GeV) these irreducible backgrounds contribute $58\%, 71\%,$ and 86%, respectively.

The reducible background from $Z+$jets is estimated using two independent methods. These methods use dedicated control regions in data where there is a dilepton pair satisfying all the requirements of a Z_1 candidate and two additional leptons satisfying certain relaxed identification requirements. In both methods, the extrapolation from the control region to the signal regions is performed using the lepton misidentification probability, $f\left(\ell, p_T^\ell, \left|\eta^\ell\right|\right)$, which is defined as the fraction of non-signal leptons identified in the analysis selection criteria evaluated on a sample of enriched non-genuine electrons and muons.

The first method uses two control regions that have a Z_1 candidate and two additional leptons with the same flavor and opposite charge. There are two categories of events that satisfy the criteria, 2P2F (composed of two leptons that pass selection and two that fail the isolation or identification criteria) and 3P1F (composed of three

leptons that pass selection and one that fails). For each event i that falls into the 2P2F or 3P1F category a weight factor of $\frac{f_3^i}{1-f_3^i}\frac{f_4^i}{1-f_4^i}$ or $\frac{f_a^i}{1-f_a^i}$ for the third and/or fourth leptons. The 3P1F region will also have a contribution from the reducible background and so the contribution is reduced by a factor of $\left(1 - \frac{n_{3P1F}^{ZZ}}{N_{3P1F}}\right)$ where n_{3P1F}^{ZZ} is the estimation of irreducible ZZ events and N_{3P1F} is the total number of events in the 3P1F region. The contribution of the 2P2F to the 3P1F is also accounted for and in the end the reducible background estimation in the signal region, $N_{\mathrm{SR}}^{\mathrm{reducible}}$, is given by equation (4.2),

$$N_{\mathrm{SR}}^{\mathrm{reducible}} = \left(1 - \frac{n_{\mathrm{3P1F}}^{ZZ}}{N_{\mathrm{3P1F}}}\right) \sum_j^{N_{\mathrm{3P1F}}} \frac{f_a^j}{1-f_a^j} - \sum_i^{N_{\mathrm{2P2F}}} \frac{f_3^i}{1-f_3^i}\frac{f_4^i}{1-f_4^i}. \tag{4.2}$$

The second method uses a control region that has a Z_1 candidate and two additional leptons with the same flavor and the same charge. This method exploits the linear dependence of the $f\left(\ell, p_T^\ell, \left|\eta^\ell\right|\right)$ probability on the fraction of loose electrons with tracks have one missing hit in the pixel detector $r_{\mathrm{miss}}\left(p_T^e, |\eta^e|\right)$, which is indicative of a possible FSR photon conversion. This r_{miss} fraction is estimated using samples with different FSR contributions and the $f\left(\ell, p_T^\ell, \left|\eta^\ell\right|\right)$ is corrected to $\tilde{f}\left(\ell, p_T^\ell, \left|\eta^\ell\right|\right)$ using the corresponding r_{miss} fraction. The expected number of reducible background events in the signal region is given by equation (4.3), where $N_{\mathrm{2P2F_{SS}}}$ is the number of observed events in the same-sign 2P2F region. The ratio $r_{\mathrm{OS/SS}}$ between the number of events in the 2P2F opposite-sign and same-sign control regions is obtained from simulation.

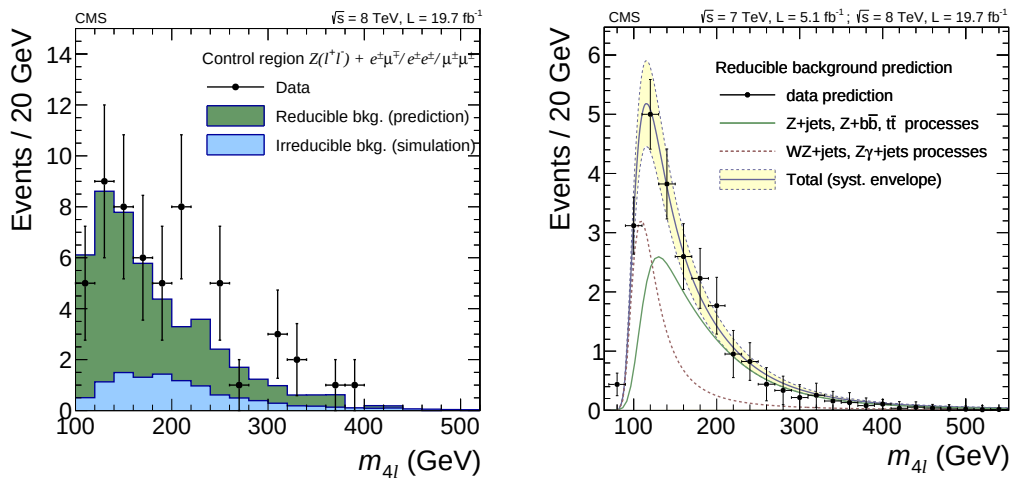

Figure 4.3: (left) Validation of the method using the SS control sample. The observed $m_{4\ell}$ distribution (black dots), prediction of the reducible background (dark green area), and expected contributions from ZZ (light blue area) are shown. (right) Prediction for the reducible background in all three decay channels together (black dots) fitted using an empirical shape (blue curve) with indicated total uncertainty (yellow band). The contributions from the 2P2F-like (solid green) and 3P1F-like (dashed red) processes are fitted separately [41].

$$N_{\mathrm{SR}}^{\mathrm{reducible}} = r_{\mathrm{OS/SS}} \cdot \sum_{i}^{N_{\mathrm{2P2L_{SS}}}} \tilde{f}_3^i \cdot \tilde{f}_4^i \tag{4.3}$$

Both of these two reducible background estimations agree well within their statistical uncertainties. Such good agreement allows the analysis to combine the two estimations of the background together, assigning a systematic unvartainty of $20\%, 25\%,$ and 40% for the $4e$, $2e2\mu$, 4μ decay channels, respectively. Validations of these two methods are shown in figure 4.3.

After all of this simulation, extrapolation, and calculation we can estimate the number of collision events we would expect to observe for the SM backgrounds and

Table 4.1: The number of observed candidate events compared to the mean expected background and signal rates for each final state. Uncertainties include statistical and systematic sources. The results are given integrated over the full mass measurement range $m_{4\ell} > 100$ GeV and for 7 and 8 TeV data combined [41].

Decay Channel	$4e$	$2e2\mu$	4μ	4ℓ
ZZ background	77 ± 10	191 ± 25	119 ± 15	387 ± 31
$Z+$jets background	7.4 ± 1.5	11.5 ± 2.9	3.6 ± 1.5	22.6 ± 3.6
All backgrounds	85 ± 11	202 ± 25	123 ± 15	410 ± 31
$m_H = 500$ GeV	5.2 ± 0.6	12.2 ± 1.4	7.1 ± 0.8	24.5 ± 1.7
$m_H = 800$ GeV	0.7 ± 0.1	1.6 ± 0.2	0.9 ± 0.1	3.1 ± 0.2
Observed	89	247	134	470

for the Higgs boson under different mass hypotheses. In the full analysis region $m_{4\ell} > 100$ GeV these estimations and the statistical and systematic uncertainty on them is shown in table 4.1.

4.4 Kinematic Distributions

Beyond counting the number of observed and expected collision events within the signal region, this analysis utilizes the kinematic distributions of three variables to separate potential signal events from background SM production. The first is the $m_{4\ell}$ distribution, second is a kinematic discriminant based on the matrix elements of both signal and background processes, the third is either the $p_T^{4\ell}$ or jet kinematic discriminant. Where either of these is used depends on the number of jets observed in addition to the four leptons.

4.4.1 Four-lepton mass spectrum

The background from $ZZ/Z\gamma^*$ and $Z+$jets processes dominates after the event selection. The reconstructed four-lepton invariant mass distribution for the combined $4e, 2e2\mu,$ and 4μ channels is shown in figure 4.4 and compared with the expectations from background processes.

The normalization and shape of the ZZ background are obtained from simulation, while the normalization of the reducible background is estimated from control samples in data, as described in section 4.3.3. The $m_{4\ell}$ distribution of the reducible background component is obtained from the opposite-sign method by fitting the $m_{4\ell}$ distributions of 2P2F and 3P1F regions separately with empirical functional forms built from Landau and exponential distributions. The systematic uncertainty in the shape is determined by the envelope that covers alternative functional forms or alternative binning.

The signal $m_{4\ell}$ distributions are also obtained from simulation. For low-mass Higgs boson hypotheses ($m_H < 400$ GeV), the Higgs boson mass distribution is described with a relativistic Breit-Wigner (BW) convolved with a double-sided Crystal-Ball (CB) distribution to parameterize the reconstructed signal $m_{4\ell}$ distributions. The resulting model for the $m_{4\ell}$ peak can be seen in figure 4.5, where the parameterization for each final state can be seen superimposed on simulated data events. At high mass ($m_H > 400$ GeV), the mass distribution is described using the complex pole scheme (CPS) [58, 113, 114]. This results in a Higgs boson width much larger than

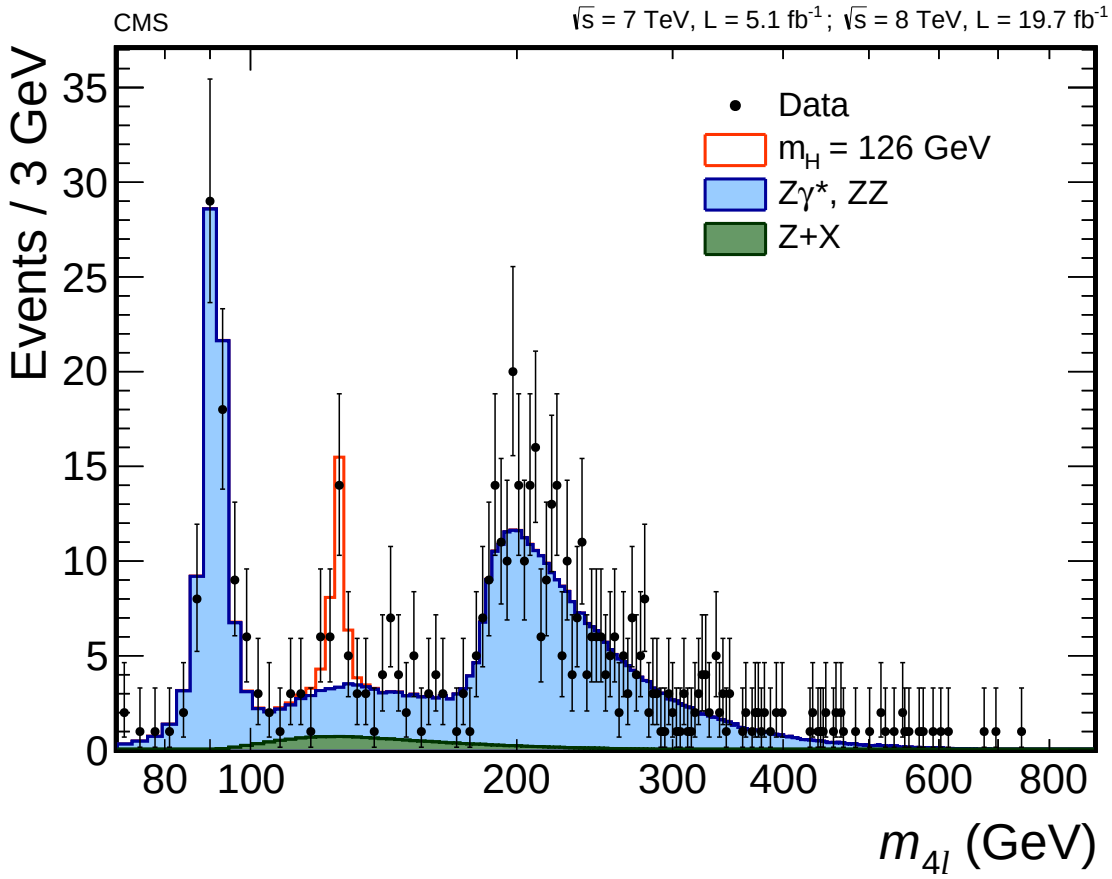

Figure 4.4: Distribution of the four-lepton reconstructed mass in the full mass range $70 < m_{4\ell} < 1000$ GeV for the sum of the $4e$, $2e2\mu$, and 4μ channels. Points with error bars represent the data, shaded histograms represent the backgrounds, and the unshaded histogram represents the signal expectation for a mass hypothesis of $m_H =$ 126 GeV. Signal and the ZZ background are normalized to the SM expectation; the $Z +$ jets background to the estimation from data. The expected distributions are presented as stacked histograms. No events are observed with $m_{4\ell} > 800$ GeV [41].

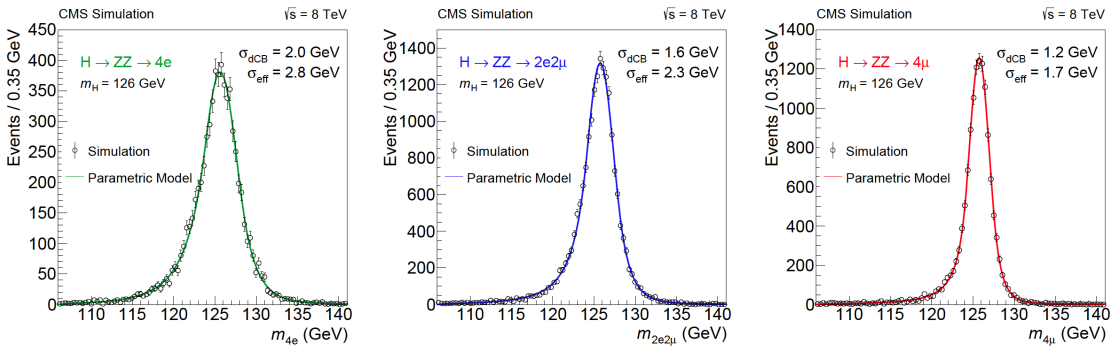

Figure 4.5: The $H \to ZZ \to 4\ell$ invariant mass distribution for $m_H = 126$ GeV in the (left) $4e$, (center) $2e2\mu$, and (right) 4μ channels. The distributions are fitted with a double-sided CB function and the fitted values of the CB width σ_{dCB} are indicated. The values of effective resolution, defined as half the smallest width that contains 68.3% of the distribution, are also indicated. The distributions are arbitrarily normalized [41].

the four-lepton mass resolution. The signal parameterization for these hypotheses are modified according to this increased width instead of using the double CB functions. Systematics on the mass distribution are incorporated by varying them as a function of the Higgs boson mass by $\pm 1\sigma$.

4.4.2 Matrix Element Likelihood Approach (MELA) kinematic discriminant

As we have mentioned the four-lepton decay mode has the advantage that the kinematics of the Higgs boson and its decay products are all visible in the detector, providing many independent observables that can be used for different purposes. In addition to the invariant mass, the angular distributions for the four leptons and

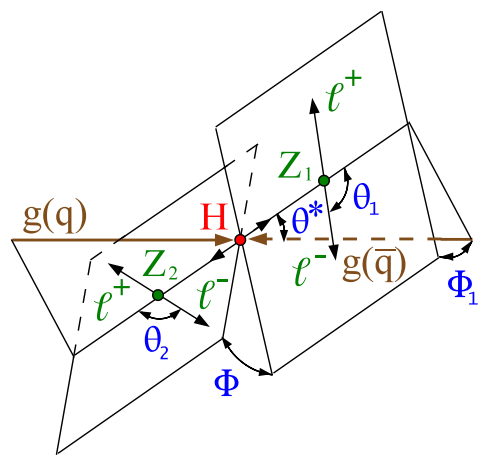

Figure 4.6: Illustration of the production and decay of a particle H, $gg(q\bar{q}) \to H \to ZZ \to 4\ell$, with the two production angles θ^* and Φ_1 shown in the H rest frame and three decay angles θ_1, θ_2, and Φ shown in the Z_1, Z_2, and H rest frames, respectively [61].

the dilepton pairs invariant masses can be used to further discriminate signal from background, increasing the sensitivity and reducing the statistical uncertainty in the observations.

Five angles $\vec{\Omega} \equiv (\theta^*, \Phi_1, \theta_1, \theta_2, \Phi)$ [61,63,64,115] seen in figure 4.6 and the invariant masses of the lepton pairs m_{Z_1} and m_{Z_2}, fully describe the kinematic configuration of a four-lepton system in its center-of-mass frame, up to an arbitrary rotation around the beam axis. These observables provide significant discriminating power between signal and background. A matrix-element likelihood approach (MELA) is used to construct a kinematic discriminant related to the decay observables [61, 63, 64, 69, 116].

Each of these five observables carries some information about how the 4ℓ event was produced. The distribution of these is shown in figure 4.7. This figure also shows predicted distributions for BSM bosons, which become relevant in later sections. In

principle, with enough computing power and effort one could construct an analysis that uses all of them as inputs. However, without loss in performance one can use the event probabilities that come from the matrix-element corresponding to a given point in phase space. This way the analysis is simplified and the correlations between these different variables are maintained.

To separate a SM signal $\left(J^P = 0^+\right)$ from background a kinematic discriminant $\left(\mathcal{D}_{\text{bkg}}^{\text{kin}}\right)$ is defined based on the event probabilities $\mathcal{P}\left(m_{Z_1}, m_{Z_1}, \vec{\Omega}|m_{4\ell}\right)$ of the background or signal probability distribution of angular and mass observables computed from the LO matrix element squared for signal or ZZ processes. This discriminant is defined as in equation (4.4), giving the added advantage that to first order acceptance and phase space factors cancel in the ratio. Thus, one does not need to integrate the matrix elements over the full kinematic range but simply calculate the magnitude of the matrix element squared at the point in phase space where each event appears.

$$\mathcal{D}_{\text{bkg}}^{\text{kin}} = \frac{\mathcal{P}_{0^+}^{\text{kin}}}{\mathcal{P}_{0^+}^{\text{kin}} + \mathcal{P}_{\text{bkg}}^{\text{kin}}} = \left[1 + \frac{\mathcal{P}_{\text{bkg}}^{\text{kin}}(m_{Z_1}, m_{Z_2}, \vec{\Omega}|m_{4\ell})}{\mathcal{P}_{0^+}^{\text{kin}}(m_{Z_1}, m_{Z_2}, \vec{\Omega}|m_{4\ell})}\right]^{-1}. \tag{4.4}$$

The expected $\mathcal{D}_{\text{bkg}}^{\text{kin}}$ shapes for signal and the $q\bar{q} \to ZZ$ and $gg \to ZZ$ backgrounds are taken from simulation of the three decay channels $4e$, $2e2\mu$, and 4μ independently. Given the low statistics and unreliable simulation, the Z+jets contribution is modeled by collision events in the control regions. The statistics are boosted by merging all decay channels and control regions together using the appropriate weight to map them to the signal region.

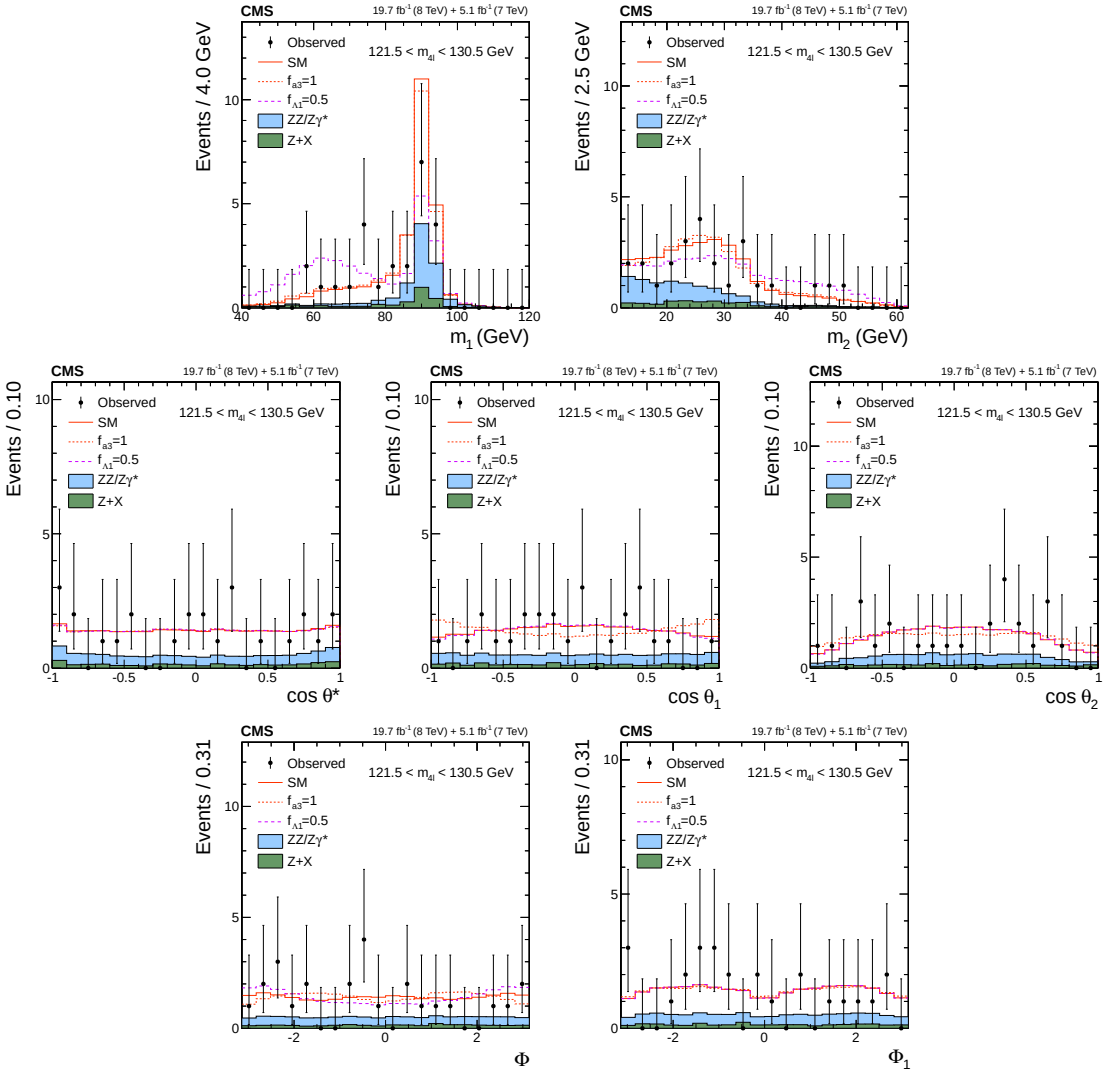

Figure 4.7: Distributions of the eight kinematic observables used in the $H \to ZZ \to 4\ell$ analysis: m_{Z_1}, m_{Z_2}, $\cos\theta^*$, $\cos\theta_1$, $\cos\theta_2$, Φ, and Φ_1. The observed data (points with error bars), the expectations for the SM background (shaded areas), the SM Higgs boson signal (open areas under the solid histogram), and the alternative spin-zero resonances (open areas under the dashed histograms) are shown, as indicated in the legend. The mass of the resonance is taken to be 125.6 GeV and the SM cross section is used. All distributions, with the exception of $m_{4\ell}$, are presented with the requirement $121.5 < m_{4\ell} < 130.5$ GeV [62].

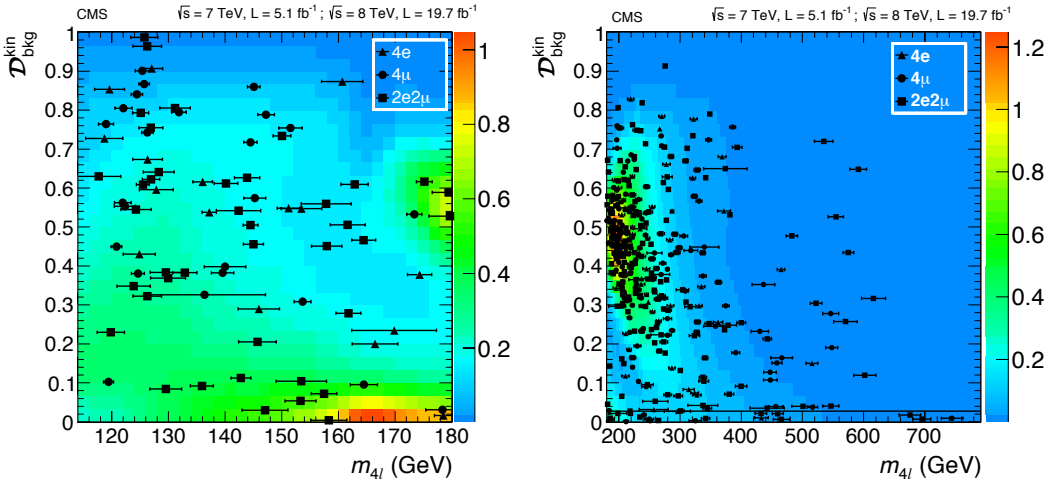

Figure 4.8: Distribution of the kinematic discriminant $\mathcal{D}_{\rm bkg}^{\rm kin}$ versus the four-lepton reconstructed mass $m_{4\ell}$ in the (left) low-mass and (right) high-mass regions. The color scale represents the expected relative density in linear scale (in arbitrary units) of background events. The points show the data and the measured per-event invariant mass uncertainties as horizontal bars. One $2e2\mu$ event with $m_{4\ell} \approx 220$ GeV and small $\mathcal{D}_{\rm bkg}^{\rm kin}$ has a huge mass uncertainty, and it is displayed as the horizontal line. No events are observed for $m_{4\ell} > 800$ GeV [41].

Because these discriminant values do not directly carry $m_{4\ell}$ discrimination power they are used as a second dimensions for discrimination between signal and background. The distributions of the $\mathcal{D}_{\rm bkg}^{\rm kin}$ versus $m_{4\ell}$ are shown for the selected events and compared to the SM background expectation in figure 4.8. The distribution of events in the $\left(m_{4\ell}, \mathcal{D}_{\rm bkg}^{\rm kin}\right)$ plane agrees well with the SM background expectation in the high-mass range, figure 4.8 (right), while discrepancies in the two-dimensional plane are observed in the low-mass range $110 < m_{4\ell} < 180$ GeV, figure 4.8 (left), indicative of the presence of a signal.

Figure 4.9 (left) shows the same data points as in figure 4.8 (left), but compared

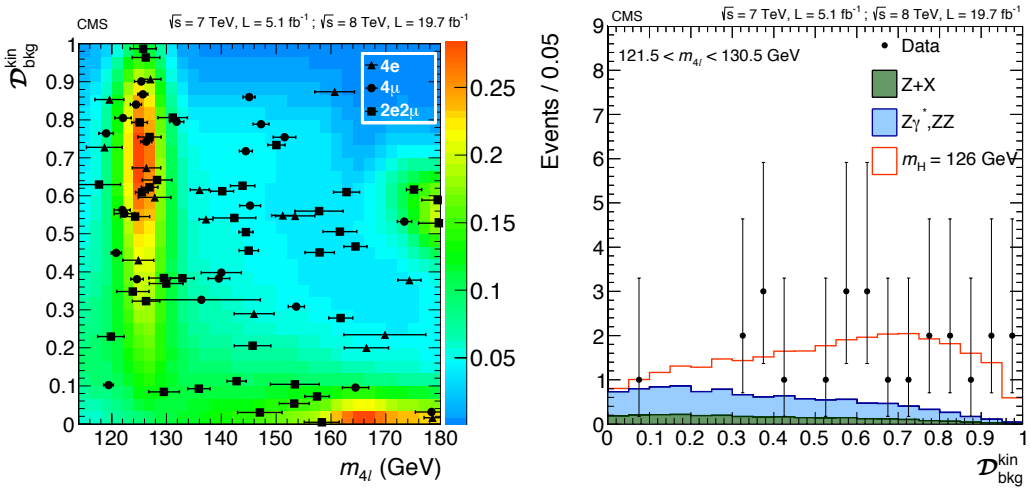

Figure 4.9: (left) Distribution of $\mathcal{D}_{\rm bkg}^{\rm kin}$ versus $m_{4\ell}$ in the low-mass range with colors shown for the expected relative density in linear scale (in arbitrary units) of background plus the Higgs boson signal for $m_H = 126$ GeV. The points show the data, and horizontal bars represent the measured mass uncertainties. (right) Distribution of the kinematic discriminant $\mathcal{D}_{\rm bkg}^{\rm kin}$ for events in the mass region $121.5 < m_{4\ell} < 130.5$ GeV. Points with error bars represent the data, shaded histograms represent the backgrounds, and the unshaded histogram the signal expectation. Signal and background histograms are stacked [41].

with the expected distribution from SM backgrounds plus the contribution of a Higgs boson with $m_H = 126$ GeV. A signal-like clustering of events is apparent at high values of $\mathcal{D}_{\rm bkg}^{\rm kin}$ and for $m_{4\ell} \approx 126$ GeV. Figure 4.9 (right) shows the distribution of the kinematic discriminant $\mathcal{D}_{\rm bkg}^{\rm kin}$ in the mass region $121.5 < m_{4\ell} < 130.5$ GeV.

4.4.3 Transverse momentum and Jet Kinematic Discriminant

While in the gluon fusion mechanism is the most likely way to produce a Higgs boson at the LHC, the cross section for VBF production is only about 1 order of magnitude smaller than that for the gluon fusion process. In the vector-boson scattering process, the two initial-state quarks deviate at a polar angle large enough such that as final-state quarks they create measurable additional jets in the event. These two jets, being remnants of the incoming proton beams, have typically a large separation in η and high momentum. These characteristics are used to distinguish VBF from gluon fusion Higgs boson production in the analysis. Jets in the final state also come from $t\bar{t}H$ and VH production, where the V decays hadronically.

In the 0/1-jet category, the transverse momentum of the four-lepton system ($p_T^{4\ell}$) is used to distinguish VBF production and associated production with a weak boson, VH, from gluon fusion, discrimination power seen in figure 4.10 (top right). In the dijet category, a linear discriminant ($\mathcal{D}_{\text{jet}}$) is formed combining two VBF-sensitive variables, the absolute difference in pseudorapidity ($|\Delta\eta_{jj}|$) and the invariant mass (m_{jj}) of the two leading jets. The discriminant maximizes the separation between vector-boson and gluon fusion processes. In the 0/1-jet (dijet) category, about 5% (20%) of the signal events are expected to come from the VBF production mechanism, as estimated from simulation. Simulations of these distributions are shown in figure

4.10.

For the final analysis, the distribution of the transverse momentum of the 4ℓ system in the 0/1-jet category and its joint distribution with $m_{4\ell}$ are shown in figure 4.11. The p_T spectrum shows good agreement with a SM Higgs boson hypothesis with $m_H = 126$ GeV in the 0/1-jet category with few events having $p_T > 60$ GeV, where VBF and VH production are more relevant.

The distribution of the production mechanism discriminant in the dijet category and its joint distribution with $m_{4\ell}$ are shown in figure 4.12. Good agreement is found with the expectation from simulation, which predicts a negligible background and a fraction of 42% of the signal events arising from vector-boson-induced production (VBF and VH). No events with a high rank of the $\mathcal{D}_{\text{jet}}$ ($\mathcal{D}_{\text{jet}} > 0.5$) discriminant are observed.

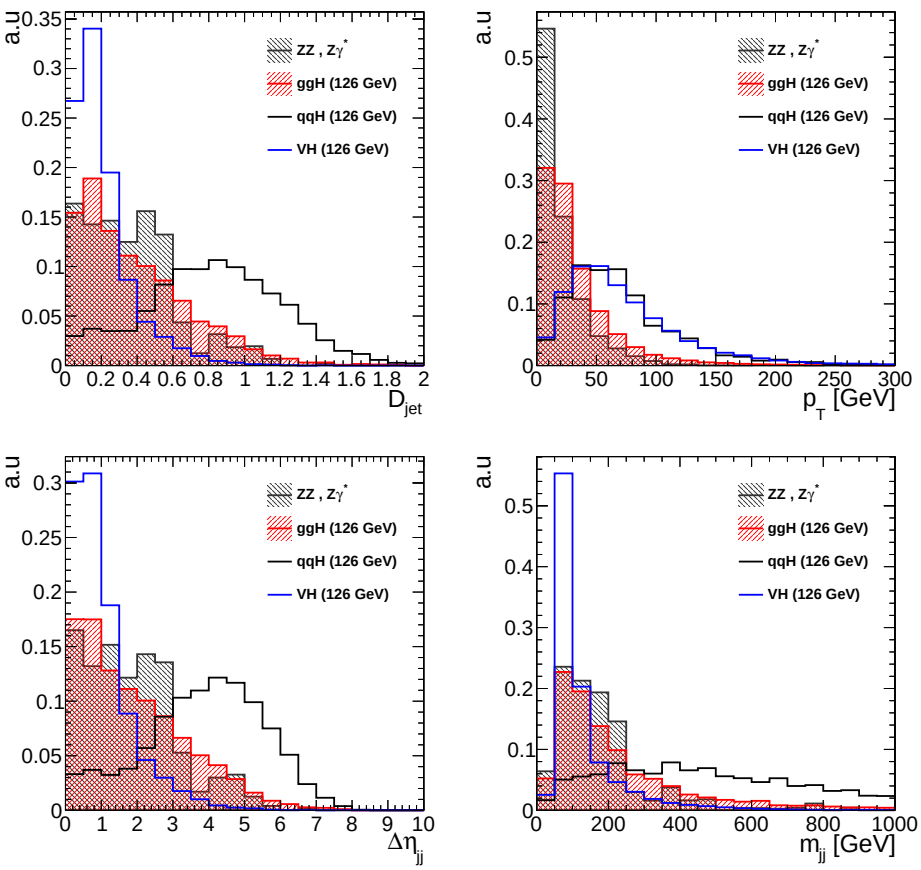

Figure 4.10: Main observables discriminating production mechanisms in 0/1 jet and Dijet categories in arbitrary units. $q\bar{q}H$ denotes VBF production. (top left) $\mathcal{D}_{\text{jet}}$ discriminant combining VBF discrimination variables. (top right) p_T of the four-lepton system. (bottom left) $\Delta\eta$ of the two leading jets. (bottom right) Invariant mass of the two jets.

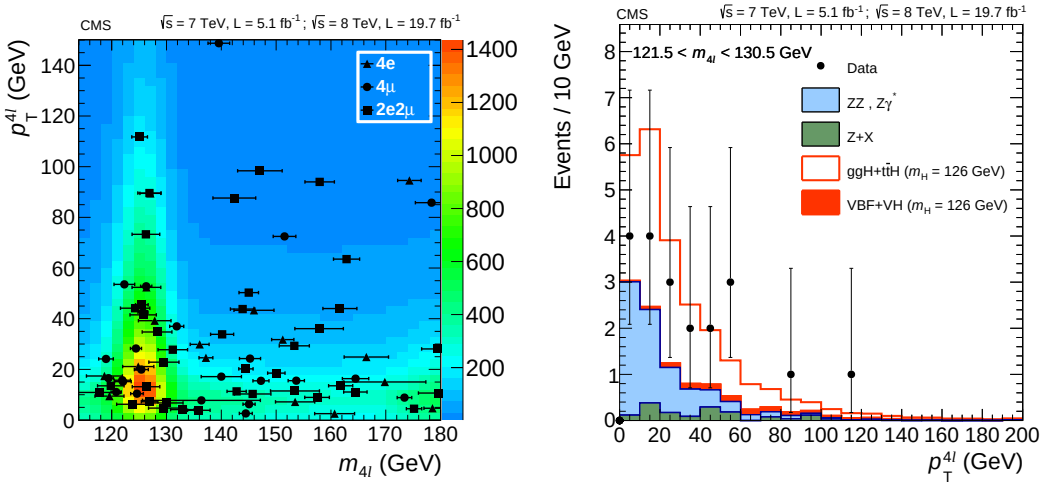

Figure 4.11: (left) Distribution of $p_T^{4\ell}$ versus $m_{4\ell}$ in the low-mass-range 0/1-jet category with colors shown for the expected relative density in linear scale (in arbitrary units) of background plus the Higgs boson signal for $m_H = 126$ GeV. No events are observed for $p_T^{4\ell} > 150$GeV. The points show the data, and horizontal bars represent the measured mass uncertainties. (right) Distribution of $p_T^{4\ell}$ in the 0/1-jet category for events in the mass region $121.5 < m_{4\ell} < 130.5$ GeV. Points with error bars represent the data, shaded histograms represent the backgrounds, and the red histograms represent the signal expectation, broken down by production mechanism. Signal and background histograms are stacked [41].

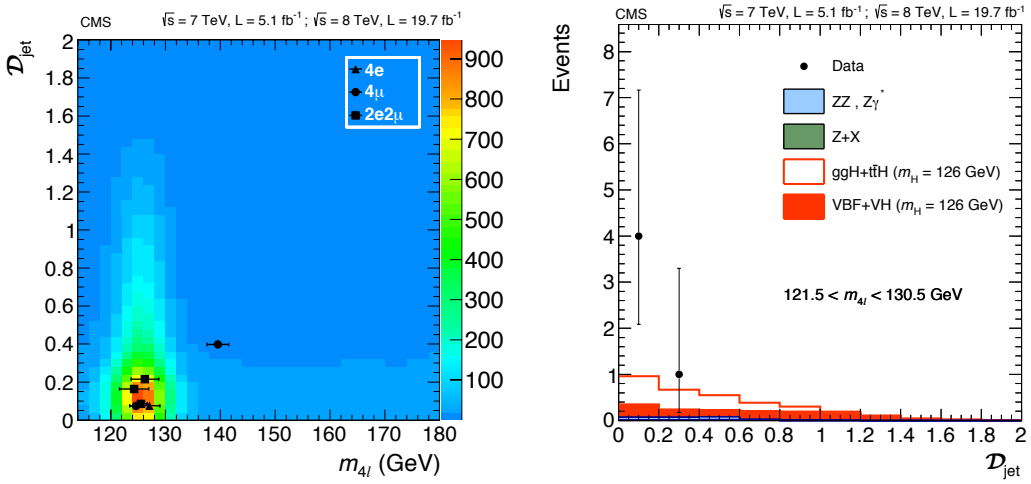

Figure 4.12: (left) Distribution of $\mathcal{D}_{\text{jet}}$ versus $m_{4\ell}$ in the low-mass-range dijet category with colors shown for the expected relative density in linear scale (in arbitrary units) of background plus the Higgs boson signal for $m_H = 126$ GeV. The points show the data and horizontal bars represent the measured mass uncertainties. (right) Distribution of $\mathcal{D}_{\text{jet}}$ in the dijet category for events in the mass region $121.5 < m_{4\ell} < 130.5$ GeV. Points with error bars represent the data, shaded histograms represent the backgrounds, and the red histograms represent the signal expectation, broken down by production mechanism. Signal and background histograms are stacked [41].

4.5 Search Results

In the low mass region of the analysis, an excess of events observed in the 4ℓ mass spectrum localized in a narrow region in the vicinity of 126 GeV. The $m_{4\ell}$ distribution for the sum of the $4e$, $2e2\mu$, and 4μ channels, in the mass region $70 < m_{4\ell} < 180$ GeV, is shown in figure 4.13. Around the observed peak, near $m_{4\ell} = 126$ GeV the expected and observed candidate event yields are given in table 4.2. Split into the categories according to the number of jets in the final state, in addition to the final state leptons, the expected and observed number of collision events is seen in table 4.3.

Experimental systematic uncertainties in the normalization of the signal and the irreducible background processes are evaluated from data for the trigger and the combined lepton reconstruction, identification, and isolation efficiencies. Data is used to validate the absolute momentum scale and resolution resulting in effects of 0.3% ($4e$), 0.1% ($2e2\mu$), and 0.1% (4μ) on the mass scale. The effect of the energy resolution uncertainties is taken into account by introducing a 20% uncertainty in the simulated

Table 4.2: The number of observed candidate events compared to the mean expected background and signal rates for each final state. Uncertainties include statistical and systematic sources. The results are integrated over the mass range from 121.5 to 130.5 GeV and for 7 and 8 TeV data combined [41].

Decay Channel	$4e$	$2e2\mu$	4μ	4ℓ
ZZ background	1.1 ± 0.1	3.2 ± 0.2	2.5 ± 0.2	6.8 ± 0.3
$Z+$jets background	0.8 ± 0.2	1.3 ± 0.3	0.4 ± 0.2	2.6 ± 0.4
All backgrounds	1.9 ± 0.2	4.6 ± 0.4	2.9 ± 0.2	9.4 ± 0.5
$m_H = 125$ GeV	3.0 ± 0.4	7.9 ± 1.0	6.4 ± 0.7	17.3 ± 1.3
$m_H = 126$ GeV	3.4 ± 0.5	9.0 ± 1.1	7.2 ± 0.8	19.6 ± 1.5
Observed	4	13	8	25

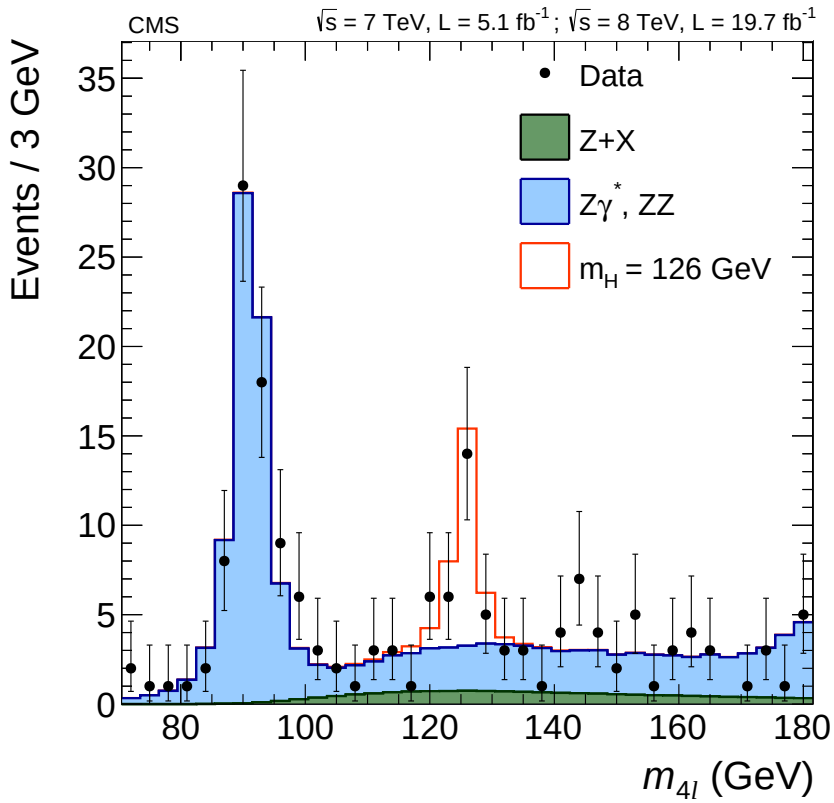

Figure 4.13: Distribution of the four-lepton reconstructed mass for the sum of the $4e$, $2e2\mu$, and 4μ channels for the mass region $70 < m_{4\ell} < 180$ GeV. Points with error bars represent the data, shaded histograms represent the backgrounds, and the unshaded histogram represents the signal expectation for a mass hypothesis of $m_H = 126$ GeV. Signal and the ZZ background are normalized to the SM expectation, the $Z+$jets background to the estimation from data [41].

Table 4.3: The number of observed candidate events compared to the mean expected background and signal rates for the sum of the three final states for each of the two analysis categories. Uncertainties include statistical and systematic sources. The results are integrated over the mass range from 121.5 to 130.5 GeV and for 7 and 8 TeV data combined. The expected signal yield for a SM Higgs boson with $m_H =$ 126 GeV is reported, broken down by the production mechanism [41].

Category	0/1-jet	Dijet
ZZ background	6.4 ± 0.3	0.38 ± 0.02
$Z +$ jets background	2.0 ± 0.3	0.5 ± 0.1
All backgrounds	8.5 ± 0.5	0.9 ± 0.1
$gg \to H$	15.4 ± 1.2	1.6 ± 0.3
$t\bar{t} \to H$	NA	0.08 ± 0.01
VBF	0.70 ± 0.03	0.87 ± 0.07
WH	0.28 ± 0.01	0.21 ± 0.01
ZH	0.21 ± 0.01	0.16 ± 0.01
All signal, $m_H = 126$ GeV	16.6 ± 1.3	3.0 ± 0.4
Observed	20	5

width of the signal mass peak, according to the maximum deviation between data and simulation observed in $Z \to \ell^+\ell^-$ events. Due to low statistics in the control regions systematic uncertainties of 20%, 25%, and 40% are assigned to the normalization of the reducible background for the $4e$, $2e2\mu$, and 4μ final states, respectively. The uncertainty in the luminosity measurement (2.2% at 7 TeV and 2.6% at 8 TeV) [117,118] is also applied to all hypothetical signals and backgrounds.

The theoretical uncertainties in the irreducible background are computed as functions of $m_{4\ell}$, varying both the renormalization and factorization scales and the parton distribution function set. Systematic uncertainties in the Higgs boson cross section and branching fraction are taken from [55,119]. In the 0/1-jet category, an additional background normalization is assigned to account for the differences in Monte Carlo

predictions, while an additional signal systematics are assigned in the dijet category to account for cross section uncertainties in H+jets and VBF production. A summary of the systematic uncertainties in the normalizations of the signal and background processes is given in table 4.4.

Shape uncertainties are applied to all three kinematic distributions used in the analysis. In the $m_{4\ell}$ dimension shape variations are used to account for variations due to the lepton scale and resolution impacts. In the $\mathcal{D}_{\text{bkg}}^{\text{kin}}$ dimension shape variations are used for the uncertainty in the $Z+$jets shape. In the 0/1-jet category the $p_T^{4\ell}$ shape is assigned a systematic to account for the theoretical uncertainty in the distribution. Both theoretical and experimental (jet energy scale and resolution) shape systematics are assigned to the $\mathcal{D}_{\text{jet}}$ distribution.

Table 4.4: Effect of systematic uncertainties on the yields of signal ($m_H = 126$ GeV) and background processes for the 8 TeV data set and 0/1-jet category. Uncertainties appearing on the same line are 100% correlated, with two exceptions: those related to the missing higher orders are not correlated, and those from the α_S + PDF (gg) in $t\bar{t}H$ are 100% anticorrelated. Uncertainties for the 7 TeV data set are similar [41].

Source	Signal ($m_H = 126$ GeV)				Backgrounds		
	$gg \to H$	VBF	VH	$t\bar{t}H$	$q\bar{q} \to ZZ$	$gg \to ZZ$	Z + jets
α_S + PDF (gg)	7.2%	—	—	7.8%	—	7.2%	—
α_S + PDF ($q\bar{q}$)	—	2.7%	3.5%	—	3.4%	—	—
Higher orders	7.5%	0.2%	0.4%, 1.6%	6.6%	2.9%	24%	—
Signal acceptance	2%				—	—	—
BR($H \to ZZ$)	2%				—	—	—
Luminosity	2.6%						—
Electron efficiency	10% ($4e$), 4.3% ($2e2\mu$)						—
Muon efficiency	4.3% (4μ), 2.1% ($2e2\mu$)						—
Control region	—	—	—	—	—	—	40%

4.5.1 Quantifying the observation

To quantify this observation and to account for all the necessary uncertainties in our analysis procedure a three-dimensional unbinned miximim-likelihood fit is performed on the selected collision events. The fits include probability density functions for five signal components (gluon fusion, VBF, WH, ZH, and $t\bar{t}H$ productions) and three background processes ($q\bar{q} \to ZZ$, $gg \to ZZ$, and $Z +$ jets). The normalizations of these components and systematic uncertainties are introduced in the fits as nuisance parameters, assuming log-normal *a priori* probability distributions, and are profiled during the minimization. The shapes of the probability density functions for the event observables are also varied within alternative shapes as experimental or theoretical systematic uncertainties.

The three main questions for the analysis to quantitatively answer are:

(1) What Higgs boson hypotheses can we exclude?

(2) What is the statistical significance of any observed deviation from the SM expectations?

(3) Does the measured cross section times branching ratio match the SM Higgs boson expectation?

The likelihood that is used to address these questions is given in equation (4.5) where m_H, Γ are the Higgs boson mass and width and the discriminants are defined in the previous section. In total, the selected events are split into twelve subcategories based

on the three final states, two data-taking periods (7 & 8 TeV), and two jet categories. The events are examined for 187 hypothetical SM-like Higgs boson masses in a range between 110 and 1000 GeV.

$$\begin{aligned}
\mathcal{L}^{\mu}_{3D} \equiv \quad & \mathcal{L}^{\mu,\,0/1\text{-jet}}_{3D}(m_{4\ell}, \mathcal{D}^{\text{kin}}_{\text{bkg}}, p^{4\ell}_{T}) = \quad \mathcal{P}(m_{4\ell}|m_H, \Gamma)\mathcal{P}(\mathcal{D}^{\text{kin}}_{\text{bkg}}|m_{4\ell})\mathcal{P}(p^{4\ell}_{T}|m_{4\ell}) \quad (4.5)\\
\mathcal{L}^{\mu}_{3D} \equiv \quad & \mathcal{L}^{\mu,\,\text{Dijet}}_{3D}(m_{4\ell}, \mathcal{D}^{\text{kin}}_{\text{bkg}}, \mathcal{D}_{\text{jet}}) = \quad \mathcal{P}(m_{4\ell}|m_H, \Gamma)\mathcal{P}(\mathcal{D}^{\text{kin}}_{\text{bkg}}|m_{4\ell})\mathcal{P}(\mathcal{D}_{\text{jet}}|m_{4\ell})
\end{aligned}$$

Question (1) is answered by fitting the data for exclusion limits as a function of the Higgs boson hypothesis mass m_H. Exclusion limits are determined by fitting the data using the CL_s modified frequentist construction [120,121] to determine the range of masses that are excluded at 95% confidence level (C.L.). By fitting for the *signal strength* ($\mu = \sigma/\sigma_{SM}$), defined as the ratio of the observed and expected SM cross section times branching ratio we can determine these confidence levels.

This is done by defining a test statistic q_μ for μ following [122] as

$$q_\mu = -2\ln\frac{\mathcal{L}^{\mu}_{3D}\,(\text{data}|\mu,\ldots)}{\mathcal{L}^{\mu}_{3D}\,(\text{data}|\hat{\mu},\ldots)} \tag{4.6}$$

where "data" can be either actual data or pseudo-data used to construct sampling distributions, and ... represents the nuisance parameters for the systematic uncertainty treatment. Under this convention $\hat{\mu}$ denotes the estimator for μ. When $\hat{\mu}$ is paired with the estimators for the nuisance parameters they correspond to the global maxi-

mum of the likelihood. We also require that $0 \leq \hat{\mu} \leq \mu$, which provides that the rate of signal events is positive and that the limits obtained are one-sided, respectively.

In addition to evaluating this test statistic on the observed data (q_μ^{obs}), probability distributions are made for two pseudo-datasets. These probability distributions are the signal+background (with the μ from data) hypothesis, $f\left(q_\mu|\mu,\ldots\right)$, and the background only ($\mu = 0$) hypothesis, $f\left(q_\mu|0,\ldots\right)$. From these two distributions, the confidence level that the observed data agrees with either is evaluated. This is done by computing the probability that our observed data has at least q_μ^{obs} for either hypothesis:

$$\begin{aligned} CL_{s+b} &= \int_{q_\mu^{\text{obs}}}^{\infty} f\left(q_\mu|\mu,\ldots\right) \mathrm{d}q_\mu \\ CL_b &= \int_{q_\mu^{\text{obs}}}^{\infty} f\left(q_\mu|0,\ldots\right) \mathrm{d}q_\mu. \end{aligned} \tag{4.7}$$

The 95% C.L. upper limit on μ at each Higgs boson mass hypothesis is found by adjusting μ until $CL_s = CL_{s+b}/CL_b < 0.05$.

When this upper limit gives $\mu > 1$ the data is consistent (within 95%) with both signal+background and background only hypotheses at that mass m_H. The region where the upper limit is at a $\mu < 1$ is the *excluded range* where the data to a 95% C.L. excludes the signal+background hypothesis at that mass.

The result of the 187 fits of the $\mathcal{L}_{3D}^{\mu}$ likelihood are shown in figure 4.14. Here one can see the observed 95% C.L. upper limit on μ for each mass point. Additionally

the median, $\pm 1\sigma$, and $\pm 2\sigma$ expected exclusion for background-only fit are shown as a dashed line, green band, and yellow bands respectively. From this plot, Higgs boson hypotheses with masses $m_H \in$ [115–750 GeV] were expected to be excluded at a 95% C.L. using the four-lepton final state if there is no signal, a large fraction of the 110–1000 GeV analysis range. From the observed number of events, bosons with masses between 114.5–119.0 GeV and 129.5–832.0 GeV can actually be excluded at a 95% C.L. using the four-lepton final state. The unexcluded region between $m_H \in$ 119.0–129.5 GeV corresponds to the excess that is seen in figure 4.13.

Question (2) is answered by computing the local p-value from the $\mathcal{L}^{\mu}_{3D}$ likelihood, this represents the the significance of a local excess relative to the background expectation. The p-value is defined in equation (4.7) as CL_b and we can interpret the p-value as a measure the number of standard deviations that the median background distributions would have to fluctuate in order to 'fake' the signal that we observe. Shown for the full mass range as a function m_H in figure 4.15 (left) and near the peak in figure 4.15 (right) only one significant excess is seen. The minimum of the local p-value is reached around $m_{4\ell} = 125.7$ GeV, and corresponds to a local significance of 6.8σ, consistent with the expected sensitivity of 6.7σ for a SM Higgs boson.

As a cross-check, 1D [$\mathcal{L}^{\mu}_{1D} \equiv \mathcal{L}^{\mu}_{1D}(m_{4\ell})$] and 2D [$\mathcal{L}^{\mu}_{2D} \equiv \mathcal{L}^{\mu}_{2D}(m_{4\ell}, \mathcal{D}^{\text{kin}}_{\text{bkg}})$] models are also studied, as shown in figures 4.15 (left) and (right), resulting in an observed local significance of 5.0σ and 6.9σ, for an expectation of 5.6σ and 6.6σ, respectively. These results are consistent with the 3D model; however, with a systematically lower

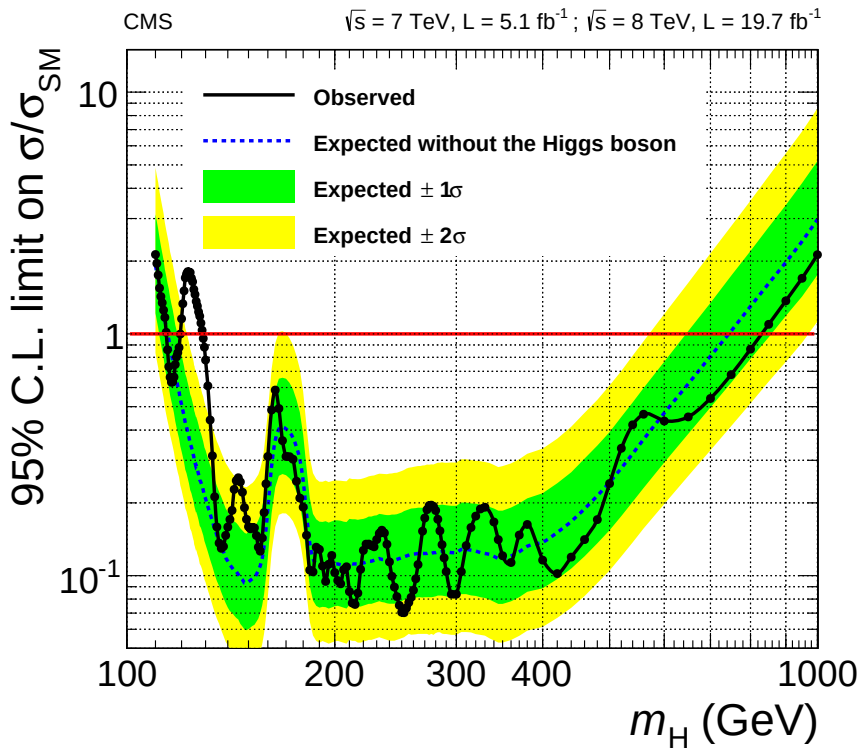

Figure 4.14: Observed and expected 95% C.L. upper limit on the ratio of the production cross section to the SM expectation. The expected $\pm 1\sigma$ and $\pm 2\sigma$ C.L. ranges of expectation for the background-only model are also shown with green and yellow bands, respectively [41].

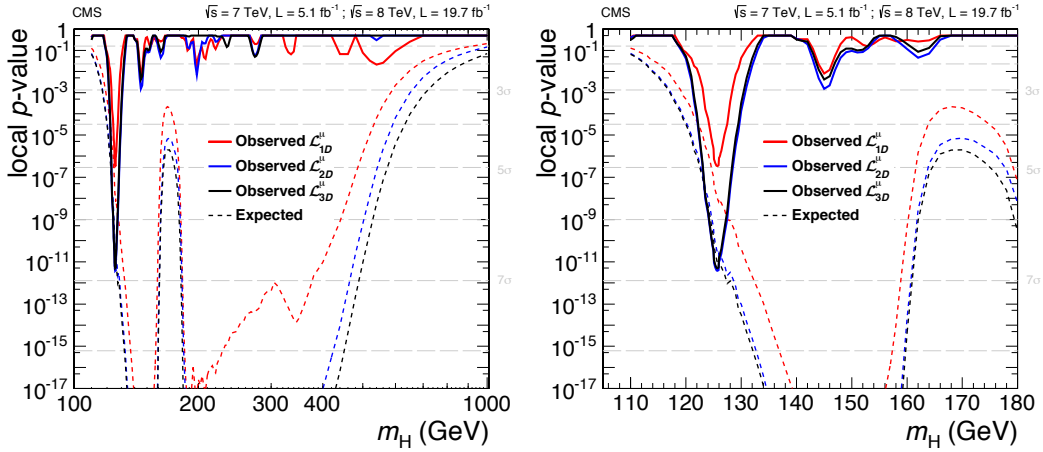

Figure 4.15: (left) Significance of the local excess with respect to the SM background expectation as a function of the Higgs boson mass in the full mass range 110–1000 GeV. Results obtained using the 1D fit, 2D fit, and the nominal 3D fit. (right) Significance of the local excess with respect to the SM background expectation as a function of the Higgs boson mass for the 1D fit, 2D fit, and the nominal 3D fit. Results are shown for the full data sample in the low-mass region only [41].

expected sensitivity to the signal. No other significant deviations with respect to the expectations is found in the mass range 110–1000 GeV. All of these results are consistent with previous CMS and ATLAS publications [67–69], and the second most significant p-value minimum is reached around $m_{4\ell} = 146$ GeV, with a local significance of 2.7σ. This computation does not take into account the look-elsewhere effect [123].

As a validation of this thesis work, plots were also made of the signal to background ratio from each of the likelihood models (1D, 2D, 3D). These distributions are shown in figure 4.16 where the background components are given in the filled histograms, the outline provides the expectation for signal, and the observed events are shown

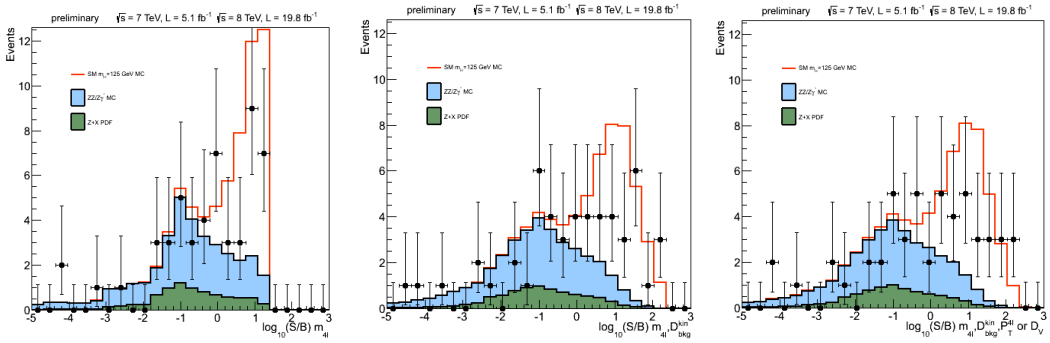

Figure 4.16: Signal to background ratio's for expected and observed events, computed from the 1D (left), 2D (middle), and 3D (right) likelihoods. These plots are made from the $m_{4\ell} \in$ 121.5–130.5 GeV region to study the observed peak. The signal used as the Higgs boson hypothesis corresponds to $m_H = 126$ GeV. These plots are unpublished.

as data points. A Higgs boson hypothesis of $m_H = 126$ GeV is used and the plots are made from the $m_{4\ell} \in$ 121.5–130.5 GeV region to study the observed peak. One can see that with each additional dimension added to the likelihood, the separation between the signal and background increases.

Question (3) asks if the observations we see are consistent with the SM Higgs boson that is predicted. Using the signal strength ($\mu = \sigma/\sigma_{SM}$) we have already defined we can quantify this. If the likelihoods minimize giving $\mu = 1$ then the data is consistent with the Higgs boson cross section times branching ratio. All of these studies are performed at the best fit mass for the Higgs boson using this 4ℓ final state, $m_H = 125.6$ GeV [41]. By fitting the signal expectations we can estimate the sensitivity based on the systematics and statistics currently available. Such a fit of the expected results gives a median expected signal strength of $\mu = 1.00^{+0.31}_{-0.26}$. The fit

of the actual data gives $\mu = 0.93^{+0.26}_{-0.23}(\text{stat.})^{+0.13}_{-0.09}(\text{syst.})$ in very good agreement with the SM Higgs boson expectations. This fit also illuminates that the statistical and systematic uncertainties are of the same order of magnitude, pointing to the need for increased study of systematic uncertainties in the future.

4.5.2 Search for additional Higgs bosons

Using a preliminary unpublished version of the analysis, where a Higgs boson of $m_H = 126$ GeV is added to the background instead of the signal, this thesis work searched the data in the four-lepton final state for additional bosons that might be observed. In BSM models that have more than one Higgs boson the four-lepton final state may see both of these bosons. In regions far away from the new peak the limits shown in figure 4.14 are valid. Near the peak, we can recreate the likelihoods with the new 126 GeV Higgs boson added as a background and perform a search for a second peak (SM-like Higgs boson) near or under the observed one. These results can be seen in figure 4.17 where no additional boson is seen. Additionally, the local significance for a (SM-like Higgs boson) BSM boson is shown and no significant deviation from the background is seen.

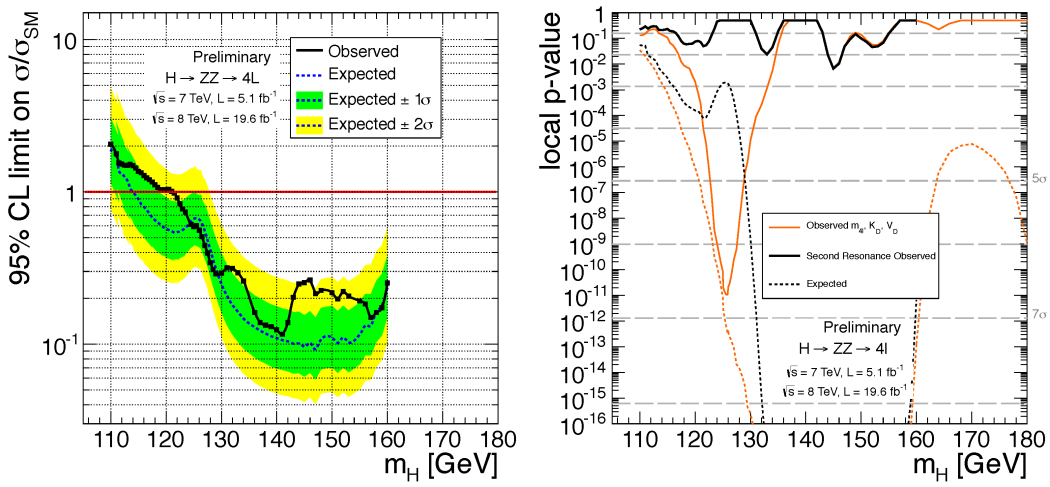

Figure 4.17: (left) Observed and expected 95% C.L. upper limit on the ratio of the production cross section to the SM expectation where a 126 GeV Higgs boson with SM cross section is added as background. The expected $\pm 1\sigma$ and $\pm 2\sigma$ C.L. ranges of expectation for the background-only model are also shown with green and yellow bands, respectively. (right) Significance of the local excess with respect to the SM background + 126 GeV Higgs boson expectation as a function of the BSM Higgs boson mass and compared to the expected and observed significance of the SM Higgs boson. These results were obtained from a preliminary version of the 4ℓ analysis and are unpublished.

4.6 Production Mechanism Results

Looking at the results presented in the previous section, the addition of the $p_T^{4\ell}$ and $\mathcal{D}_{\text{jet}}$ shapes don't add too much to the sensitivity of the search. However these distributions allow the three-dimensional likelihood to be sensitive to the production mechanism of the Higgs boson.

To investigate these quantities, modified definitions of the signal strength are used. These modified quantities measure the ratio of the interesting cross section times branching ratio to the SM expectation for this value. In this way, $\mu_{\text{X}} = 1$ is the standard model, while a μ_{X} inconsistent with 1 would be a sign of non-SM behavior.

The signal strength results are also split into two categories, 0/1-jet and dijet. These results are presented in figure 4.18 (left). The vertical blue line, and green band shows the combined μ fit presented in section 4.5.1, while the black points and red horizontal bars indicate the fit of the signal strength in the two individual categories. The result is $\mu_{0/1\text{-jet}} = 0.83^{+0.31}_{-0.25}$ in the 0/1-jet category and $\mu_{\text{dijet}} = 1.45^{+0.89}_{-0.62}$ in the dijeft category. For each category, the signal strength is consistent with SM expectations within the uncertainties, which are dominated by statistical uncertainties.

To disentangle the production mechanisms of the observed new state, the production mechanisms are split into two families depending on whether the production is through couplings to fermions (gluon fusion, $t\bar{t}H$) or vector bosons (VBF, VH). For $m_H = 126$ GeV, about 55% of the VBF events are expected to be included in the dijet

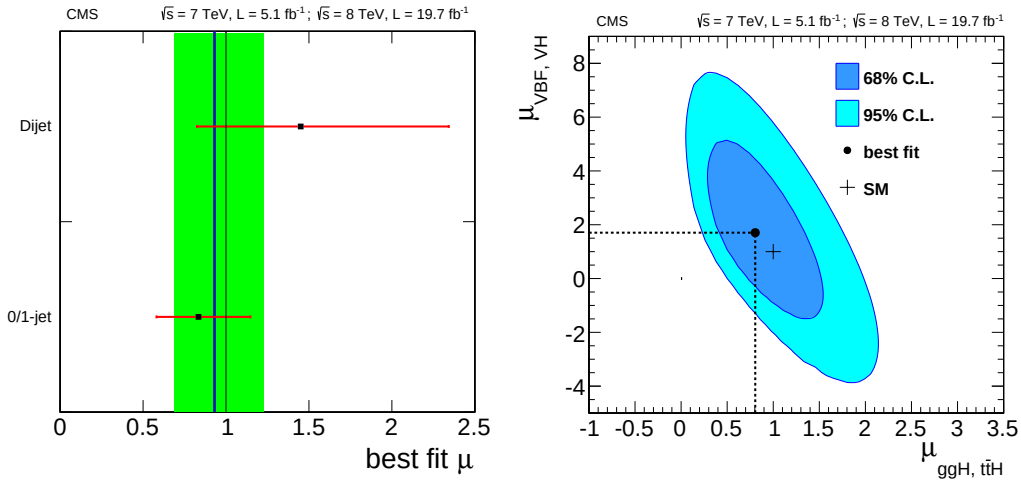

Figure 4.18: (left) Values of μ for the two categories. The vertical line shows the combined μ together with its associated $\pm 1\sigma$ uncertainties, shown as a green band. The horizontal bars indicate the $\pm 1\sigma$ uncertainties in μ for the different categories. The uncertainties include both statistical and systematic sources of uncertainty. (right) Likelihood contours on the signal-strength modifiers associated with fermions ($\mu_{ggH,t\bar{t}H}$) and vector bosons ($\mu_{\mathrm{VBF},VH}$) shown at a 68% and 95% C.L. [41].

category, while only 8% of the gluon fusion events are included in the dijet category. As shown in table 4.3, a fraction of 43% of WH and ZH production contributes to the dijet category. Events that contribute are those in which the vector boson decays hadronically.

Two modified signal-strengths ($\mu_{ggH,t\bar{t}H}$ and $\mu_{\mathrm{VBF},VH}$) are introduced as scale factors for the fermion and vector-boson induced contribution to the expected SM cross section. A fit is performed for the two signal-strength modifiers simultaneously, assuming a mass hypothesis of $m_H = 125.6$ GeV. The likelihood is profiled for all nuisance parameters and 68% and 95% C.L. contours in the ($\mu_{ggH,t\bar{t}H}$, $\mu_{\mathrm{VBF},VH}$) plane are obtained. Figure 4.18 (right) shows the result of the fit leading to the measurements

of $\mu_{ggH,t\bar{t}H}$ and $\mu_{\mathrm{VBF},VH}$. The measured values are consistent with the expectations for the SM Higgs boson, $(\mu_{ggH,t\bar{t}H}, \mu_{\mathrm{VBF},VH}) = (1, 1)$. With the current limited statistics, we cannot establish yet the presence of VBF and VH production, since $\mu_{\mathrm{VBF},VH} = 0$ is also compatible with the data. Since the decay (into ZZ) is vector-boson mediated, it is necessary that such a coupling must exist in the production side and that the SM VBF and SM VH production mechanisms must be present. The fitted value of $\mu_{\mathrm{VBF},VH} = 1.7^{+2.2}_{-2.1}$ is driven partly by the hard $p_T^{4\ell}$ spectrum of the events observed in data when compared to the expectation from the production of the SM Higgs boson (figure 4.11). While the fitted value of $\mu_{ggH,t\bar{t}H} = 0.80^{+0.46}_{-0.36}$ is very close to the SM expectations and dominates the measurement of the total signal strength.

Chapter 5

Total Width of the Higgs Boson

As discussed in section 3.3, using the four lepton final state we can measure the total width of the recently observed Higgs boson using the ratio of on and off mass resonance production. This section presents a brief overview of the analysis followed by a discussion of the 4ℓ and $2\ell 2\nu$ analyses. Then, we will discuss the kinematic variables that are used to boost the sensitivity of the analysis. Finally, we will present the statistical formulation used in this measurement and results obtained. This section follows the publication of this work in [60].

5.1 General Overview of Width Measurement

The discovery of a new boson consistent with the standard model (SM) Higgs boson by the ATLAS and CMS Collaborations was recently reported [67–69]. The mass

of the new boson (m_H) was measured to be near 125 GeV, the spin-parity properties were further studied by both experiments, favoring the scalar, $\mathrm{J^{PC}} = 0^{++}$, hypothesis [41, 116, 124, 125] (discussed in detail in later sections). The measurements were found to be consistent with a single narrow resonance, and an upper limit of 3.4 GeV at a 95% confidence level (C.L.) on its decay width (Γ_H) was reported by the CMS experiment in the four-lepton decay channel [41]. This direct width measurement at the resonance peak is limited by experimental resolution, and is only sensitive to values far larger than the expected width of around 4 MeV for the SM Higgs boson [55, 57].

As discussed in section 3.3, it was recently proposed [59] to constrain the Higgs boson width using its off-shell production and decay to two Z bosons away from the resonance peak [58]. In the dominant gluon fusion production mode the off-shell production cross section is known to be sizable. This arises from an enhancement in the decay amplitude due to the interplay of either the Higgs boson or Z boson going offshell. A further enhancement comes, in gluon fusion production, from the top-quark pair production threshold. The zero-width approximation is inadequate and the ratio of the off-shell cross section above $2m_Z$ to the on-shell signal is of the order of 8% [58, 126]. Further developments to the measurement of the Higgs boson width were proposed in [127, 128].

We present constraints on the Higgs boson width using its off-shell production and decay to Z-boson pairs, in the final states where one Z boson decays to an electron or a muon pair and the other to either an electron or a muon pair, $H \to ZZ \to 4\ell$

(4ℓ channel), or a pair of neutrinos, $H \to ZZ \to 2\ell 2\nu$ ($2\ell 2\nu$ channel). Measuring on the observed Higgs boson signal in the resonance peak region [41] and the signal in the high-mass region leads to constraints on the Higgs boson width Γ_H in the 4ℓ decay channel. The $2\ell 2\nu$ decay channel, which benefits from a higher branching fraction [129,130], is used in the high-mass region to further increase the sensitivity to the Higgs boson width. The analysis is performed for the tree-level HVV coupling of a scalar Higgs boson. The Higgs boson mass is set to the measured value in the 4ℓ decay channel of $m_H = 125.6$ GeV [41] and for reference purposes the default Higgs boson width is set to the corresponding expected value in the SM of $\Gamma_H^{\mathrm{SM}} = 4.15$ MeV [55,57].

5.2 Event Selection, Simulation, & Categorization

The measurement is based on pp collision data collected with the CMS detector at the LHC in 2011, corresponding to an integrated luminosity of 5.1 fb^{-1} at a centre-of-mass energy $\sqrt{s} = 7$ TeV (4ℓ channel), and in 2012, corresponding to an integrated luminosity of 19.7 fb^{-1} at $\sqrt{s} = 8$ TeV (4ℓ and $2\ell 2\nu$ channels). The CMS detector, provides excellent resolution for the measurement of electron and muon transverse momenta (p_T) over a wide range. The 4ℓ signal candidates are selected using well-identified and isolated prompt leptons. The analysis presented here is based on the same event selection as used in the previous section and [41], while the $2\ell 2\nu$ selection

has been published in [129].

The analysis in the 4ℓ channel uses the four-lepton invariant mass distribution as well as a matrix element likelihood (MELA) discriminant to separate the ZZ components originating from gluon- and quark-initiated processes. We define the on-shell signal region as $105.6 < m_{4\ell} < 140.6$ GeV and the off-shell signal region as $m_{4\ell} > 220$ GeV. The final state in the 4ℓ channel is characterized by four well-identified and isolated leptons forming two pairs of opposite-sign and same-flavor leptons consistent with two Z bosons. This channel benefits from a precise reconstruction of all final state leptons and from a very low instrumental background. The event selection and the reducible background evaluation are performed following the methods described in the previous section. After the selection, the 4ℓ data sample is dominated by the quark-initiated $q\bar{q} \to ZZ \to 4\ell$ ($q\bar{q} \to 4\ell$) and $gg \to 4\ell$ productions.

While the details of the $2\ell 2\nu$ analysis are beyond the scope of this thesis. It is summarized here because a large portion of this analysis was to correctly combine the two analyses together, correlating signals, backgrounds and systematic uncertianties. The $2\ell 2\nu$ analysis is performed on the 8 TeV data set only. The final state in the $2\ell 2\nu$ channel is characterized by two oppositely-charged leptons of the same flavor compatible with a Z boson, together with a large $E_{\mathrm{T}}^{\mathrm{miss}}$ from the undetectable neutrinos. We require $E_{\mathrm{T}}^{\mathrm{miss}} > 80$ GeV. The event selection and background estimation is performed as described in [129], with the exception that the jet categories defined in [129] are here grouped into a single category, i.e. the analysis is performed in an inclusive way.

The analysis in the $2\ell 2\nu$ channel relies on the transverse mass distribution m_T,

$$m_T^2 = \left[\sqrt{{p_{\mathrm{T}}^{2\ell}}^2 + {m_{2\ell}}^2} + \sqrt{{E_{\mathrm{T}}^{\mathrm{miss}}}^2 + {m_{2\ell}}^2}\right]^2 - \left[\vec{p}_{\mathrm{T}}^{\,2\ell} + \vec{E}_{\mathrm{T}}^{\mathrm{miss}}\right]^2, \tag{5.1}$$

where $p_{\mathrm{T}}^{2\ell}$ and $m_{2\ell}$ are the measured transverse momentum and invariant mass of the dilepton system, respectively. The missing transverse energy, $E_{\mathrm{T}}^{\mathrm{miss}}$, is defined as the magnitude of the transverse momentum imbalance evaluated as the negative of the vectorial sum of transverse momenta of all the reconstructed particles in the event. In the $2\ell 2\nu$ channel, the off-shell signal region is defined as $m_T > 180$ GeV.

5.2.1 Simulated Data Samples

Simulated Monte Carlo (MC) samples of $gg \to 4\ell$ and $gg \to 2\ell 2\nu$ events are generated at leading order (LO) in perturbative quantum chromodynamics (QCD), including the Higgs boson signal, the continuum background, and the interference contributions using recent versions of two different MC generators, GG2VV 3.1.5 [58,131] and MCFM 6.7 [107], in order to cross-check theoretical inputs. The QCD renormalization and factorization scales are set to $m_{ZZ}/2$ (dynamic scales) and MSTW2008 LO parton distribution functions [132] are used. Higher-order QCD corrections for the gluon fusion signal process are known to an accuracy of next-to-next-to-leading order (NNLO) and next-to-next-to-leading logarithms for the total cross section [55,57] and to NNLO as a function of m_{ZZ} [128]. These correction factors are applied to the

signal, interference, and background processes [128, 133].

Vector boson fusion events are generated with PHANTOM [134]. Off-shell and interference effects with the nonresonant production are included at LO in these simulations. The event yield is normalized to the cross section at NNLO QCD and next-to-leading order (NLO) electroweak (EW) [55, 57] accuracy.

In order to parameterize and validate the distributions of all the components for both gluon fusion and VBF processes, specific simulated samples are also produced that describe only the signal or the continuum background, as well as several scenarios with scaled couplings and width.

In both the 4ℓ and $2\ell 2\nu$ channels the dominant background is $q\bar{q} \to ZZ$. We assume SM production rates for this background, the contribution of which is evaluated by POWHEG simulation at NLO in QCD [103]. Next-to-leading order EW calculations [135, 136] are taken into account as well.

All simulated events undergo parton showering and hadronization using PYTHIA. As is described in the section 4.3, for LO samples, the parton showering settings are tuned to approximately reproduce the ZZ p_T spectrum predicted at NNLO for the Higgs boson production [97]. Generated events are then processed with the detailed CMS detector simulation based on GEANT4 [111, 112] as previously discussed.

5.3 Kinematic Distributions

Here we present the different kinematic distributions that are used in the off resonance peak region. These are used in concert with the three-dimensional fit of the signal peak. For detailed discussion of the analysis of the signal peak see the previous sections. The first two subsections present the two kinematic variables that are used to fit the off resonance region for the 4ℓ final state while the third presents the kinematic variable that is used in the $2\ell 2\mu$ analysis.

5.3.1 Four-lepton mass spectrum

Similar to the $m_{4\ell}$ distribution that is used in the signal peak fit the shape of the $m_{4\ell}$ distribution is key to separating the $q\bar{q} \to ZZ$ background from the $gg \to \ldots \to ZZ$ process that now contains our signal. Figure 5.1 presents the measured $m_{4\ell}$ distribution over the full mass range, $m_{4\ell} > 100$ GeV, together with the expected SM contributions. The $gg \to \ldots \to 4\ell$ contribution is treated as signal in this analysis and is clearly visible in the on-shell signal region and at the Z-boson pair production threshold, above the $q\bar{q} \to 4\ell$ background. The observed distribution is consistent with the expectation from SM processes.

Focusing on the off mass resonance peak region, figure 5.2(left) presents the 4ℓ invariant mass distribution for the off peak signal region ($m_{4\ell} > 220$GeV) while the plot on the (right) presents the same region with an artificial cut on the MELA

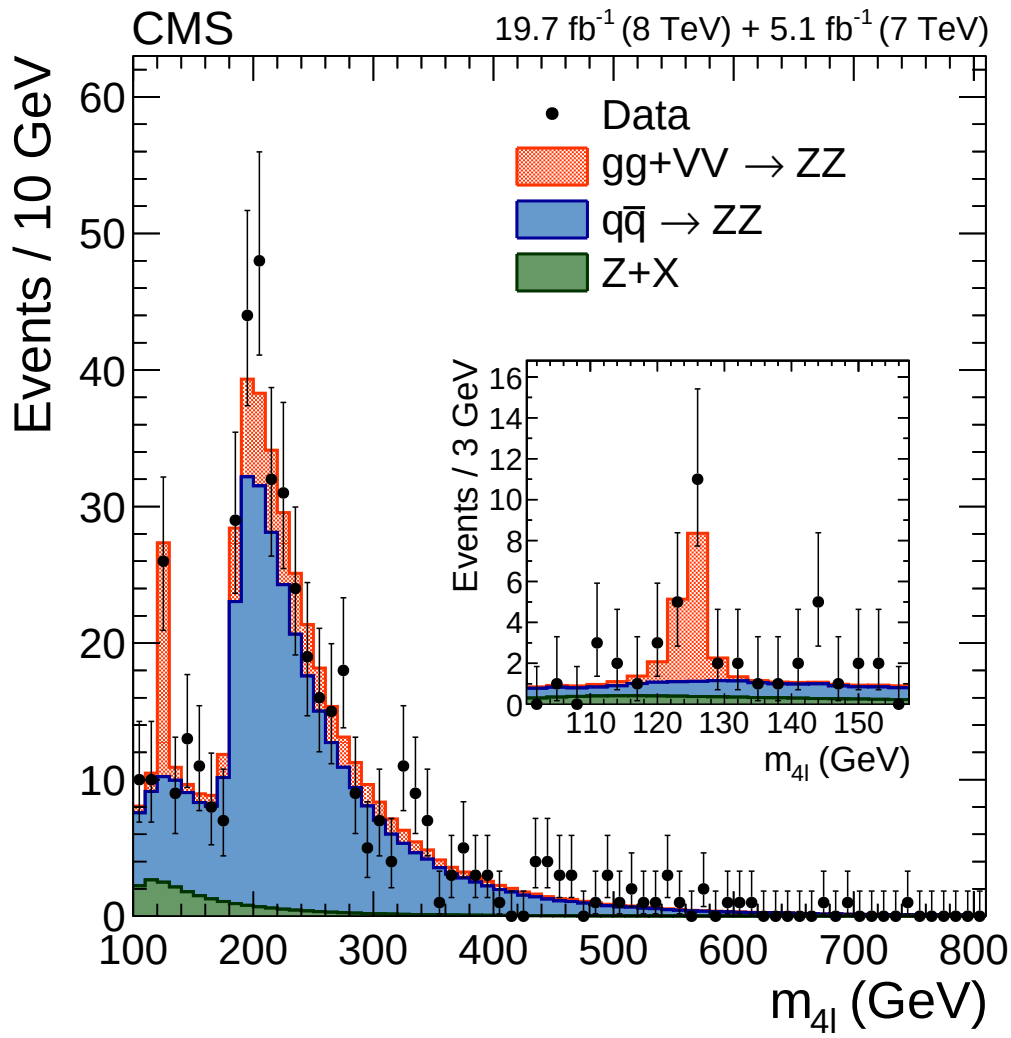

Figure 5.1: Distribution of the four-lepton invariant mass in the range $100 < m_{4\ell} < 800$ GeV. Points represent the data, filled histograms the expected contributions from the reducible (Z+jets) and $q\bar{q}$ backgrounds, and from the sum of the gluon fusion (gg) and vector boson fusion (VV) processes, including the Higgs boson mediated contributions. The inset shows the distribution in the low mass region after a selection requirement on the MELA likelihood discriminant $\mathcal{D}_{\rm bkg}^{\rm kin} > 0.5$ [41]. In this region, the contribution of the $t\bar{t}H$ and VH production processes is added to the dominant gluon fusion and VBF contributions [60].

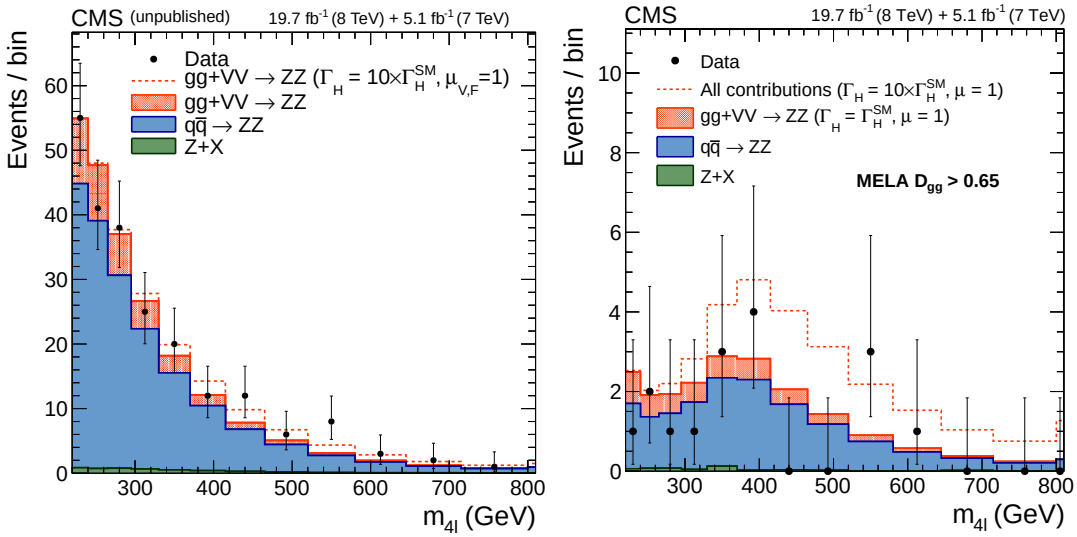

Figure 5.2: Distributions of (left) the four-lepton invariant mass as used in that analysis (right) the four-lepton invariant mass after an artificial selection requirement on the MELA likelihood discriminant $\mathcal{D}_{gg} > 0.65$. Points represent the data, filled histograms the expected contributions from the reducible (Z+X) and $q\bar{q}$ backgrounds, and from the gluon fusion (gg) and vector boson fusion (VV) SM processes (including the Higgs boson mediated contributions). The dashed line corresponds to the total expected yield for a Higgs boson width and a squared product of the couplings scaled by a factor 10 with respect to their SM values. In the top plot, the bin size varies from 20 to 85 GeV and the last bin includes all entries with masses above 800 GeV [60].

discriminant used in this analysis, $\mathcal{D}_{gg} > 0.65$, which will be introduced as the next kinematic distribution used in the analysis. The expected contributions from the $q\bar{q} \to 4\ell$ and reducible backgrounds, as well as for the total gluon fusion (gg) and vector boson fusion (VV) contributions, including the Higgs boson signal, are shown. The expected $\mathrm{m}_{4\ell}$ distributions for the sum of all the processes, with a Higgs boson width $\Gamma_H = 10 \times \Gamma_H^{\mathrm{SM}}$ (while the squared product of the couplings are scaled to keep the on peak cross section equal to the one predicted by the SM) are also shown.

5.3.2 Four-lepton MELA discriminant

In order to enhance the sensitivity to the gg production in the off peak region, a likelihood discriminant $\mathcal{D}_{gg}$ is used, which characterizes the event topology in the 4ℓ centre-of-mass frame using the observables $(m_{Z_1}, m_{Z_2}, \vec{\Omega})$ for a given value of $m_{4\ell}$, where $\vec{\Omega}$ denotes the five angles defined in the previous sections. The discriminant is built from the probabilities $\mathcal{P}^{gg}_{\text{tot}}$ and $\mathcal{P}^{q\bar{q}}_{\text{bkg}}$ for an event to originate from either the $gg \to 4\ell$ or the $q\bar{q} \to 4\ell$ process. We use the matrix element likelihood approach (MELA) [64, 68] for the probability computation using the MCFM matrix elements for both $gg \to 4\ell$ and $q\bar{q} \to 4\ell$ processes. The probability $\mathcal{P}^{gg}_{\text{tot}}$ for the $gg \to 4\ell$ process includes the signal ($\mathcal{P}^{gg}_{\text{sig}}$), the background ($\mathcal{P}^{gg}_{\text{bkg}}$), and their interference ($\mathcal{P}^{gg}_{\text{int}}$), as introduced for the discriminant computation [61]. The discriminant is defined as

$$\mathcal{D}_{gg} = \frac{\mathcal{P}^{gg}_{\text{tot}}}{\mathcal{P}^{gg}_{\text{tot}} + \mathcal{P}^{q\bar{q}}_{\text{bkg}}} = \left[1 + \frac{\mathcal{P}^{q\bar{q}}_{\text{bkg}}}{a \times \mathcal{P}^{gg}_{\text{sig}} + \sqrt{a} \times \mathcal{P}^{gg}_{\text{int}} + \mathcal{P}^{gg}_{\text{bkg}}}\right]^{-1}, \tag{5.2}$$

where the parameter a is the strength of the unknown anomalous gg contribution with respect to the expected SM contribution ($a = 1$). We set $a = 10$ in the definition of $\mathcal{D}_{gg}$ according to the expected sensitivity. Studies show that the expected sensitivity of the analysis is relatively independent of the value of a chosen[1]. It should be stressed that fixing the parameter a to a given value only affects the sensitivity of the analysis.

Individual distributions of the kinematic variables input into the $\mathcal{D}_{gg}$ calculation

[1] Values within a factor of 2.

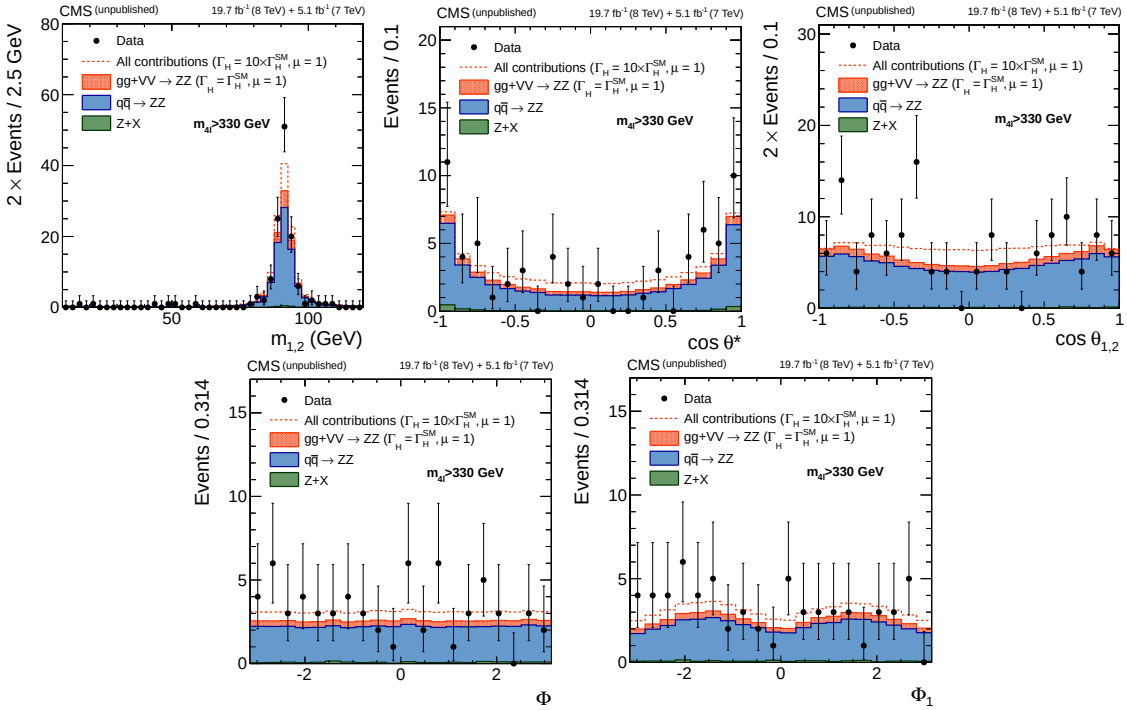

Figure 5.3: Distributions of the kinematic observables used in the $\mathcal{D}_{gg}$ discriminant: m_{Z_i}, $\cos\theta^*$, $\cos\theta_i$, Φ, and Φ_1. The distributions for m_{Z_1} and m_{Z_2}, and $\cos\theta_1$ and $\cos\theta_2$, are summed together. The observed data (points with error bars), the expectations for the SM background and the SM Higgs boson signal (shaded area), and the Higgs boson with a width $\Gamma_H = 10 \times \Gamma_H^{\mathrm{SM}}$ (unfilled area) are shown. The mass of the resonance is taken to be 125.6 GeV and the gg enriched off resonance region is shown ($m_{4\ell} > 330$ GeV) [60].

are shown in figure 5.3 for a gg enriched selection of $m_{4\ell} > 330$ GeV. These are simplified by summing together the m_{Z_1} and m_{Z_2} and $\cos\theta_1$ and $\cos\theta_2$ distributions.

Figure 5.4(left) presents the $\mathcal{D}_{gg}$ distribution for the off peak signal region ($m_{4\ell} >$ 220GeV) while the plot on the (right) presents the same region with the requirement that the mass, $m_{4\ell} > 330$ GeV. The expected contributions from the $q\bar{q} \to 4\ell$ and reducible backgrounds, as well as for the total gluon fusion (gg) and vector boson fusion (VV) contributions, including the Higgs boson signal, are shown. The expected

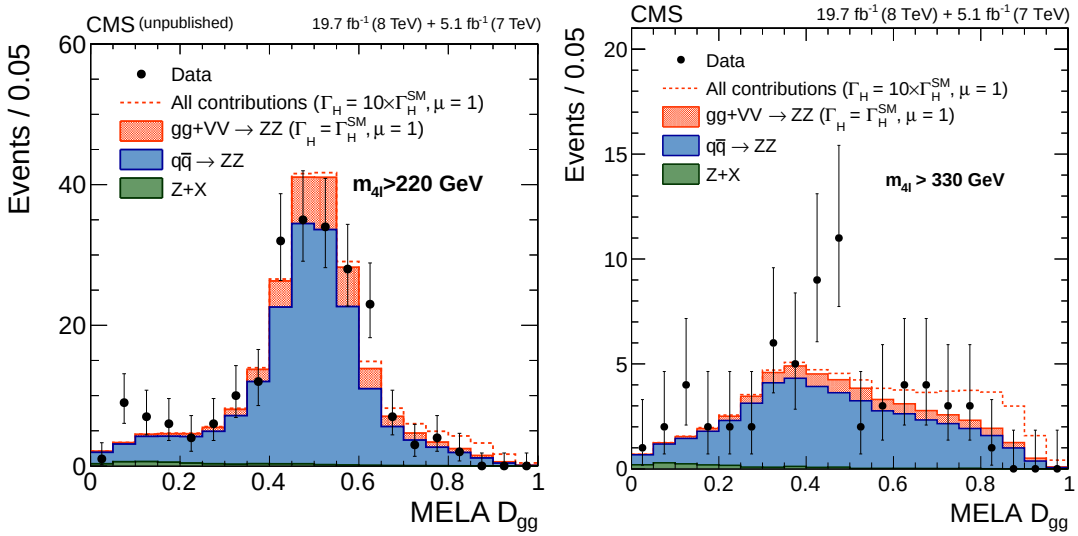

Figure 5.4: (left) Distribution of the MELA discriminant $\mathcal{D}_{gg}$ in full analysis mass range for the sum of the $4e$, 4μ, and $2e2\mu$ channels. Points represent the data, shaded histograms represent the background and dotted-shaded histogram the $gg + VV \rightarrow ZZ$ expectations for a Higgs mass of 125.6 GeV. The expected distributions are presented as stacked histograms. The measurements are presented for of the data collected at $\sqrt{s} = 7$ and 8 TeV in the 220–1600 GeV range. (right) The $\mathcal{D}_{gg}$ likelihood discriminant for $m_{4\ell} > 330$ GeV in the 4ℓ channel. Points represent the data, filled histograms the expected contributions from the reducible (Z+jets) and $q\bar{q}$ backgrounds, and from the gluon fusion (gg) and vector boson fusion (VV) SM processes (including the Higgs boson mediated contributions). The dashed line corresponds to the total expected yield for a Higgs boson width and a squared product of the couplings scaled by a factor 10 with respect to their SM values [60].

kinematic distributions for the sum of all the processes, with a Higgs boson width $\Gamma_H = 10 \times \Gamma_H^{\mathrm{SM}}$ and a relative on peak cross section with respect to the SM cross section equal to unity in both gluon fusion and VBF production modes, are also presented, showing the enhancement arising from the scaling of the squared product of the couplings.

5.3.3 $2\ell 2\nu$ m_T discriminant

The previous section introduced the m_T variable and that is an important distribution used to define the $2\ell 2\nu$ signal region. It is also used as a kinematic distribution used in the final likelihood fit. Shown in figure 5.5, the m_T distribution contains information about the width of the boson observed in the 4ℓ final state. This distribution is used as a one-dimensional shape discriminant in each of the categories in this final state.

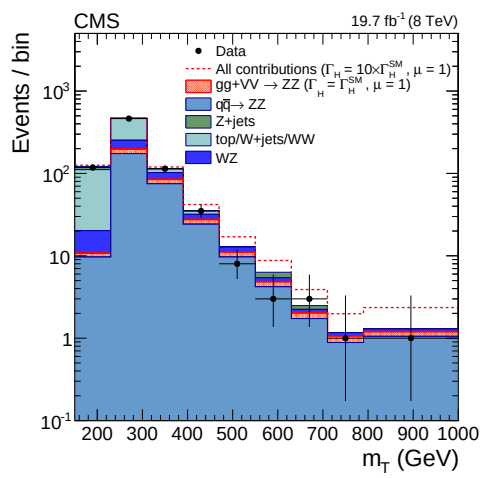

Figure 5.5: Distribution of the transverse mass in the $2\ell 2\nu$ channel. Points represent the data, filled histograms the expected contributions from the backgrounds, and from the gluon fusion (gg) and vector boson fusion (VV) SM processes (including the Higgs-mediated contributions). The dashed line corresponds to the total expected yield for a Higgs boson width and a squared product of the couplings scaled by a factor 10 with respect to their SM values. The bin size varies from 80 to 210 GeV and the last bin includes all entries with transverse masses above 1 TeV [60].

Final state	$4e$	$2e2\mu$	4μ	4ℓ
gg signal (SM)	$0.50\ ^{+0.07}_{-0.06}$	$1.19\ ^{+0.13}_{-0.14}$	$0.70\ ^{+0.09}_{-0.09}$	$2.39\ ^{+0.17}_{-0.19}$
gg background	$7.5\ ^{+1.4}_{-1.1}$	$17.9\ ^{+2.8}_{-3.0}$	$10.8\ ^{+1.6}_{-1.6}$	$36.2\ ^{+3.4}_{-3.6}$
total gg (SM)	$7.1\ ^{+1.2}_{-1.2}$	$17.0\ ^{+2.5}_{-2.6}$	$9.9\ ^{+1.4}_{-1.6}$	$34.0\ ^{+3.0}_{-3.1}$
VBF signal (SM)	0.048	0.115	0.065	0.228
VBF background	0.49	1.17	0.67	2.33
total VBF (SM)	0.43	1.03	0.59	2.05
$q\bar{q}$	36.2 ± 4.0	87.9 ± 6.4	53.0 ± 3.6	177.1 ± 8.1
reducible	2.2 ± 0.5	1.7 ± 0.4	0.6 ± 0.2	4.5 ± 0.7
All contributions (SM)	45.9 ± 4.3	107.6 ± 7.1	$64.1\ ^{+3.9}_{-4.0}$	217.6 ± 9.5
Observed	41	122	60	223

Table 5.1: Expected and observed number of events for $m_{ZZ} \geq 220$ GeV per channel and for the sum of the $4e$, 4μ and $2e2\mu$ channels. The numbers for the gg signal and the total gg contribution are given for $\mu = 1$ (SM). The numbers correspond to the sum of 7 and 8 TeV data. VBF errors are negligible with respect to the corresponding gg sources, so they are not reported [60].

5.4 Off Resonance Width Results

In the 4ℓ final state the number of observed events for the high mass region ($m_{4l} \geq$ 220 GeV) as well as the number of expected events for the signal, the background and the interference contributions are presented on table 5.1. A good agreement is observed between the measured and SM predicted yields. Yields for the low-mass region ($105.6 \geq m_{4l} \geq 140.6$ GeV) are taken from the section 4.5 [41]. As an illustration of the sensitivity of the kinematic variables used in this analysis, a modified set of yields are presented where the selection is modified from the actual analysis to the gg enhanced region, table 5.2

The systematic uncertainties used to estimate the uncertain quantities in this analysis comprise of experimental uncertainties on the signal efficiency and back-

Table 5.2: Expected and observed numbers of events in the 4ℓ and $2\ell 2\nu$ channels in gg-enriched regions, defined by $m_{4\ell} \geq 330$ GeV and $\mathcal{D}_{gg} > 0.65$ (4ℓ), and by $m_T > 350$ GeV and $E_T^{\text{miss}} > 100$ GeV ($2\ell 2\nu$). The numbers of expected events are given separately for the gg and VBF processes, and for a SM Higgs boson ($\Gamma_H = \Gamma_H^{\text{SM}}$) and a Higgs boson width and squared product of the couplings scaled by a factor 10 with respect to their SM values. The unphysical expected contributions for the signal and background components are also reported separately, for the gg and VBF processes. For both processes, the sum of the signal and background components differs from the total due to the negative interferences. The quoted uncertainties include only the systematic sources [60].

		4ℓ	$2\ell 2\nu$
(a)	Total gg ($\Gamma_H = \Gamma_H^{\text{SM}}$)	1.8 ± 0.3	9.6 ± 1.5
	gg Signal component ($\Gamma_H = \Gamma_H^{\text{SM}}$)	1.3 ± 0.2	4.7 ± 0.6
	gg Background component	2.3 ± 0.4	10.8 ± 1.7
(b)	Total gg ($\Gamma_H = 10 \times \Gamma_H^{\text{SM}}$)	9.9 ± 1.2	39.8 ± 5.2
(c)	Total VBF ($\Gamma_H = \Gamma_H^{\text{SM}}$)	0.23 ± 0.01	0.90 ± 0.05
	VBF signal component ($\Gamma_H = \Gamma_H^{\text{SM}}$)	0.11 ± 0.01	0.32 ± 0.02
	VBF background component	0.35 ± 0.02	1.22 ± 0.07
(d)	Total VBF ($\Gamma_H = 10 \times \Gamma_H^{\text{SM}}$)	0.77 ± 0.04	2.40 ± 0.14
(e)	$q\bar{q}$ background	9.3 ± 0.7	47.6 ± 4.0
(f)	Other backgrounds	0.05 ± 0.02	35.1 ± 4.2
(a+c+e+f)	Total expected ($\Gamma_H = \Gamma_H^{\text{SM}}$)	11.4 ± 0.8	93.2 ± 6.0
(b+d+e+f)	Total expected ($\Gamma_H = 10 \times \Gamma_H^{\text{SM}}$)	20.1 ± 1.4	124.9 ± 7.8
	Observed	11	91

ground yield evaluation, as well as uncertainties on the signal and background from theoretical predictions. Since the measurement is performed in wide m_{ZZ} regions, there are sources of systematic uncertainties that only affect the total normalization and others that affect both the normalization and the shape of the observables used in this analysis. In the 4ℓ final state, only the latter type of systematic uncertainty affects the measurement of Γ_H, since normalization uncertainties change the on-shell and off-shell yields by the same amount and do not affect the ratio.

Among the signal uncertainties, experimental systematic uncertainties are evaluated from observed events for the trigger efficiency (1.5%), and combined object reconstruction, identification and isolation efficiencies (3–4% for muons, 5–11% for electrons) [41]. In the $2\ell 2\nu$ final state, the effects of the lepton momentum scale (1–2%) and jet energy scale (1%) are taken into account and propagated to the evaluation of E_T^{miss}. The uncertainty in the b-jet veto (1–3%) is estimated from simulation using correction factors for the b-tagging and b-misidentification efficiencies as measured from the dijet and $t\bar{t}$ decay control samples [137].

Theoretical uncertainties from QCD scales in the $q\bar{q}$ background contribution are within 4–10% depending on m_{ZZ} [41]. An additional uncertainty of 2–6% is included to account for missing higher order contributions with respect to a full NLO QCD and NLO EW evaluation. The systematic uncertainty in the normalization of the reducible backgrounds is evaluated following the methods described in [41, 129]. In the $2\ell 2\nu$ channel, for which these contributions are not negligible at high mass, the estimation

from control samples for the Z+jets and for the sum of the $t\bar{t}$, tW and WW contributions leads to uncertainties of 25% and 15% in the respective background yields. Theoretical uncertainties in the high mass contribution from the gluon-induced processes, which affect both the normalization and the shape, are especially important in this analysis (in particular for the signal and interference contributions that are scaled by large factors). However, these uncertainties partially cancel when measuring simultaneously the yield from the same process in the on-shell signal region. The remaining uncertainties in the QCD renormalization and factorization scales amount to 2–4% from [128]. For the $gg \to ZZ$ continuum background production, we assign a 10% additional uncertainty on the LO–NNLO matching, following [133]. This uncertainty also affects the interference with the signal. The parton distribution function uncertainties are estimated to be about 1% from comparing different calculations of these functions (MSTW2008 [132], CT10 [110], NNPDF2.1 [138]). For the VBF processes, no significant QCD scales or parton distribution function uncertainties are added because they are much smaller than for the gluon fusion processes [55, 57]. In the $2\ell 2\nu$ final state, additional uncertainties on the yield arising from the theoretical description of the parton shower and underlying event are taken into account (6%).

5.4.1 Fitting for Width

We perform a simultaneous unbinned maximum likelihood fit of a signal-plus-background model to the measured distributions in the 4ℓ and $2\ell 2\nu$ channels. In the

4ℓ channel the analysis is performed in the on-shell and off-shell signal regions defined above. In the on-shell region, a three-dimensional distribution $\vec{x} = (m_{4\ell}, \mathcal{D}_{\text{bkg}}^{\text{kin}}, p_T^{4\ell}$ or $\mathcal{D}_{\text{jet}})$ is analyzed, following the analysis presented in section 4.5.

In the off-shell 4ℓ region, a two-dimensional distribution $\vec{x} = (m_{4\ell}, \mathcal{D}_{gg})$ is analyzed. In the $2\ell 2\nu$ channel, only the off-shell Higgs boson production is analyzed, using the $\vec{x} = m_{\text{T}}$ distribution.

The parameterization of probability distributions function of the $gg \to ZZ$ and VBF on resonance processes requires a dedicated approach. It includes three correlated distributions for two processes and their interference. A similar approach had already been developed for the spin-parity studies presented later and we adopt a similar methodology here. The total probability distribution function for the off-shell region includes the interference of two contributions in each production process:

$$\begin{aligned}
\mathcal{P}_{\text{tot}}^{\text{off-shell}} \quad (\vec{x}) \quad &= \left[\mu_{\text{ggH}} \times \left(\Gamma_H/\Gamma_H^{\text{SM}}\right) \times \mathcal{P}_{\text{sig}}^{\text{gg}}(\vec{x}) + \sqrt{\mu_{\text{ggH}} \times \left(\Gamma_H/\Gamma_H^{\text{SM}}\right)} \times \mathcal{P}_{\text{int}}^{\text{gg}}(\vec{x}) + \mathcal{P}_{\text{bkg}}^{\text{gg}}(\vec{x})\right] \\
&+ \quad \left[\mu_{\text{VBF}} \times \left(\Gamma_H/\Gamma_H^{\text{SM}}\right) \times \mathcal{P}_{\text{sig}}^{\text{VBF}}(\vec{x}) + \sqrt{\mu_{\text{VBF}} \times \left(\Gamma_H/\Gamma_H^{\text{SM}}\right)} \times \mathcal{P}_{\text{int}}^{\text{VBF}}(\vec{x}) + \mathcal{P}_{\text{bkg}}^{\text{VBF}}(\vec{x})\right] \\
&+ \quad \mathcal{P}_{\text{bkg}}^{q\bar{q}ZZ}(\vec{x}) + \ldots
\end{aligned} \tag{5.3}$$

where $\mathcal{P}(\vec{x})$ is the normalized probability distribution for each process defined as a template of two observables (or one observable in case of a 1D fit), and $\mu_{\text{ggH}}, \mu_{\text{VBF}}$ are the on peak signal strength modifiers that were defined in section 4.6[2]. The list of background processes is extended beyond those quoted depending on the final state (Z+jets, top, W+jets, WW, WZ). The parameter $(\Gamma_H/\Gamma_H^{\text{SM}})$ is the scale factor

[2]While the $t\bar{t}H$ and VH components are negligible away from the resonance peak.

which modifies the observed width with respect to the Γ_H^{SM} value used in the reference parameterization.

The three parameters Γ_H, μ_{ggH}, and μ_{VBF} are left unconstrained in the fit. The μ_{ggH} and μ_{VBF} fitted values are found to be almost identical to those found in section 4.6, and can be seen in table 5.3.

Parameter	Γ_H (MeV)	μ_{ggH}	μ_{VBF}	μ
On-peak only	-	$0.81^{+0.49}_{-0.38}$	$1.72^{+2.21}_{-1.72}$	$0.94^{+0.30}_{-0.25}$
$m_{4\ell}$ and $\mathcal{D}_{gg}$ (Γ_H fixed)	-	$0.78^{+0.46}_{-0.36}$	$1.65^{+2.11}_{-1.65}$	$0.91^{+0.28}_{-0.24}$
$m_{4\ell}$ and $\mathcal{D}_{gg}$	$1.9^{+11.7}_{-1.9}$	$0.79^{+0.47}_{-0.36}$	$1.67^{+2.15}_{-1.67}$	$0.92^{+0.29}_{-0.24}$

Table 5.3: Detailed fit results on the signal strength in several combinations from the 4ℓ final state on and off resonance peak. The μ column represents alternative fits where we make the hypothesis $\mu_{\mathrm{VBF}} = \mu_{\mathrm{ggH}} = \mu$ (only two parameters floated) [139].

We first present the one-dimensional fit results from the 4ℓ final state only. The fit results are shown as scans of the negative log-likelihood, $-2\Delta \ln \mathcal{L}$, as a function of Γ_H. These are obtained using the measured mass distribution only and the $\mathcal{D}_{gg}$ discriminant only, where the two-dimensional templates are projected into a one-dimensional analysis over the respective dimension. Figure 5.6 (left) shows the width constraint from the $m_{4\ell}$ distribution alone. While figure 5.6 (right) shows the width constraint from the $\mathcal{D}_{gg}$ discriminant only. The results of these one-dimensional fits, and the expectations are summarized along with the final fit results in table 5.4

The full fit results are shown in figure 5.7 and summarized in table 5.4. Combining the 4ℓ and $2\ell 2\nu$ channels a limit is observed (expected) on the total width of $\Gamma_H <$ 22 MeV (33 MeV) at a 95% C.L., which is 5.4 (8.0) times the expected value in the SM.

Figure 5.6: Fit results for (left) the 1D analysis using $m_{4\ell}$, and (right) 1D analysis using $\mathcal{D}_{gg}$, observed limits from data (solid) and expected (dashed) results are both shown [60].

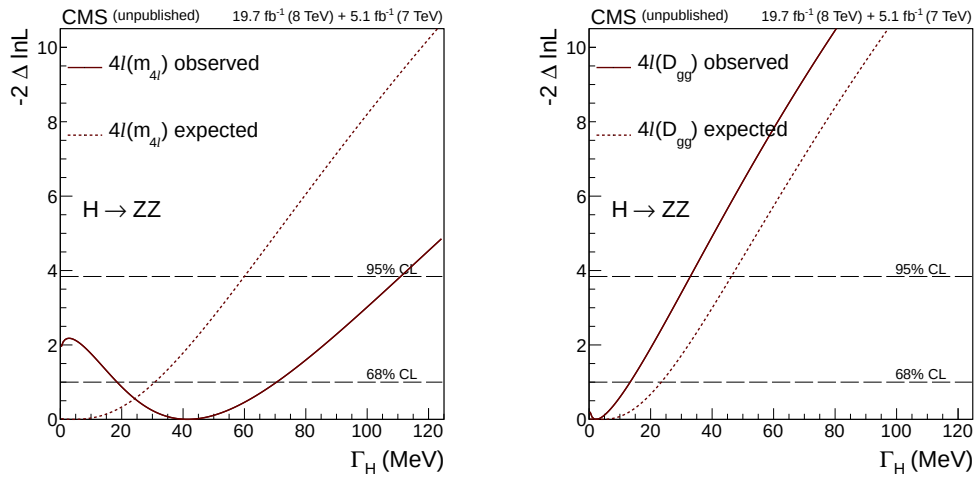

The best fit value and 68% C.L. interval correspond to $\Gamma_H = 1.8^{+7.7}_{-1.8}$ MeV. The result of the 4ℓ analysis alone is an observed (expected) limit of $\Gamma_H < 33$ MeV (42 MeV) at a 95% C.L., which is 8.0 (10.1) times the SM value, and the result of the analysis combining the 4ℓ on-shell and $2\ell 2\nu$ off-shell regions is $\Gamma_H < 33$ MeV (44 MeV) at a 95% C.L., which is 8.1 (10.6) times the SM value. The best fit values and 68% C.L. intervals are $\Gamma_H = 1.9^{+11.7}_{-1.9}$ MeV and $\Gamma_H = 1.8^{+12.4}_{-1.8}$ MeV for the 4ℓ analysis and for the analysis combining the 4ℓ on-shell and $2\ell 2\nu$ off-shell regions, respectively.

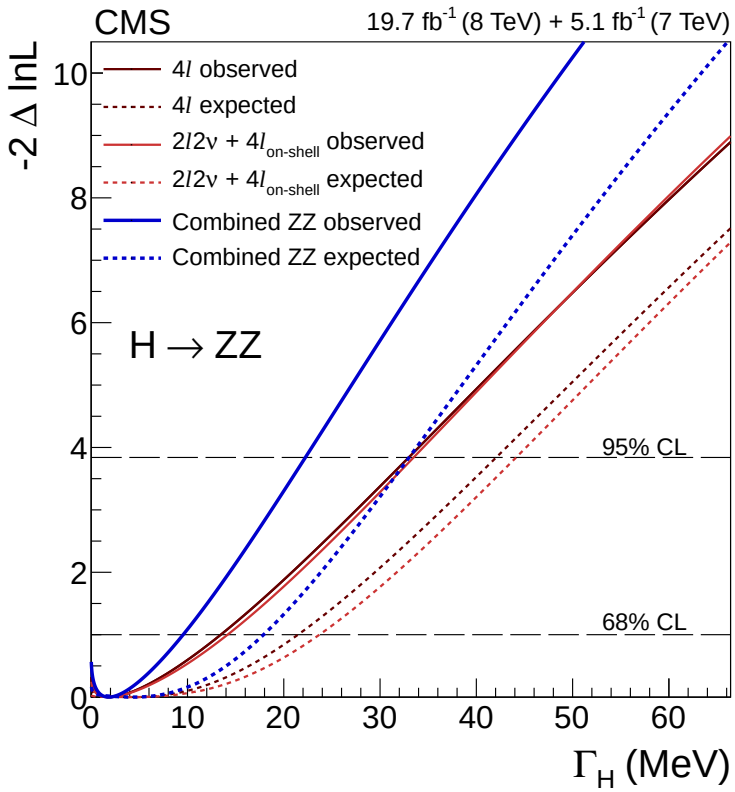

Figure 5.7: Scan of the negative log-likelihood, $-2\Delta \ln \mathcal{L}$, as a function of Γ_H for the combined fit of the 4ℓ and $2\ell 2\nu$ channels (blue thick lines), for the 4ℓ channel alone in the off-shell and on-shell regions (dark red lines), and for the $2\ell 2\nu$ channel in the off-shell region and 4ℓ channel in the on-shell region (light red lines). The solid lines represent the observed values, the dotted lines the expected values [60].

Table 5.4: Expected and observed 95% C.L. limits for the 4ℓ and $2\ell 2\nu$ analyses and for the combination. For the observed results, the central fitted values and the 68% C.L. total uncertainties are also quoted. The Higgs mass is set to the measured value in the 4ℓ decay channel of 125.6 GeV [60, 139].

Analysis	Observed/ Expected	95% C.L. limit on Γ_{H} (MeV)	95% C.L. limit on $\Gamma_{\mathrm{H}}/\Gamma_{\mathrm{H}}^{\mathrm{SM}}$
$4\ell\,(m_{4\ell})$	Expected	57.7	13.9
	Observed	112.5	27.1
$4\ell\,(\mathcal{D}_{gg})$	Expected	44.3	10.7
	Observed	33.0	8.0
$4\ell\,(m_{4\ell}, \mathcal{D}_{gg})$	Expected	42	10.1
	Observed	33	8.0
$4\ell_{\mathrm{on-shell}} + 2\ell 2\nu$	Expected	44	10.6
	Observed	33	8.1
Combined	Expected	33	8.0
	Observed	22	5.4

Chapter 6

Spin & Parity of a Higgs Boson

In this thesis, an extensive study of the spin-parity properties of the Higgs boson and of the tensor structure of its interactions with electroweak gauge bosons is presented using the $H \to ZZ/Z\gamma^*/\gamma^*\gamma^* \to 4\ell$ decay channel, where the interference between the three intermediate states is included. The study focuses on testing for the presence of anomalous effects in HZZ and interactions under spin-zero, -one, and -two hypotheses, but also probes the $Z\gamma^*$ or $\gamma^*\gamma^* \to 4\ell$ terms. Constraints are set on eight anomalous coupling contributions to the HVV interactions[1], where V is a gauge vector boson, under the spin-zero assumption of the Higgs boson. Extending the exclusion of 0^- (2^+_m) hypotheses in favor of the SM and the original measurement of the f_{a3} parameter [116], this thesis work developed the most comprehensive study of the spin-parity and tensor structure measurements to date. These studies have

[1]Eleven when the HWW extensions are included.

been published in [41, 62]. A summary of the measurements performed is outlined first. The second section gives a summary of the simulated data and four lepton event selection is discussed. Then a description of the analysis techniques is given in the third section. Finally, the results of this analysis are presented. The results section first presents spin-one and spin-two exclusions followed by the study of spin-zero HVV couplings.

6.1 Summary of Spin/Parity Measurements

The analysis is based on theoretical and phenomenological studies that describe the couplings of a Higgs-like boson to two gauge bosons presented in section 3.4. They provide techniques and ideas for measuring the spin and CP properties of a particle interacting with vector bosons [61, 63, 64]. Much of the relevant phenomenological introduction has already been presented, but here we summarize the tests performed.

For spin-zero tests are performed to measure the effective cross section fractions f_i^{VV}. The analysis studies the effects of the anomalous couplings listed in table 6.1, where the mass of the hypothesized boson is assumed to be $m_H = 125.6$ GeV [41]. When testing the HZZ terms, the superscript is dropped from the fraction definition to be consistent with earlier publications. In this table WW terms are listed, they are also tested following the phenomenological work in this thesis and as part of the analysis presented in [62], but are beyond the scope of this thesis. Given the

Table 6.1: List of anomalous HVV couplings considered in the measurements assuming a spin-zero Higgs boson. The definition of the effective fractions is discussed in the text and the translation constant is given in each case. The effective cross sections correspond to the processes $H \to VV \to 2e2\mu$ and the Higgs boson mass $m_H = 125.6$ GeV using the JHUGen [61,63,64] calculation. The cross-section ratios for the $HZ\gamma$ and $H\gamma\gamma$ couplings include the requirement $\sqrt{q_V^2} \geq 4$ GeV [62].

Interaction	Anomalous Coupling	Coupling Phase	Effective Fraction	Translation Constant
HZZ	Λ_1	$\phi_{\Lambda 1}$	$f_{\Lambda 1}$	$\sigma_1/\tilde{\sigma}_{\Lambda 1} = 1.45 \times 10^4 \mathrm{TeV}^{-4}$
	a_2	ϕ_{a2}	f_{a2}	$\sigma_1/\sigma_2 = 2.68$
	a_3	ϕ_{a3}	f_{a3}	$\sigma_1/\sigma_3 = 6.36$
HWW	Λ_1^{WW}	$\phi_{\Lambda 1}^{WW}$	$f_{\Lambda 1}^{WW}$	$\sigma_1^{WW}/\tilde{\sigma}_{\Lambda 1}^{WW} = 1.87 \times 10^4 \mathrm{TeV}^{-4}$
	a_2^{WW}	ϕ_{a2}^{WW}	f_{a2}^{WW}	$\sigma_1^{WW}/\sigma_2^{WW} = 1.25$
	a_3^{WW}	ϕ_{a3}^{WW}	f_{a3}^{WW}	$\sigma_1^{WW}/\sigma_3^{WW} = 3.01$
$HZ\gamma$	$\Lambda_1^{Z\gamma}$	$\phi_{\Lambda 1}^{Z\gamma}$	$f_{\Lambda 1}^{Z\gamma}$	$\sigma_1'/\tilde{\sigma}_{\Lambda 1}^{Z\gamma} = 5.76 \times 10^3 \mathrm{TeV}^{-4}$
	$a_2^{Z\gamma}$	$\phi_{a2}^{Z\gamma}$	$f_{a2}^{Z\gamma}$	$\sigma_1'/\sigma_2^{Z\gamma} = 22.4 \times 10^{-4}$
	$a_3^{Z\gamma}$	$\phi_{a3}^{Z\gamma}$	$f_{a3}^{Z\gamma}$	$\sigma_1'/\sigma_3^{Z\gamma} = 27.2 \times 10^{-4}$
$H\gamma\gamma$	$a_2^{\gamma\gamma}$	$\phi_{a2}^{\gamma\gamma}$	$f_{a2}^{\gamma\gamma}$	$\sigma_1'/\sigma_2^{\gamma\gamma} = 28.2 \times 10^{-4}$
	$a_3^{\gamma\gamma}$	$\phi_{a3}^{\gamma\gamma}$	$f_{a3}^{\gamma\gamma}$	$\sigma_1'/\sigma_3^{\gamma\gamma} = 28.8 \times 10^{-4}$

measured values of the effective fractions, it is possible to extract the ratios of the coupling constants a_i/a_1, the scale of BSM physics Λ_1, or the ratios of the $Z\gamma^*$ ($\gamma^*\gamma^*$) cross sections with respect to the SM predictions in any parameterization.

For spin-one, using the continuous parameter f_{b2} that we have previously defined in equation (3.7), the 4ℓ final state can test if the observed boson is consistent with any mixture of 1^+ and 1^- (including pure states) hypotheses. CMS performed this test using both production-independent and production-dependent methods, using this fraction to test if the data favor the SM Higgs boson scalar hypothesis or some particular mixture of the vector and pseudovector states.

As already introduced in section 3.4.3, we test if a new observation is more consistent with the SM Higgs boson or a spin-two boson as well. We study the ten

spin-two scenarios listed in table 3.1, under the assumption that the production is via gluon-gluon fusion, $q\bar{q}$ production, or without any assumption about the production mechanism.

6.2 Simulated Data and 4ℓ Selection

To study the $H \to VV \to 4\ell$ decay, the analysis follows that presented in section 4. Collision events are selected with at least four identified and isolated electrons or muons. A $V \to \ell^+\ell^-$ candidate originating from a pair of leptons of the same flavor and opposite charge is required. The $\ell^+\ell^-$ pair with an invariant mass, m_{Z_1}, nearest to the nominal Z boson mass is retained and is denoted Z_1 if it is in the range $40 \leq m_{Z_1} \leq 120$ GeV. A second $\ell^+\ell^-$ pair, denoted Z_2, is required to have $12 \leq m_{Z_2} \leq 120$ GeV. If more than one Z_2 candidate satisfies all criteria, the pair of leptons with the highest scalar p_T sum is chosen. At least one lepton should have $p_T \geq 20$ GeV, another one $p_T \geq 10$ GeV and any oppositely charged pair of leptons among the four selected must satisfy $m_{\ell\ell} \geq 4$ GeV. Events are restricted to a window around the observed 125.6 GeV resonance, $105.6 \leq m_{4\ell} \leq 140.6$ GeV.

After the selection, the dominant background for $H \to VV \to 4\ell$ originates from the $q\bar{q} \to ZZ/Z\gamma^*$ and $gg \to ZZ/Z\gamma^*$ processes and is evaluated from simulation, following [41] while the $Z +$ jets background is evaluated as previously described [41]. The number of estimated background and signal events, and the number of

observed candidates after the final selection in data in the narrow mass region around 125.6 GeV is given in table 6.2.

Table 6.2: Number of background (Bkg.) and signal events expected in the SM, and number of observed candidates, for the $H \to VV \to 4\ell$ analysis after the final selection in the mass region $105.6 < m_{4\ell} < 140.6$ GeV. The signal and ZZ background are estimated from MC simulation, while the $Z+$jets background is estimated from data. Only systematic uncertainties are quoted [62].

Channel	$4e$		4μ		$2e2\mu$	
Energy	7 TeV	8 TeV	7 TeV	8 TeV	7 TeV	8 TeV
$q\bar{q} \to ZZ$	0.84 ± 0.10	2.94 ± 0.33	1.80 ± 0.11	7.65 ± 0.49	2.24 ± 0.28	8.86 ± 0.68
$gg \to ZZ$	0.03 ± 0.01	0.20 ± 0.05	0.06 ± 0.02	0.41 ± 0.10	0.07 ± 0.02	0.50 ± 0.13
$Z+$jets	0.62 ± 0.14	2.77 ± 0.62	0.22 ± 0.09	1.19 ± 0.48	1.06 ± 0.29	4.29 ± 1.10
Bkg.	1.49 ± 0.17	5.91 ± 0.71	2.08 ± 0.14	9.25 ± 0.69	3.37 ± 0.40	13.65 ± 1.30
Signal	0.70 ± 0.11	3.09 ± 0.47	1.24 ± 0.14	5.95 ± 0.71	1.67 ± 0.26	7.68 ± 0.98
Observed	1	9	3	15	6	16

6.2.1 Simulated Data

The simulation of the signal process is essential for the study of anomalous couplings in HVV interactions, and all the relevant Monte Carlo (MC) samples are generated following the description in section 3.4. A dedicated simulation program, JHUGen 4.8.1 [61,63,64], is used to describe anomalous couplings in the production and decay to two vector bosons of spin-zero, spin-one, and spin-two resonances in hadron-hadron collisions, including all the models listed in tables 3.1 and 6.1. For the spin-zero and spin-one studies, interference effects are included by generating mixed samples produced with either of the different tensor structures shown in equations (3.4) and (3.6).

For gluon fusion production of a spin-zero state, the kinematics of the Higgs boson decay products and of an associated jet are not affected by the anomalous Hgg interactions, and therefore the next-to-leading-order (NLO) QCD effects are introduced in production with the SM couplings through the POWHEG [83–85] event generator. It is also found that the NLO QCD effects that are relevant for this analysis are well approximated with the combination of leading-order (LO) QCD matrix elements and parton showering [61], in which case JHUGen is adopted for the simulation of anomalous interactions in all other production processes where it is important to model the correlations between production and the kinematics of the final state particles, such as in VBF and VH production of a spin-zero state, $q\bar{q} \to X$ production of a spin-one state, and $q\bar{q}$ and $gg \to X$ production of a spin-two state.

In all cases, the decays $H/X \to ZZ$ / $Z\gamma^*$ / $\gamma^*\gamma^* \to 4\ell$ are simulated with JHUGEN, including all spin correlations in the production and decay processes and interference effects between all contributing amplitudes.

To increase the number of events in the simulated samples for each hypothesis studied, the MELA package [61,63,64,68] is adopted to apply weights to events in any $H \to VV \to 4\ell$ spin-zero sample to model any other spin-zero sample. The same re-weighting technique has also been used in the study of the $q\bar{q}$ and $gg \to ZZ/Z\gamma^*$ backgrounds.

As discussed in previous sections all MC samples are interfaced with PYTHIA 6.4.24 [86] for parton showering and further processing through a dedicated simulation of the CMS detector based on GEANT4 [111]. The simulation includes overlapping pp interactions (pileup) matching the distribution of the number of interactions per LHC beam crossing observed in data. Most of the background event simulation is also unchanged from the analyses presented in the previous sections.

6.3 MELA Spin/Parity Analysis

6.3.1 Observables in the $H \to VV \to 4\ell$ analysis

In the new bosons center-of-mass frame, the four-momenta of the $H \to 4\ell$ decay products carry eight independent degrees of freedom, which fully describe the kinematic configuration of a four-lepton system, except for an arbitrary rotation around

the beam axis. These can be conveniently expressed in terms of the five angles $\vec{\Omega} \equiv (\theta^*, \Phi_1, \theta_1, \theta_2, \Phi)$ previously defined in figure 4.6, the invariant masses of the dilepton pairs, m_1 and m_2, and of the four-lepton system, $m_{4\ell}$. The boost of the H boson system in the laboratory frame, expressed as p_T and rapidity, depends on the production mechanism and generally carries some but limited discrimination power between either signal or background hypotheses originating from different production processes. These observables are not used in the analysis to remove the dependence of the results on the production model. For the same reason, information about particles produced in association with H boson is not used either. This approach differs from the study including production information in section 4, where such observables were used to investigate the production mechanisms of the Higgs boson.

The distributions of the eight kinematic observables $(m_1, m_2, m_{4\ell}, \vec{\Omega})$ in data, as well as the expectations for the SM background, the Higgs boson signal, and some characteristic alternative spin-zero scenarios are shown in figure 6.1. All distributions in figure 6.1, with the exception of the $m_{4\ell}$ distribution, are presented using events in the $m_{4\ell}$ range of 121.5–130.5 GeV to enhance the signal purity. The observables with their correlations are used in the analysis to establish the consistency of the spin and parity quantum numbers and tensor structure of interactions with respect to the SM predictions. As previously discussed, these observables also permit a further discrimination of signal from background, increasing the signal sensitivity and reducing the statistical uncertainty in the measurements.

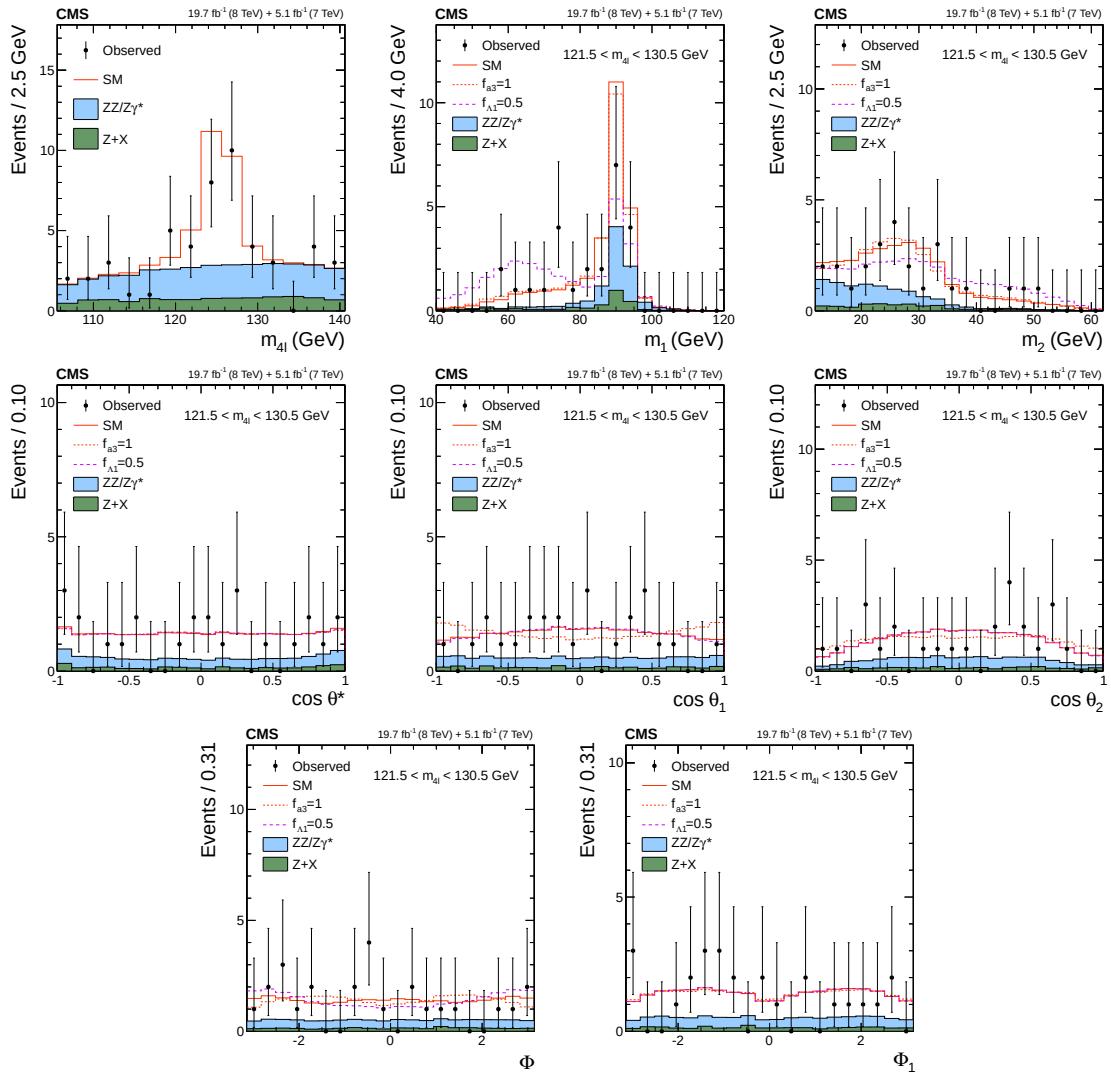

Figure 6.1: Distributions of the eight kinematic observables used in the $H \to VV \to 4\ell$ analysis: $m_{4\ell}$, m_1, m_2, $\cos\theta^*$, $\cos\theta_1$, $\cos\theta_2$, Φ, and Φ_1. The observed data (points with error bars), the expectations for the SM background (shaded areas), the SM Higgs boson signal (open areas under the solid histogram), and the alternative spin-zero resonances (open areas under the dashed histograms) are shown, as indicated in the legend. The mass of the resonance is taken to be 125.6 GeV and the SM cross section is used. All distributions, with the exception of $m_{4\ell}$, are presented with the requirement $121.5 < m_{4\ell} < 130.5$ GeV [62].

6.3.2 MELA Observables

A comprehensive analysis of the kinematics of the decay of a Higgs boson could include up to eight observables, as discussed above. In such an analysis, it is required to have a parameterization of the multidimensional distributions as a function of the parameters of interest. However, it becomes challenging to describe all the correlations of the observables and detector effects. It is possible to reduce the number of observables and keep the necessary information using the matrix element likelihood approach (MELA). In this approach, the kinematic information is stored in a discriminant designed for the separation of either background, the alternative signal components, or interference between those components. The parameterization of up to three observables can be performed with full simulation or data from the control regions.

The use of kinematic discriminants in Higgs boson studies was introduced in previous CMS analyses [41, 60, 68, 116, 140] and feasibility studies [61, 64], and here it is extended both to a number of new models and to new techniques. The construction of the kinematic discriminants follows the probabilities for an event to be signal or background. These probabilities are calculated using the LO matrix elements as a function of angular and mass observables. In this way, the kinematic information, which fully characterizes the 4ℓ event topology of a certain process in its center-of-mass frame, is condensed to a reduced number of observables.

The kinematic discriminants used in this study are computed using the MELA

package [61, 63, 64, 68], which provides the full set of processes studied in this paper and uses JHUGEN matrix elements for the signal, gg or $q\bar{q} \to X \to ZZ$ / $Z\gamma^*$ / $\gamma^*\gamma^* \to 4\ell$, and MCFM matrix elements for the background, gg or $q\bar{q} \to ZZ$ / $Z\gamma^*$ / $\gamma^*\gamma^*$ / $Z \to 4\ell$. This library of processes is also consistent with the MC simulation used, and also includes other production and decay mechanisms. Within the MELA framework, an analytic parameterization of the matrix elements for signal [63,64] and background [141] was adopted in the previous CMS analyses, reported in [68,69,116]. The above matrix element calculations are validated against each other and other methods for a subset of processes implemented in common.

Given several signal hypotheses defined for gg or $q\bar{q} \to X \to ZZ$ / $Z\gamma^*$ / $\gamma^*\gamma^* \to 4\ell$, and the main background hypotheses gg or $q\bar{q} \to ZZ$ / $Z\gamma^*$ / $\gamma^*\gamma^*$ / $Z \to 4\ell$, the effective probabilities are defined for each event using a set of kinematic observables $(m_1, m_2, m_{4\ell}, \vec{\Omega})$

$$
\begin{aligned}
\mathcal{P}_{\mathrm{SM}} =& \mathcal{P}^{\mathrm{kin}}_{\mathrm{SM}}(m_1, m_2, \vec{\Omega}|m_{4\ell}) \times \mathcal{P}^{\mathrm{mass}}_{\mathrm{sig}}(m_{4\ell}|m_H), \\
\mathcal{P}_{J^P} =& \mathcal{P}^{\mathrm{kin}}_{J^P}(m_1, m_2, \vec{\Omega}|m_{4\ell}) \times \mathcal{P}^{\mathrm{mass}}_{\mathrm{sig}}(m_{4\ell}|m_H), \\
\mathcal{P}^{\mathrm{int}}_{J^P} =& \left(\mathcal{P}^{\mathrm{kin}}_{\mathrm{SM+J^P}}(m_1, m_2, \vec{\Omega}|m_{4\ell}) - \mathcal{P}^{\mathrm{kin}}_{J^P}(m_1, m_2, \vec{\Omega}|m_{4\ell}) - \mathcal{P}^{\mathrm{kin}}_{\mathrm{SM}}(m_1, m_2, \vec{\Omega}|m_{4\ell})\right), \\
\mathcal{P}^{\mathrm{int}\perp}_{J^P} =& \left(\mathcal{P}^{\mathrm{kin}}_{\mathrm{SM+J^P}\perp}(m_1, m_2, \vec{\Omega}|m_{4\ell}) - \mathcal{P}^{\mathrm{kin}}_{J^P}(m_1, m_2, \vec{\Omega}|m_{4\ell}) - \mathcal{P}^{\mathrm{kin}}_{\mathrm{SM}}(m_1, m_2, \vec{\Omega}|m_{4\ell})\right), \\
\mathcal{P}_{q\bar{q}ZZ} =& \mathcal{P}^{\mathrm{kin}}_{q\bar{q}ZZ}(m_1, m_2, \vec{\Omega}|m_{4\ell}) \times \mathcal{P}^{\mathrm{mass}}_{q\bar{q}ZZ}(m_{4\ell}), \\
\mathcal{P}_{ggZZ} =& \mathcal{P}^{\mathrm{kin}}_{ggZZ}(m_1, m_2, \vec{\Omega}|m_{4\ell}) \times \mathcal{P}^{\mathrm{mass}}_{ggZZ}(m_{4\ell}),
\end{aligned}
\tag{6.1}
$$

where $\mathcal{P}^{\text{kin}}(m_1, m_2, \vec{\Omega}|m_H) = |A(m_1, m_2, \vec{\Omega}|m_H)|^2$ are the probabilities computed from the LO matrix elements and generally are not normalized. The variable $\mathcal{P}^{\text{mass}}(m_{4\ell}|m_H)$ is the probability as a function of the four-lepton reconstructed mass and is calculated using the $m_{4\ell}$ parameterization described previously in section 4 including the $m_H = 125.6$ GeV hypothesis for signal. The probabilities $\mathcal{P}^{\text{int}}_{J^P}$ parameterize interference between contributions from the SM and anomalous couplings, where J^P refers to a spin-zero tensor structure of interest, and are allowed to have both positive and negative values. In the calculation of the mixed amplitude used for $\mathcal{P}^{\text{kin}}_{\text{SM+J}^{\text{P}}}$, the same coupling strengths are used as in the individual probabilities $\mathcal{P}^{\text{kin}}_{\text{SM}}$ and $\mathcal{P}^{\text{kin}}_{J^P}$, and these couplings are required to provide equal cross sections for the two individual processes. The quantity $\mathcal{P}^{\text{int}\perp}_{J^P}$ is constructed in the same way as $\mathcal{P}^{\text{int}}_{J^P}$ except that the phase of the J^P amplitude is changed by $\pi/2$. The matrix element calculations in equation (6.1) are also used for the re-weighting of simulated samples.

Several kinematic discriminants are constructed for the main signal and background processes from the set of probabilities described above

$$\begin{aligned}
\mathcal{D}_{\text{bkg}} =& \frac{\mathcal{P}_{\text{SM}}}{\mathcal{P}_{\text{SM}} + \mathcal{P}_{q\bar{q}ZZ}} = \left[1 + \frac{\mathcal{P}^{\text{kin}}_{q\bar{q}ZZ}(m_1, m_2, \vec{\Omega}|m_{4\ell}) \times \mathcal{P}^{\text{mass}}_{q\bar{q}ZZ}(m_{4\ell})}{\mathcal{P}^{\text{kin}}_{\text{SM}}(m_1, m_2, \vec{\Omega}|m_{4\ell}) \times \mathcal{P}^{\text{mass}}_{\text{sig}}(m_{4\ell}|m_H)}\right]^{-1}, \\
\mathcal{D}_{J^P} =& \frac{\mathcal{P}_{\text{SM}}}{\mathcal{P}_{\text{SM}} + \mathcal{P}_{J^P}} = \left[1 + \frac{\mathcal{P}^{\text{kin}}_{J^P}(m_1, m_2, \vec{\Omega}|m_{4\ell})}{\mathcal{P}^{\text{kin}}_{\text{SM}}(m_1, m_2, \vec{\Omega}|m_{4\ell})}\right]^{-1}, \\
\mathcal{D}_{\text{int}} =& \frac{\mathcal{P}^{\text{int}}_{J^P}(m_1, m_2, \vec{\Omega}|m_{4\ell})}{\mathcal{P}^{\text{kin}}_{\text{SM}} + \mathcal{P}^{\text{kin}}_{J^P}}.
\end{aligned} \tag{6.2}$$

The observable $\mathcal{D}_{\text{bkg}}$ is used to separate signal from $q\bar{q} \to ZZ$, $gg \to ZZ$, and

$Z+$ jets backgrounds, using the $m_{4\ell}$ probability in addition to $\mathcal{P}^{\text{kin}}$. The discriminant $\mathcal{D}_{J^P}$ is created to separate the SM signal from an alternative J^P state. The discriminant $\mathcal{D}_{\text{int}}$ is created to isolate interference between the SM and anomalous coupling contributions. Since the analysis is designed to probe small anomalous couplings, interference between different anomalous contributions is a negligible effect and dedicated discriminants for those contributions are not considered. The variable $\mathcal{D}_{\text{int}}$ is denoted as $\mathcal{D}_{CP}$ for interference between the a_1 and a_3 contributions because it is sensitive to CP violation [61].

To remove the dependence of the spin-one and spin-two discriminants on the production model, the probability $\mathcal{P}^{\text{kin}}$ is averaged over the two production angles $\cos\theta^*$ and Φ_1, defined in figure 4.6, or equivalently the signal matrix element squared is averaged over the polarization of the resonance [61]. The production independent discriminants are defined as

$$\begin{aligned}
\mathcal{D}^{\text{dec}}_{\text{bkg}} &= \left[1 + \frac{\frac{1}{4\pi}\int \mathrm{d}\Phi_1 \mathrm{d}\cos\theta^* \mathcal{P}^{\text{kin}}_{q\bar{q}ZZ}(m_1, m_2, \vec{\Omega}|m_{4\ell}) \times \mathcal{P}^{\text{mass}}_{q\bar{q}ZZ}(m_{4\ell})}{\mathcal{P}^{\text{kin}}_{\text{SM}}(m_1, m_2, \vec{\Omega}|m_{4\ell}) \times \mathcal{P}^{\text{mass}}_{\text{sig}}(m_{4\ell}|m_H)}\right]^{-1}, \\
\mathcal{D}^{\text{dec}}_{J^P} &= \left[1 + \frac{\frac{1}{4\pi}\int \mathrm{d}\Phi_1 \mathrm{d}\cos\theta^* \mathcal{P}^{\text{kin}}_{J^P}(m_1, m_2, \vec{\Omega}|m_{4\ell})}{\mathcal{P}^{\text{kin}}_{\text{SM}}(m_1, m_2, \vec{\Omega}|m_{4\ell})}\right]^{-1}.
\end{aligned} \tag{6.3}$$

The decay kinematics of a spin-zero resonance are already independent of the production mechanism, due to the lack of spin correlations for any spin-zero particle. The small differences in the distributions of the production-independent discriminants with the different production mechanisms are due to detector acceptance effects and

Table 6.3: List of observables $\vec{x}$ used in the analysis of the HVV couplings. The J^P notation for spin-two refers to the ten scenarios defined in table 3.1 [62].

Measurement	Observables $\vec{x}$		
$f_{\Lambda 1}$	$\mathcal{D}_{\text{bkg}}$	$\mathcal{D}_{\Lambda 1}$	
f_{a2}	$\mathcal{D}_{\text{bkg}}$	$\mathcal{D}_{0h+}$	$\mathcal{D}_{\text{int}}$
f_{a3}	$\mathcal{D}_{\text{bkg}}$	$\mathcal{D}_{0-}$	$\mathcal{D}_{CP}$
$f_{\Lambda 1}^{Z\gamma}$	$\mathcal{D}_{\text{bkg}}$	$\mathcal{D}_{\Lambda 1}^{Z\gamma}$	$\mathcal{D}_{\text{int}}^{Z\gamma,\Lambda 1}$
$f_{a2}^{Z\gamma}$	$\mathcal{D}_{\text{bkg}}$	$\mathcal{D}_{a2}^{Z\gamma}$	$\mathcal{D}_{\text{int}}^{Z\gamma}$
$f_{a3}^{Z\gamma}$	$\mathcal{D}_{\text{bkg}}$	$\mathcal{D}_{a3}^{Z\gamma}$	$\mathcal{D}_{CP}^{Z\gamma}$
$f_{a2}^{\gamma\gamma}$	$\mathcal{D}_{\text{bkg}}$	$\mathcal{D}_{a2}^{\gamma\gamma}$	$\mathcal{D}_{\text{int}}^{\gamma\gamma}$
$f_{a3}^{\gamma\gamma}$	$\mathcal{D}_{\text{bkg}}$	$\mathcal{D}_{a3}^{\gamma\gamma}$	$\mathcal{D}_{CP}^{\gamma\gamma}$
spin-one $q\bar{q} \to X(f_{b2}) \to ZZ$	$\mathcal{D}_{\text{bkg}}$	$\mathcal{D}_{1-}$	$\mathcal{D}_{1+}$
spin-one decay $X(f_{b2}) \to ZZ$	$\mathcal{D}_{\text{bkg}}^{\text{dec}}$	$\mathcal{D}_{1-}^{\text{dec}}$	$\mathcal{D}_{1+}^{\text{dec}}$
spin-two $q\bar{q} \to X(J^P) \to ZZ$	$\mathcal{D}_{\text{bkg}}$	$\mathcal{D}_{J^P}^{q\bar{q}}$	
spin-two $gg \to X(J^P) \to ZZ$	$\mathcal{D}_{\text{bkg}}$	$\mathcal{D}_{J^P}^{gg}$	
spin-two decay $X(J^P) \to ZZ$	$\mathcal{D}_{\text{bkg}}^{\text{dec}}$	$\mathcal{D}_{J^P}^{\text{dec}}$	

are treated as systematic uncertainties.

A complete list of all the discriminants used in the analysis is presented in table 6.3. Some examples of the distributions as expected from simulation and as observed in data can be seen in figure 6.2 for all the discriminants used in the study of the spin-zero HZZ couplings. A complete list of the measurements performed and observables used is discussed in sections 6.4.2 and 6.4.3.

From figure 6.2 the special role of $\mathcal{D}_{CP}$ can be observed. For the SM background processes, including a SM Higgs boson, this distribution is completely symmetric. However, if the observed boson contains a CP-violating component it will appear as an asymmetry in this distribution as shown by the $f_{a3} = 0.5$ example in the figure.

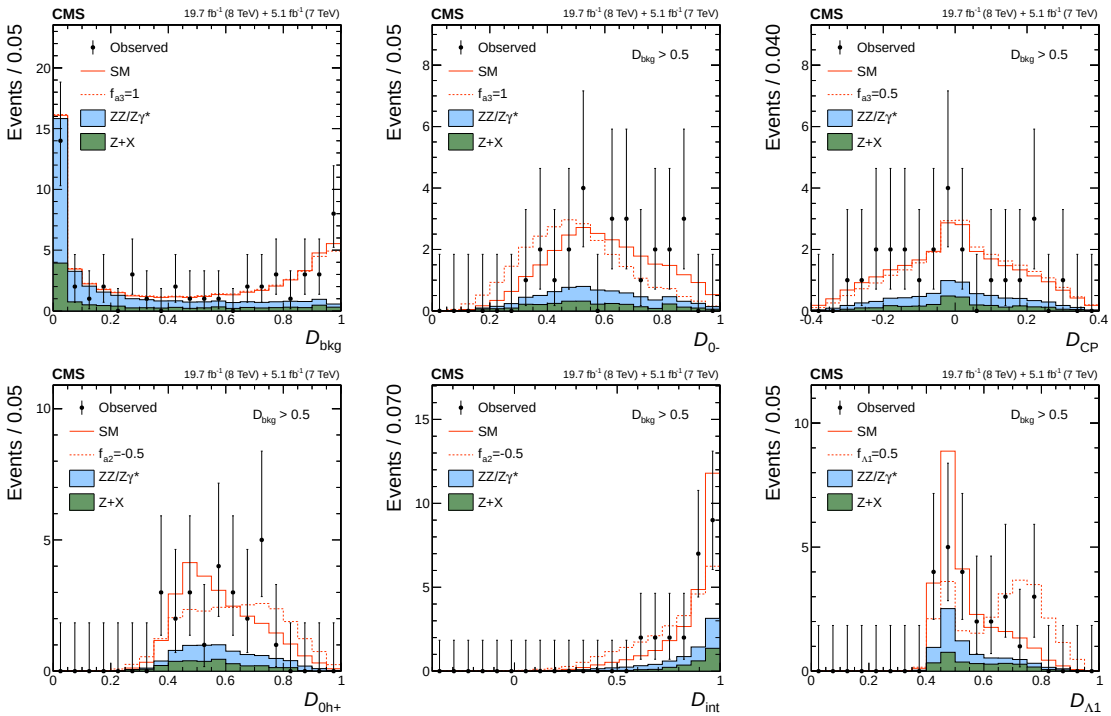

Figure 6.2: Distributions of the kinematic discriminants for the observed data (points with error bars), the expectations for the SM background (shaded areas), the SM Higgs boson signal (open areas under the solid histogram), and the alternative spin-zero resonances (open areas under the dashed histograms) are shown, as indicated in the legend. The mass of the resonance is taken to be 125.6 GeV and the SM cross section is used. Top row from left to right: $\mathcal{D}_{\rm bkg}$, $\mathcal{D}_{0-}$, $\mathcal{D}_{CP}$; bottom row from left to right: $\mathcal{D}_{0h+}$, $\mathcal{D}_{\rm int}$, $\mathcal{D}_{\Lambda 1}$. All distributions, with the exception of $\mathcal{D}_{\rm bkg}$, are shown with the requirement $\mathcal{D}_{\rm bkg} > 0.5$ to enhance signal purity [62].

6.4 Spin/Parity Results

Before giving a detailed description of the likelihoods that are created for this analysis and discussion of the results, we want to mention that the systematic uncertainties in the $H \to VV \to 4\ell$ channel are generally the same as the ones investigated in section 4.5 and [41].

6.4.1 Likelihood fits

The goal of the analysis is to determine if a set of anomalous coupling parameters $\vec{\zeta}$, defined both for the production and decay of a resonance with either spin zero, one, or two is consistent, for a given set of observables $\vec{x}$, with the data. The coupling parameters $\vec{\zeta}$ are discussed in detail in section 6.1. They are summarized in equations (3.4), (3.6) and table 6.1 for spin-zero, in equations (3.6) and (3.7) for spin-one, and in equation (3.8) and table 3.1 for spin-two. The observables $\vec{x}_i$ are defined for each event i, listed in table 6.3, and discussed above. The extended likelihood function is defined for N candidate events as

$$\mathcal{L} = \exp\Big(- n_{\text{sig}} - \sum_k n^k_{\text{bkg}}\Big) \prod_i^N \Big(n_{\text{sig}} \times \mathcal{P}_{\text{sig}}(\vec{x}_i;\ \vec{\zeta}) + \sum_k n^k_{\text{bkg}} \times \mathcal{P}^k_{\text{bkg}}(\vec{x}_i)\Big), \quad (6.4)$$

where n_{sig} is the number of signal events and n^k_{bkg} is the number of background events of type k. The probability density functions $\mathcal{P}_{\text{sig}}(\vec{x}_i; \vec{\zeta})$ and $\mathcal{P}^k_{\text{bkg}}(\vec{x}_i)$ are defined for the signal and background, respectively.

There are several event categories, such as $4e$, 4μ, and $2e2\mu$ in the $H \to VV \to 4\ell$ analysis, or the 7 TeV and 8 TeV categories, and several types of background. The total signal yield n_{sig} is a free parameter to avoid using the overall signal event yield as a part of the discrimination between alternative hypotheses. However, when several channels are used in the same decay, such as $H \to VV \to 4e$, $2e2\mu$, and 4μ, the relative yields between the channels depend on the terms considered in the tensor structure due to interference effects in the presence of identical leptons, and this information is exploited in the analysis.

The probability density functions $\mathcal{P}_{\text{sig}}$ and $\mathcal{P}^{k}_{\text{bkg}}$ are described as histograms (templates) with two or three dimensions, see observables in table 6.3, and with up to 50 bins in each dimension. The number of dimensions used is limited by the number of simulated events that can be generated or the number of events in the control regions in data. However, an optimal construction of observables allows for the retention of all the necessary information for the measurement with up to three observables. The templates are built for signal and background from histograms of fully simulated events, or from control regions in data. In the $H \to VV \to 4\ell$ analyses, statistical fluctuations are removed using a smoothing algorithm [142, 143].

The signal probability density functions $\mathcal{P}_{\text{sig}}$ depend on the coupling parameters $\vec{\zeta}$. For spin-zero, these functions can be parameterized as a linear combination of the terms originating from the SM-like and anomalous amplitudes and their interfer-

ence [61]

$$\mathcal{P}_{\text{sig}}\left(\vec{x};\vec{\zeta}=\{f_{ai},\phi_{ai}\}\right)=\left(1-\sum_{ai}f_{ai}\right)\mathcal{P}_{0^+}\left(\vec{x}\right)+\sum_{ai}f_{ai}\,\mathcal{P}_{ai}\left(\vec{x}\right)$$
$$+\sum_{ai}\sqrt{f_{ai}\left(1-\sum_{aj}f_{aj}\right)}\,\mathcal{P}^{\text{int}}_{ai,0^+}\left(\vec{x};\phi_{ai}\right)$$
$$+\sum_{ai<aj}\sqrt{f_{ai}f_{aj}}\,\mathcal{P}^{\text{int}}_{ai,aj}\left(\vec{x};\phi_{ai}-\phi_{aj}\right),\quad(6.5)$$

where $\mathcal{P}_{ai}$ is the probability of a pure a_i term and $\mathcal{P}^{\text{int}}_{ai,aj}$ describes the interference between the two terms, each parameterized as a template. Each term in equation (6.5) is extracted from the dedicated simulation and includes proper normalization.

The likelihood in equation (6.4) can be used in two different ways. In both approaches, the likelihood is maximized with respect to the nuisance parameters which include the signal yield and constrained parameters describing the systematic uncertainties discussed above.

In one approach the likelihood is maximized to estimate the values of anomalous couplings, and the confidence intervals are determined from profile likelihood scans of the respective parameters. This is used for the measurement of anomalous couplings under the spin-zero hypothesis. The allowed 68% and 95% C.L. intervals are defined using the profile likelihood function, $-2\,\Delta\ln\mathcal{L}=1.00$ and 3.84, for which exact coverage is expected in the asymptotic limit [144].

The other approach is used to distinguish an alternative spin-one or spin-two

signal hypothesis from the SM Higgs boson. In this case, the test statistic $q = -2\ln(\mathcal{L}_{J^P}/\mathcal{L}_{0^+})$ is defined using the ratio of signal plus background likelihoods for two signal hypotheses. To quantify the consistency of the observed test statistic q_{obs} with respect to the SM Higgs boson hypothesis (0^+), the probability $p = P(q \leq q_{\text{obs}} \,|\, 0^+ + \text{bkg})$ is assessed and converted into a number of standard deviations via the Gaussian one-sided tail integral. The consistency of the observed data with the alternative signal hypothesis (J^P) is assessed from $P(q \geq q_{\text{obs}} \,|\, J^P + \text{bkg})$. The CL_s criterion [120, 121], defined as $CL_s = P(q \geq q_{\text{obs}} \,|\, J^P + \text{bkg}) \;/\; P(q \geq q_{\text{obs}} \,|\, 0^+ + \text{bkg}) < \alpha$, is used for the final inference of whether a particular alternative signal hypothesis is excluded or not at a given confidence level $(1 - \alpha)$.

6.4.2 Exotic-spin study with the $H \to ZZ \to 4\ell$ channel

The study of the exotic-spin J^P hypotheses of the observed boson with mass of 125.6 GeV using the $X \to ZZ$ decay channel is summarized in this section. Mixed spin-one state hypotheses, as well as the spin-two models listed in table 6.3 are examined.

In the case of the spin-one studies, the hypothesis testing is performed for a discrete set of values of the parameter f_{b2}. The input observables are $(\mathcal{D}_{\text{bkg}}, \mathcal{D}_{1-}, \mathcal{D}_{1+})$. It has been demonstrated in the context of this study that the distributions of these

observables are not sensitive to the phase between the b_1 and b_2 coupling parameters in equation (3.6) and therefore the results of the f_{b2} scan are valid for any value of the phase term in the interference. The spin-one hypothesis is tested for two scenarios, $q\bar{q}$ production and using only decay information. The latter requires the input observables $\left(\mathcal{D}_{\text{bkg}}^{\text{dec}}, \mathcal{D}_{1-}^{\text{dec}}, \mathcal{D}_{1+}^{\text{dec}}\right)$.

The expected and observed separations of spin-one models from the test statistic distributions are summarized in table 6.4 and in figure 6.3. The expected separation between the alternative signal hypotheses is quoted for two cases. In the first case, the expected SM Higgs boson signal strength and the alternative signal cross section are the ones obtained in the fit to the data. The second case assumes the nominal SM Higgs boson signal strength (defined as $\mu = 1$), while the cross section for the alternative signal hypothesis is taken to be the same as for the SM Higgs boson (the $2e2\mu$ channel at 8 TeV is taken as a reference). Since the observed signal strength is very close to unity, the two results for the expected separations are also similar.

All spin-one tests are consistent with the expectation for the SM Higgs boson. While the decay-only analysis uses less information and is expected to provide weaker constraints, the fluctuations in the observed data lead to stronger constraints for spin-one models. Any arbitrary spin-one model for the resonance observed in the $X \to ZZ \to 4\ell$ decay mode with any mixture of parity-even and parity-odd interactions and any production mechanism is excluded at a C.L. of 99.97% or higher.

In the case of the spin-two studies, hypothesis testing is performed for ten models

Table 6.4: List of spin-one models tested in the $X \to ZZ$ analysis. The expected separation is quoted for two scenarios, for the signal production cross section obtained from the fit to data for each hypothesis and using the SM expectation ($\mu = 1$). The observed separation shows the consistency of the observation with the SM Higgs boson model or the alternative J^P model, from which the CL_s value is derived [62].

$f_{b2}(J^P)$ Model	J^P Prod.	Expected (μ=1)	Obs. 0^+	Obs. J^P	CL_s
$0.0(1^-)$	$q\bar{q}$	2.9σ (2.8σ)	-1.4σ	$+5.0\sigma$	<0.001%
0.2	$q\bar{q}$	2.6σ (2.6σ)	-1.4σ	$+4.6\sigma$	0.002%
0.4	$q\bar{q}$	2.5σ (2.4σ)	-1.3σ	$+4.4\sigma$	0.005%
0.6	$q\bar{q}$	2.4σ (2.4σ)	-1.2σ	$+4.1\sigma$	0.015%
0.8	$q\bar{q}$	2.4σ (2.4σ)	-1.0σ	$+4.0\sigma$	0.021%
$1.0(1^+)$	$q\bar{q}$	2.4σ (2.4σ)	-0.8σ	$+3.8\sigma$	0.031%
$0.0(1^-)$	any	2.9σ (2.7σ)	-2.0σ	$>5.0\sigma$	<0.001%
0.2	any	2.7σ (2.5σ)	-2.2σ	$>5.0\sigma$	<0.001%
0.4	any	2.5σ (2.4σ)	-2.3σ	$>5.0\sigma$	<0.001%
0.6	any	2.5σ (2.3σ)	-2.4σ	$>5.0\sigma$	<0.001%
0.8	any	2.4σ (2.3σ)	-2.3σ	$>5.0\sigma$	<0.001%
$1.0(1^+)$	any	2.5σ (2.3σ)	-2.3σ	$>5.0\sigma$	<0.001%

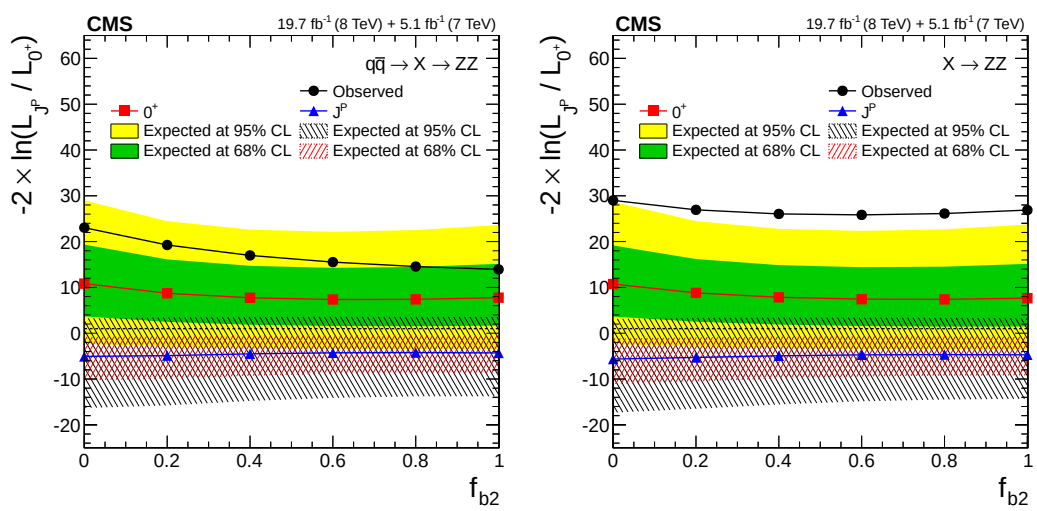

Figure 6.3: Distributions of the test statistic $q = -2\ln(\mathcal{L}_{J^P}/\mathcal{L}_{0^+})$ as a function of f_{b2} for the spin-one J^P models tested against the SM Higgs boson hypothesis in the $q\bar{q} \to X \to ZZ$ (left) and decay-only $X \to ZZ$ (right) analyses. The median expectation for the SM Higgs boson is represented by the red squares with the green (68% C.L.) and yellow (95% C.L.) solid color regions and for the alternative J^P hypotheses by the blue triangles with the red (68% C.L.) and blue (95% C.L.) hatched regions. The observed values are indicated by the black dots [62].

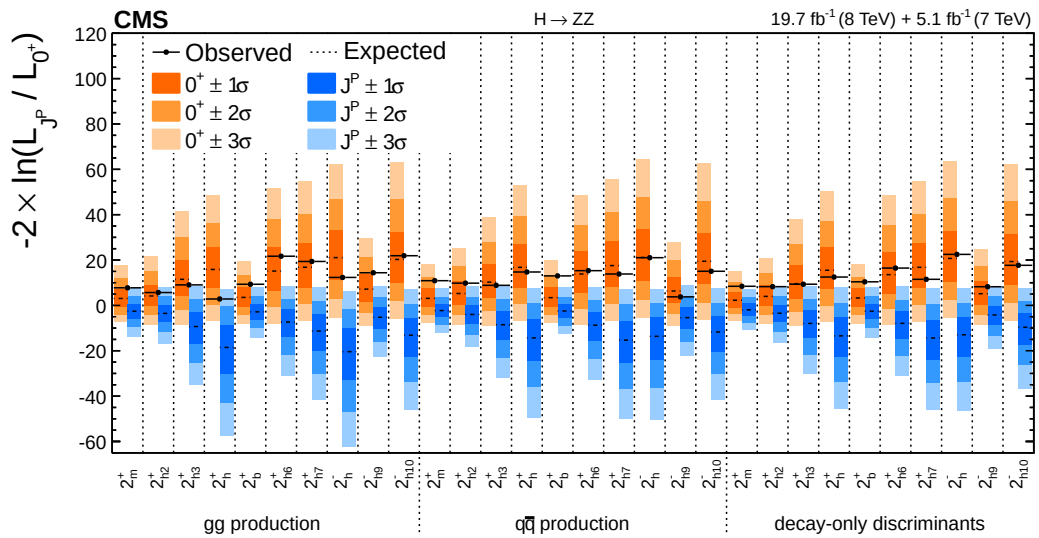

Figure 6.4: Distributions of the test statistic $q = -2\ln(\mathcal{L}_{J^P}/\mathcal{L}_{0^+})$ for the spin-two J^P models tested against the SM Higgs boson hypothesis in the $X \to ZZ$ analyses. The expected median and the 68.3%, 95.4%, and 99.7% C.L. regions for the SM Higgs boson (orange, the left for each model) and for the alternative J^P hypotheses (blue, right) are shown. The observed q values are indicated by the black dots [62].

and three scenarios: gg, $q\bar{q}$ production, and using only decay information. Two input observables are used since interference between the different amplitude components is not considered. These results cover all the lowest order terms in the amplitude without considering mixing of different contributions.

The data disfavor all the spin-two $X \to ZZ \to 4\ell$ hypotheses tested in favor of the SM hypothesis $J^P = 0^+$ with $1 - CL_s$ values larger than 99% C.L. when only decay information is used (table 6.5). The most motivated of these is the 2^+_m model, which represents a massive graviton-like boson as suggested in models with warped extra dimensions [70, 71] and is excluded at 99.1% C.L. by the 4ℓ final state.

Table 6.5: List of spin-two models tested in the $X \to ZZ$ analysis. The expected separation is quoted for two scenarios, for the signal production cross section obtained from the fit to data for each hypothesis, and using the SM expectation ($\mu = 1$). The observed separation shows the consistency of the observation with the SM Higgs boson or an alternative J^P model, from which the CL_s value is derived [41, 62].

J^P Model	J^P Prod.	Expected (μ=1)	Obs. 0^+	Obs. J^P	CL_s
2^+_m	gg	1.9σ (1.8σ)	-1.1σ	$+3.0\sigma$	0.90%
2^+_{h2}	gg	2.0σ (2.1σ)	-0.3σ	$+2.4\sigma$	2.0%
2^+_{h3}	gg	3.2σ (3.4σ)	$+0.3\sigma$	$+3.0\sigma$	0.17%
2^+_h	gg	3.8σ (4.0σ)	$+1.8\sigma$	$+2.0\sigma$	2.3%
2^+_b	gg	1.6σ (1.8σ)	-1.4σ	$+3.4\sigma$	0.50%
2^+_{h6}	gg	3.4σ (3.7σ)	-0.6σ	$+4.9\sigma$	<0.001%
2^+_{h7}	gg	3.8σ (4.5σ)	-0.3σ	$+4.5\sigma$	<0.001%
2^-_h	gg	4.2σ (4.5σ)	$+1.0\sigma$	$+3.2\sigma$	0.090%
2^-_{h9}	gg	2.5σ (2.6σ)	-1.1σ	$+4.0\sigma$	0.029%
2^-_{h10}	gg	4.2σ (4.3σ)	-0.1σ	$+4.8\sigma$	<0.001%
2^+_m	$q\bar{q}$	1.7σ (1.7σ)	-1.7σ	$+3.8\sigma$	0.17%
2^+_{h2}	$q\bar{q}$	2.2σ (2.2σ)	-0.8σ	$+3.3\sigma$	0.26%
2^+_{h3}	$q\bar{q}$	3.1σ (3.0σ)	$+0.2\sigma$	$+3.0\sigma$	0.21%
2^+_h	$q\bar{q}$	4.0σ (3.9σ)	$+0.2\sigma$	$+3.9\sigma$	0.008%
2^+_b	$q\bar{q}$	1.7σ (1.7σ)	-1.9σ	$+4.1\sigma$	0.062%
2^+_{h6}	$q\bar{q}$	3.4σ (3.3σ)	-0.2σ	$+4.0\sigma$	0.008%
2^+_{h7}	$q\bar{q}$	4.1σ (3.9σ)	$+0.4\sigma$	$+3.8\sigma$	0.010%
2^-_h	$q\bar{q}$	4.3σ (4.4σ)	$+0.0\sigma$	$+4.6\sigma$	<0.001%
2^-_{h9}	$q\bar{q}$	2.4σ (2.2σ)	$+0.5\sigma$	$+2.0\sigma$	3.1%
2^-_{h10}	$q\bar{q}$	4.0σ (3.9σ)	$+0.4\sigma$	$+4.0\sigma$	0.006%
2^+_m	any	1.5σ (1.5σ)	-1.6σ	$+3.4\sigma$	0.71%
2^+_{h2}	any	1.9σ (2.0σ)	-0.9σ	$+3.0\sigma$	0.74%
2^+_{h3}	any	3.0σ (3.1σ)	$+0.0\sigma$	$+3.1\sigma$	0.18%
2^+_h	any	3.8σ (4.0σ)	$+0.3\sigma$	$+3.6\sigma$	0.025%
2^+_b	any	1.7σ (1.7σ)	-1.6σ	$+3.6\sigma$	0.29%
2^+_{h6}	any	3.3σ (3.4σ)	-0.3σ	$+4.2\sigma$	0.003%
2^+_{h7}	any	4.0σ (4.2σ)	$+0.6\sigma$	$+3.5\sigma$	0.032%
2^-_h	any	4.2σ (4.6σ)	-0.2σ	$+4.8\sigma$	<0.001%
2^-_{h9}	any	2.2σ (2.1σ)	-0.6σ	$+2.9\sigma$	0.57%
2^-_{h10}	any	3.9σ (4.0σ)	$+0.1\sigma$	$+4.3\sigma$	0.002%

6.4.3 Study of spin-zero HVV couplings

Given the exclusion of the exotic spin-one and spin-two scenarios presented in section 6.4.2, detailed studies of HVV interactions under the assumption that the new boson is a spin-zero resonance are performed.

First, constraints are applied on the presence of only one anomalous term in the HVV amplitude where the couplings are considered to be real. A summary of such results is presented in table 6.6 and figure 6.5. The details of these and other measurements are presented in the following subsections, with further measurements considering simultaneously up to four fraction and/or phase parameters in several cases.

6.4.3.1 Study of HZZ couplings with the $H \to ZZ \to 4\ell$ channel

The study of the anomalous HVV couplings starts with the test of three contributions to the HZZ interaction as shown in equation (3.4). Only real couplings are considered in this test, $\phi_{ai} = 0$ or π, where ϕ_{ai} generically refers to the phase of the coupling in question, such as $\phi_{\Lambda 1}$, ϕ_{a2}, or ϕ_{a3}. Since the expansion of terms in equation (3.4) is considered for small anomalous contributions, all other parameters are set to zero when the anomalous couplings of interest are considered. These constraints of real couplings and zero contribution from other terms are relaxed in

Table 6.6: Summary of allowed 68% C.L. (central values with uncertainties) and 95% C.L. (ranges in square brackets) intervals on anomalous coupling parameters in HVV interactions under the assumption that all the coupling ratios are real ($\phi_{ai}^{VV} = 0$ or π). The ranges are truncated at the physical boundaries of $f_{ai}^{VV} = 1$. The last column indicates the observed (expected) confidence level of a pure anomalous coupling corresponding to $f_{ai}^{VV} = 1$ when compared to the SM expectation $f_{ai}^{VV} = 0$ [62].

Parameter	Observed	Expected	$f_{ai}^{VV} = 1$
$f_{\Lambda 1}\cos(\phi_{\Lambda 1})$	$0.22^{+0.10}_{-0.16}$ $[-0.25, 0.37]$	$0.00^{+0.16}_{-0.87}$ $[-1.00, 0.27]$ $\cup[0.92, 1.00]$	1.1% (16%)
$f_{a2}\cos(\phi_{a2})$	$0.00^{+0.41}_{-0.06}$ $[-0.66, -0.57]$ $\cup[-0.15, 1.00]$	$0.00^{+0.38}_{-0.08}$ $[-0.18, 1.00]$	5.2% (5.0%)
$f_{a3}\cos(\phi_{a3})$	$0.00^{+0.14}_{-0.11}$ $[-0.40, 0.43]$	$0.00^{+0.33}_{-0.33}$ $[-0.70, 0.70]$	0.02% (0.41%)
$f_{\Lambda 1}^{WW}\cos(\phi_{\Lambda 1}^{WW})$	$0.21^{+0.18}_{-1.21}$ $[-1.00, 1.00]$	$0.00^{+0.34}_{-1.00}$ $[-1.00, 0.41]$ $\cup[0.49, 1.00]$	78% (67%)
$f_{a2}^{WW}\cos(\phi_{a2}^{WW})$	$-0.02^{+1.02}_{-0.16}$ $[-1.00, -0.54]$ $\cup[-0.29, 1.00]$	$0.00^{+1.00}_{-0.12}$ $[-1.00, -0.58]$ $\cup[-0.22, 1.00]$	42% (46%)
$f_{a3}^{WW}\cos(\phi_{a3}^{WW})$	$-0.03^{+1.03}_{-0.97}$ $[-1.00, 1.00]$	$0.00^{+1.00}_{-1.00}$ $[-1.00, 1.00]$	34% (49%)
$f_{\Lambda 1}^{Z\gamma}\cos\left(\phi_{\Lambda 1}^{Z\gamma}\right)$	$-0.27^{+0.34}_{-0.49}$ $[-1.00, 1.00]$	$0.00^{+0.83}_{-0.53}$ $[-1.00, 1.00]$	26% (16%)
$f_{a2}^{Z\gamma}\cos\left(\phi_{a2}^{Z\gamma}\right)$	$0.00^{+0.14}_{-0.20}$ $[-0.49, 0.46]$	$0.00^{+0.51}_{-0.51}$ $[-0.78, 0.79]$	<0.01% (0.01%)
$f_{a3}^{Z\gamma}\cos\left(\phi_{a3}^{Z\gamma}\right)$	$0.02^{+0.21}_{-0.13}$ $[-0.40, 0.51]$	$0.00^{+0.51}_{-0.51}$ $[-0.75, 0.75]$	<0.01% (<0.01%)
$f_{a2}^{\gamma\gamma}\cos(\phi_{a2}^{\gamma\gamma})$	$0.12^{+0.20}_{-0.11}$ $[-0.04, +0.51]$	$0.00^{+0.11}_{-0.09}$ $[-0.32, 0.34]$	<0.01% (<0.01%)
$f_{a3}^{\gamma\gamma}\cos(\phi_{a3}^{\gamma\gamma})$	$-0.02^{+0.06}_{-0.13}$ $[-0.35, 0.32]$	$0.00^{+0.15}_{-0.11}$ $[-0.37, 0.40]$	<0.01% (<0.01%)

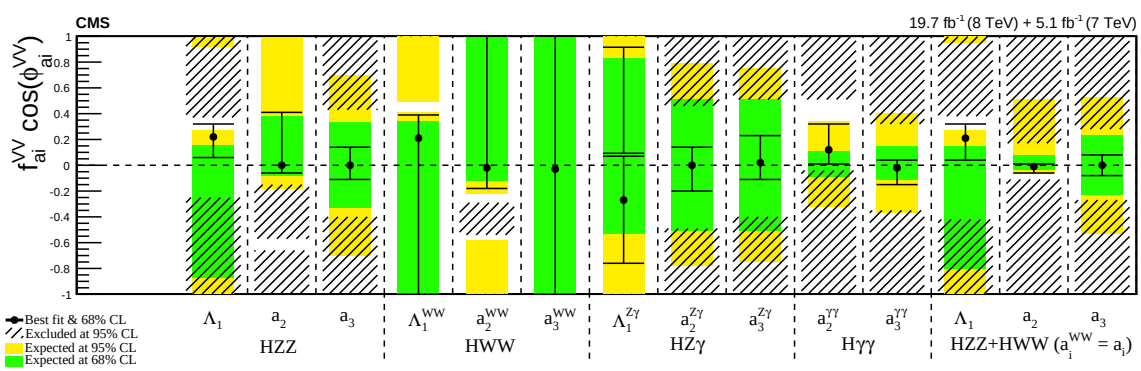

Figure 6.5: Summary of allowed confidence level intervals on anomalous coupling parameters in HVV interactions under the assumption that all the coupling ratios are real ($\phi_{ai}^{VV} = 0$ or π). The expected 68% and 95% C.L. regions are shown as the green and yellow bands. The observed constraints at 68% and 95% C.L. are shown as the points with errors and the excluded hatched regions. In the case of the $f_{\Lambda 1}^{Z\gamma}$ measurement, there are two minima and two 68% C.L. intervals, while only one global minimum is indicated with a point. The combination of the HZZ and HWW measurements is presented, assuming the symmetry $a_i = a_i^{WW}$ [62].

further tests discussed below.

The results of the likelihood function scan for the three parameters, $f_{ai}\cos\phi_{ai}$, are shown in figure 6.6 (left), where the $\cos\phi_{ai}$ term allows for a signed quantity with $\cos\phi_{ai} = -1$ or $+1$. The 68% and 95% C.L. intervals are shown in table 6.6. These results can be interpreted for the coupling parameters used in equation (3.4), as shown in table 6.7. Strong destructive interference of the SM and anomalous contributions at $f_{\Lambda 1}\cos(\phi_{\Lambda 1}) \sim +0.5$ or $f_{a2}\cos(\phi_{a2}) \sim -0.5$ leads to very different kinematic distributions and exclusions with high confidence levels. Additional features with multiple likelihood function maxima observed in the $f_{\Lambda 1}$ likelihood scan are due to the superposition of measurements in the $4e/4\mu$ and $2e2\mu$ channels, which have different maxima due to the interference between the leptons.

Next, two parameters f_{ai} and ϕ_{ai} are considered at the same time. For example, if the coupling is known to be either positive or negative, such a scenario is considered in table 6.8. In this case, constraints are set on f_{ai} for a given phase value. More generally, one can allow ϕ_{ai} to be unconstrained, that is, to have any value between $-\pi$ and $+\pi$ with a generally complex coupling. Such a fit is performed for $f_{\Lambda 1}$ and f_{a2} using the same configuration, but with additional $\phi_{\Lambda 1}$ and ϕ_{a2} parameters in equation (6.5). The results with ϕ_{ai} unconstrained (any) are shown in table 6.8 as well. The f_{a3} measurement with ϕ_{a3} unconstrained is performed with a different technique where the $\mathcal{D}_{CP}$ observable is removed from the fit and the result becomes insensitive to the phase of the amplitude. This technique is adopted due to its simpler implementation

Table 6.7: Summary of the allowed 95% C.L. intervals on the anomalous couplings in HZZ interactions using results in table 6.6 [62]. The coupling ratios are assumed to be real (including $\cos(\phi_{\Lambda_1}) = 0$ or π).

Parameter	Observed	Expected
$(\Lambda_1\sqrt{\lvert a_1\rvert})\cos(\phi_{\Lambda_1})$	$[-\infty, -119\text{GeV}] \cup [104\text{GeV}, \infty]$	$[-\infty, 50\text{GeV}] \cup [116\text{GeV}, \infty]$
a_2/a_1	$[-2.28, -1.88] \cup [-0.69, \infty]$	$[-0.77, \infty]$
a_3/a_1	$[-2.05, 2.19]$	$[-3.85, 3.85]$

and equivalent performance.

The next step in generalizing the constraints is to consider two anomalous contributions at the same time, both with and without the constraints that the couplings are real. Therefore, up to four parameters are considered at the same time: f_{ai}, ϕ_{ai}, f_{aj}, and ϕ_{aj}. Constraints on one parameter, when other parameters are left unconstrained in the full allowed parameter space, with $0 \leq f_{ai} \leq 1$, are presented in table 6.8. Even though the expansion with only three anomalous contributions in equation (3.4) becomes incomplete when large values of $f_{ai} \sim 1$ are considered, this is still a valuable test of the consistency of the data with the SM. All of the above results, with phases fixed or unconstrained and with other anomalous couplings unconstrained are shown in figure 6.6 (right). Some observed f_{ai} constraints appear to be tighter when compared to the one-parameter fits shown in figure 6.6 (left). This happens because the values of other profiled parameters are away from the SM expectation at the minimum of $-2\ln\mathcal{L}$, though still consistent with the SM. The expected constraints are always weaker with additional free parameters.

The above one-parameter measurements, with other couplings also considered to be unconstrained, are obtained from the fit configurations used for the two-parameter

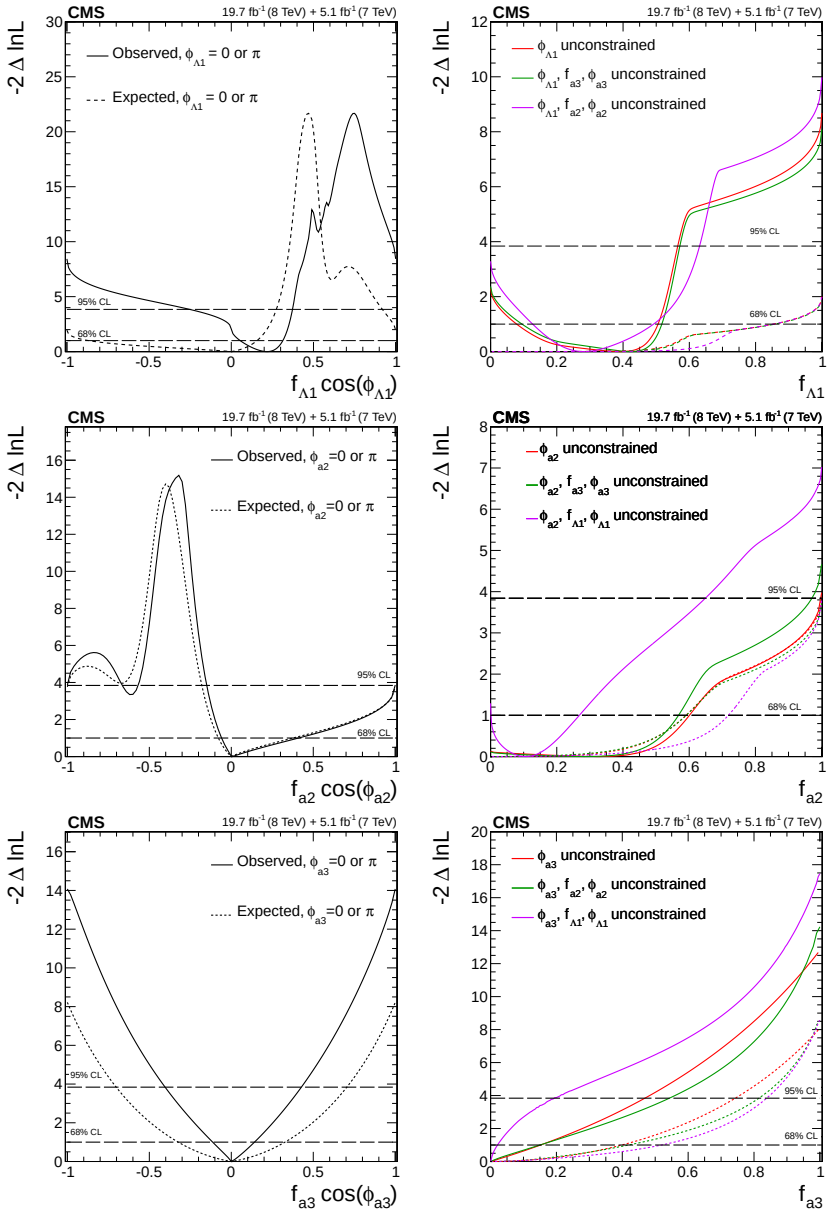

Figure 6.6: Expected (dashed) and observed (solid) likelihood scans for the effective fractions $f_{\Lambda 1}$, f_{a2}, f_{a3} (from top to bottom) describing HZZ interactions. Plots on the left show the results when the couplings studied are constrained to be real and all other couplings are fixed to the SM predictions. The $\cos\phi_{ai}$ term allows a signed quantity where $\cos\phi_{ai} = -1$ or $+1$. Plots on the right show the results where the phases of the anomalous couplings and additional HZZ couplings are left unconstrained, as indicated in the legend. The f_{a3} result with ϕ_{a3} unconstrained (in the bottom-right plot) is from [41] otherwise these results are from [62].

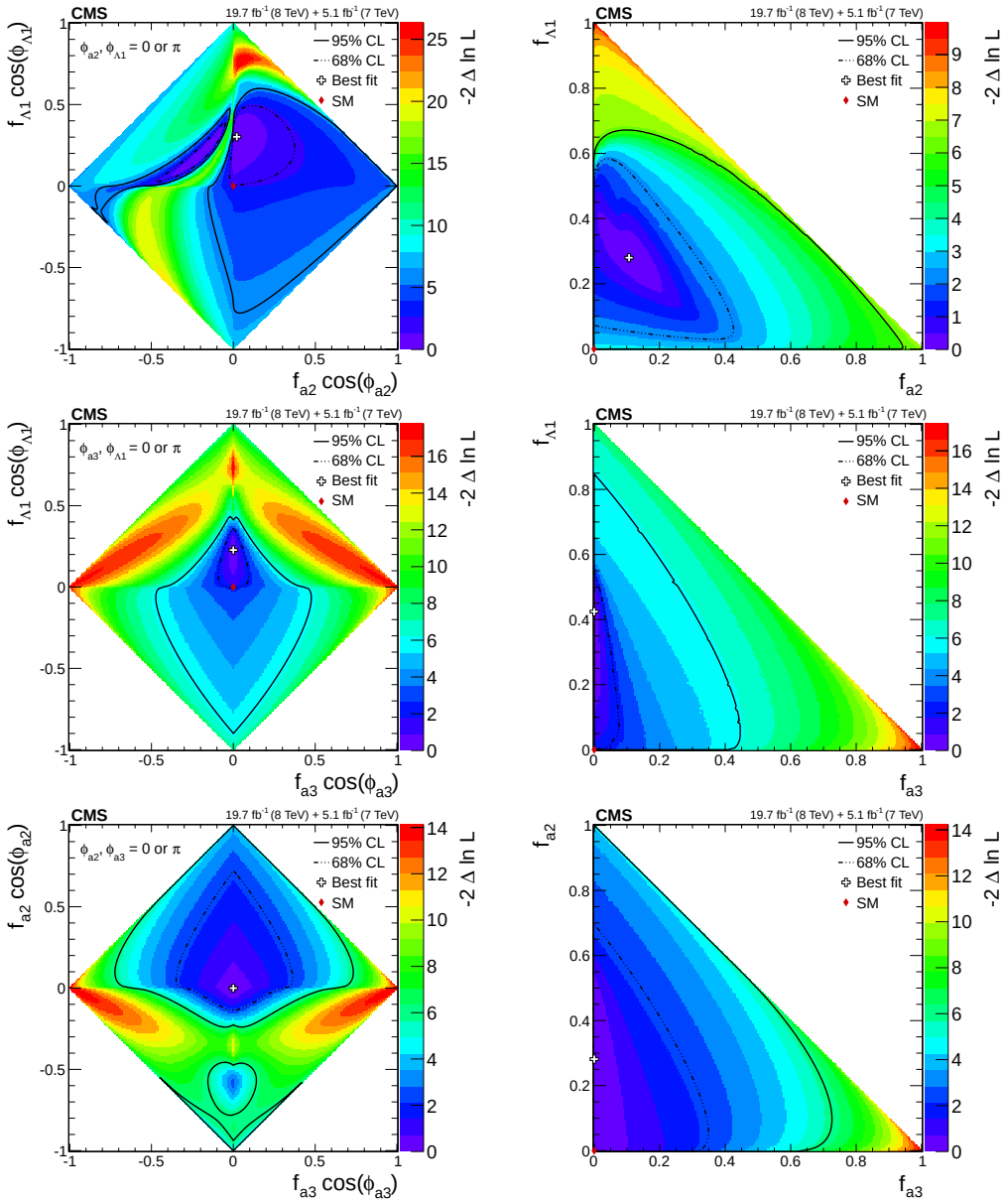

Figure 6.7: Observed likelihood scans for pairs of effective fractions $f_{\Lambda 1}$ vs. f_{a2}, $f_{\Lambda 1}$ vs. f_{a3}, and f_{a2} vs. f_{a3} (from top to bottom) describing HZZ interactions. Plots on the left show the results when the couplings studied are constrained to be real and all other couplings are fixed to the SM predictions. Plots on the right show the results when the phases of the anomalous couplings are left unconstrained. The SM expectations correspond to points (0,0) and the best fit values are shown with the crosses. The confidence level intervals are indicated by the corresponding $-2\,\Delta\ln\mathcal{L}$ contours [62].

measurements shown in figure 6.7. Both options are considered, either with or without the assumption that the couplings are real. To simplify the analysis the number of observables is kept to a maximum of three, the following discriminants are used to set the constraints, ($\mathcal{D}_{\text{bkg}}$, $\mathcal{D}_{\Lambda 1}$, $\mathcal{D}_{0h+}$), ($\mathcal{D}_{\text{bkg}}$, $\mathcal{D}_{\Lambda 1}$, $\mathcal{D}_{0-}$), and ($\mathcal{D}_{\text{bkg}}$, $\mathcal{D}_{0-}$ or $\mathcal{D}_{0h+}$), for the measurements of $f_{\Lambda 1}$ vs. f_{a2}, $f_{\Lambda 1}$ vs. f_{a3}, and f_{a2} vs. f_{a3}, respectively. The left set of plots in figure 6.7 shows constraints on two real couplings, and the right set of plots in figure 6.7 shows constraints on two couplings that are allowed to have any complex phase. Similarly to the one-parameter constraints, the allowed 95% C.L. regions are formally defined using the profile likelihood function ($-2\Delta \ln \mathcal{L} = 5.99$). The results in Table 6.8 are obtained from these two-parameter likelihood scans by profiling one parameter.

Overall, all anomalous HZZ couplings are found to be consistent with zero, which is also consistent with the expectation from the SM where these couplings are expected to be very small, well below the current sensitivity.

6.4.3.2 Study of $HZ\gamma$ and $H\gamma\gamma$ couplings with the $H \to VV \to 4\ell$ channel

In the following, constraints on anomalous $HZ\gamma$ and $H\gamma\gamma$ interactions are obtained using the $H \to VV \to 4\ell$ data. Five anomalous couplings are considered, following equation (3.4) and table 6.3, where the three observables for each measurement are listed. Only real couplings, $\phi_{ai} = 0$ or π, are considered in this test. The

Table 6.8: Summary of the allowed 68% C.L. (central values with uncertainties) and 95% C.L. (ranges in square brackets) intervals on anomalous coupling parameters in the HZZ interactions under the condition of a given phase of the coupling (0 or π) or when the phase or other parameters are unconstrained (any value allowed). Expectations are quoted in parentheses following the observed values. The results for f_{a3} with ϕ_{a3} unconstrained are from [41] while the other results are form [62].

	$f_{\Lambda 1}$	f_{a2}	f_{a3}
$\phi_{ai} = 0$	$0.22^{+0.10}_{-0.16}$ $[0.00, 0.37]$ ($0.00^{+0.16}_{-0.00}$ $[0.00, 0.27]$ $\cup[0.92, 1.00]$)	$0.00^{+0.42}_{-0.00}$ $[0.00, 1.00]$ ($0.00^{+0.35}_{-0.00}$ $[0.00, 1.00]$)	$0.00^{+0.14}_{-0.00}$ $[0.00, 0.43]$ ($0.00^{+0.33}_{-0.00}$ $[0.00, 0.70]$)
$\phi_{ai} = \pi$	$0.00^{+0.08}_{-0.00}$ $[0.00, 0.82]$ ($0.00^{+0.87}_{-0.00}$ $[0.00, 1.00]$)	$0.00^{+0.06}_{-0.00}$ $[0.00, 0.15]$ $\cup[0.56, 0.68]$ ($0.00^{+0.08}_{-0.00}$ $[0.00, 0.18]$ $\cup$ $[0.62, 0.73]$)	$0.00^{+0.11}_{-0.00}$ $[0.00, 0.40]$ ($0.00^{+0.32}_{-0.00}$ $[0.00, 0.70]$)
any ϕ_{ai}	$0.39^{+0.16}_{-0.31}$ $[0.00, 0.57]$ ($0.00^{+0.85}_{-0.00}$ $[0.00, 1.00]$)	$0.32^{+0.28}_{-0.32}$ $[0.00, 1.00]$ ($0.00^{+0.59}_{-0.00}$ $[0.00, 1.00]$)	$0.00^{+0.17}_{-0.00}$ $[0.00, 0.47]$ ($0.00^{+0.40}_{-0.00}$ $[0.00, 0.74]$)
any ϕ_{ai}, $f_{\Lambda 1}, \phi_{\Lambda 1}$		$0.11^{+0.16}_{-0.11}$ $[0.00, 0.65]$ ($0.00^{+0.72}_{-0.00}$ $[0.00, 1.00]$)	$0.00^{+0.02}_{-0.00}$ $[0.00, 0.19]$ ($0.00^{+0.52}_{-0.00}$ $[0.00, 0.84]$)
any ϕ_{ai}, f_{a2}, ϕ_{a2}	$0.28^{+0.21}_{-0.15}$ $[0.00, 0.63]$ ($0.00^{+0.85}_{-0.00}$ $[0.00, 1.00]$)		$0.00^{+0.15}_{-0.00}$ $[0.00, 0.54]$ ($0.00^{+0.42}_{-0.00}$ $[0.00, 0.81]$)
any ϕ_{ai}, f_{a3}, ϕ_{a3}	$0.42^{+0.09}_{-0.33}$ $[0.00, 0.57]$ ($0.00^{+0.86}_{-0.00}$ $[0.00, 1.00]$)	$0.28^{+0.29}_{-0.28}$ $[0.00, 0.97]$ ($0.00^{+0.59}_{-0.00}$ $[0.00, 1.00]$)	

results of the likelihood function scan for the three parameters, $f_{ai} \cos \phi_{ai}$, are shown in figure 6.8, following the same formalism presented for the HZZ couplings in section 6.4.3.1. The 68% and 95% C.L. intervals are shown in table 6.6. In the case of the $f_{\Lambda 1}^{Z\gamma}$ measurement, there are two minima and only one central value with its 68% C.L. interval is shown in table 6.6, while both 68% C.L. intervals are presented in figure 6.5.

These results can be interpreted in terms of the coupling parameters used in equation (3.4) as shown in table 6.9. The ratio $(\sigma_i^{V\gamma}/\sigma_{\rm SM}^{V\gamma})(2a_i^{V\gamma}/a_1)^2$ approximates the ratio $\mu = \sigma/\sigma_{\rm SM}$ of the measured and expected SM cross sections for a Higgs boson decay $H \to V\gamma$. The ratio $(2/a_1)^2$ scales this measurement with respect to the

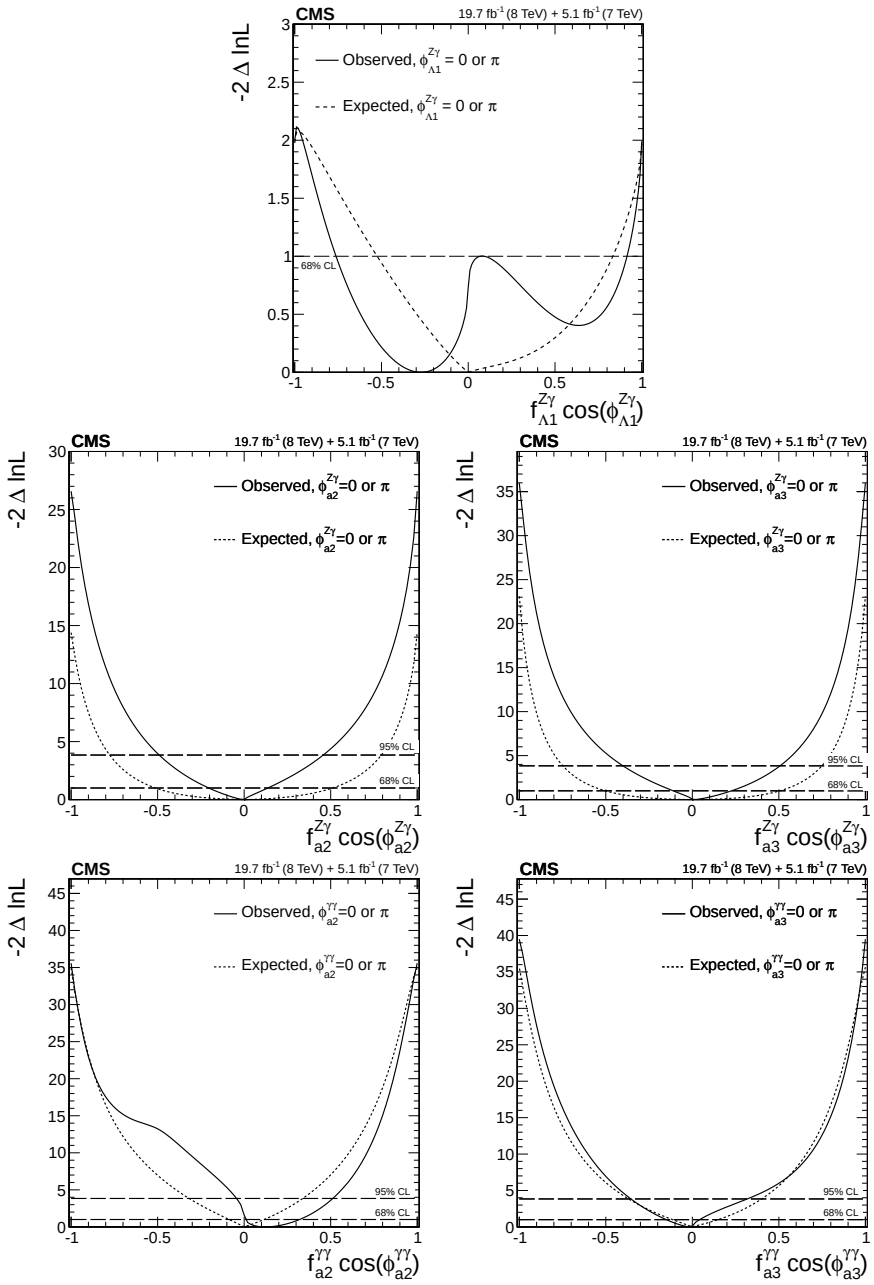

Figure 6.8: Expected (dashed) and observed (solid) likelihood scans for the effective fractions $f_{\Lambda 1}^{Z\gamma}$ (top), $f_{a2}^{Z\gamma}$ (middle left), $f_{a3}^{Z\gamma}$ (middle right), $f_{a2}^{\gamma\gamma}$ (bottom left), and $f_{a3}^{\gamma\gamma}$ (bottom right). The couplings studied are constrained to be real and all other couplings are fixed to the SM predictions [62]. The $\cos\phi_{ai}^{VV}$ term allows a signed quantity where $\cos\phi_{ai}^{VV} = -1$ or $+1$.

Table 6.9: Summary of the allowed 95% C.L. intervals on the anomalous couplings in $HZ\gamma$ and $H\gamma\gamma$ interactions using results in table 6.6 [62]. The coupling ratios are assumed to be real ($\cos\left(\phi_{ai}^{VV}\right) = 0$ or π).

Parameter	Observed	Expected
$(\Lambda_1^{Z\gamma}\sqrt{\lvert a_1\rvert})\cos\left(\phi_{\Lambda_1}^{Z\gamma}\right)$	$[-\infty, +\infty]$	$[-\infty, +\infty]$
$a_2^{Z\gamma}/a_1$	$[-0.046, 0.044]$	$[-0.089, 0.092]$
$a_3^{Z\gamma}/a_1$	$[-0.042, 0.053]$	$[-0.090, 0.090]$
$a_2^{\gamma\gamma}/a_1$	$[-0.011, 0.054]$	$[-0.036, 0.038]$
$a_3^{\gamma\gamma}/a_1$	$[-0.039, 0.037]$	$[-0.041, 0.044]$
$(\sigma_2^{Z\gamma}/\sigma_{\rm SM}^{Z\gamma})(2a_2^{Z\gamma}/a_1)^2\cos\left(\phi_{a2}^{Z\gamma}\right)$	$[-1.7, 1.6]\times 10^2$	$[-6.5, 6.9]\times 10^2$
$(\sigma_3^{Z\gamma}/\sigma_{\rm SM}^{Z\gamma})(2a_3^{Z\gamma}/a_1)^2\cos\left(\phi_{a2}^{Z\gamma}\right)$	$[-1.2, 1.9]\times 10^2$	$[-5.5, 5.5]\times 10^2$
$(\sigma_2^{\gamma\gamma}/\sigma_{\rm SM}^{\gamma\gamma})(2a_2^{\gamma\gamma}/a_1)^2\cos(\phi_{a2}^{\gamma\gamma})$	$[-0.3, 7.3]\times 10^2$	$[-3.3, 3.6]\times 10^2$
$(\sigma_3^{\gamma\gamma}/\sigma_{\rm SM}^{\gamma\gamma})(2a_3^{\gamma\gamma}/a_1)^2\cos(\phi_{a3}^{\gamma\gamma})$	$[-3.8, 3.3]\times 10^2$	$[-4.1, 4.7]\times 10^2$

$H \to ZZ$ coupling and is expected to be 1.0 in the SM. As can be seen in table 6.9, the constraints presented on these ratios (<170 for $\left|a_2^{Z\gamma}\right|$ or <730 for $|a_2^{\gamma\gamma}|$ at 95% C.L.) are about one or three orders of magnitude higher than from the analyses of the direct $H \to Z\gamma$ ($\mu < 9.5$ at 95% C.L. [145]) or $H \to \gamma\gamma$ ($\mu = 1.14^{+0.26}_{-0.23}$ at 68% C.L. [146]) decays with on-shell photons, respectively. Therefore, the constraints presented on $f_{a2}^{Z\gamma}$, $f_{a3}^{Z\gamma}$, $f_{a2}^{\gamma\gamma}$, $f_{a3}^{\gamma\gamma}$ are not competitive compared with the direct cross-section measurements in $H \to Z\gamma$ or $\gamma\gamma$ decays. However, eventually with sufficiently large integrated luminosity it might be possible to measure $f_{a2}^{V\gamma}$ and $f_{a3}^{V\gamma}$ separately in the $H \to VV \to 4\ell$ decay, allowing for measurements of the CP properties in these couplings [147, 148]. The measurements in the on-shell analyses $H \to Z\gamma$ or $\gamma\gamma$ are sensitive only to the sum of the two cross-section fractions $f_{a2}^{V\gamma}$ and $f_{a3}^{V\gamma}$, and therefore cannot distinguish the two. Moreover, the $f_{\Lambda 1}^{Z\gamma}$ measurement is not possible with on-shell photons.

As in the case of the HZZ couplings, anomalous $HZ\gamma$ and $H\gamma\gamma$ couplings are found to be consistent with zero, as expected in the SM with the current precision. Since the measurement of the $HZ\gamma$ and $H\gamma\gamma$ couplings in the $H \to VV \to 4\ell$ decay is not yet competitive with the on-shell measurements, further investigation of several parameters simultaneously is not considered with the current data.

Chapter 7

Conclusions & Extensions

Obtaining experimental evidence for the Higgs boson has been a major goal of the particle physics research since the conception of the LHC. Finding and characterizing this boson is key to the complete picture of electroweak symmetry breaking. This effort has been a major focus of the CMS collaboration. This thesis work focused on this search and characterization using the four-lepton final state. It offers a series of extremely important and groundbreaking measurements that were proposed and carried out on the observed data.

This thesis presents the observation of the new boson, studies of its production and decay rates, constraints on the total width, and measurements of its spin and parity properties. When the Higgs boson was discovered in 2012, it was widely believed that the study of these properties would require much more time and data than CMS has collected so far. Using the kinematics of the four-lepton final state in novel

and efficient ways made these measurements possible far before more conventional approaches.

All of the measurements presented here will improve with time, simply by collecting more LHC data from 2015 and beyond, because they are statistically limited. Additionally, many of these measurements have already been extended including information from other decay channels to say more about the observed boson. Many of these extensions were directly inspired and made possible by the work presented here, while others developed their own techniques.

7.1 $H \to ZZ \to 4\ell$ Search & Production Mechanism

The observation of the new boson is confirmed in the 4ℓ final state, using data from an integrated luminosity of 5.1 fb^{-1} of proton-proton collisions at a center of mass energy of $\sqrt{s} = 7$ TeV, and 19.7 fb^{-1} at $\sqrt{s} = 8$ TeV. The $H \to ZZ \to 4\ell$ data shows a local significance of 6.8 standard deviations above the expected background. Upper limits at the 95% C.L. exclude the SM-like Higgs boson in the mass ranges 114.5–119.0 GeV and 129.5–832.0 GeV, for an expected exclusion range for the background-only hypothesis of 115–740 GeV. The production cross section of the new boson times the branching fraction to four leptons is measured to be $\mu = 0.93^{+0.26}_{-0.23}(\text{stat.})^{+0.13}_{-0.09}(\text{syst.})$ times that predicted by the standard model ($\mu = 1$

is SM Higgs boson). Those cross sections times branching ratios associated with production couplings to fermions and vector bosons are $\mu_{ggH,t\bar{t}H} = 0.80^{+0.46}_{-0.36}$ and $\mu_{\mathrm{VBF},VH} = 1.7^{+2.2}_{-2.1}$, respectively, consistent with the SM expectations ($\mu = 1$). All production and decay properties of the observed new boson in the four-lepton final state are consistent, within their uncertainties, with the expectations for the SM Higgs boson.

7.1.1 Extensions

The limits that were found using the 4ℓ final state have been extended by combining the results with the other $H \to ZZ$ and $H \to WW$ final state results. In [149] a heavy Higgs boson with standard model-like couplings and decays are excluded from 145–1000 GeV shown in figure 7.1. Additionally, these results are re-interpreted as a search for a heavy, narrow resonance as electroweak singlet partner of the standard model Higgs boson. No significant excess over the expected standard model background has been observed and exclusion limits have been set [149]. These results actually use a MELA discriminant based on the jet kinematics to separate signal from background rather than the $\mathcal{D}_{jet}$ discriminant. This discriminant takes the four-momenta of the jets produced in addition to the leptons and outputs a discriminating variable based on the matrix element calculation of VBF and $gg \to H + 2\mathrm{jets}$ [61].

The study of the production mechanisms has also been used to make a robust set of CMS results combining many different Higgs search channels. In [150] the results from

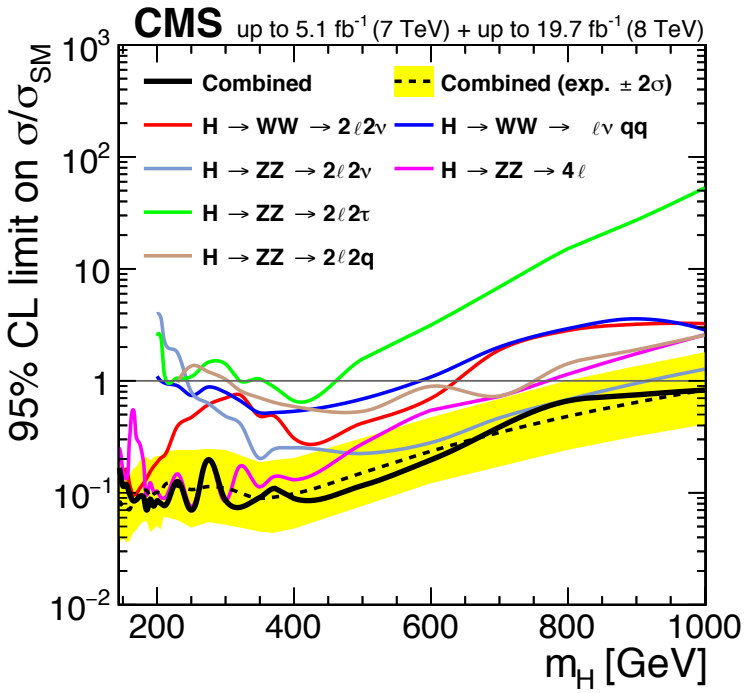

Figure 7.1: Combined results of $H \to ZZ$ and $H \to WW$ in the search of a heavy, SM-like Higgs boson with SM couplings, line shape and decays. Upper limits at 95% C.L. set for each of the contributing final states and their combination [149].

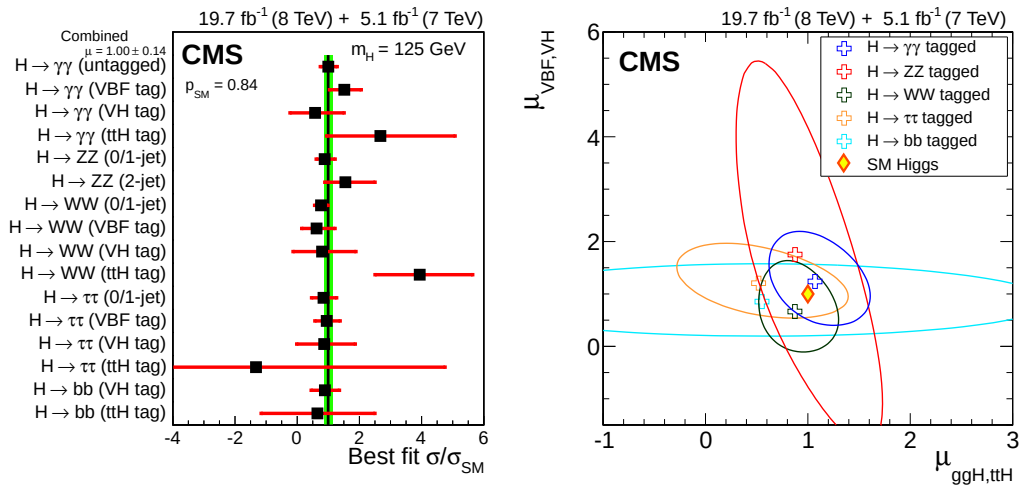

Figure 7.2: (left) Values of the best-fit σ/σ_{SM} for the combination (solid vertical line) and for subcombinations by predominant decay mode and additional tags targeting a particular production mechanism. (right) The 68% C.L. regions (bounded by the solid curves) for signal strength of the ggH and $t\bar{t}H$, and of the VBF and VH production mechanisms: $\mu_{ggH,t\bar{t}H}$ and $\mu_{\mathrm{VBF},VH}$, respectively [150].

the 4ℓ studies were combined with other final states where a Higgs boson signal is observed to set extremely robust limits on the global $\mu = 1.00 \pm 0.09(\mathrm{stat.})^{+0.08}_{-0.07}(\mathrm{theo.}) \pm 0.07(\mathrm{syst.})$ (at $m_H = 125.0$ GeV) and to show the consistency of the 0/1 jet and dijet signal strengths with the other decay channels, figure 7.2. Similarly, the results for the production mechanism can be compared to the other final states and used to show how consistent the data from CMS is with the predicted SM Higgs boson.

7.2 $H \to ZZ$ Constraints on Total Width

We have presented constraints on the total Higgs boson width using its relative on-shell and off-shell production and decay rates to four leptons or two leptons and

two neutrinos. The analysis is based on the 2011 and 2012 data sets corresponding to integrated luminosities of 5.1 fb^{-1} at $\sqrt{s} = 7\text{TeV}$ and 19.7 fb^{-1} at $\sqrt{s} = 8\text{TeV}$. The four-lepton analysis uses the measured invariant mass distribution near the peak and above the Z-boson pair production threshold, as well as a likelihood discriminant to separate the gluon fusion ZZ production from the $q\bar{q} \to ZZ$ background, while the two-lepton plus two-neutrino off-shell analysis relies on the transverse mass distribution. The presented analysis determines the independent contributions of the gluon fusion and VBF production mechanisms from the data in the on-shell region. The combined fit of the 4ℓ and $2\ell 2\nu$ channels leads to an upper limit on the Higgs boson width of $\Gamma_H < 22$ MeV at a 95% confidence level, which is 5.4 times the expected width of the SM Higgs boson. This result improves by more than two orders of magnitude upon previous experimental constraints on the new boson decay width from the direct measurement at the resonance peak.

7.2.1 Extensions

An obvious extension of these results is to repeat what is done in the $ZZ \to 4\ell$ final state in the $WW \to 2\ell 2\nu$ decay channel. This way the constraints can be made tighter by including the information from the WW decay channel as well. This study has been performed by the ATLAS experiment [151] in their response to the CMS ZZ results. The CMS experiment should publish this $ZZ + WW$ combination soon.

A comprehensive test of anomalous HVV couplings of the Higgs boson has been

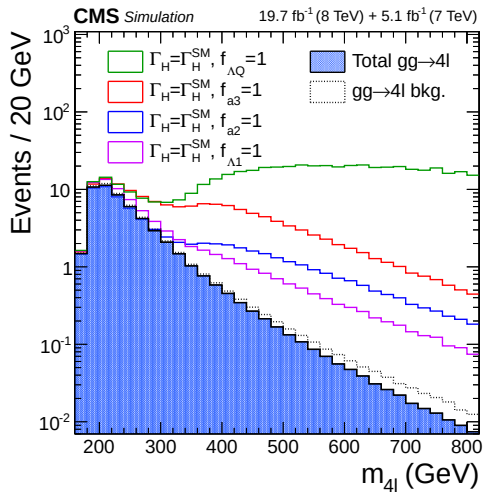

Figure 7.3: The $m_{4\ell}$ distributions in the off-shell region in the simulation of the $gg \to 4\ell$ process with the anomalous Λ_Q, a_3, a_2, and Λ_1 terms (open histograms) as well as the a_1 (SM filled histogram) term in decreasing order of enhancement at high $m_{4\ell}$. In all cases, the background and its interference with the different signal hypotheses are included except in the case of the pure background (dashed black). The on-shell signal yield and the width Γ_H are constrained to the SM expectations [152].

presented in section 6 and [62]. All anomalous contributions up to dimension five operators have been tested in the on-shell Higgs boson decay. However, in off-shell production these anomalous couplings will have a huge impact. The CMS experiment is now attempting to constrain some of these terms and the width simultaneously. Figure 7.3 shows a comparison of the $m_{4\ell}$ distribution between the SM and pure BSM hypotheses for $\Gamma_H = \Gamma_H^{SM}$. The analysis in the off-shell region for the Higgs boson width can be expanded by taking into account the changes in the off-shell contribution due to these new couplings.

7.3 $H \to VV \to 4\ell$ Spin/Parity Measurements

The interactions of a spin-zero, -one, or -two boson with the SM particles is studied based on a scattering amplitude with terms corresponding to operators up to dimension five. A maximum likelihood fit of the signal and background distributions provides constraints on the anomalous couplings of the H boson. The study focused on testing for the presence of anomalous effects in HZZ interactions under spin-zero, -one, and -two hypotheses. The $HZ\gamma$ and $H\gamma\gamma$ interactions were probed using the 4ℓ final state as well.

The exotic-spin study covers the analysis of mixed-parity spin-one states and ten spin-two hypotheses under the assumption of production either via gluon fusion or quark-antiquark annihilation, or without such an assumption. The spin-one hypotheses are excluded at a greater than 99.999% C.L. while the spin-two boson with gravity-like minimal couplings is excluded at a 99.87% C.L., and the other spin-two hypotheses tested are excluded at a 99% C.L. or higher.

Given the exclusion of the spin-one and spin-two scenarios, constraints are set on the contribution of anomalous couplings to the HZZ, $HZ\gamma$, and $H\gamma\gamma$ interactions of a spin-zero H boson, as summarized in table 6.6. Among these is the measurement of the f_{a3} parameter, which is defined as the fractional pseudoscalar cross section in the $H \to ZZ$ channel. The constraint is $f_{a3} < 0.43$ (0.40) at a 95% C.L. for the positive

(negative) phase of the pseudoscalar coupling with respect to the dominant SM-like coupling and $f_{a3} = 1$ exclusion of a pure pseudoscalar hypothesis at a 99.98% C.L.

All observations of the new particles spin/parity and tensor structure are consistent with the expectations for a scalar SM-like Higgs boson with $J^{PC} = 0^{++}$.

7.3.1 Extensions

We can perform a combination of the $H \to ZZ$ and $H \to WW$ measurements leading to tighter constraints on the H boson spin-parity and anomalous HVV interactions and higher exclusions of the spin-one and spin-two scenarios. Some of these combined results have already been presented in previous figures. For the 2^+_m hypothesis, in addition to the $H \to ZZ$ and $H \to WW$ final states combination with the $H \to \gamma\gamma$ final state is also helpful. A full summary of these results has been published in [62]. Figures 7.4 and 7.5 give a few examples of these combinations.

Additionally, this thesis work investigated the feasibility to measure anomalous HVV couplings using either decay or production information in the future. These studies were not limited to high luminosity LHC experiments but also investigated a future e^+e^- collider as well. These studies looked at many different kinds of Higgs boson production and decay to project the “ultimate" sensitivity of the MELA technique for these purposes. The results of these projection studies is shown in figure 7.6, and additional studies in combining all information (production, decay, and off resonance production) are underway.

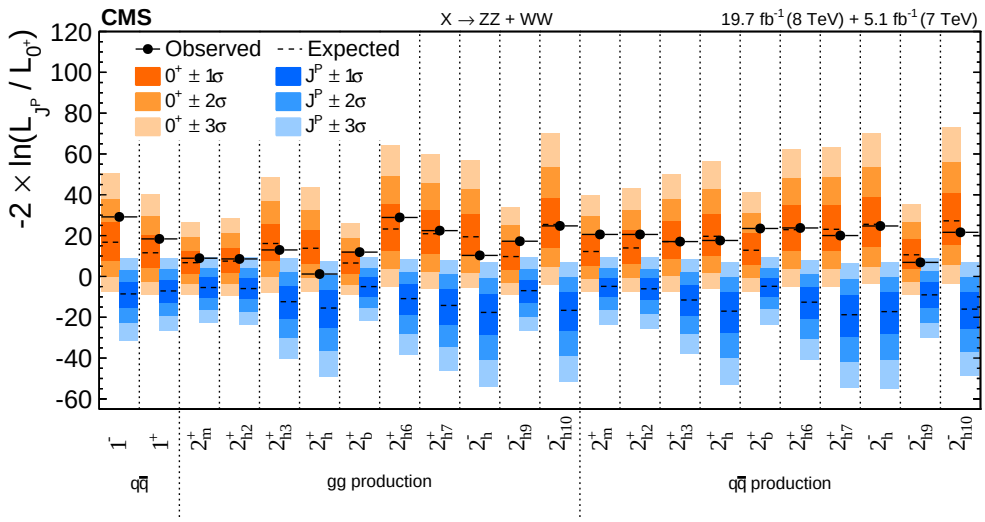

Figure 7.4: Distributions of the test statistic $q = -2\ln(\mathcal{L}_{J^P}/\mathcal{L}_{0^+})$ for the spin-one and spin-two J^P models tested against the SM Higgs boson hypothesis in the combined $X \to ZZ$ and WW analyses [62]. The expected median and the 68.3%, 95.4%, and 99.7% C.L. regions for the SM Higgs boson (orange, the left for each model) and for the alternative J^P hypotheses (blue, right) are shown. The observed q values are indicated by the black dots.

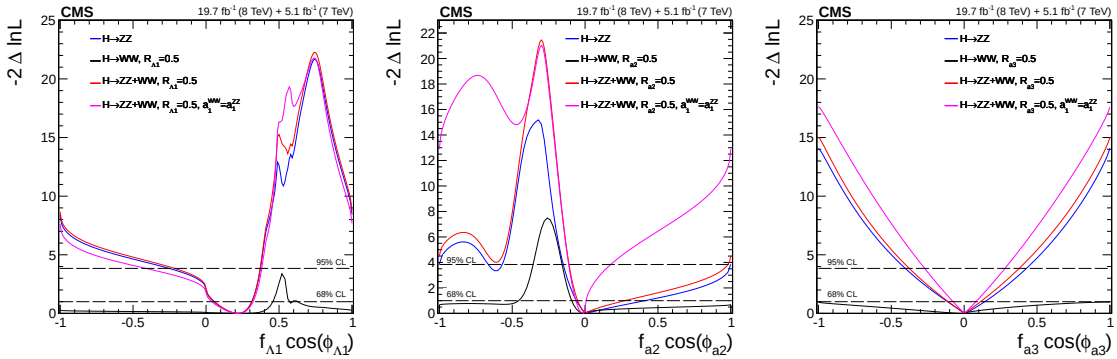

Figure 7.5: Expected (dashed) and observed (solid) likelihood scans for effective fractions $f_{\Lambda 1}$ (left), f_{a2} (middle), f_{a3} (right). The couplings studied are constrained to be real and all other anomalous couplings are fixed to the SM predictions. The $\cos\phi_{ai}$ term allows a signed quantity where $\cos\phi_{ai} = -1$ or $+1$. Plots show the combined $H \to WW$ and $H \to ZZ$ results in terms of the HZZ couplings for well motivated choices of the WW and ZZ coupling relationships [62].

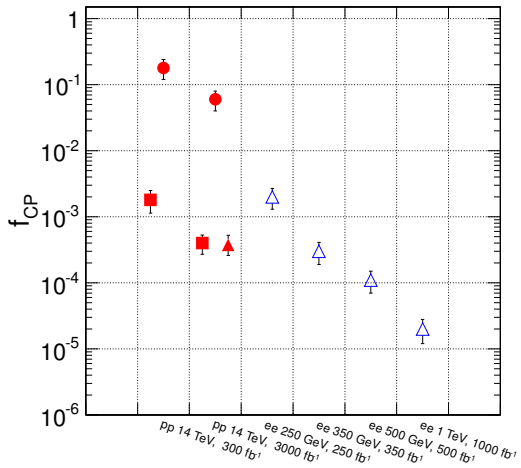

Figure 7.6: Summary of precision in f_{CP}(generalization of f_{a3}) for HVV couplings ($V = W, Z$) at the moment of 3σ measurement. Points indicate central values and error bars indicate 1σ deviations in the generated experiments modeling different luminosity scenarios at proton (solid red) or e^+e^- (open blue) colliders. Measurements in three topologies VH (triangles), VBF (squares), and decay $H \to VV$ (circles) are shown [61].

7.4 Implications: What did we find?

This document has presented the search, discovery, and classification of a new particle decaying into four-leptons. With only about 20 events seen by CMS in the resonance peak at 125 GeV these studies have made significant progress in characterizing this Higgs boson. The production mode matches with the expectations for the SM Higgs boson, showing vector and fermion induced production in rates that agree with the SM. The total width also seems to be consistent with theory predictions for this particle, and the 4ℓ final state, both near and away from the new peek seems to be consistent with a SM Higgs boson prediction. The spin-parity quantum numbers of the new boson disfavor many other potential bosons and strongly favor a scalar

SM-like Higgs boson with $J^{PC} = 0^{++}$.

Beyond finding and understanding the Higgs boson, this work can be helpful in understanding if the Higgs boson could be a window to BSM physics. The information that we have gathered does not give complete answers to these questions, nor is it the best ways to search for BSM physics, but it does help focus the picture. Specifically, the tests of f_{a3} are designed to see if there is any CP-violating component to the observed resonance. To the current sensitivity of these measurements, no deviations from a pure CP-even state are observed. This does not rule out the observed boson as a source of significant CP-violation but the current data does not support it. Offering a quantum explanation for gravity is also tested by some of the spin-two studies presented in this work which have motivations deeply connected to graviton hypotheses. Again, the data we observe strongly favor the SM Higgs boson over a spin-two particle.

The potential connection between the observed Higgs boson and dark matter is also probed. If there was a significant branching fraction of the observed boson to dark matter the production mechanism could show a deviation from SM behavior. Additionally, a significant Higgs boson – dark matter coupling would produce an increased total width of the Higgs boson that could be observed in the off shell width measurements. Given that all observations are currently consistent with the SM Higgs boson, dark matter still remains one of the most interesting mysteries in the universe.

Overall this thesis work presents some of the most comprehensive search and

characterization studies of the new Higgs boson that have been undertaken. The LHC accelerator and CMS experiment should be congratulated for their wonderful performance leading to these studies. While many questions about the SM remain, all signs point to the observed boson being consistent with one that would arise from the Higgs mechanism, offering the solution to at least one question.

Bibliography

[1] E. Noether, "Invariant Variation Problems," *Gott.Nachr.*, vol. 1918, pp. 235–257, 1918.

[2] Wikipedia, "Euler angles," 2015, [Accessed Feb. 9, 2015]. [Online]. Available: http://en.wikipedia.org/wiki/Euler_angles

[3] M. Maggiore, *A Modern Introduction to Quantum Field Theory.* Oxford University Press, 2005, ch. 5.1.

[4] F. Schwabl, *Quantum Mechanics*, 3rd ed. Springer, 2002.

[5] D. P. Hogan, "The Jayhawk Process," 2007, design for University of Kansas SPS T-shirts.

[6] S. L. Glashow, "Partial Symmetries of Weak Interactions," *Nucl. Phys.*, vol. 22, pp. 579–588, 1961.

[7] S. Weinberg, "A Model of Leptons," *Phys. Rev. Lett.*, vol. 19, pp. 1264–1266, 1967.

[8] A. Salam, "Elementary Particle Physics," *N. Svartholm ed., Almquvist and Wiksell, Stockholm*, 1968.

[9] S. L. Glashow, J. Iliopoulos, and L. Maiani, "Weak Interactions with Lepton-Hadron Symmetry," *Phys. Rev.*, vol. D2, pp. 1285–1292, 1970.

[10] D. Galbraith and C. Burgard, "UX: Standard Model of the Standard Model," 2012, CERN Webfest 2012. [Online]. Available: http://davidgalbraith.org/portfolio/ux-standard-model-of-the-standard-model/

[11] R. Aaij *et al.*, "Observation of the resonant character of the $Z(4430)^-$ state," *Phys.Rev.Lett.*, vol. 112, no. 22, p. 222002, 2014.

[12] M. A. Armstrong, *Groups and Symmetry.* Springer-Verlag, 1988.

[13] W. Miller, *Symmetry Groups and their Applications.* Academic Press, Inc., 1972.

[14] P. Oliver, *Applications of Lie Groups to Differential Equations*, 2nd ed. Springer-Verlag, 1993.

[15] W. Tung, *Group Theory in Physics.* World Scientific Publishing, 1985.

[16] D. J. Griffiths, *Introduction to Elementary Particles.* John Wiley & Sons, Inc., 1987, ch. 9 Quantum Chromodynamics.

[17] P. W. Higgs, "Broken symmetries, massless particles and gauge fields," *Phys.Lett.*, vol. 12, pp. 132–133, 1964.

[18] P. W. Higgs, "Broken Symmetries and the Masses of Gauge Bosons," *Phys.Rev.Lett.*, vol. 13, pp. 508–509, 1964.

[19] P. W. Higgs, "Spontaneous Symmetry Breakdown without Massless Bosons," *Phys.Rev.*, vol. 145, pp. 1156–1163, 1966.

[20] F. Englert and R. Brout, "Broken Symmetry and the Mass of Gauge Vector Mesons," *Phys.Rev.Lett.*, vol. 13, pp. 321–322, 1964.

[21] G. Guralnik, C. Hagen, and T. Kibble, "Global Conservation Laws and Massless Particles," *Phys.Rev.Lett.*, vol. 13, pp. 585–587, 1964.

[22] T. Kibble, "Symmetry breaking in nonAbelian gauge theories," *Phys.Rev.*, vol. 155, pp. 1554–1561, 1967.

[23] S. Dawson, "Introduction to Electroweak Symmetry Breaking," *AIP Conf.Proc.*, vol. 1116, pp. 11–34, 2009.

[24] Wolfram Research, Inc., "Mathematica," Champaign, Illinois, 2015, Version 10.1.

[25] M. Maggiore, *A Modern Introduction to Quantum Field Theory.* Oxford University Press, 2005, ch. 11.2.

[26] K. Olive *et al.*, "Review of Particle Physics," *Chin.Phys.*, vol. C38, p. 090001, 2014.

[27] M. Kobayashi and T. Maskawa, "CP Violation in the Renormalizable Theory of Weak Interaction," *Prog.Theor.Phys.*, vol. 49, pp. 652–657, 1973.

[28] O. Klein, "The Atomicity of Electricity as a Quantum Theory Law," *Nature*, vol. 118, p. 516, 1926.

[29] S. Weinberg, *The First Three Minutes. A Modern View of the Origin of the Universe.* Basic Books, 1977.

[30] V. Trimble, "Existence and Nature of Dark Matter in the Universe," *Ann.Rev.Astron.Astrophys.*, vol. 25, pp. 425–472, 1987.

[31] Brüning, Oliver Sim and Collier, Paul and Lebrun, P and Myers, Stephen and Ostojic, Ranko and Poole, John and Proudlock, Paul, *LHC Design Report.* Geneva: CERN, 2004. [Online]. Available: http://cds.cern.ch/record/782076

[32] LHC Programme Coordination, "LHC Luminosity Plots for the 2012(2011) Proton Run," 2011, 2012. [Online]. Available: http://lpc.web.cern.ch/lpc/

[33] O. S. Bruning and P. Collier, "Building a behemoth," *Nature*, vol. 448, pp. 285–289, 2007.

[34] Public CMS Luminosity Information, "2012(2011) Proton-Proton Collisions, Luminosity versus day," 2011, 2012. [Online]. Available: https://twiki.cern.ch/twiki/bin/view/CMSPublic/LumiPublicResults

[35] G. L. Bayatian *et al.*, *CMS Physics: Technical Design Report Volume 1: Detector Performance and Software*, ser. Technical Design Report CMS. Geneva: CERN, 2006, there is an error on cover due to a technical problem for some items. [Online]. Available: https://cds.cern.ch/record/922757

[36] T. Sakuma and T. McCauley, "Detector and Event Visualization with SketchUp at the CMS Experiment," *J.Phys.Conf.Ser.*, vol. 513, p. 022032, 2014.

[37] S. Chatrchyan *et al.*, "Precise Mapping of the Magnetic Field in the CMS Barrel Yoke using Cosmic Rays," *JINST*, vol. 5, p. T03021, 2010.

[38] S. Chatrchyan *et al.*, "Alignment of the CMS tracker with LHC and cosmic ray data," *JINST*, vol. 9, p. P06009, 2014.

[39] D. Kotlinski, R. Baur, R. P. Horisberger, R. Schnyder, W. Erdmann, and K. Gabathuler, "Readout of the CMS pixel detector," *CERN Document Server*, 2000. [Online]. Available: https://cds.cern.ch/record/478252

[40] S. Chatrchyan *et al.*, "The CMS experiment at the CERN LHC. The Compact Muon Solenoid experiment," *J. Instrum.*, vol. 3, p. S08004. 361 p, 2008, also published by CERN Geneva in 2010. [Online]. Available: https://cds.cern.ch/record/1129810

[41] S. Chatrchyan *et al.*, "Measurement of the properties of a Higgs boson in the four-lepton final state," *Phys.Rev.*, vol. D89, no. 9, p. 092007, 2014.

[42] S. Chatrchyan *et al.*, "Performance of CMS Hadron Calorimeter Timing and Synchronization using Test Beam, Cosmic Ray, and LHC Beam Data," *JINST*, vol. 5, p. T03013, 2010.

[43] S. Chatrchyan *et al.*, "Particle-Flow Event Reconstruction in CMS and Performance for Jets, Taus, and MET," CERN, 2009. Geneva, Tech. Rep. CMS-PAS-PFT-09-001, Apr 2009. [Online]. Available: https://cds.cern.ch/record/1194487

[44] S. Chatrchyan *et al.*, "Electron reconstruction and identification at sqrt(s) = 7 TeV," CERN, Geneva, Tech. Rep. CMS-PAS-EGM-10-004, 2010. [Online]. Available: http://cds.cern.ch/record/1299116

[45] S. Chatrchyan *et al.*, "Electron performance with 19.6 fb^{-1} of data collected at $\sqrt{s} = 8$ TeV with the CMS detector." *CERN Document Server*, Mar 2013. [Online]. Available: http://cds.cern.ch/record/1523273

[46] M. Cacciari, G. P. Salam, and G. Soyez, "The Anti-k(t) jet clustering algorithm," *JHEP*, vol. 0804, p. 063, 2008.

[47] S. Chatrchyan *et al.*, "Determination of Jet Energy Calibration and Transverse Momentum Resolution in CMS," *JINST*, vol. 6, p. P11002, 2011.

[48] S. Chatrchyan *et al.*, "Alignment of the CMS Silicon Tracker during Commissioning with Cosmic Rays," *JINST*, vol. 5, p. T03009, 2010.

[49] V. Blobel and C. Kleinwort, "A New method for the high precision alignment of track detectors," *eConf*, pp. URL–STR(9), 2002.

[50] V. Karimaki, T. Lampen, and F. Schilling, "The HIP algorithm for track based alignment and its application to the CMS pixel detector," *CERN Document Server*, 2006.

[51] A. Bonato *et al.*, "Application of Survey Measurements in Tracker Alignment," *CMS Internal Note*, 2009.

[52] W. Adam *et al.*, "Alignment of the CMS Silicon Strip Tracker during stand-alone Commissioning," *JINST*, vol. 4, p. T07001, 2009.

[53] S. Chatrchyan *et al.*, "Alignment of the CMS Tracking-Detector with First 2015 Cosmic-Ray and Collision Data," *CERN Document Server*, Aug 2015. [Online]. Available: http://cds.cern.ch/record/2041841

[54] S. Chatrchyan *et al.*, "2012 CMS Tracker Alignment: Performance Plots," *CERN Document Server*, May 2013. [Online]. Available: https://cds.cern.ch/record/1552581

[55] LHC Higgs Cross Section Working Group, S. Dittmaier, C. Mariotti, G. Passarino, and R. Tanaka (Eds.), "Handbook of LHC Higgs Cross Sections: 1. Inclusive Observables," *CERN-2011-002*, CERN, Geneva, 2011.

[56] LHC Higgs Cross Section Working Group, S. Dittmaier, C. Mariotti, G. Passarino, and R. Tanaka (Eds.), "Handbook of LHC Higgs Cross Sections: 2. Differential Distributions," *CERN-2012-002*, CERN, Geneva, 2012.

[57] LHC Higgs Cross Section Working Group, S. Heinemeyer, C. Mariotti, G. Passarino, and R. Tanaka (Eds.), "Handbook of LHC Higgs Cross Sections: 3. Higgs Properties," *CERN-2013-004*, CERN, Geneva, 2013.

[58] N. Kauer and G. Passarino, "Inadequacy of zero-width approximation for a light Higgs boson signal," *JHEP*, vol. 1208, p. 116, 2012.

[59] F. Caola and K. Melnikov, "Constraining the Higgs boson width with ZZ production at the LHC," *Phys.Rev.*, vol. D88, p. 054024, 2013.

[60] V. Khachatryan *et al.*, "Constraints on the Higgs boson width from off-shell production and decay to Z-boson pairs," *Phys.Lett.*, vol. B736, p. 64, 2014.

[61] I. Anderson, S. Bolognesi, F. Caola, Y. Gao, A. V. Gritsan *et al.*, "Constraining anomalous HVV interactions at proton and lepton colliders," *Phys.Rev.*, vol. D89, no. 3, p. 035007, 2014.

[62] V. Khachatryan *et al.*, "Constraints on the spin-parity and anomalous HVV couplings of the Higgs boson in proton collisions at 7 and 8 TeV," *Phys. Rev.*, vol. D92, no. 1, p. 012004, 2015.

[63] Y. Gao, A. V. Gritsan, Z. Guo, K. Melnikov, M. Schulze *et al.*, "Spin determination of single-produced resonances at hadron colliders," *Phys.Rev.*, vol. D81, p. 075022, 2010.

[64] S. Bolognesi, Y. Gao, A. V. Gritsan, K. Melnikov, M. Schulze *et al.*, "On the spin and parity of a single-produced resonance at the LHC," *Phys.Rev.*, vol. D86, p. 095031, 2012.

[65] L. Landau, "On the angular momentum of a two-photon system," *Dokl.Akad.Nauk Ser.Fiz.*, vol. 60, pp. 207–209, 1948.

[66] C.-N. Yang, "Selection Rules for the Dematerialization of a Particle Into Two Photons," *Phys.Rev.*, vol. 77, pp. 242–245, 1950.

[67] G. Aad *et al.*, "Observation of a new particle in the search for the Standard Model Higgs boson with the ATLAS detector at the LHC," *Phys.Lett.*, vol. B716, pp. 1–29, 2012.

[68] S. Chatrchyan *et al.*, "Observation of a new boson at a mass of 125 GeV with the CMS experiment at the LHC," *Phys.Lett.*, vol. B716, pp. 30–61, 2012.

[69] S. Chatrchyan *et al.*, "Observation of a new boson with mass near 125 GeV in pp collisions at $\sqrt{s} = 7$ and 8 TeV," *JHEP*, vol. 1306, p. 081, 2013.

[70] L. Randall and R. Sundrum, "An Alternative to compactification," *Phys.Rev.Lett.*, vol. 83, pp. 4690–4693, 1999.

[71] L. Randall and R. Sundrum, "A Large mass hierarchy from a small extra dimension," *Phys.Rev.Lett.*, vol. 83, pp. 3370–3373, 1999.

[72] K. Agashe, H. Davoudiasl, G. Perez, and A. Soni, "Warped Gravitons at the LHC and Beyond," *Phys.Rev.*, vol. D76, p. 036006, 2007.

[73] J. M. Cornwall, D. N. Levin, and G. Tiktopoulos, "Derivation of gauge invariance from high-energy unitarity bounds on the s matrix," *Phys. Rev. D*, vol. 10, pp. 1145–1167, Aug 1974. [Online]. Available: http://link.aps.org/doi/10.1103/PhysRevD.10.1145

[74] B. W. Lee, C. Quigg, and H. B. Thacker, "Weak interactions at very high energies: The role of the higgs-boson mass," *Phys. Rev. D*, vol. 16, pp. 1519–1531, Sep 1977. [Online]. Available: http://link.aps.org/doi/10.1103/PhysRevD.16.1519

[75] J. M. Cornwall, D. N. Levin, and G. Tiktopoulos, "Uniqueness of spontaneously broken gauge theories," *Phys. Rev. Lett.*, vol. 30, pp. 1268–1270, Jun 1973. [Online]. Available: http://link.aps.org/doi/10.1103/PhysRevLett.30.1268

[76] C. L. Smith, "High energy behaviour and gauge symmetry," *Physics Letters B*, vol. 46, no. 2, pp. 233 – 236, 1973. [Online]. Available: http://www.sciencedirect.com/science/article/pii/0370269373906928

[77] L. E. W. Group, "Precision Electroweak Measurements and Constraints on the Standard Model," *Eprint Only*, 2010.

[78] R. Barate *et al.*, "Search for the standard model Higgs boson at LEP," *Phys.Lett.*, vol. B565, pp. 61–75, 2003.

[79] T. Aaltonen *et al.*, "Higgs Boson Studies at the Tevatron," *Phys.Rev.*, vol. D88, no. 5, p. 052014, 2013.

[80] T. Aaltonen *et al.*, "Evidence for a particle produced in association with weak bosons and decaying to a bottom-antibottom quark pair in Higgs boson searches at the Tevatron," *Phys.Rev.Lett.*, vol. 109, p. 071804, 2012.

[81] M. Cacciari and G. P. Salam, "Pileup subtraction using jet areas," *Phys.Lett.*, vol. B659, pp. 119–126, 2008.

[82] M. Cacciari, G. P. Salam, and G. Soyez, "The Catchment Area of Jets," *JHEP*, vol. 0804, p. 005, 2008.

[83] P. Nason and C. Oleari, "NLO Higgs boson production via vector-boson fusion matched with shower in POWHEG," *JHEP*, vol. 1002, p. 037, 2010.

[84] E. Bagnaschi, G. Degrassi, P. Slavich, and A. Vicini, "Higgs production via gluon fusion in the POWHEG approach in the SM and in the MSSM," *JHEP*, vol. 1202, p. 088, 2012.

[85] S. Frixione, P. Nason, and C. Oleari, "Matching NLO QCD computations with Parton Shower simulations: the POWHEG method," *JHEP*, vol. 0711, p. 070, 2007.

[86] T. Sjostrand, S. Mrenna, and P. Z. Skands, "PYTHIA 6.4 Physics and Manual," *JHEP*, vol. 0605, p. 026, 2006.

[87] S. Dawson, "Radiative corrections to higgs boson production," *Nuclear Physics B*, vol. 359, no. 2âĂŽÃĎÃň3, pp. 283 – 300, 1991. [Online]. Available: http://www.sciencedirect.com/science/article/pii/0550321391900612

[88] A. Djouadi, M. Spira, and P. Zerwas, "Production of higgs bosons in proton colliders. {QCD} corrections," *Physics Letters B*, vol. 264, no. 3âĂŽÃĎÃň4, pp. 440 – 446, 1991. [Online]. Available: http://www.sciencedirect.com/science/article/pii/037026939190375Z

[89] S. Actis, G. Passarino, C. Sturm, and S. Uccirati, "NLO Electroweak Corrections to Higgs Boson Production at Hadron Colliders," *Phys.Lett.*, vol. B670, pp. 12–17, 2008.

[90] S. Catani, D. de Florian, M. Grazzini, and P. Nason, "Soft gluon resummation for Higgs boson production at hadron colliders," *JHEP*, vol. 0307, p. 028, 2003.

[91] V. Ravindran, J. Smith, and W. L. van Neerven, "NNLO corrections to the

total cross-section for Higgs boson production in hadron hadron collisions," *Nucl.Phys.*, vol. B665, pp. 325–366, 2003.

[92] C. Anastasiou and K. Melnikov, "Higgs boson production at hadron colliders in NNLO QCD," *Nucl.Phys.*, vol. B646, pp. 220–256, 2002.

[93] R. V. Harlander and W. B. Kilgore, "Next-to-next-to-leading order Higgs production at hadron colliders," *Phys.Rev.Lett.*, vol. 88, p. 201801, 2002.

[94] M. Spira, A. Djouadi, D. Graudenz, and P. Zerwas, "Higgs boson production at the LHC," *Nucl.Phys.*, vol. B453, pp. 17–82, 1995.

[95] J. Baglio and A. Djouadi, "Higgs production at the lHC," *JHEP*, vol. 1103, p. 055, 2011.

[96] C. Anastasiou, R. Boughezal, and F. Petriello, "Mixed QCD-electroweak corrections to Higgs boson production in gluon fusion," *JHEP*, vol. 0904, p. 003, 2009.

[97] D. de Florian, G. Ferrera, M. Grazzini, and D. Tommasini, "Higgs boson production at the LHC: transverse momentum resummation effects in the H to 2gamma, H to WW to lnu lnu and H to ZZ to 4l decay modes," *JHEP*, vol. 1206, p. 132, 2012.

[98] M. Ciccolini, A. Denner, and S. Dittmaier, "Strong and electroweak correc-

tions to the production of Higgs + 2jets via weak interactions at the LHC," *Phys.Rev.Lett.*, vol. 99, p. 161803, 2007.

[99] M. Ciccolini, A. Denner, and S. Dittmaier, "Electroweak and QCD corrections to Higgs production via vector-boson fusion at the LHC," *Phys.Rev.*, vol. D77, p. 013002, 2008.

[100] T. Figy, C. Oleari, and D. Zeppenfeld, "Next-to-leading order jet distributions for Higgs boson production via weak boson fusion," *Phys.Rev.*, vol. D68, p. 073005, 2003.

[101] K. Arnold, M. Bahr, G. Bozzi, F. Campanario, C. Englert *et al.*, "VBFNLO: A Parton level Monte Carlo for processes with electroweak bosons," *Comput.Phys.Commun.*, vol. 180, pp. 1661–1670, 2009.

[102] P. Bolzoni, F. Maltoni, S.-O. Moch, and M. Zaro, "Higgs production via vector-boson fusion at NNLO in QCD," *Phys.Rev.Lett.*, vol. 105, p. 011801, 2010.

[103] T. Melia, P. Nason, R. Rontsch, and G. Zanderighi, "W+W-, WZ and ZZ production in the POWHEG BOX," *JHEP*, vol. 1111, p. 078, 2011.

[104] T. Binoth, N. Kauer, and P. Mertsch, "Gluon-induced QCD corrections to pp to ZZ to l anti-l l-prime anti-l-prime," *Eprint only*, p. 142, 2008.

[105] J. M. Campbell, R. K. Ellis, and C. Williams, "Vector boson pair production at the LHC," *JHEP*, vol. 1107, p. 018, 2011.

[106] J. M. Campbell and R. K. Ellis, "An Update on vector boson pair production at hadron colliders," *Phys.Rev.*, vol. D60, p. 113006, 1999.

[107] J. M. Campbell and R. Ellis, "MCFM for the Tevatron and the LHC," *Nucl.Phys.Proc.Suppl.*, vol. 205-206, pp. 10–15, 2010.

[108] J. Alwall, P. Demin, S. de Visscher, R. Frederix, M. Herquet *et al.*, "MadGraph/MadEvent v4: The New Web Generation," *JHEP*, vol. 0709, p. 028, 2007.

[109] H.-L. Lai, J. Huston, Z. Li, P. Nadolsky, J. Pumplin *et al.*, "Uncertainty induced by QCD coupling in the CTEQ global analysis of parton distributions," *Phys.Rev.*, vol. D82, p. 054021, 2010.

[110] H.-L. Lai, M. Guzzi, J. Huston, Z. Li, P. M. Nadolsky *et al.*, "New parton distributions for collider physics," *Phys.Rev.*, vol. D82, p. 074024, 2010.

[111] S. Agostinelli *et al.*, "Geant4-a simulation toolkit," *Nuclear Instruments and Methods in Physics Research Section A: Accelerators, Spectrometers, Detectors and Associated Equipment*, vol. 506, no. 3, pp. 250 – 303, 2003. [Online]. Available: http://www.sciencedirect.com/science/article/pii/S0168900203013688

[112] J. Allison, K. Amako, J. Apostolakis, H. Araujo, P. Dubois *et al.*, "Geant4 developments and applications," *IEEE Trans.Nucl.Sci.*, vol. 53, p. 270, 2006.

[113] G. Passarino, C. Sturm, and S. Uccirati, "Higgs Pseudo-Observables, Second Riemann Sheet and All That," *Nucl.Phys.*, vol. B834, pp. 77–115, 2010.

[114] S. Goria, G. Passarino, and D. Rosco, "The Higgs Boson Lineshape," *Nucl.Phys.*, vol. B864, pp. 530–579, 2012.

[115] N. Cabibbo and A. Maksymowicz, "Angular correlations in K_{e4} decays and determination of low-energy $\pi - \pi$ phase shifts," *Phys. Rev.*, vol. 168, pp. 1926–1926, Apr 1968. [Online]. Available: http://link.aps.org/doi/10.1103/PhysRev.168.1926

[116] S. Chatrchyan *et al.*, "Study of the Mass and Spin-Parity of the Higgs Boson Candidate Via Its Decays to Z Boson Pairs," *Phys.Rev.Lett.*, vol. 110, no. 8, p. 081803, 2013.

[117] CMS, "Absolute Calibration of Luminosity Measurement at CMS: Summer 2011 Update," CERN, Geneva, Tech. Rep. CMS-PAS-EWK-11-001, 2011. [Online]. Available: http://cds.cern.ch/record/1376102

[118] CMS, "CMS Luminosity Based on Pixel Cluster Counting - Summer 2013 Update," CERN, Geneva, Tech. Rep. CMS-PAS-LUM-13-001, 2013. [Online]. Available: http://cds.cern.ch/record/1598864

[119] A. Denner, S. Heinemeyer, I. Puljak, D. Rebuzzi, and M. Spira, "Standard

Model Higgs-Boson Branching Ratios with Uncertainties," *Eur.Phys.J.*, vol. C71, p. 1753, 2011.

[120] T. Junk, "Confidence level computation for combining searches with small statistics," *Nucl.Instrum.Meth.*, vol. A434, pp. 435–443, 1999.

[121] A. L. Read, "Presentation of search results: The CL(s) technique," *J.Phys.*, vol. G28, pp. 2693–2704, 2002.

[122] ATLAS and CMS, "Procedure for the LHC Higgs boson search combination in Summer 2011," CERN, Geneva, Tech. Rep. CMS-NOTE-2011-005. ATL-PHYS-PUB-2011-11, Aug 2011. [Online]. Available: http://cds.cern.ch/record/1379837

[123] E. Gross and O. Vitells, "Trial factors or the look elsewhere effect in high energy physics," *Eur.Phys.J.*, vol. C70, pp. 525–530, 2010.

[124] G. Aad *et al.*, "Measurements of Higgs boson production and couplings in diboson final states with the ATLAS detector at the LHC," *Phys.Lett.*, vol. B726, pp. 88–119, 2013.

[125] G. Aad *et al.*, "Evidence for the spin-0 nature of the Higgs boson using ATLAS data," *Phys.Lett.*, vol. B726, pp. 120–144, 2013.

[126] N. Kauer, "Inadequacy of zero-width approximation for a light Higgs boson signal," *Mod.Phys.Lett.*, vol. A28, p. 1330015, 2013.

[127] J. M. Campbell, R. K. Ellis, and C. Williams, "Bounding the Higgs width at the LHC using full analytic results for $gg- > e^-e^+\mu^-\mu^+$," *JHEP*, vol. 1404, p. 060, 2014.

[128] G. Passarino, "Higgs CAT," *Eur.Phys.J.*, vol. C74, p. 2866, 2014.

[129] S. Chatrchyan *et al.*, "Search for a standard-model-like Higgs boson with a mass in the range 145 to 1000 GeV at the LHC," *Eur.Phys.J.*, vol. C73, p. 2469, 2013.

[130] S. Chatrchyan *et al.*, "Search for the standard model Higgs boson in the H to ZZ to 2 $\ell 2\nu$ channel in pp collisions at $\sqrt{s} = 7$ TeV," *JHEP*, vol. 1203, p. 040, 2012.

[131] N. Kauer, "Interference effects for H $\rightarrow$ WW/ZZ $\rightarrow \ell\bar{\nu}_\ell\bar{\ell}\nu_\ell$ searches in gluon fusion at the LHC," *JHEP*, vol. 1312, p. 082, 2013.

[132] A. Martin, W. Stirling, R. Thorne, and G. Watt, "Parton distributions for the LHC," *Eur.Phys.J.*, vol. C63, pp. 189–285, 2009.

[133] M. Bonvini, F. Caola, S. Forte, K. Melnikov, and G. Ridolfi, "Signal-background interference effects for $ggHW^+W^-$ beyond leading order," *Phys.Rev.*, vol. D88, no. 3, p. 034032, 2013.

[134] A. Ballestrero, A. Belhouari, G. Bevilacqua, V. Kashkan, and E. Maina, "PHANTOM: A Monte Carlo event generator for six parton final states at high energy colliders," *Comput.Phys.Commun.*, vol. 180, pp. 401–417, 2009.

[135] A. Bierweiler, T. Kasprzik, and J. H. KÃijhn, "Vector-boson pair production at the LHC to $\mathcal{O}(\alpha^3)$ accuracy," *JHEP*, vol. 1312, p. 071, 2013.

[136] J. Baglio, L. D. Ninh, and M. M. Weber, "Massive gauge boson pair production at the LHC: a next-to-leading order story," *Phys.Rev.*, vol. D88, p. 113005, 2013.

[137] S. Chatrchyan *et al.*, "Identification of b-quark jets with the CMS experiment," *JINST*, vol. 8, p. P04013, 2013.

[138] R. D. Ball, V. Bertone, F. Cerutti, L. Del Debbio, S. Forte *et al.*, "Impact of Heavy Quark Masses on Parton Distributions and LHC Phenomenology," *Nucl.Phys.*, vol. B849, pp. 296–363, 2011.

[139] N. Amapane *et al.*, "A measurement of the Higgs boson width using off-shell production and decay to 4 leptons," *CMS Internal Analysis Note*, vol. 2014/018, 2014.

[140] S. Chatrchyan *et al.*, "Search for a Higgs boson in the decay channel H to ZZ(*) to q qbar ℓ^- l+ in pp collisions at $\sqrt{s} = 7$ TeV," *JHEP*, vol. 04, p. 036, 2012.

[141] Y. Chen, N. Tran, and R. Vega-Morales, "Scrutinizing the Higgs Signal and Background in the $2e2\mu$ Golden Channel," *JHEP*, vol. 1301, p. 182, 2013.

[142] M. Rosenblatt, "Remarks on some nonparametric estimates of a density

function," *Ann. Math. Statist.*, vol. 27, no. 3, pp. 832–837, 09 1956. [Online]. Available: http://dx.doi.org/10.1214/aoms/1177728190

[143] E. Parzen, "On estimation of a probability density function and mode," *Ann. Math. Statist.*, vol. 33, no. 3, pp. 1065–1076, 09 1962. [Online]. Available: http://dx.doi.org/10.1214/aoms/1177704472

[144] S. Wilks, "The Large-Sample Distribution of the Likelihood Ratio for Testing Composite Hypotheses," *Annals Math.Statist.*, vol. 9, no. 1, pp. 60–62, 1938.

[145] S. Chatrchyan *et al.*, "Search for a Higgs boson decaying into a Z and a photon in pp collisions at $\sqrt{s} = 7$ and 8 TeV," *Phys.Lett.*, vol. B726, pp. 587–609, 2013.

[146] V. Khachatryan *et al.*, "Observation of the diphoton decay of the Higgs boson and measurement of its properties," *Eur.Phys.J.*, vol. C74, no. 10, p. 3076, 2014.

[147] S. Dawson *et al.*, "Working Group Report: Higgs Boson," in *Community Summer Study 2013: Snowmass on the Mississippi (CSS2013) Minneapolis, MN, USA, July 29-August 6, 2013*, 2013. [Online]. Available: https://inspirehep.net/record/1262795/files/arXiv:1310.8361.pdf

[148] Y. Chen, R. Harnik, and R. Vega-Morales, "Probing the Higgs Couplings to Photons in hâĘŠ4âĎŞ at the LHC," *Phys.Rev.Lett.*, vol. 113, no. 19, p. 191801, 2014.

[149] V. Khachatryan *et al.*, "Search for a Higgs boson in the mass range from 145 to

1000 GeV decaying to a pair of W or Z bosons," 2015, comments: Submitted to JHEP.

[150] V. Khachatryan *et al.*, "Precise determination of the mass of the Higgs boson and tests of compatibility of its couplings with the standard model predictions using proton collisions at 7 and 8 TeV," *Eur.Phys.J.*, vol. C75, no. 5, p. 212, 2015.

[151] G. Aad *et al.*, "Constraints on the off-shell Higgs boson signal strength in the high-mass ZZ and WW final states with the ATLAS detector," *Eur. Phys. J.*, vol. C75, no. 7, p. 335, 2015.

[152] N. Amapane *et al.*, "Lifetime of the Higgs boson and constraints on its width considering anomalous couplings with H to 4l," *CMS Internal Analysis Note*, vol. 2014/247, 2014.

Vita

Christopher B. Martin was born in Kansas, USA. He attended the University of Kansas (KU) in graduating in 2010 with Distinction, University Honors, and Physics Departmental Honors with a B.Sc in Physics and a B.Sc in Mathematics. For the fall semester of 2008 he studied abroad at Eidgenössische Technische Hochschule (ETH) in Zürich, Switzerland. As an undergraduate he worked as a research assistant on the CMS experiment and as part of an NSF PIRE grant to develop silicon pixel detector tech-nology. As part of the PIRE program he performed research at KU and at the Paul Scherrer Institut (PSI) in Villigen, Switzerland.

He enrolled in the physics Ph.D program at Johns Hopkins University, researching experimental particle physics on the CMS experiment. He focused on the search, discovery, and characterization of the Higgs boson. He authored many papers as part of the CMS Collaboration and was a main author of many Higgs boson related results, both within the collaboration and with an independent group of collaborators. Chris taught multiple basic physics courses as a graduate student and served as the

Observatory Technician for the Maryland Space Grant Consortium.

Chris will go on to a postdoctoral research position at The Ohio State University Department of Physics. He will be based at CERN in Genevé, Switzerland working on the ATLAS Experiment.